

UNIVERSITÀ DEGLI STUDI DI PADOVA

Dipartimento di Fisica e Astronomia “Galileo Galilei”

Master Degree in Physics

Final Dissertation

Lower mass bounds on FIMP Dark Matter

Thesis supervisor

Dr. Francesco D’Eramo

Candidate

Alessandro Lenoci

Academic Year 2019/2020

Abstract

Over the last decades, strong evidence for dark matter (DM) has been accumulated. However, its nature is still unknown in fundamental physics. A cold relic produced via thermal freeze-out has been the leading paradigm for a long period, both for its simplicity and versatility to include candidates offered by extensions of the Standard Model of particle physics. Despite a large experimental effort to detect these candidates, no conclusive evidence has been found yet. The outcome of these negative searches has been motivating the community to explore alternative paradigms to the freeze-out. One of these is the freeze-in scenario, first introduced by Hall et al. (2009), which shares the advantages of the freeze-out paradigm but in which DM is produced out of thermal equilibrium. In this work, after a review of the evidence of DM and the Boltzmann equation formalism, we present the main features of the freeze-in paradigm proving its efficiency in reproducing the relic density. Despite the usually smaller couplings between DM and visible matter in the freeze-in scenario, frozen-in DM candidates, called Feebly Interacting Particles (FIMPs), can have interesting observational features through which freeze-in models can be constrained. Among them, stringent bounds can come from structure formation data. In particular, too light FIMP DM is in tension with small-scales structures such as the Lyman- α forest. We develop a model independent procedure to constrain the parameter space of a FIMP model and to extract the value of the minimum DM mass allowed, which is of crucial importance in model building. The methodology is based on the comparison of the linear matter power spectrum, computed with the CLASS code, from the non-thermal FIMP phase-space distribution, with the limit power spectrum obtained from a Warm Dark Matter (WDM) model, found by M. Viel et al. (2017). To test our procedure and compare with the literature, we consider three simple scalar FIMP DM toy models involving renormalizable interactions with hypothetical scalars belonging to the thermal bath. These are benchmarks models in which DM production is dominated by decays and scatterings and can be used to draw general conclusions on FIMP DM produced via these mechanisms. The developed procedure can also be applied to concrete freeze-in models and frameworks in which the DM production occurs in modified cosmologies and can be generalized to include also additional external bounds on the linear matter power spectrum.

Contents

Introduction	1
1 Evidence for Dark Matter	3
1.1 Galactic scales	5
1.1.1 Galactic rotation curves	5
1.1.2 Gravitational lensing	7
1.2 Galaxy cluster scales	7
1.3 Cosmological scales	10
1.3.1 Structure formation	10
1.3.2 Cosmic Microwave Background	15
1.3.3 Type Ia supernovae	20
1.3.4 Big Bang Nucleosynthesis	20
1.4 Beyond the Standard Model of Particle Physics	23
1.4.1 The Standard Model is incomplete	23
1.4.2 SM neutrinos as Dark Matter?	24
1.5 What we <i>do</i> know about Dark Matter	27
2 Boltzmann Equation Formalism	35
2.1 Evolution of phase-space distribution	35
2.1.1 The Liouville operator	36
2.1.2 The collision operator	37
2.2 Equilibrium phase-space distributions	40
2.3 Evolution of number density	41
2.4 Standard application: freeze-out production of DM	42
2.4.1 Hot Relics: $x_{\text{FO}} \lesssim 1$	47
2.4.2 Cold Relics: $x_{\text{FO}} > 1$	48
2.4.3 The fall of the WIMP paradigm	51
3 Freeze-in production of Dark Matter	55
3.1 General features of freeze-in	55
3.2 Evolution of FIMP abundance	57
3.2.1 Freeze-in from decays	58
3.2.2 Freeze-in from collisions	61

3.3	Observational features of frozen-in Dark Matter	69
3.3.1	Direct detection signatures	70
3.3.2	Indirect detection signatures	73
3.3.3	Collider signatures	75
3.3.4	Large-scales signatures	76
3.3.5	Small-scales signatures	77
4	Constraints on FIMP parameters: methodology	83
4.1	General procedure	84
4.2	Phase-space distribution for our models	87
4.2.1	Trilinear scalar interaction	88
4.2.2	Quadrilinear scalar interaction for single production	92
4.2.3	Quadrilinear scalar interaction for pair production	95
4.3	The linear matter power spectrum from CLASS	97
4.3.1	The CLASS code	97
4.3.2	WDM and Lyman- α bounds	99
5	Constraints on FIMP parameters: results	111
5.1	Our code	111
5.1.1	Structure	112
5.1.2	Input	114
5.1.3	Output	115
5.2	Constraints on m_χ	116
5.2.1	Trilinear model	116
5.2.2	Quadrilinear model for single production	121
5.2.3	Quadriliner model for pair production	123
	Conclusions	135
	Acknowledgements	139
A	Friedmann-Roberston-Walker cosmology	141
A.1	The expanding Universe	141
A.1.1	The Friedmann-Robertson-Walker metric	142
A.1.2	Friedmann equations	143
A.1.3	The equation of state	146
A.2	Thermodynamics in the expanding Universe	148
A.2.1	Equilibrium results	149
A.2.2	Effective number of degrees of freedom	152
A.2.3	Temperature as time variable	155
B	ΛCDM on small scales	157
B.1	Controversies	157
B.2	Possible solutions	160
B.2.1	Baryonic physics	160

B.2.2	Warm dark matter	161
B.2.3	Self Interacting dark matter	161
C	The collision operator from first principles	163
D	Collision terms for various processes	167
D.1	Two-body decays	167
D.2	Scatterings	170
D.2.1	Single production	170
D.2.2	Pair production	174
D.3	Three-body decays	175
D.3.1	Single production	175
D.3.2	Pair production	177

Introduction

A prominent challenge for modern fundamental physics is to answer the fundamental question: "What is our Universe made of?", or better "What is the mass-energy content of our Universe?". Up to now, we were able to split the energy budget of today's Universe in two: the *known* ordinary baryonic matter and radiation, described by the Standard Model of Particle Physics (SM) and accounting for about 5% of the total energy density, and the *unknown*, made of dark matter (DM) accounting for about 27% and dark energy (DE) for about 68%. The nature of the dark constituents remains a mystery.

The accumulation of evidence in the last three decades has suggested that dark matter is made of particles very weakly coupled with the SM states, whose velocity dispersion in the early Universe was too small to erase observed structures on galactic or sub-galactic scales. This DM paradigm is called Cold Dark Matter (CDM). The outlined energy budget – SM particles described as baryons and radiation fluids plus CDM pressureless fluid and a cosmological constant to account for dark energy – together with the hypothesis of a geometrically flat Universe, verified to permille accuracy, has been implemented in the standard cosmological model. This paradigm, called Λ CDM, has been remarkably successful in describing cosmological observables during the last decades.

Many extensions of the SM have been proposed, trying to give us a fundamental picture for the constituents of our Universe and their interactions, but none of them has been experimentally successful so far. The most natural mechanisms for the production of DM particles, the thermal *freeze-out* of Weakly Interacting Massive Particles (WIMPs), has received great attention by the particle physics and cosmology community and has been implemented in beyond-SM (BSM) theories. However, the proposed particle candidates in such models have avoided any direct or indirect detection, so far. Nowadays, increasingly accurate experiments are constraining the parameter space for BSM theories involving a thermal DM candidate, limiting model building within the freeze-out paradigm.

Motivated by the crisis of this paradigm, there is a growing interest in the community for non-thermal models. In this work, we focus on the so-called *freeze-in* mechanism, first proposed in [1]. In the basic scenario, the DM consists of Feebly Interacting Massive Particles (FIMPs), which interact so weakly with the baryon-photon fluid in the early Universe, that they never attained thermal equilibrium. In particular, we will study

the phase-space properties of such DM candidates in the Boltzmann equation formalism, improving the present constraints on parameters of freeze-in models.

The work is organized as follows: in Chapter 1, we outline the present evidence for DM at our disposal and we summarize the main known features of a generic DM particle candidate. Then in Chapter 2, we review the Boltzmann equation formalism and the standard thermal-freeze-out paradigm to compute the relic abundance. In Chapter 3 we present the freeze-in mechanism highlighting analogies and differences with the freeze-out and see for some scalar toy models how the paradigm can reproduce the observed abundance; we conclude the chapter with a review of the observational signatures of FIMP DM particles and the way observations are exploited to constrain the models. Subsequently, in Chapter 4 we outline the general methodology to constrain a given freeze-in model with data from structure formation and apply the developed scheme to some toy models. In particular, we consider a scalar DM candidate interacting with simple four-dimensional operators with scalar particle belonging to the primordial thermal bath. To prove the efficiency of our methodology we find the lower mass bounds on these DM candidates. We conclude in Chapter 5 presenting the obtained results for the considered models and comment on the obtained bounds.

Throughout the work we refer to Appendices A-D where we report specific computations and insights on topics mentioned in the text. In particular, in Appendix A we review the basic formalism of the Friedmann-Robertson-Walker (FRW) cosmology, to describe the behaviour of particle species in the expanding Universe. In Appendix B we review the small-scales shortcomings of the leading Λ CDM model, as well as possible solutions involving baryonic physics or, more interestingly for us, new physics and particular features of the dark matter. In Appendix C we present the calculation of the collision operator starting from first principles in the Boltzmann equation formalism, whose computation is the starting point to characterize the evolution of particle species in the early Universe. Finally, in Appendix D we show in detail the calculation of explicit collision terms for the most common DM production processes – two- and three-body decays, scattering and pair production – in a model-independent way.

Chapter 1

Evidence for Dark Matter

In this chapter, we review, following [2–4], the most important evidence for DM that the scientific community has accumulated over the last decades. We shall briefly see how, historically, the very first clues of missing mass in some systems merged into a single anomaly at all scales, ranging from (sub-)galactic scales (pc - 100 kpc) and clusters of galaxies (1 - 100 Mpc) to cosmological scales of the size of the observable Universe (100 - 10^4 Mpc). All these observations support the evidence for DM, consistently agreeing on its abundance. Remarkably, the DM abundance is inferred only from the gravitational effect it has on the visible matter (baryons¹ and radiation), as we will call particle states described by the Standard Model (apart from neutrinos). At present, we have no clue of other interactions between the dark and visible matter and between the DM particles themselves, but only bounds we shall discuss in the last section of the chapter. As we shall emphasize more than once, the DM particle candidate must be *non-baryonic* or, even more restrictively, beyond Standard Model (BSM), that is we need new physics (matter content and interactions) to explain the observations.

For more than two centuries Newton's laws of motion and theory of universal gravitation were the basic tools by which scientists could be able to deduce the mass of celestial bodies from their dynamics. Through the universal nature of the gravitational interaction, one can model the motion of visible bodies to infer the presence and the mass of *invisible*, or *dark* bodies i.e. objects we do not observe with light. This idea was applied first by F. Bessel in 1844, who predicted the presence of faint companion stars for Sirius and Procyon to explain the motion of the latter, and by U. Le Verrier and J.C. Adams in 1846, who proposed the existence of a new planet, Neptune, to explain anomalies in the orbit of Uranus. The same principle in a more advanced form is the basis of all the DM evidence we have at our disposal. The difference is that the *dark* objects the 19th-century astronomers were hypothesising were only bodies which were not resolved by the instruments at the time: what they predicted were just faint celestial bodies. Today instead we do not know

¹According to the literature, we call baryons and leptons together baryons, since the formers are more relevant for the energy budget.

the origin and composition of DM, we just know it cannot be ordinary matter. Physicists and astronomers in the early years of 20th century proceeded along this way, trying to estimate the amount of invisible and faint matter in the Milky Way.

The first evidence of DM in the literature, in the modern sense of the term, was found by the Swiss-American astronomer F. Zwicky in 1933 [5]. He was studying the dynamics of the ~ 800 galaxies within the Coma cluster. From the redshifts of the galaxies, measured by E. Hubble and M. Humanson, he deduced that their velocity dispersion was too high to keep the system stable. He applied the virial theorem to infer the average mass density of the cluster from the velocity dispersion and found that the obtained value was much higher than the one predicted from visible matter. However, Zwicky was still thinking that the dark matter was made of invisible ordinary matter: faint stars, cool bodies and gas nebulae. As carefully reviewed in [6], the following decades were indeed characterized by a “confusing situation” in the field, with an increasing number of observations of systems with very high mass-to-light ratios on galactic and super-galactic scales: many ideas to explain the discrepancies were proposed and the fact that a large amount of mass was invisible, hence not observable, was just one possibility to solve the issue, among many others.

New evidence for the existence of dark matter came out in the 1970s, when the study of galactic rotation curves became prominent, after the discovery of the 21-cm radio emission line and the explosion of radioastronomy. Rotation curves are plots of the measured orbital velocity of gas and stars in a galaxy as a function of the radial distance from the galactic centre. They can be used to infer the radial density profile of a galaxy. While the Newtonian prediction for the density profile inferred from visible matter was a decreasing velocity of the gas at large radii, the measured rotation curves were flat even at large distances from the galactic centre. This fact suggests the presence of a large amount of invisible matter embedding the galaxy, which, in a modern language, we call a dark matter *halo*. These were the implicit experimental outcomes of the studies of K. Freeman [8] and separately of V. Rubin and K. Ford [9] in 1970, which however did not elaborate much on the implications for the existence of undetected matter, but just stated the discrepancies clearly.

Still, the problems of high galactic velocity dispersions and flat rotation curves were studied separately and in the community, there was not the feeling of a global anomaly, rather of different uncomplete pictures about the measurement of mass and mass-to-light ratios in galaxy and clusters. As argued in the historical review [7], only with a rising interest in cosmology in the 1970s, together with a change in the expertise of physicists and astronomers, the attention was finally driven to the missing mass problem. The General Relativity (GR) Friedmann-Robertson-Walker (FRW) model, based on the metric

$$ds^2 = -dt^2 + a(t)^2 \left[\frac{1}{1 - kr^2} dr^2 + r^2 d\Omega^2 \right], \quad (1.1)$$

for the expansion of a homogeneous and isotropic Universe, was already the leading

paradigm: to understand the history of the Universe, its mass-energy density ρ was a crucial parameter to be determined, as it is clear from the Friedmann equation, the 00-Einstein equation for the above metric:

$$H^2 = \left(\frac{\dot{a}}{a}\right)^2 = \frac{8\pi G}{3}\rho - \frac{k}{a^2} \iff 1 = \Omega - \frac{k^2}{a^2 H^2}. \quad (1.2)$$

It was a common (a priori) belief that the Universe was *just closed*, i.e. characterized by a energy density parameter $\Omega = \rho/\rho_c \gtrsim 1$. By the approximate knowledge of the Hubble constant H_0 , the critical density necessary to close the Universe was determined to be $\rho_c \sim 10^{-29} \text{ g cm}^{-3}$. This value was found to be two orders of magnitude higher than the one estimated from the average mass of galaxies and their spatial distribution. It was only at this point that the community acquired a particular focus on unobserved matter and the high galactic velocity dispersions and flat rotation curves discrepancies came together as evidence for the dark, invisible matter.

Afterwards, the problem of dark matter evolved dramatically, with a growing interest in the particle physics community: by the late 1980s, the hypothesis that the missing mass was made of one or more unknown particle species had become the leading paradigm among other explanations, such as theories of modified gravity (from the standard general relativity paradigm), e.g. M. Milgrom and Bekenstein theories.

1.1 Galactic scales

1.1.1 Galactic rotation curves

Still today, the most prominent evidence for DM on galactic scales comes from measurements of the circular velocity of stars and gas in the galactic disks as a function of their distance from the centre, i.e. *galactic rotation curves* (GRCs). The measurements of the velocity of visible matter are obtained combining observations of redshifts of the 21cm line with optical surface photometry. If $\rho_0(r)$ is the visible matter density profile, and $M(r) = 4\pi \int dr' r'^2 \rho_0(r')$ the enclosed mass, from the equation of motion of a visible object, its expected circular velocity $v(r)$ is

$$v(r) = \sqrt{\frac{GM(r)}{r}} \propto \begin{cases} r & r \ll r_c & M(r) \propto \rho_0 r^3 \\ r^{-1/2} & r \gg r_c & M(r) \simeq \text{const} \end{cases} \quad (1.3)$$

where r_c is some kpc-scale characteristic radius of the galaxy. The enclosed visible mass is increasing with volume in the disk and is saturated outside the disk. Instead, as shown in the left panel of Fig. 1.1 velocity data points flatten at large distances. This implies the existence of a superimposed dark density profile, a dark matter halo with $M(r) \propto r$ at large radii, hence a density profile $\rho(r) \propto r^{-2}$ for $r \gg r_c$.

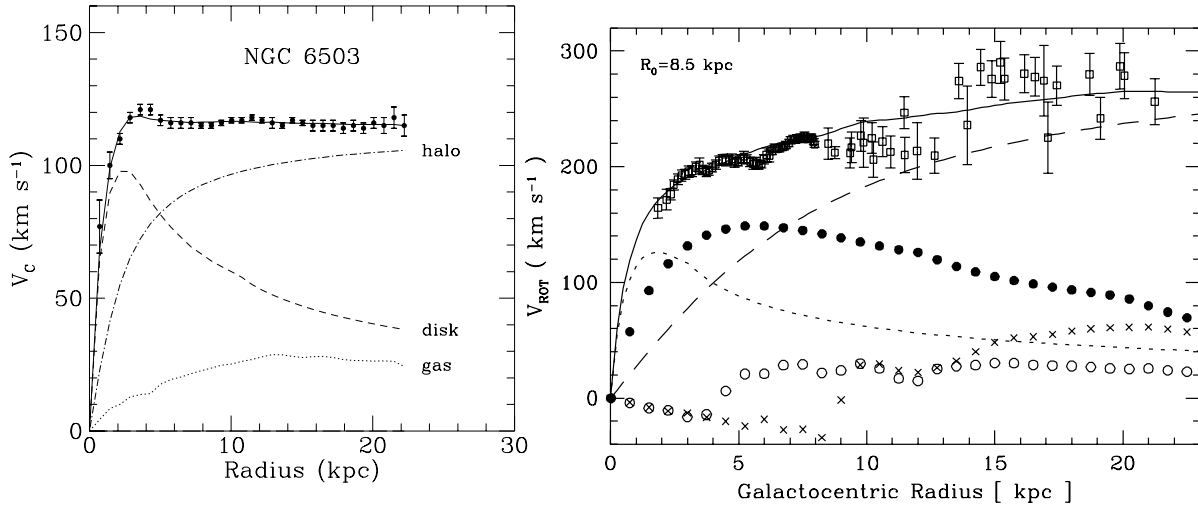


Figure 1.1: Left: Rotation curve of NGC 6503 from [10]. The dotted, dashed and dash-dotted lines are respectively the contributions of gas, disk and DM. The solid line is the sum of all contributions. Right: the Milky Way rotation curve from [13]. The different lines represent the contributions from the bulge (dotted), the stellar disk (filled circles), the HI gas layer (crosses), the H₂ gas layer (circles), and a smooth dark halo (dashed). The solid line represents the sum of the contributions.

Today, we have a large set of galactic rotation curves, extending to ~ 100 kpc, where there are no stars. So far all the galaxies show flat velocity profiles at the largest radii probed. In particular, we also measured the rotation curve for our galaxy, the Milky Way, that is crucial to know the local DM density, which is relevant for DM laboratory searches. The measurement is complicated, since we are inside the galaxy, about 8 kpc from the galactic centre. The result of one of the first measurements is shown in the right panel of Fig. 1.1. A more recent study about DM in the Milky Way has been carried on in [11]: the authors claim that current data strongly disfavour baryons as the only ingredient in the galactic mass budget and point out the existence of DM, independently on its assumed distribution.

Of peculiar interest among GRCs are Low Surface Brightness (LSB) galaxies, which are probably DM dominated, because of the low presence of visible matter. Their study can be used to characterize with precision DM density profiles avoiding the difficulties due to modelling of baryonic matter.

An alternative hypothesis to DM to explain GRCs data is that Newton's universal gravitation (i.e. the small field limit of General Relativity) has to be modified on galactic scales. This fact leads to theories of modified gravity (MOND) among all Tensor-Vector-Scalar gravity (TeVeS), which drew attention in the past decades, for its ability to reproduce observations of hundreds of GRCs [6]. However, this is an ad hoc theory, with a large number of free parameters, which was not able to be consistent with GR in reproducing all

the observation on larger scales (e.g. cluster scales). In particular, TeVeS was definitively ruled out by the LIGO-Virgo observation of the gravitational wave (GW) signal GW170817 and of the electromagnetic counterpart [14], which proved the GW propagation velocity to be equal to the speed of light up to a part over 10^{15} .

1.1.2 Gravitational lensing

The limitation of GRCs is that one can only look out as far as there is light or neutral hydrogen, namely to distances of ~ 100 kpc. Thus, one can see the presence of DM halos, but cannot trace where most of the DM is. We can overcome this limitation exploiting *gravitational lensing*, i.e. the effect predicted by GR that mass bends light passing nearby. In practice, the light of distant objects, like quasars, gets lensed by halos of galaxies far (> 100 kpc) from galactic centres. Lensing measurements confirm the existence of enormous quantities of DM both in galaxies and in clusters of galaxies, which we treat in the next section.

Interestingly, the gravitational lensing signal behind them, in agreement with dynamical analysis, shows that both the DM and baryonic components contribute to producing an overall so-called isothermal $\rho \propto r^{-2}$ density profile out to very large radii [12]. As shown in Fig. 1.2, to explain the observed lensing signal in this extended range of scales, many ingredients have to come together: baryons at small scales, the galaxy's DM halo, and the haloes of neighbouring galaxies at farther distances. Moreover, the agreement between the location of the transition from the host halo to large-scale structure and the typical size of DM structures expected from N -body simulations provides strong support for the CDM paradigm.

Other evidence for DM, both on sub-galactic and inter-galactic scales, also comes from a great variety of data (see [2] and references therein) like weak modulation of lensing and velocity dispersion measurements of dwarf spheroidal galaxies and spiral galaxy satellites.

1.2 Galaxy cluster scales

The evidence for DM is also prominent when we observe clusters, i.e. gravitationally bound systems of galaxies of size 1-10 Mpc. As we said in the historical review, this was also the first kind of system where evidence for DM was found: Zwicky observed the velocity dispersion of galaxies in the Coma cluster finding it was too high for the system to be stable if the mass was consistent with the one estimated from the counting of the galaxies. In other words, he measured a mass-to-light ratio of around $400 M_{\odot}$ comparing the mass density obtained from the velocity dispersion – exploiting the virial theorem – and the value estimated from visible matter – as average mass of a galaxy \times number of galaxies in the cluster $\sim 10^9 M_{\odot} \times 10^3$.

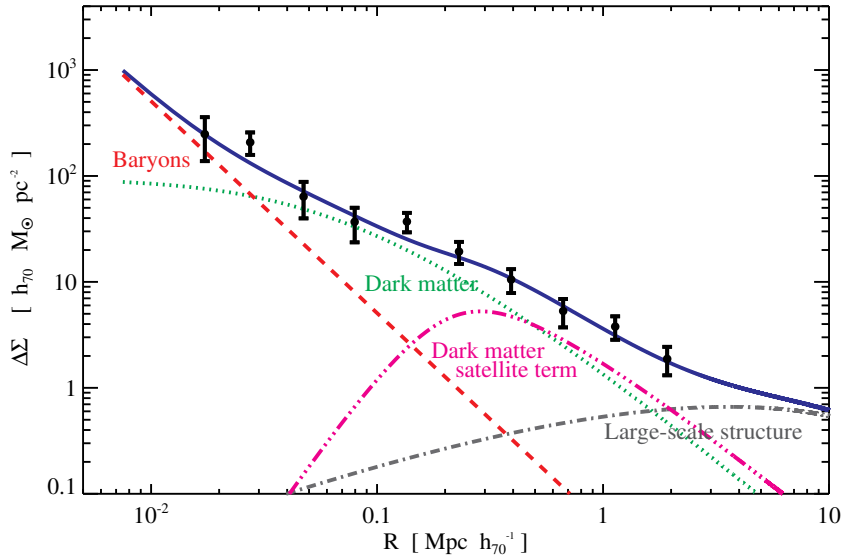


Figure 1.2: The observed radial mass density around elliptical galaxies in the Hubble Space Telescope COSMOS survey, decomposed into its various components (cfr. [12] and reference therein). The solid blue curve shows the total “galaxy-galaxy” weak gravitational lensing signal. On small scales around 10 kpc, the signal is dominated by the baryonic content of galaxies (red dashed curve). At intermediate scales, around 100 kpc, DM haloes become dominant: we distinguish the main $\rho \propto r^{-2}$ halo term (dotted green), from the additional contribution (triple-dot-dash magenta) when the analysis focuses on satellite galaxies in the subhaloes rather than main galaxies. On larger scales, above 3 Mpc, the lensing signal is just the cosmic shear signal from large-scale structure hosting the galaxy (dot-dash grey).

An alternative method to estimate the mass of a cluster is to compare the weak gravitational lensing to the observed profile of X-ray emission tracing the distribution of hot gas in clusters: the existence of this gas in the cluster can only be explained by a large DM component providing the potential well to keep the gas in hydrostatic equilibrium. If we impose hydrostatic equilibrium of the gas, modelled as an ideal gas in good approximation, $P = (\rho/(\mu m_p))k_B T$ with $\mu \simeq 0.6$ the average molecular weight and m_p the proton mass, we have

$$\begin{aligned} -g(r) &= -\frac{GM(r)}{r^2} = \frac{1}{\rho} \frac{dP}{dr} = \frac{1}{\rho} \frac{d}{dr} \left(\frac{\rho}{\mu m_p} k_B T \right) \\ &= \frac{k_B}{\mu m_p} \times \frac{T}{r} \left(\frac{d \log \rho}{d \log r} + \frac{d \log T}{d \log r} \right), \end{aligned} \quad (1.4)$$

where $g(r)$ is the gravitational acceleration of the gas and $M(r) = 4\pi \int dr' r'^2 \rho(r')$. Then we fairly assume $T \simeq \text{const}$ and $\rho \propto r^{-\alpha}$ with $\alpha \in [1.5, 2]$ at large radii. We find that the temperature of the gas at hydrostatic equilibrium should go as

$$k_B T \simeq \frac{G \mu m_p M(r)}{r} \simeq 1.5 \text{ keV} \left(\frac{M(r)}{10^{14} M_\odot} \right) \left(\frac{1 \text{ Mpc}}{r} \right), \quad (1.5)$$

having normalized to typical cluster values and used the baryonic enclosed mass. This

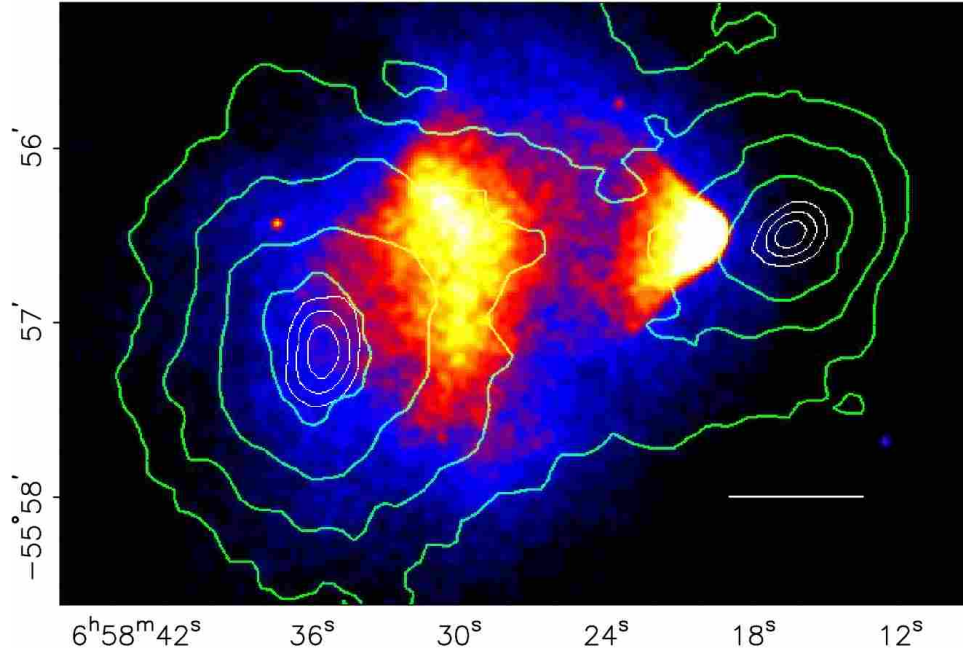


Figure 1.3: The bullet cluster. The coloured map represents the image of the X-ray emission of this system of merging clusters, from a 500-seconds exposure with Chandra telescope. The white bar shows a distance of 200 kpc at the location of the cluster. The green contours denote the reconstructed gravitational lensing map which shows that the gravitational potential: the map does not trace the gas distribution, the dominant baryonic mass component, but rather approximately traces the distribution of galaxies. Figure from [15].

temperature is an order of magnitude lower than the observed temperature of $T \simeq 10$ keV, suggesting the presence of a large amount of DM in the cluster, about 6 times the visible matter.

Another way to detect the presence of gas in clusters is via the Sunyaev-Zel'dovich (SZ) effect, which is just inverse Compton of CMB photons, hence scales proportionally to the gas density. The SZ effect produces spectral distortions of the CMB spectrum from the perfect black body one, hence it is not difficult to detect.

These results can be compared to the gravitational map obtained from the lensing of background objects by the cluster gravitational potential. In [15] this technique has been applied to the Bullet cluster, a pair of merging clusters shown in Fig. 1.3. As a result of the clusters collision, the distribution of stars and galaxies is spatially separated from the hot X-ray emitting gas (i.e. the baryonic mass of the system). The authors compared the X-ray image to the lensing map, obtaining that the 8-sigma significance spatial offset of the centre of the total mass from the centre of the baryonic mass peaks cannot be explained with an alteration of the gravitational force law (i.e. MONDs), and thus proves that the majority of the matter in the system is dark.

1.3 Cosmological scales

Despite the strength of the DM evidence on galactic and cluster scales, the observations discussed so far do not allow us to determine precisely the total amount of DM in the Universe, but only to give rough estimates based on the mass-to-light ratio. Observations on cosmological scales, i.e. at redshift $z > 0.03$ or distances > 100 Mpc, such as Lyman- α forest, galaxy surveys, or the Cosmic Microwave Background (CMB), can give us information on the energy budget of the Universe. In particular, it is only on such large scales that the DM rather than only invisible appears to unveil its intrinsic non-baryonic nature.

1.3.1 Structure formation

A prominent way to characterize the nature of DM and its behaviour at different length scales is to compare observations of the distribution of matter to the theory of structure formation. In the standard paradigm, all the structures we observe in our Universe, e.g. galaxies, clusters and super-clusters, arose from small primordial inhomogeneities generated during the inflationary era. These originally small and linear fluctuations evolved in time under the opposite effects of gravity and the Hubble expansion. The relevant random field whose statistical properties we want to study is the dimensionless density fluctuation

$$\delta(\vec{x}, t) = \frac{\rho(\vec{x}, t) - \bar{\rho}(t)}{\bar{\rho}(t)} = \int \frac{d^3k}{(2\pi)^3} \delta(\vec{k}, t) e^{-i\vec{k}\cdot\vec{x}}, \quad (1.6)$$

with $\bar{\rho}(t)$ the background FRW mean matter density. If we study the evolution of small non-relativistic matter density fluctuations on scales λ smaller than the horizon $\lambda_H = H^{-1}$, we can use a Newtonian description of gravity. In fact, under these hypotheses, the gravitational perturbation to the flat metric is small and the Poisson equation gives, for φ

$$\nabla^2 \varphi = 4\pi G \bar{\rho} \delta = \frac{3}{2} H^2 \delta \implies \varphi \sim \left(\frac{\lambda}{\lambda_H} \right)^2 \delta \ll 1, \quad (1.7)$$

consistently. If we combine the Poisson equation with the Friedmann equation, the continuity and Euler equation for the perturbed fluid in Fourier space, we obtain the *Jeans equation* for the perturbation

$$\ddot{\delta} + 2H\dot{\delta} + \left[\frac{c_s^2 k^2}{a^2} - 4\pi G \bar{\rho} \right] \delta = 0, \quad (1.8)$$

with dots denoting derivatives with respect to cosmic time. This is the basic equation used to compute the evolution of perturbations in a FRW Universe. In the square brackets, we see the competition between gravity, which induces a compression (increasing δ), and pressure, which favours rarefaction (decreasing δ). The scale at which gravity is balanced

by pressure is the Jeans scale:

$$\lambda_J = \frac{2\pi}{k_J} = 2\pi \sqrt{\frac{c_s^2}{4\pi G a^2 \bar{\rho}}} = 2\pi r_H \sqrt{\frac{2}{3}} c_s \quad (1.9)$$

with $r_H = (aH)^{-1}$ the comoving Hubble radius. Perturbations smaller than λ_J get washed out by pressure while those greater than the Jeans scale grow under gravity. Let us sketch the solution of the Jeans equation in various regimes.

- $\lambda \ll \lambda_J, \lambda_H$ (perturbations on sub-Jeans scales and sub-horizon scales). If we neglect the gravity term, the Jeans equation gets the form of a damped harmonic oscillator with damped frequency $\omega(k, a) = c_s k/a$ and amplitude:

$$\ddot{\delta} + 2H\dot{\delta} + \frac{c_s^2 k^2}{a^2} \delta = 0 \implies \delta(k, t) \propto A(k, t)e^{-i\omega t} + B(k, t)e^{i\omega t}. \quad (1.10)$$

Therefore perturbations with sub-Jeans length scale undergo damped acoustic oscillations.

- $\lambda_J \ll \lambda < \lambda_H$ (perturbations on super-Jeans and sub-horizon scales). In this case, we can neglect the effect of pressure and solve the equation. Let us do it in two separate sub-cases.

- *Radiation domination:* $a \propto t^{1/2}$, $H = 1/(2t)$ and the matter-energy density $\bar{\rho}$ is a negligible component in the Universe so it can be set to zero. Therefore

$$\ddot{\delta} + \frac{1}{t}\dot{\delta} = 0 \implies \delta(k, t) = A(k) + B(k) \log t \quad (1.11)$$

So, in the radiation-dominated era, perturbations stay constant or weakly grow logarithmically with time.

- *Matter domination:* $a \propto t^{2/3}$, $H = 2/(3t)$ and $H^2 = 8\pi G \bar{\rho}/3$. So we get

$$\ddot{\delta} + \frac{4}{3t}\dot{\delta} - \frac{2}{3t^2}\delta = 0 \implies \delta(k, t) = A(k)t^{-1} + B(k)t^{2/3} \propto B(k)a(t) \quad (1.12)$$

During the matter-dominated era, perturbations grow with time as the scale factor.

- $\lambda > \lambda_H, \lambda_J$ (perturbations on super-horizon and super-Jeans scales). In this case, the Newtonian treatment is no longer valid, so we have to rely on a full GR analysis. Let us sketch here reasoning which will lead us to the correct result, following the simple argument of Kolb and Turner [20]. Perturbations in GR suffer the gauge ambiguity problem, that is they depend on the definition of the map between the physical (perturbed) model and the reference (unperturbed) one. What is relevant is the difference between physical and reference model having set a specific map: of course, physical observables are gauge independent. Therefore, in principle, the

perturbation δ will be gauge dependent. To fix the gauge, one has to exploit a fixing condition. Let us consider two models, a reference unperturbed flat FRW model

$$H^2 = \frac{8\pi G}{3}\rho_0 \quad (1.13)$$

and a model with the same Hubble parameter H (gauge fixing condition) but with higher density $\rho_1 > \rho_0$ and therefore closed (positively curved) $k > 0$

$$H^2 = \frac{8\pi G}{3}\rho_1 - \frac{k}{a^2} \quad (1.14)$$

The choice of gauge is called the uniform Hubble flow condition. The density contrast is given by

$$\delta \equiv \frac{\rho_1 - \rho_0}{\rho_0} = \frac{k/a^2}{8\pi G\rho_0/3} \quad (1.15)$$

As long as δ is small, the scale factors of the two models differ only by a factor $\sim (1 + \delta)$. Therefore we can use the above equation to see the behaviour of a super-horizon density perturbation during radiation $\rho_0 \propto a^{-4}$ and matter $\rho_0 \propto a^{-3}$ domination epochs

$$\delta \propto \frac{a^{-2}}{\rho_0} \propto \begin{cases} a^2 \propto t & \text{radiation domination} \\ a \propto t^{2/3} & \text{matter domination} \end{cases} \quad (1.16)$$

We can visualize the growth of perturbations on sub-horizon scales in Fig. 1.4. We can

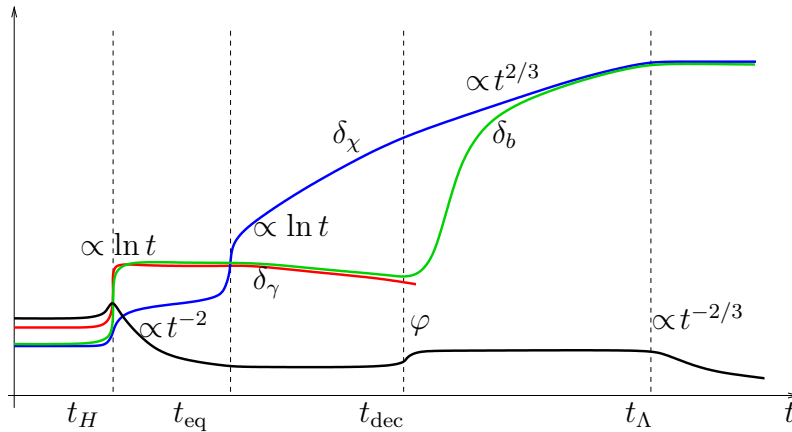


Figure 1.4: A sketch of the time dependence, in the linear regime, of density contrasts of DM, baryons and photons, δ_χ , δ_b and δ_γ , respectively, as well as the Newtonian potential φ . All perturbations cross the horizon at time t_H before matter-radiation equality; t_{eq} and t_Λ correspond to the transitions from radiation domination to matter domination, and from decelerated expansion to accelerated expansion, t_{dec} refers to the recombination epoch. Notice the huge difference between δ_b and δ_χ because baryons are coupled to photons to recombination. Acoustic oscillations of baryons and photons until decoupling are neglected. Figure elaborated from the lectures [21]

summarize the evolution of perturbations as

$$\delta(a, k) \propto \begin{cases} \exp[\pm ic_s k/a] & k > k_J, k_H \\ \log a & k_H < k \ll k_J, \text{ radiation domination} \\ a & k_H < k \ll k_J, \text{ matter domination} \\ a^2 & k < k_H, \text{ radiation domination} \\ a & k < k_H, \text{ matter domination} \end{cases} \quad (1.17)$$

In particular, we can use the formula for sub-horizon sub-Jeans perturbations in a matter-dominated era to compute the density perturbation today. Knowing that during decoupling $\delta_{\text{CMB}} \sim 10^{-5}$ and neglecting the late cosmological constant domination, we have

$$\delta_0 = \frac{a_0}{a_{\text{dec}}} \delta_{\text{CMB}} \simeq \frac{T_{\text{dec}}}{T_0} \delta_{\text{CMB}} \sim 10^3 \times 10^{-5} \sim 10^{-2}. \quad (1.18)$$

This value is too small to account for present structures, where we have $\delta \sim 1 - 10^5$. The smallness of CMB density fluctuations in the baryon-photon plasma is a striking proof that we are missing a crucial ingredient to form structures: cold dark matter, which provides the potential wells allowing the perturbations to go non-linear. So DM is the reason why we do exist: if DM was not present, our Universe would be homogeneous, with just per cent fluctuations in density.

To compare the theory of structure formation with observations and probe the crucial impact of DM, we model the fluctuations as Gaussian random fields, whose statistical properties are all described by the linear matter power spectrum today $P(k)$, defined as

$$\langle \delta(\vec{k}, t)^* \delta(\vec{k}', t) \rangle = (2\pi)^3 \delta_D(\vec{k} - \vec{k}') P(k). \quad (1.19)$$

This form is due to isotropy and homogeneity of the background Universe. Since we are using linear theory, this quantity is found from the product of the primordial power spectrum (given by inflation) and a transfer function $T^2(k)$ we have to determine: it takes into account the scale dependence of the evolution of perturbations. Following [16], we write the power spectrum in the form

$$P(k) = \frac{2\pi^2 \delta_H^2}{H_0^3} \left(\frac{k}{H_0} \right)^n T^2(k), \quad (1.20)$$

such that, defining the dimensionless power spectrum

$$\Delta^2(k) \equiv \frac{k^3 P(k)}{2\pi^2}, \quad (1.21)$$

for an horizon-sized scale $k = H_0$, we have $\Delta^2 = \delta_H^2$. The parameters of the primordial power spectrum are measured: δ_H is fixed by the amplitude of CMB anisotropies on largest scales and n is the spectral index of scalar perturbations from inflation, measured with

good accuracy by the Planck satellite [17]

$$n = 0.965 \pm 0.004. \quad (1.22)$$

This value shows a slight red tilt with respect to the scale-invariant Harrison-Zel'dovich value of $n = 1$. We can understand the behaviour of the transfer function considering two trial modes equal at some time: one entering the horizon *before* equality $\delta(k > k_{\text{eq}})$ and another entering *during* matter domination $\delta(k < k_{\text{eq}})$. The former mode is practically frozen until matter domination. This is the so-called *Meszaros effect*, which leads to a suppression of small scales modes. The suppression is given by the missing growth factor: given that on super-horizon scales, during radiation dominations, modes grow as $\delta \propto a^2$, this is just the square of the change in a^2 during this period. In radiation domination $d\eta = da^2/a \sim da$ and horizon crossing is obtained at $k \sim 1/\eta$, so we have that the suppression factor is

$$\frac{\delta(k > k_{\text{eq}})}{\delta(k < k_{\text{eq}})} = \left(\frac{a_{\text{eq}}}{a}\right)^2 \simeq \left(\frac{\eta_{\text{eq}}}{\eta}\right)^2 \simeq \left(\frac{k}{k_{\text{eq}}}\right)^2, \quad (1.23)$$

since the numerator is frozen and the denominator grows as a^2 until a_{eq} . Therefore the transfer function will have the form (see [16], chapter 7 for a full derivation)

$$T^2(k) \simeq \begin{cases} 1 & k \ll k_{\text{eq}} \\ (k/k_{\text{eq}})^{-4} & k \gg k_{\text{eq}} \end{cases} \quad (1.24)$$

This suggests the following scaling of the linear matter power spectrum

$$P(k) \propto \frac{2\pi^2 \delta_H^2}{H_0^3} \times \begin{cases} k & k \ll k_{\text{eq}} \\ (k/k_{\text{eq}})^{-3} & k \gg k_{\text{eq}} \end{cases} \quad (1.25)$$

We realize that there is a turnover in the power spectrum, i.e. a smooth peak around the scale k_{eq} , that is the wavenumber of a mode entering the horizon at matter-radiation equality. We can find it as $k_{\text{eq}} = 1/\eta_{\text{eq}}$. The comoving distance in a Universe with only matter and radiation with equality at $a_{\text{eq}} = \Omega_r/\Omega_m$ is given by

$$\begin{aligned} \eta(a) &= \int_0^a \frac{da}{a^2 H(a)} = \int_0^a \frac{da}{a^2 H_0 \sqrt{\Omega_m a^{-3} [1 + a_{\text{eq}} a^{-1}]^{1/2}}} \\ &= \frac{2}{H_0} \sqrt{\frac{a_{\text{eq}}}{\Omega_m}} \left[\sqrt{1 + \frac{a}{a_{\text{eq}}}} - 1 \right], \end{aligned} \quad (1.26)$$

Therefore

$$k_{\text{eq}} = \eta_{\text{eq}}^{-1} = 2(\sqrt{2} - 1) \sqrt{\frac{H_0^2 \Omega_m}{a_{\text{eq}}}} \simeq 0.009 \text{ hMpc}^{-1}. \quad (1.27)$$

In the top panel of Fig. 1.5 we compare the linear power spectrum today predicted from the Λ CDM model to observations. The scalings and the peak of the spectrum are in agreement with data. Another important scale to point out is the scale k_{NL} below which

non-linearities in the matter perturbation evolution cannot be neglected anymore. This value is set by the condition $\Delta(k_{\text{NL}}) \simeq 1$, that bears $k_{\text{NL}} \simeq 0.2 h\text{Mpc}^{-1}$, as we see from the bottom panel of Fig. 1.5. At such small scales $k > k_{\text{NL}}$, the extraction of the linear power spectrum from observations is more complicated.

We conclude this section remarking the crucial role of DM in the description of the matter power spectrum. As it is clear from the bottom panel of Fig. 1.5, baryons alone cannot reproduce observations. This fact stresses the non-baryonic nature of DM.

1.3.2 Cosmic Microwave Background

Today, the analysis of Cosmic Microwave Background (CMB) temperature anisotropies and polarization provides us with the most accurate testing of cosmological models and the tightest constraints on cosmological parameters. Let us briefly review the CMB physics following the excellent book of Dodelson [16] and the review [4] to understand the importance of the CMB in modern cosmology.

The existence of background radiation originating from the propagation of photons in the early Universe decoupled from baryons at a temperature about $T_{\text{dec}} \simeq 0.1 \text{ eV}$ was predicted by G. Gamow and collaborators in 1948 and accidentally discovered by A. Penzias and R. Wilson in 1965, worth them the Nobel Prize. The CMB was measured carefully by many experiments during the last decades and ultimately by the most accurate so far, the Planck satellite. The CMB was found to be with extraordinary precision the spectrum of a black body, corresponding to a temperature of

$$T_0 = 2.726 \text{ K.} \quad (1.28)$$

The main observables offered by the CMB are the photon intensity (hence temperature) and polarization, which however is less important concerning the DM. Of physical interest are temperature fluctuations in different directions in the sky, i.e. anisotropies. Any deviation of the early Universe from an isotropic and homogeneous Universe made out of a thermal bath of photons, baryons, neutrinos and DM particles is evident as a modification of a constant photon temperature over the so-called *last scattering surface*, which is the way we can think of the CMB.

The major temperature fluctuation is due to the relative motion of the observers (the Earth, solar system, Milky Way etc.) with respect to the CMB. Subtracting this dipole correlation, one obtains an isotropic background with temperature fluctuations of order $\delta T/T_0 \sim 10^{-5}$. Homogeneity at such large scales (the quadrupole scale) is a hint of an early inflationary phase which has two main outcomes: it offers a scenario where all scales were initially in causal contact and provides, from the density fluctuations of the field responsible of inflation, the primordial seeds for large scales perturbations, hence the CMB anisotropies too.

The symmetry of the problem suggests a convenient basis to expand the temperature fluctuations: spherical harmonics.

$$\delta T(\theta, \phi) = \sum_{\ell=0}^{\infty} \sum_{m=-\ell}^{\ell} a_{\ell m} Y_{\ell m}(\theta, \phi). \quad (1.29)$$

Experimentally, the sum over multipoles ℓ starts from $\ell = 2$ (having discarded the monopole $\ell = 0$, which is an overall unphysical constant and the dipole $\ell = 1$ for the aforementioned reason) and ends at a small scale $\ell_{\max} \sim \pi/\theta_{\min}$, set by the resolution of the experiment. The Planck satellite is sensitive to very small scales: $\ell_{\max} \sim 2500$.

If the fluctuations are assumed to be Gaussian (which is a very good approximation), all the information is included in the angular power spectrum

$$\langle a_{\ell m} a_{\ell' m'} \rangle = C_{\ell} \delta_{\ell \ell'} \delta_{m m'}, \quad (1.30)$$

which is diagonal in multipoles, with entries C_{ℓ} , thanks to isotropy. Therefore the angular power spectrum is given by

$$\langle \delta T(\theta_i, \phi_i) \delta T(\theta_j, \phi_j) \rangle = \sum_{\ell} (2\ell + 1) C_{\ell} P_{\ell}(\cos \theta_{ij}), \quad (1.31)$$

with P_{ℓ} the Legendre polynomials and θ_{ij} the angle between directions i and j . The power spectrum coefficients C_{ℓ} depend on the cosmological parameters, so, measuring the formers, we can get the latter ones. In Fig. 1.6, we show the angular power spectrum coefficients normalized in a peculiar way $\mathcal{D}_{\ell}^{\text{TT}} = \ell(\ell + 1)C_{\ell}/2\pi$ as measured by the Planck satellite [17] together with the best fit model. We see that the measured power spectrum essentially consists of a set of peaks called *acoustic peaks*, each of them giving us an angular scale with a particularly large contribution to the temperature fluctuations. The leading physical effects generating such shape are:

- *acoustic oscillations* of the coupled baryon-photon fluid around the time of decoupling. Photons are initially tightly coupled to electrons through Thomson scattering, hence also to baryons since protons interact strongly with electrons via Coulomb scattering. This fluid interacts gravitationally with DM particles, so it is pulled into gravitational wells. The baryon-photon plasma is characterized by pressure and sound speed c_s , which goes to $c/\sqrt{3}$ in the limit of vanishing baryon density. While falling in the potential well, the fluid undergoes a kind of adiabatic expansion that causes an increase in pressure, due to a reduction of volume. This pressure counters gravity making the fluid oscillate: the photons moving to and fro in the gravitational potential induce fluctuations in intensity, hence in temperature, located around the regions which are dense of DM. This oscillation can be decomposed in reciprocal space in a tower of fluctuation modes (each one with an associated power) characterized by multipoles ℓ . The associated power to each mode is an imprint of the gravitational potential around decoupling.

- *Sachs-Wolfe effect.* It is the impact of gravity, described by GR, on the propagation of CMB photons to us, during and after decoupling. The effect is due mainly to (dark) matter (dominating the Universe during decoupling) accumulations, which generate a gravitational potential evolving in time during the travel of CMB photons through it. Naively, the photons escaping the wells are much colder than they were inside; actually, the redshift effect on photons climbing up potential wells dominates over the temperature gain associated to the overdensity so that the cold spots we observe in the CMB today are associated to overdense regions at recombination, while hot spots are associated to underdense regions. The free-streaming Sachs-Wolfe effect leads to a dependence $C_\ell \propto [\ell(\ell+1)]^{-1}$: this is the reason for the normalization used to plot the CMB anisotropy power spectrum. The later the photons see such gravitational potential, the more likely they are to probe the geometry of the Universe and the cosmological constant (late-time Integrated Sachs-Wolfe effect). The latter parameters are, in fact, degenerate as we shall see.

From both effects, we see the crucial role played by DM in creating the potential wells affecting the oscillations of the photon-baryon fluid and the streaming of decoupled photons.

Now we further analyse the dependence of the spectrum on the cosmological parameters. In particular, we are interested in the today energy budget of the Universe. We can neglect the contribution of relativistic degrees of freedom (photons plus relativistic neutrinos²), which is easily obtained from the CMB temperature T_0 :

$$\begin{aligned} \Omega_r(t_0)h^2 &= \Omega_\gamma(t_0)h^2 + \Omega_\nu(t_0)h^2 = \frac{\pi^2}{15} h^2 \frac{g_{\text{eff}}(T_0)T_0^4}{\rho_c(t_0)} \\ &\simeq 0.66 \times (1 + 0.22N_\nu) \frac{(2.36 \times 10^{-4} \text{ eV})^4}{8.4 \times 10^{-11} \text{ eV}^4} \simeq 2.44 \times (1 + 0.22N_\nu) \times 10^{-5}, \end{aligned} \quad (1.32)$$

with $h = H_0/(100 \text{ km s}^{-1}\text{Mpc}^{-1})$ the unknown normalized value of the Hubble constant (it is indeed a fit parameter). We focus on the following crucial parameters, which can be determined from the CMB temperature anisotropies spectrum:

$$\Omega(t_0), \quad \Omega_m(t_0)h^2, \quad \Omega_b(t_0)h^2, \quad \Omega_\Lambda(t_0). \quad (1.33)$$

These parameters make the energy budget of a flat FRW Universe (see Appendix A for details): the total density parameter, the density parameter of matter (total non-relativistic matter, dark plus baryons), of baryons and the cosmological constant. h^2 is found from the combination of the parameters above

$$h^2 \simeq \frac{\Omega_m(t_0)h^2}{\Omega(t_0) - \Omega_\Lambda(t_0)}. \quad (1.34)$$

Despite this choice, the shape of the power spectrum is affected by many other parameters

²We will account for the uncertainty on whether all the neutrinos are non-relativistic today or not leaving the number of relativistic neutrinos as a free parameter N_ν .

we will not consider here, such as the spectral index of primordial perturbations n , tensor-to-scalar ratio r , reionization τ , since they are less interesting for DM.

An important observable is the angular scale associated to the first and most pronounced peak $\theta_0 \sim \pi/\ell_0$: it corresponds to the size of patches of the sky that were not in causal contact during and since decoupling. It is intuitively given by the ratio of a characteristic length scale on the last scattering surface, called the *sound horizon* $r_s(\eta_{\text{dec}})$, i.e. the comoving distance travelled by a sound wave by time corresponding to η_{dec} , indicating the conformal time with η ($d\eta = dt/a$)

$$r_s(\eta_{\text{dec}}) = \int_0^{\eta_{\text{dec}}} d\eta' c_s(\eta') \quad (1.35)$$

and the comoving distance (travelled by light) between us and the last scattering surface

$$d_C(\eta_{\text{dec}}) = \int_{\eta_{\text{dec}}}^{\eta_0} d\eta' \quad (1.36)$$

Notice that both comoving distances depend on the cosmological parameters introduced above (neglecting radiation density parameter). In particular,

$$d_C = \eta = \frac{1}{H_0} \int \frac{da}{\sqrt{a(1-a)\Omega(t_0) - a(1-a^3)\Omega_\Lambda(t_0) + a^2}}. \quad (1.37)$$

Therefore

$$\sin \theta_0 = \frac{r_s(\eta_{\text{dec}})}{d_C(\eta_{\text{dec}})}. \quad (1.38)$$

sets the position of the first peak. Since comoving distances are strongly affected by the geometry of the Universe, the position of the first peak is considered a measure of the flatness of the Universe. Physically, the first peak corresponds to a sound wave with wavelength twice the size of the horizon at decoupling, hence that underwent one compression, while the other peaks are higher-order modes. Odd-numbered peaks are associated with the level of *compression* the baryon-photon fluid experiences due to the gravitational potential while even-numbered peaks show the *expansion* counter effect of the fluid pressure. Acoustic oscillations, and so the peaks, are washed out at small scales. This is because the last scattering surface has a non-negligible thickness: acoustic oscillations get exponentially erased $C_\ell \propto \exp(-\ell^2/\ell_\star^2)$ by the incoherent superposition of modes when the scale is comparable to the spatial resolution at time of last scattering $\ell \gtrsim \ell_\star$.

We can summarize the effect of parameters on CMB spectrum shape:

1. $\Omega(t_0)$ affects the comoving distance, hence the position of the first peak, in such a way that increasing $\Omega(t_0)$, d_C is reduced. However, it also enters H_0 lowering it, hence increasing d_C . The net effect is that d_C decreases and the first peak ℓ_0 moves to smaller values.
2. $\Omega_\Lambda(t_0)$ also affects the comoving distance directly but with an opposite sign with

respect to $\Omega(t_0)$ and the same regarding H_0 . The net effect is again that increasing $\Omega_\Lambda(t_0)$ the acoustic peaks move to smaller multipoles. We see the effect of Ω_Λ and Ω is the same, hence in our basis, we have a strong *geometry degeneracy*.

3. $\Omega_b(t_0)h^2$ measures the baryon density. If the relative baryon content in the plasma is higher, the pressure decreases and odd (compression) peaks get higher (also because baryons contribute to the gravitational potential) while even (expansion) peaks get lower. This behaviour is a unique signature and it is easy to disentangle from the effect of other parameters. Hence $\Omega_b h^2$ affects the relative height between odd and even peaks and we can measure its value from this effect.
4. $\Omega_m(t_0)h^2$ is dominated by DM, which, effectively, is not coupled other than gravitationally to the baryon-photon fluid: it provides the gravitational wells for acoustic oscillations. Increasing the contribution of DM, the gravitational potential is stabilized and acoustic oscillations are suppressed. This reduces the height of all peaks, most sensibly the first two. So a high third peak is a signature of a large DM component, as it is the case in Fig. 1.6. Moreover, an increased DM density reduces the characteristic length of the gravitational potential, bringing peaks at higher multipoles closer together.

Separating these four effects from each other and from other astrophysical and cosmological parameters becomes easier when we can analyse higher-order peaks. This is why CMB experiments try to be sensitive at the smallest scales possible. The Planck satellite clearly identified seven peaks and measured at their best of accuracy our parameter of interest:

$$\begin{aligned}
 \Omega_b(t_0)h^2 &= 0.0224 \pm 0.0001, \\
 \Omega_m(t_0)h^2 &= 0.142 \pm 0.001, \\
 \Omega_\Lambda(t_0) &= 0.684 \pm 0.009, \\
 H_0 &= 67.4 \pm 0.5 \text{ km s}^{-1}\text{Mpc}^{-1}, \\
 |1-\Omega(t_0)| &< 10^{-3},
 \end{aligned}
 \tag{1.39}$$

and, most importantly for us, the DM relic density

$$\Omega_{\text{DM}}(t_0)h^2 = 0.120 \pm 0.001.
 \tag{1.40}$$

During the whole discussion, we had the need to treat DM as a completely independent component of the Universe with respect to baryons, since it interacts with CMB photons only gravitationally, unlike baryons. This confirms the non-baryonic nature of DM and the fact that it cannot be made of ultrafaint objects of ordinary matter. There are at least two other independent observables on cosmological scales that can probe $\Omega_b h^2$ and Ω_m : the former can be measured from Big Bang Nucleosynthesis (BBN) in the very early Universe, the latter with analysis of Supernovae Ia and is a late Universe measurement. The fact that the whole picture is consistent is strong evidence for the existence of DM and its

non-baryonic nature as a crucial ingredient in the cosmic inventory.

1.3.3 Type Ia supernovae

The fundamental assumption underlying the past and proposed use of Type Ia supernovae (SNIa) to measure the expansion history is that they are “standardizable candles”. SNIa occur when material accreting onto a white dwarf from a companion drives the mass of the white dwarf above the maximum that can be supported by electron degeneracy pressure, the Chandrasekhar limit of about 1.4 solar masses. This triggers the collapse of the star and the explosive onset of carbon fusion, in turn powering the supernova explosion. Because the collapse happens at a particular critical mass, all SNIa are similar, hence they can be used as (nearly) standard candles.

Standard candles are very useful in trying to estimate distances of astrophysical objects. The principle is simple: a standard candle is an object with a fixed intrinsic luminosity L , even unknown, and we can use this information to get the distance of this object to us knowing the light flux f received

$$d_L^2 = \frac{L}{4\pi f}. \quad (1.41)$$

If we have many of these objects, we can relate their distances (if L is unknown) to the measured fluxes. SNIa are fortunately bright enough to be seen at cosmological distances and they can be considered standard candles, with their intrinsic luminosity pretty much constant. At the same time, we can be able to measure the redshift of the host galaxy of these SNIa and correlate the information about z and d_L in a dataset to reconstruct the time dependence of the scale factor (Hubble diagram). One can fit the Hubble curves to specific cosmological models, finding the value for the dark energy density parameter $\Omega_\Lambda(t_0)$ responsible for the late-time acceleration and the matter density parameter $\Omega_m(t_0)$. Experimentally, we measure the fluxes in terms of magnitudes: we have the *apparent magnitude* m , which is related to luminosity distances d_L by the relation

$$m = M + 5 \log_{10} \left(\frac{d_L}{10 \text{ pc}} \right). \quad (1.42)$$

M is the (unknown) absolute magnitude of SNIa. As shown in the right panel of Fig. 1.7 the best fit model ($\Omega_m(t_0), \Omega_\Lambda(t_0)$) gives, in a flat cosmology for the matter density parameter

$$\Omega_m(t_0) = 0.28_{-0.04}^{+0.05}, \quad (1.43)$$

in agreement with CMB data.

1.3.4 Big Bang Nucleosynthesis

At temperatures around $T \sim 0.1$ MeV, Big Bang Nucleosynthesis (BBN) took place: protons and neutrons fused together to form light nuclei (D, ^3He , ^4He , Li). This phenomenon

is strongly dependent on the number of baryons that were around at those times. In the left panel of Fig. 1.8 we show a recent fit [18] on light elements abundances. BBN can accurately constrain the amount of baryonic matter in the Universe and, for this reason, when compared instead to the total matter density, one obtains the evidence for missing matter. Rather being only the first important observational evidence for the Big Bang scenario, BBN is also an excellent probe of beyond Standard Model physics as it is very sensitive to the particle content of the Universe through the number of relativistic degrees of freedom present and to the strength of gravitational and weak interactions. Let us be a bit more quantitative, sketching the main dependences of the relic abundance of ${}^4\text{He}$. This element is produced from deuterium D through the following two processes



The formation of deuterium is the bottleneck of the ${}^4\text{He}$ formation and it sets the amount of final stable ${}^4\text{He}$ nuclei. If we define the mass fraction of a nucleus $Y_i = A_i n_i / n_b$, with A_i its mass number and n_b the baryon number density, we want to reproduce today abundance of $Y_{{}^4\text{He}} \simeq 0.25$. The key ingredient in this process is the behaviour of the neutron number density n_n . Neutrons are unstable particles with lifetime $\tau_n \sim 881$ s, however, at high temperatures $T \gg 1$ MeV, the Universe is younger than a second. Above the MeV neutrons are in equilibrium with the thermal plasma and, just like protons, they formed during QCD phase transition already as non-relativistic particles. Neutrons interact with the thermal plasma only through weak interactions, with processes such as:



Of crucial importance in the formation of deuterium is the ratio of the abundances of neutrons and protons, which is the ratio of their equilibrium abundances in the non-relativistic limit; neglecting chemical potentials (see Appendix A.2)

$$R(T) \equiv \left. \frac{n_n}{n_p} \right|_T \simeq \left(\frac{m_n}{m_p} \right)^{3/2} e^{-\Delta m/T}, \quad (1.46)$$

with $\Delta m = m_n - m_p \simeq 1.3$ MeV.³ So, at $T \gg \Delta m$ the ratio is practically one, while at lower temperatures it quickly decreases. This happens as far as the neutrons remain in thermal equilibrium with the plasma. However, weak interactions become ineffective around⁴ $T_{\text{weak}}^{\text{dec}} \simeq 0.8$ MeV⁵. Below this temperature, the process (1.45) decouples and the ratio becomes

$$R(T_{\text{weak}}^{\text{dec}}) \simeq \left(\frac{m_n}{m_p} \right)^{3/2} e^{-\Delta m/T_{\text{weak}}^{\text{dec}}} \simeq 0.197. \quad (1.47)$$

³If this value was different, or perhaps negative, our Universe would have been very different from how it is.

⁴The precise value is crucial since the decay is exponential, but it is not easy to compute: we will stick to the naive estimate we will do in Section 1.4.

⁵It is just by luck that this temperature is very similar to Δm : again, if their ratio were different things would have ended up differently for us.

From this time on, the only variation in this ratio is due to neutron decay which is starting to be effective

$$R(t) \simeq 0.197 e^{-(t-t_{\text{weak}}^{\text{dec}})/\tau_n} \quad (1.48)$$

where $t_{\text{weak}}^{\text{dec}} \simeq 1$ s is the time at neutron decoupling. Now we can assume that deuterium production is still at equilibrium to get an estimate of the temperature at which a suitable deuterium fraction has formed, allowing helium production. Let us compute

$$\frac{n_{\text{D}}}{n_p n_n} = \frac{3}{4} \left(\frac{2\pi m_{\text{D}}}{m_p m_n T} \right)^{3/2} e^{B_{\text{D}}/T}, \quad (1.49)$$

with $B_{\text{D}} = m_n + m_p - m_{\text{D}} \simeq 2.2$ MeV. Now we use the fact that $n_n = n_b/(1+1/R) \simeq n_b = \eta n_\gamma$, with η the so-called baryon-to-photon ratio. This is the main parameter we want to find from BBN, since it is directly related to $\Omega_b h^2$. We impose $n_{\text{D}}/n_p \simeq 1$ and solve for T ,

$$1 \simeq \eta \frac{2\zeta(3)T^3}{\pi^2} \frac{3}{4} \left(\frac{2\pi m_{\text{D}}}{m_p m_n T} \right)^{3/2} e^{B_{\text{D}}/T}, \quad (1.50)$$

giving, approximately

$$T_{\text{BBN}} \simeq -B_{\text{D}} \left[1 + \log \eta + \frac{3}{2} \log \left(- \frac{B_{\text{D}} m_{\text{D}}}{m_p m_n \log \eta} \right) \right]^{-1}. \quad (1.51)$$

This value is sensitive to the unknown value of η . Now we show that if $\eta \simeq 10^{-10}$, we reproduce the observed ${}^4\text{He}$ mass fraction. For this choice of η , $T_{\text{BBN}} \simeq 0.06$ MeV and $t_{\text{BBN}} \simeq 360$ s. Now the final abundance of ${}^4\text{He}$ is set by the ratio R at t_{BBN} , that is, from Eq. (1.48), $R(t_{\text{BBN}}) \simeq 0.13$. Finally we obtain

$$Y_{4\text{He}} = 4 \frac{n_{4\text{He}}}{n_b} = \frac{2n_n}{n_n + n_p} = \frac{2R(t_{\text{BBN}})}{1 + R(t_{\text{BBN}})} = 0.23. \quad (1.52)$$

If we go back on our steps, we see that in our calculation we needed two ingredients: the value of $T_{\text{weak}}^{\text{dec}}$ and the value of η . This two quantities set the final helium abundance.

- $T_{\text{weak}}^{\text{dec}}$: naively it is given by imposing that the rate of weak interactions is equal to the Hubble rate:

$$T_{\text{weak}}^{\text{dec}} = G_F^{-2/3} M_{\text{Pl}}^{-1/3} g_{\star\rho}^{1/6} \simeq 1 \text{ MeV} \left(\frac{g_{\star\rho}}{10.75} \right)^{1/6}. \quad (1.53)$$

From this formula, we see that, if we increase the strength of the weak interactions, we lower $T_{\text{weak}}^{\text{dec}}$, thus decreasing R and the final helium abundance. On the contrary, if we increase the strength of gravity (decreasing M_{Pl}) we increase also $T_{\text{weak}}^{\text{dec}}$, enhancing helium production. Moreover, we have a very important dependence on the number of relativistic degrees of freedom. This implies BBN is sensitive to all the active relativistic degrees of freedom around 1 MeV: increasing $g_{\star\rho}$, e.g. adding another neutrino species, increases $T_{\text{weak}}^{\text{dec}}$, enhancing the ${}^4\text{He}$ production.

- η : this quantity is directly related to $\Omega_b(t_0) = m_p \eta n_\gamma(t_0) / \rho_c(0)$. In BBN it enters the temperature at which deuterium forms. Increasing η , we increase the number of baryons, favouring deuterium production, which happens earlier, at higher T_{BBN} . Hence the final helium mass fraction increases because neutrons have less time to decay. In the left panel of Fig. 1.8 we show the results of the fit over primordial abundances.

1.4 Beyond the Standard Model of Particle Physics

Rather than only non-baryonic, DM particles must be made of states which are not included in the Standard Model. In this section, we shall see why DM cannot be described by SM physics.

1.4.1 The Standard Model is incomplete

Despite being a very successful theory in describing physics at colliders at energy scales as high as 10 TeV, we know from many hints that the Standard Model is only a low energy effective theory of some more fundamental theory. Let us cite the most compelling motivations.

From the theoretical point of view, the more concerning one is the *hierarchy problem*. It is because the Higgs boson is a fundamental scalar and in the Standard Model it is not protected by any symmetry from receiving very large corrections to its mass from the virtual loop contributions of heavier particles, which are expected to appear at the Planck energy scale $M_{\text{Pl}} = (8\pi G)^{-1/2}$. Then, the observed Higgs mass at Large Hadron Collider appears to be the unnatural result of a fine-tuned cancellation between the intrinsic contribution and the virtual correction terms. Theories try to introduce additional particles and symmetries to cancel these large corrections: one example is supersymmetry (SUSY). Another compelling problem is the unification of gravity with other forces.

On the experimental side, the most striking evidence for beyond Standard Model physics concerns known particles: neutrinos. Indeed there is strong evidence for neutrino flavour oscillations, both for neutrinos originating from cosmic rays decays and interactions in the atmosphere and for neutrinos produced in the nuclear reactions happening in the Sun. Neutrinos are produced and detected in given flavour states since they interact with given flavour charged leptons only. However, when they propagate, both in the vacuum and in the matter, they can change their flavour. This oscillation mechanism can be explained if the neutrinos have mass and their flavour eigenstates are not mass eigenstates. The tightest bounds on neutrino mass come from cosmology, in particular from the CMB analysis [17]

(95%, PlanckTT, TE, EE + lowE + lensing + BAO),

$$\sum_i m_\nu^i < 0.12 \text{ eV}, \quad (1.54)$$

with m_ν^i the mass of i flavour neutrino, as given by the combination of m_j masses of the neutrino mass eigenstates with the mixing matrix U , the Pontecorvo-Maki-Nakagawa-Sakata matrix:

$$m_\nu^i = \sqrt{\sum_j |U_{ij}|^2 m_j^2}. \quad (1.55)$$

We shall see briefly in the next subsection where this bound comes from. Neutrinos are the lightest known massive particles. However, there is no way to account for neutrino masses in a gauge-invariant way within the Standard Model. The lepton Lagrangian reads

$$\mathcal{L}_{\text{SM}} \supset \sum_{\text{flavours}} \left[\bar{E}_L^i i \not{D} E_L^i + \bar{e}_R^i i \not{D} e_R^i \right] - \left[y_e^{ij} \bar{E}_L^i e_R^j H + \text{h.c.} \right]. \quad (1.56)$$

We can generate only gauge-invariant masses for charged leptons as we do not have right neutrinos in the Standard Model. One possibility is that left-handed neutrinos are Majorana particles, but Majorana mass terms, involving left fields only, are not consistent with $U(1)$ symmetries and violate the $U(1)_Y$ gauge symmetry. We need to extend the SM and add new degrees of freedom, for example, some right-handed neutrinos being singlets under the SM gauge group. Indeed, models trying to account for neutrino masses involve an additional heavy right-handed field sterile neutrino N_R and exploit the so-called *see-saw mechanism*. This model tries also to account for the mass hierarchy of the Standard Model: in this way one can explain the masses of ν_L neutrinos being suppressed by 12 orders of magnitude with respect to the top quark, justifying an infinitesimal unnatural Yukawa coupling y_ν .

1.4.2 SM neutrinos as Dark Matter?

Provided we have hints of beyond Standard Model physics in the neutrino sector we can explore the possibility of neutrinos as DM particle candidates.

Being massive, weakly coupled to baryonic matter, invisible and very abundant in the Universe, Standard Model, or active, (meaning charged under $SU(2)_L$) neutrinos were among the first candidates to be proposed. They are a classical example of a *thermal relic*, that is a particle which was in thermal equilibrium with the primordial plasma in the early Universe at high temperature. The departure from thermal equilibrium is the process that set the relic density of neutrinos: if they were coupled to the plasma when they became non-relativistic – as they should sooner or later, being massive – their abundance would have been exponentially suppressed. We will compute this relic density under some assumptions: the proper way to compute the abundance of thermal candidates in the early Universe involves the Boltzmann Equation formalism we will introduce in the following

chapter.

At temperatures $T \sim 10$ MeV neutrinos are coupled to the plasma of electrons and positrons through weak interactions, thus indirectly also to photons and nucleons. The processes which maintain thermal equilibrium are the following ones:

$$\nu\bar{\nu} \leftrightarrow e^-e^+, \quad \nu e^\pm \rightarrow \nu e^\pm, \quad \bar{\nu} e^\mp \rightarrow \bar{\nu} e^\mp. \quad (1.57)$$

However, weak interactions are mediated by massive gauge bosons W^\pm and Z with masses about 80 - 90 GeV. Thanks to naive dimensional analysis, we know that the weak interactions cross-section for the processes above scales as

$$\sigma \sim G_F^2 T^2, \quad (1.58)$$

where $G_F = 1.16 \times 10^{-5} \text{ GeV}^{-2}$ is the Fermi constant. The interaction rate Γ between leptons, i.e. the number of interactions per unit time given the species number density n , can be estimated as

$$\Gamma \sim n\sigma, \quad (1.59)$$

considering relativistic collisions. Weak interactions start to be unable to keep neutrinos coupled to the plasma when the interaction rate drops below the Hubble rate, that means we have less than one interaction in a Hubble time:

$$\Gamma < H \iff n\sigma < \frac{T^2}{M_{\text{Pl}}} g_{\star\rho}^{1/2}(T). \quad (1.60)$$

Assuming $n \propto a^{-3} \sim T^3$ we can get a simple estimate of the *decoupling temperature* of weak interactions $T_{\text{weak}}^{\text{dec}}$, i.e. the temperature at which weak interactions cannot keep the neutrinos coupled to the plasma:

$$T_{\text{weak}}^{\text{dec}} = G_F^{-2/3} M_{\text{Pl}}^{-1/3} g_{\star\rho}^{1/6} \simeq 1 \text{ MeV} \left(\frac{g_{\star\rho}}{10.75} \right)^{1/6}. \quad (1.61)$$

Weak interactions also mediate the annihilation process of neutrinos into charged leptons. When these processes are no more efficient, we say that neutrinos *freeze-out*, since their comoving abundance gets frozen to a nearly constant value. Therefore in a first approximation, we can assume that neutrinos froze-out at 1 MeV. This temperature is well above the mass of neutrinos, as we get from experiments (careful studies of β -decays) or the bound obtained by the Planck Collaboration Eq. (1.54). For this reason, neutrinos are called *hot relics* and are a perfect candidate for Hot Dark Matter (HDM). In this case, the freeze-out happens when the particles are still relativistic and are very far from experiencing Maxwell-Boltzmann suppression by the factor $e^{-m/T}$. Hence the precise value of the freeze-out temperature T_{FO} is not crucial to determine the relic yield. So we can take $T_{\text{FO}} \simeq T_{\text{weak}}^{\text{dec}}$ since the number density of neutrinos is not changing fast. We define the yield

$$Y = \frac{n_\nu}{s}, \quad (1.62)$$

with s the entropy density. This quantity is a comoving number density and stays constant during the history of the Universe if no processes are changing the number of neutrinos. We can assume

$$Y(T_0) \simeq Y_{\text{eq}}(T_{\text{weak}}^{\text{dec}}) = \frac{n_{\nu}^{\text{eq}}}{s} = \frac{\zeta(3)}{\pi^2} \times \frac{3}{4} g_{\nu} \times \left[\frac{2\pi^2}{45} g_{*s}(T_{\text{weak}}^{\text{dec}}) \right]^{-1} = 0.039 \left(\frac{10.75}{g_{*s}(T_{\text{weak}}^{\text{dec}})} \right). \quad (1.63)$$

Then considering only photons as contributing to the entropy density today s_0 , we obtain

$$\Omega_{\nu}(t_0)h^2 = \frac{\sum_i m_{\nu}^i s_0}{\rho_c(t_0)} Y(T_0) = \sum_i m_{\nu}^i \times 0.039 \left(\frac{10.75}{g_{*s}(T_{\text{weak}}^{\text{dec}})} \right) \frac{1519 \text{ cm}^{-3}}{1.1 \times 10^4 \text{ eV cm}^{-3}}, \quad (1.64)$$

yielding

$$\Omega_{\nu}(t_0)h^2 < 6.5 \times 10^{-4} \left(\frac{10.75}{g_{*s}(T_{\text{weak}}^{\text{dec}})} \right) \frac{\sum_i m_{\nu}^i}{0.12 \text{ eV}}. \quad (1.65)$$

This result is very far from the value the DM relic density measured fitting CMB anisotropies or the matter power spectrum.

However, this is not the only reason why neutrinos cannot account for all the DM. The tightest constraints come from structure formation. As we have mentioned in the introduction, DM needs to be cold, i.e. if produced thermally, it has to decouple when it is non-relativistic with a mass above the keV scale. If this condition is not fulfilled, structure formation is compromised because of the large dispersion velocity of the DM, which induces collisionless free streaming on small scales. This impacts heavily on the power spectrum at small scales, since matter perturbation entering the horizon before the DM particles are non-relativistic are damped. Perturbations are erased up to a lengthscale of k_{fs} we now estimate. Let us call $a_{\text{fs}} < a_{\text{eq}}$ the scale factor when the hot relic becomes non-relativistic $T_{\text{fs}} \simeq m$. Assuming radiation domination and that the number of relativistic degrees of freedom between T_{fs} and T_{eq} stays constant,

$$a_{\text{fs}} = a_{\text{eq}} \frac{T_{\text{eq}}}{m}. \quad (1.66)$$

Then, in the limit $a_{\text{fs}} \ll a_{\text{eq}}$,

$$k_{\text{fs}} \simeq \frac{1}{\eta_{\text{fs}}} = H_0 \sqrt{\frac{\Omega_m}{a_{\text{eq}}}} \frac{m}{T_{\text{eq}}} \simeq 0.01 \frac{m}{\text{eV}} h \text{ Mpc}^{-1}, \quad (1.67)$$

with a minor variation for SM neutrinos, which have a temperature smaller than the photons of a factor $(4/11)^{1/3}$. Scales $k > k_{\text{fs}}$ are suppressed with respect to CDM. In the top panel of Fig. 1.9 we show the transfer function for HDM as well as for mixed CDM plus HDM models (MDM). We see for $m \sim 1$ eV candidates that the power spectrum of HDM will be suppressed at scales near k_{fs} . HDM accounts for a relevant fraction of DM only if the candidate is $m \sim 20$ eV, but such candidates are too light to avoid erasing small-scale perturbations. Then if we use the value of the mass for which structure formation is left untouched, $m > 1$ keV, HDM is overproduced. This is why Standard Model neutrinos and

in general thermal HDM is ruled out as a DM candidate. We have finally arrived to the conclusion that DM must be described by beyond Standard Model physics.

Before leaving the topic, let us comment the bound on neutrino masses from Planck, Eq. (1.54). It comes from the above reasoning. Since neutrinos are HDM, if we increase their mass we increase the relevance of HDM concerning the total DM and suppress small-scale perturbations. This has an evident impact on the CMB power spectrum [17]. An observable which is particularly sensitive to this effect is the lensing of CMB photons. In the bottom panel of Fig. 1.9 we show the effect of lensing on the CMB power spectrum: more lensing erases acoustic peaks on small scales. If neutrino masses are higher, small scales structures are suppressed and we have less lensing.

1.5 What we *do* know about Dark Matter

In the last section of this chapter, we want to summarize the key properties of DM, the ones to keep in mind when building models. In this discussion we assume that all the DM is made of a single particle candidate χ with mass m_χ . A recent review of DM features can be found in [25].

1. **Relic density** From Planck measurements [17]

$$\Omega_{\text{DM}}(t_0)h^2 = 0.120 \pm 0.001 . \quad (1.68)$$

2. **Coldness** From structure formation constraints, we know that DM has to be cold, i.e. non-relativistic when the Universe had a temperature around $T \simeq 1 - 10$ keV so that its velocity dispersion is not large enough to compromise structure formation. Below this temperature DM behaves like a pressureless fluid. This fact rules out *thermal* candidates with mass $m_\chi < 1 - 10$ keV such as Standard Model neutrinos [56]. In our work, these constraints will be of crucial importance in studying DM models.
3. **Neutrality** DM cannot interact electromagnetically, otherwise it would be visible and more importantly, it would have been coupled to the photon fluid with a huge impact on the CMB power spectrum. Nevertheless, observations do not exclude completely the possibility DM has a very small electric charge [26].
4. **Self-interactions** The self interaction cross-section of DM σ_{self} cannot be arbitrary large. The tightest limit comes from the careful study of the dynamics in the Bullet cluster, we described in the Section 1.2. The evinced bound is [27]

$$\frac{\sigma_{\text{self}}}{m_\chi} \lesssim 1 \text{ cm}^2 \text{g}^{-1} \simeq 1 \text{ barn GeV}^{-1} = 2.57 \times 10^3 \text{ GeV}^{-3}. \quad (1.69)$$

We see that the bound is not so strict: this value corresponds to a self-interaction

cross-section comparable to one of strong-interacting particles of mass 1 GeV. Actually, there is some tension between observations of small-scale structures (see Appendix B for more details) and predictions of the cold DM paradigm: self-interactions may alleviate this tension [28].

5. **Mass** We still do not know a precise range where the mass of the DM candidate should lie. The upper bound is the Planck mass since we should not expect elementary particles heavier than this value. In fact, in such a case, the Compton wavelength of the particle would be smaller than the Schwarzschild radius of the particle, forming a black hole. To avoid this,

$$\lambda_C > r_S \iff \frac{\hbar}{m_\chi c} > \frac{m_\chi G}{c^2} \iff m_\chi < \left(\frac{\hbar c}{G}\right)^{1/2}. \quad (1.70)$$

Therefore

$$m_\chi < 10^{19} \text{ GeV}. \quad (1.71)$$

We can estimate lower bounds on the DM particle candidate mass, on the base of their statistics, using the knowledge of the size of the smallest DM-dominated structures observed: dwarf spheroidal galaxies with size $R_{\text{dSph}} \simeq 1 \text{ kpc} \simeq 1.6 \times 10^{26} \text{ eV}^{-1}$.

- *Bosons.* The smallest DM structures would be erased if particles could not be confined in a system of size R_{dwarf} . This happens if the de Broglie wavelength of the particles exceeds this size. We exploit the estimated velocity of DM particles $v \sim 10^{-3}c$:

$$\lambda_{\text{dB}} = \frac{1}{m_\chi v_\chi} > R_{\text{dSph}} \implies m_\chi > \frac{1}{v_\chi R_{\text{dSph}}} \simeq 10^{-23} \text{ eV}. \quad (1.72)$$

- *Fermions.* In the case of fermionic DM, we can exploit the Pauli exclusion principle, which imposes limits on the density of fermions in the phase-space. We assume a singular isothermal sphere DM density profile in the central region of the dwarf spheroidal, with σ_{dSph} the velocity dispersion of stars in the dwarf galaxy

$$\rho(r) \simeq \frac{\sigma_{\text{dSph}}^2 M_{\text{Pl}}^2}{4r^2}, \quad (1.73)$$

Then, the velocity of DM particles is Maxwellian-distributed and the phase-space density will be bound by the degenerate value

$$f = \frac{\rho(r)}{(2\pi\sigma_{\text{dSph}}^2)^{3/2} m_\chi^4} < \frac{g_\chi}{(2\pi)^3}, \quad (1.74)$$

where g_χ is the number of internal degrees of freedom of the DM particle. We

obtain

$$m_\chi > \left[\frac{(2\pi)^{3/2}}{4g_\chi} \frac{M_{\text{Pl}}^2}{\sigma_{\text{dSph}} r^2} \right]^{1/4} \simeq 38 \text{ eV} \left(\frac{100 \text{ km s}^{-1}}{\sigma_{\text{dSph}}} \right)^{1/4} \left(\frac{1 \text{ kpc}}{r} \right)^{1/2} g_\chi^{-1/4}. \quad (1.75)$$

This is the so-called Tremaine-Gunn bound [29]. By the way, again it excludes Standard Model neutrinos, just from the observation of dwarf spheroidals.

6. **Lifetime** The particle accounting for the present DM relic density, whatever that is, has to be at least stable over the time scale of the age of the Universe

$$\tau_H \sim H^{-1} \simeq 14 \text{ Gyr} \simeq 4 \times 10^{17} \text{ s}. \quad (1.76)$$

If the DM particle is not stable, then the actual limit depends on the decay products. Limits are very severe if the decays are visible, being them photons or baryons, because they affect the CMB spectrum: $\tau_\chi \gtrsim 10^{25} \div 10^{29} \text{ s}$ [30]. Model-independent bounds come from structures formation, since decays affect the evolution of structures: $\tau_\chi \gtrsim 10^{19}$ [31]

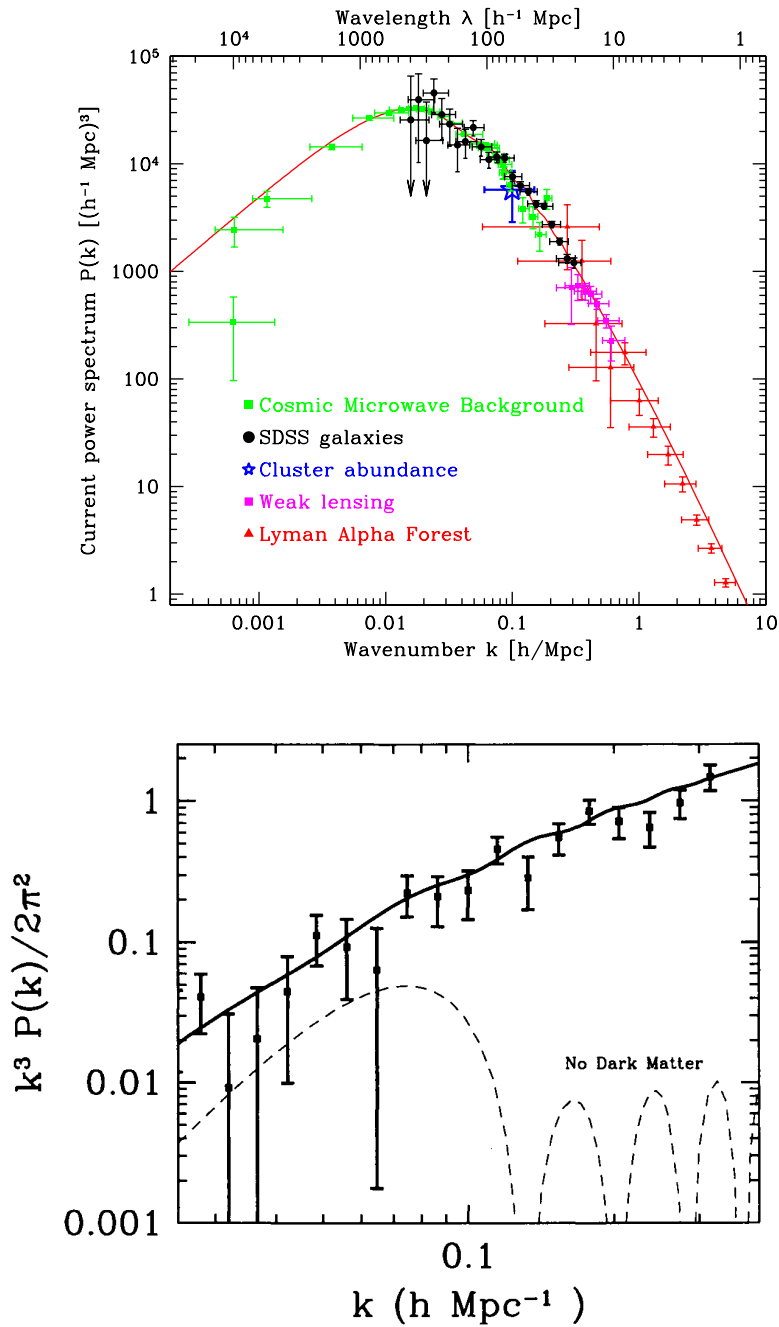


Figure 1.5: Top: the theoretically predicted linear matter power spectrum from the Λ CDM model compared to experimental data from various sources. Note that SDSS and CMB measures mostly arrive at the scales of non-linearities. Figure from [22]. Bottom: the dimensionless power spectrum. Experimental points come from the PSCz galaxy survey while the solid line and dashed lines are the prediction of Λ CDM and baryons only, respectively. Notice that the baryons show the so-called collisional Silk damping which is due to the coupling to the photons: the plasma density perturbations shows damped oscillations once they become sub-horizon scales. This feature is incompatible with data. Figure from [16] and references therein.

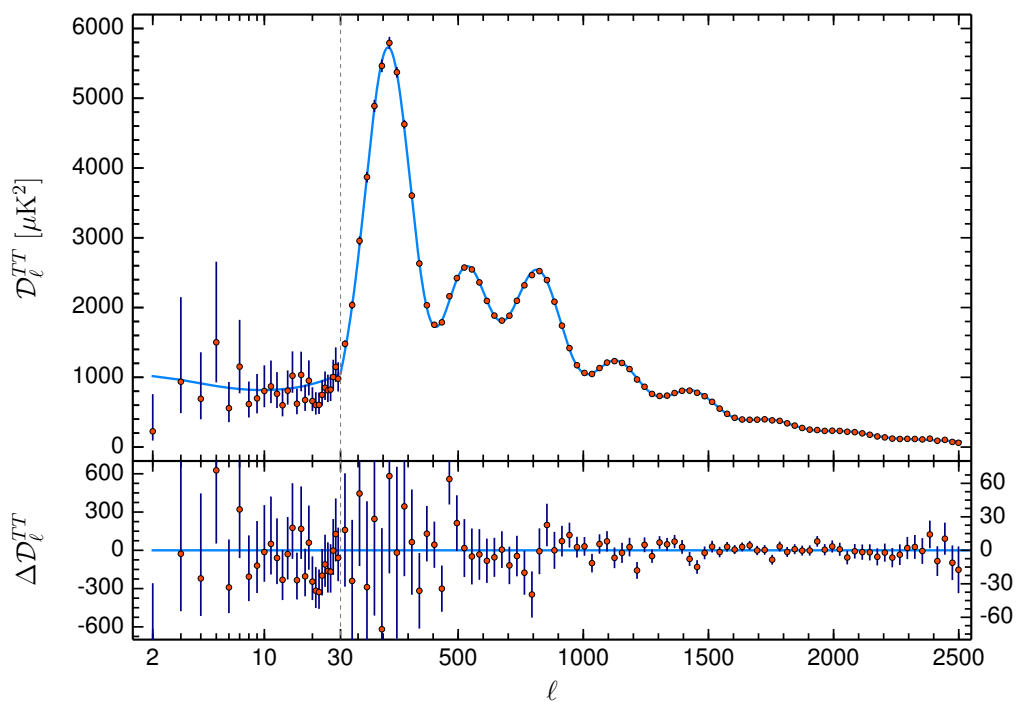


Figure 1.6: The Planck 2018 temperature anisotropies power spectrum from [17]. The upper panel shows the base- Λ CDM theoretical spectrum best fit to the Planck TT,TE,EE+lowE+lensing likelihoods while the lower panel shows residuals with respect to this model. The error bars show the 1σ diagonal uncertainties, including cosmic variance. Note that the vertical scale changes at $\ell = 30$, where the horizontal axis switches from logarithmic to linear. This scale separates large scales from small ones, which are analysed in different ways.

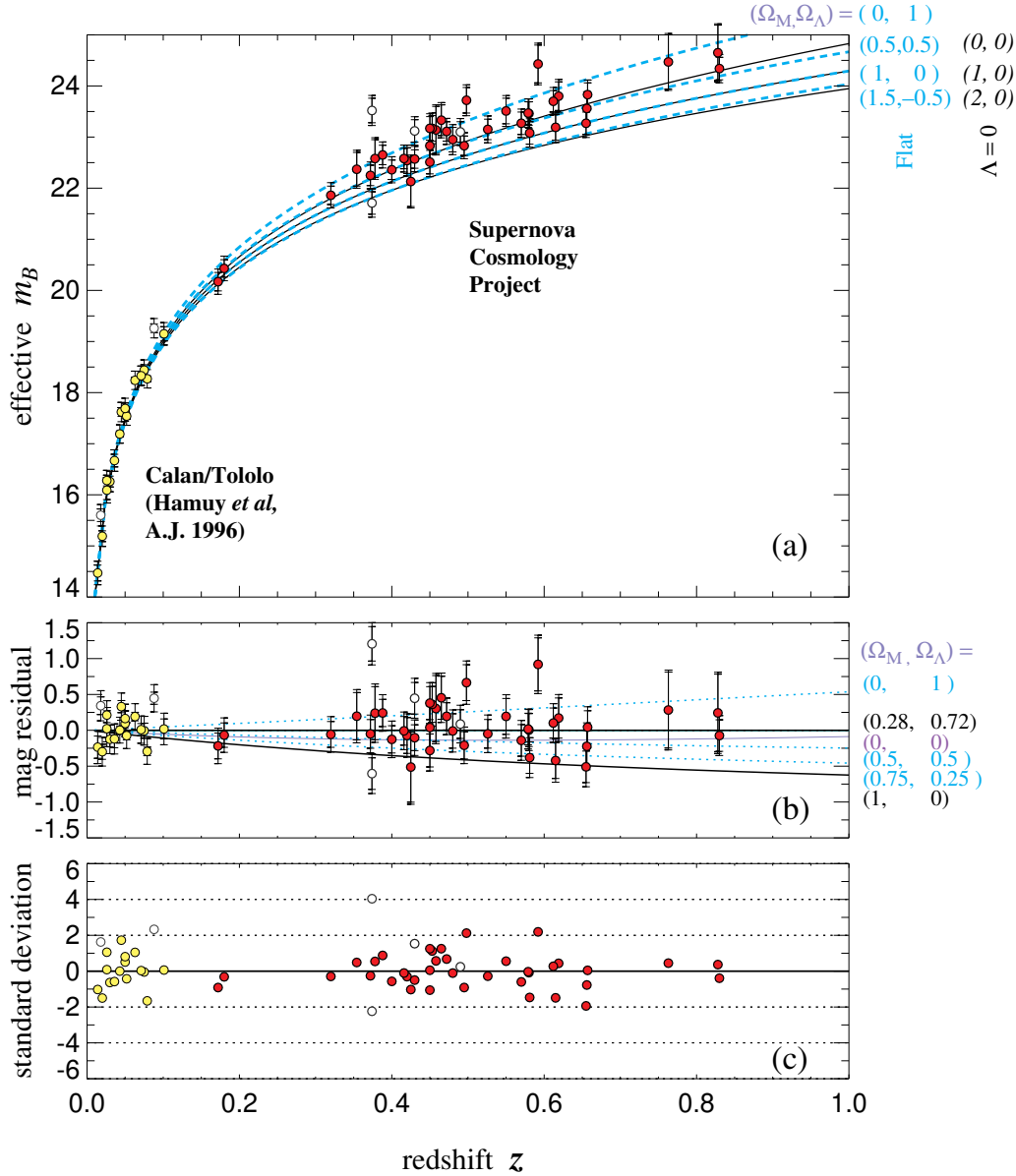


Figure 1.7: Hubble diagram for 42 high-redshift Type Ia supernovae from the Supernova Cosmology Project, and 18 low-redshift Type Ia supernovae from the Calán/Tololo Supernova Survey, plotted on a linear redshift scale to display details at high redshift. In the middle panel, is shown the magnitude residuals from the best-fit flat cosmology supernova subset, $(\Omega_m(t_0), \Omega_\Lambda(t_0)) = (0.28, 0.72)$ with dashed curves for a range of flat cosmological models. In the lower panel, we have the uncertainty-normalized residuals from the best-fit flat cosmology. Figure from [19].

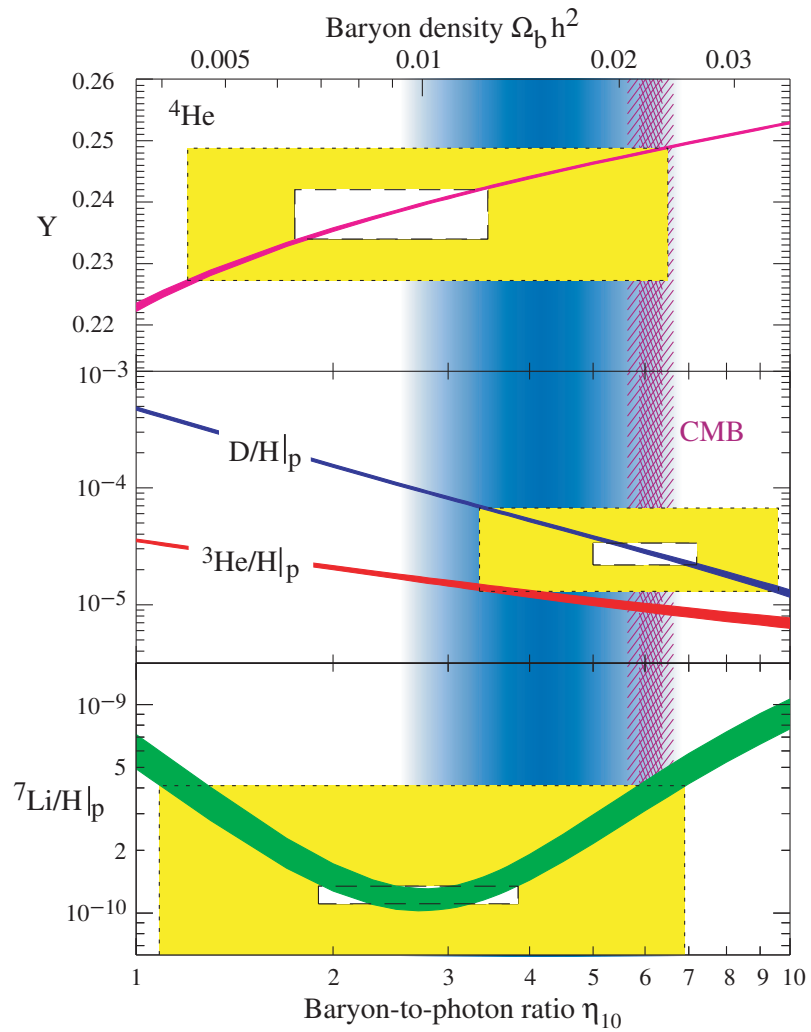


Figure 1.8: The primordial abundances of ${}^4\text{He}$, D, ${}^3\text{He}$ and ${}^7\text{Li}$ as predicted by the standard model of BBN. Boxes indicate the observed light element abundances obtained by different statistical hypothesis. Figure from [18].

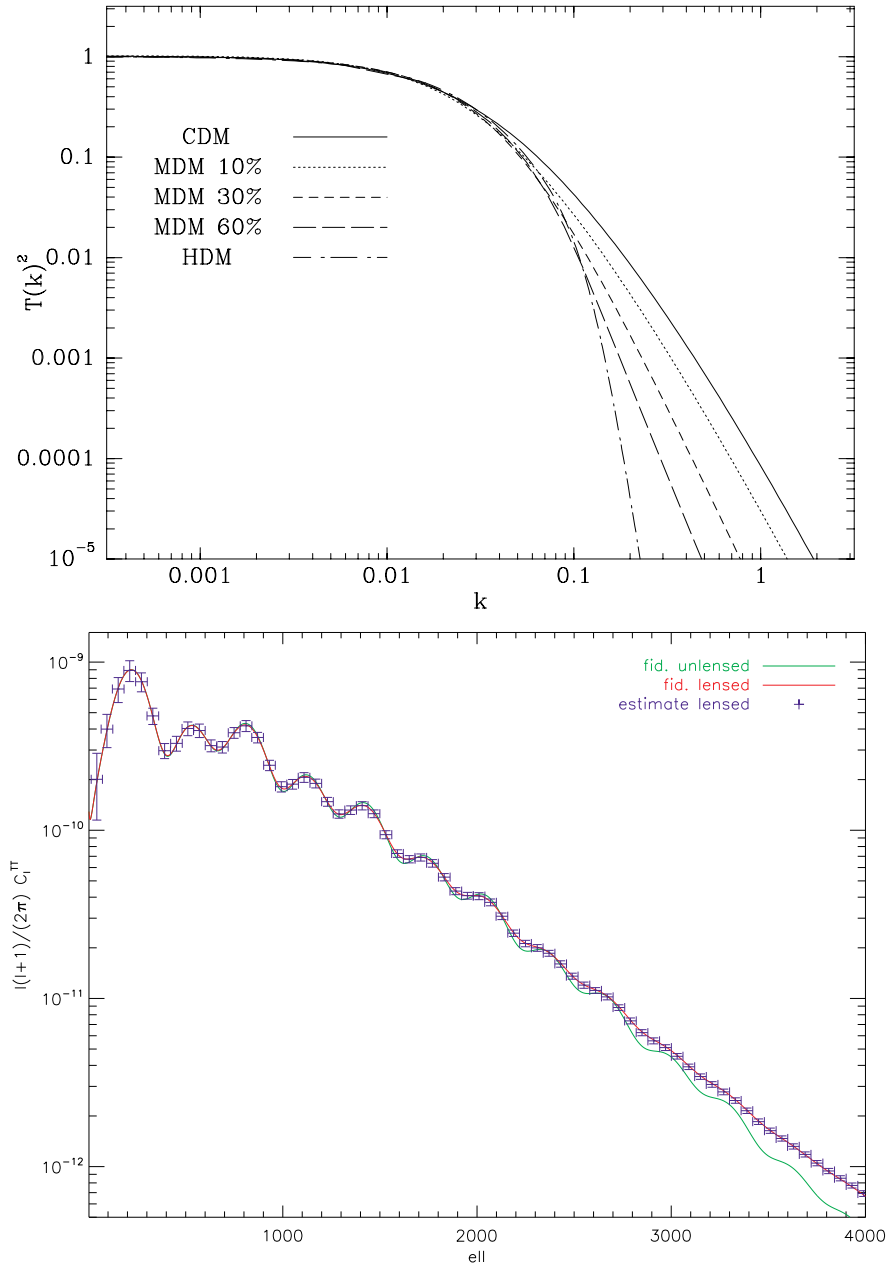


Figure 1.9: Top: transfer functions for WDM (top) and MDM (bottom) models compared. k is in units of $h\text{Mpc}^{-1}$ as usual. Figure from [23]. Bottom: CMB temperature anisotropy power spectrum. The red (green) line is the lensed (unlensed) power spectrum. The blue data points are the mean of the binned power spectrum reconstructed on 500 simulated lensed temperature maps. Figure from [24].

Chapter 2

Boltzmann Equation Formalism

If our Universe had always been in thermal equilibrium, it would be very simple to describe: we would need only one parameter, the temperature of the thermal plasma. In such a Universe, we would not be there asking ourselves fundamental questions: departure from equilibrium is what makes physics interesting and our Universe so non-trivial to describe.

In this work, we are interested in studying the properties and the production mechanisms of DM. The landscape of DM models can be divided in a broad way considering *thermal* candidates and *non-thermal* candidates. For thermal models, the DM particle was in thermal equilibrium in the early Universe at very high temperature and the departure from thermal equilibrium is the process which sets the relic density. Non-thermal models include all other possibilities. The proper tool to carefully study the general evolution of interacting and decoupled particle species in the early Universe is the Boltzmann equation formalism. In this chapter, we will develop the useful formalism, following [16] and [20], to study DM production. We will conclude with a standard example we have already anticipated in treating neutrino relic density: the freeze-out production of thermal candidates.

2.1 Evolution of phase-space distribution

If we want to study the DM production accurately, we have to track the particle properties throughout their history, i.e. while the species is in thermal equilibrium with the primordial plasma or while it is not. The properties of a given particle species are described by their phase-space distribution $f(\vec{x}, \vec{p}, t)$. This function counts, in a probabilistic sense, the number of particles dN at time t within a phase-space cell of volume $d^3x d^3p$ centred about the point corresponding to position \vec{x} and momentum \vec{p} .

$$\frac{g}{(2\pi)^3} d^3x d^3p f(\vec{x}, \vec{p}, t) = dN. \quad (2.1)$$

Here g is the number of internal degrees of freedom of the particle considered and the $(2\pi)^3 = h^3$ (in our units) accounts for the size of the unit phase-space cell as a normalization. The phase-space distribution is normalized such that, in the continuum limit, integrating over the whole phase-space one gets the total number of particles N in the system.

The proper framework to study the evolution of phase-space distributions in the expanding Universe is that of General Relativity. In this case, we rewrite our phase-space distribution as

$$f = f(x^\mu, P^\mu), \quad (2.2)$$

with $x^\mu = (t, \vec{x}) = x^\mu(\lambda)$ the particle trajectory (worldline) in spacetime, parametrized by an affine parameter λ ; P^μ is the particle's comoving four-momentum, defined as

$$P^\mu = P^\mu(\lambda) = \frac{dx^\mu}{d\lambda} = (E, P^i). \quad (2.3)$$

Notice the number of independent parameters is still seven as it was before: the P^μ vector is constrained by the on-shellness condition $P^\mu P_\mu = -m^2$. The definition of f is such that

$$dN = -2a^3 dS_\mu P^\mu d^4 P f(x, P) \delta(P^2 + m^2) \quad (2.4)$$

is the number of worldlines crossing the spacelike surface orthogonal to dS_μ .

The Boltzmann equation describes the evolution of the phase-space distribution under two effects: the geometry of spacetime, which is affected by both gravity and the expansion of the Universe, and interactions with other particle species. These two contributions are accounted for by the two sides of the Boltzmann equation:

$$L[f] = C[f]. \quad (2.5)$$

Let us study the two sides separately.

2.1.1 The Liouville operator

On the left-hand side of Eq. (2.5) we have the Liouville operator L modelling the evolution of the phase-space distribution because of the spacetime geometry, determined by the metric. We are interested in the evolution of the phase-space distribution along a particle's worldline, parametrized by the affine parameter λ . $L[f]$ is defined as the total derivative of f with respect to λ

$$L[f] \equiv \frac{d}{d\lambda} f(x^\mu, P^\mu) = \left[\frac{dx^\mu}{d\lambda} \frac{\partial}{\partial x^\mu} + \frac{dP^\mu}{d\lambda} \frac{\partial}{\partial P^\mu} \right] f. \quad (2.6)$$

Now we use the definition of four-momentum and the geodesic equation in a spacetime with affine connection Γ

$$\frac{dP^\mu}{d\lambda} + \Gamma^\mu_{\rho\sigma} P^\rho P^\sigma = 0, \quad (2.7)$$

to write the Liouville operator in its general covariant form

$$L[f] = \left[P^\mu \frac{\partial}{\partial x^\mu} - \Gamma_{\rho\sigma}^\mu P^\rho P^\sigma \frac{\partial}{\partial P^\mu} \right] f. \quad (2.8)$$

To write the Liouville operator in a more specific form, we have to explicit the spacetime metric $g_{\mu\nu}$. If we neglect spatial anisotropies and inhomogeneities, the phase-space distribution will not depend on chosen space points or directions. Firstly, assuming homogeneity and isotropy together with a zero spatial curvature, we are constraining the metric to be of the form of the flat Friedmann Robertson Walker (FRW) one, derived in Appendix A. Secondly, the phase-space distribution is uniform in space, due to homogeneity, and depend only on the physical spatial modulus of momentum $p^2 = g_{ij}p^i p^j = a^2 \delta_{ij} P^i P^j$, due to isotropy. We can write it simply as

$$f = f(t, p(t)), \quad (2.9)$$

with time dependence in the physical momentum, since it redshifts with time as $p \propto 1/a$. Therefore, under our hypothesis, our goal is to characterize the phase-space distribution as a function of time and momentum magnitude. In Appendix A, we compute the affine connection coefficients for the flat FRW metric. Substituting these expressions and using the definition of the Hubble parameter $H(t) \equiv a^{-1} da/dt$, the Liouville operator becomes

$$L[f] = E \left[\frac{\partial}{\partial t} - pH \frac{\partial}{\partial p} \right] f = E \frac{df}{dt}. \quad (2.10)$$

The total derivative with respect to cosmic times takes into account the redshift of physical momentum. We shall use this form when we are interested in computing directly $f(t, p)$. Instead, when dealing with moments of the phase-space distributions, such as densities, usually p is traded for the energy $E = \sqrt{p^2 + m^2}$, so that

$$f = f(t, E(t)) \quad (2.11)$$

and we have an equivalent form of the Liouville operator:

$$L[f] = E \frac{\partial f}{\partial t} - H(t)[E^2 - m^2] \frac{\partial f}{\partial E}. \quad (2.12)$$

If the particle species we are considering experiences no collisions at all, the Boltzmann equation reads simply $L[f] = 0$ and then we have a partial differential equation the distribution function has to satisfy.

2.1.2 The collision operator

The right-hand side of the Boltzmann equation Eq. (2.5) is the collision operator which is the term accounting for all the interactions the considered particle species experience among themselves or with other species. In general, this includes all the processes in which

the particle species is involved: decays, inverse decays, (in)elastic scatterings, annihilations, and so on. To obtain the general form of the collision operator, let us consider a generic process involving the particle of interest, we label as χ :

$$\chi + a + b + \dots \longleftrightarrow i + j + k + \dots . \quad (2.13)$$

Schematically, the collision term is the difference of two terms, one increasing the probability distribution f_χ for the species χ , the other decreasing it. For example, if we have a process in which χ is destroyed passing from initial to final state as above, we will have two contributions of opposite sign related to the two directions the process can happen. The crucial ingredient to characterize the collisions are: (i) energy and momentum conservation, (ii) the scattering amplitude of the process and the phase-space distributions, which tell how likely is the process to happen (iii) the distributions of all the species involved which tell how many particles are available with given momentum to let the reaction happen. If we are interested in the spatially uniform and isotropic distribution $f_\chi = f(t, E)$ (quantities related to χ are written with no labels), we need to integrate out all the energy/momentum dependence appearing in the other phase-space distributions $f_\alpha = f(t, E_\alpha)$. To do that, it is useful to consider the Lorentz-invariant measure for the generic species α

$$d\Pi_\alpha = \frac{g_\alpha}{(2\pi)^3} \frac{d^3 p_\alpha}{2E_\alpha}. \quad (2.14)$$

The $(2\pi)^3$ at the denominator is just the proper normalization, the phase-space cell size h^3 in units $\hbar = 1$, while the factor g_α accounts for the internal degrees of freedom of species α . Basing on the above reasoning, one can show that the collision term for the particle χ interacting with the above process only is

$$\begin{aligned} C[f_\chi] = & \frac{1}{2} \int d\Pi_a d\Pi_b \dots d\Pi_i d\Pi_j d\Pi_k \dots (2\pi)^4 \delta^{(4)}(p_\chi + p_a + p_b + \dots - p_i - p_j - p_k - \dots) \\ & \times \left[- |\mathcal{M}_{\chi+a+b+\dots \rightarrow i+j+k+\dots}|^2 f_\chi f_a f_b \dots (1 \mp f_i)(1 \mp f_j)(1 \mp f_k) \dots \right. \\ & \left. + |\mathcal{M}_{i+j+k+\dots \rightarrow \chi+a+b+\dots}|^2 f_i f_j f_k \dots (1 \mp f_\chi)(1 \mp f_a)(1 \mp f_b) \dots \right]. \end{aligned} \quad (2.15)$$

In Appendix C, we find from first principles the expression for the collision operator for a generic process in a flat Minkowski spacetime, neglecting quantum degeneracies; this form for the collision operator is independent on the spacetime geometry. If χ is involved in more than one process (with different initial or final states) the total collision term is the sum of each process' collision term. Let us comment the formula Eq. (2.15). As needed, we have the sum, with opposite signs, of the process and its inverse, with a plus sign for the process producing χ in the final state. The $\delta^{(4)}(\dots)$ enforces energy and momentum conservation. The matrix elements $|\mathcal{M}|^2$ are determined from fundamental physics and are *averaged* over initial and final spins¹ including the appropriate symmetry factor $1/N!$ for N identical particles in the initial or final states. We see that the variation

¹In Appendix C this fact is derived explicitly.

of f_χ induced by the collision operator is proportional to the initial state phase-space distributions $f_\chi f_a f_b \dots$ (or $f_i f_j f_k \dots$ for the inverse process). The $(1 \mp f_\alpha)$ factors, with a plus sign for bosons and a minus sign for fermions, are for the final states of the processes and represent, respectively, the phenomena of Bose enhancement and Pauli blocking. For fermions, for example, if final state occupation number f_α is non-negligible, i.e. there are already a fair number of α particles in the final state, the production of more α particles is disfavoured by the Pauli exclusion principle since some of the cells in the phase-space are already occupied. The opposite holds for bosons, for which the production of more particles in the final state is enhanced.

The very general Eq. (2.15) can be simplified under two important assumptions we often make in dealing with DM production:

1. T or CP invariance. If the considered process preserves time-reversal discrete symmetry T (i.e. CP , thanks to the CPT theorem), we can write

$$|\mathcal{M}_{\chi+a+b+\dots \rightarrow i+j+k+\dots}|^2 = |\mathcal{M}_{i+j+k+\dots \rightarrow \chi+a+b+\dots}|^2 \equiv |\mathcal{M}|^2. \quad (2.16)$$

and collect the amplitudes in Eq. (2.15). This is often the case in processes we study to model DM production. An important exception is when we deal with mechanisms requiring explicitly CP violation, such as asymmetric DM production or baryogenesis.

2. No Bose-Einstein condensation or Fermi degeneracy. If in the final states occupation numbers are low $f_\alpha \ll 1$, we can neglect the Bose enhancement and Pauli blocking factors and assume in a good approximation

$$(1 \mp f_\alpha) \simeq 1 \quad (2.17)$$

If we exploit this approximation, we have to neglect the quantum statistics in the corresponding equilibrium distributions f_α^{eq} for consistency with the detailed balance using equilibrium distributions

$$f_\chi^{\text{eq}} f_a^{\text{eq}} f_b^{\text{eq}} \dots (1 \mp f_i^{\text{eq}})(1 \mp f_j^{\text{eq}})(1 \mp f_k^{\text{eq}}) \dots = f_i^{\text{eq}} f_j^{\text{eq}} f_k^{\text{eq}} \dots (1 \mp f_\chi^{\text{eq}})(1 \mp f_a^{\text{eq}})(1 \mp f_b^{\text{eq}}) \dots \quad (2.18)$$

This fact will be important in specific cases.

Therefore, under these assumptions Eq. (2.15) becomes

$$\begin{aligned} C[f_\chi] &= \frac{1}{2} \int d\Pi_a d\Pi_b \dots d\Pi_i d\Pi_j d\Pi_k \dots (2\pi)^4 \delta^{(4)}(p_\chi + p_a + p_b + \dots - p_i - p_j - p_k - \dots) \\ &\quad \times |\mathcal{M}|^2 \left[f_i f_j f_k \dots - f_\chi f_a f_b \dots \right] \quad CP \text{ conservation} + \text{no degeneracies} \end{aligned} \quad (2.19)$$

Finally, we can rewrite explicitly the Boltzmann equation Eq. (2.5) for particle species χ in a standard flat FRW Universe experiencing only CP conserving processes and neglecting

quantum degeneracies, in the form

$$E \frac{\partial f_\chi}{\partial t} - H(t)[E^2 - m_\chi^2] \frac{\partial f_\chi}{\partial E} = \frac{1}{2} \int \Pi_a d\Pi_b \cdots d\Pi_i d\Pi_j d\Pi_k \cdots \\ \times (2\pi)^4 \delta^{(4)}(p_\chi + p_a + p_b + \cdots - p_i - p_j - p_k - \cdots) |\mathcal{M}|^2 \left[f_i f_j f_k \cdots - f_\chi f_a f_b \cdots \right]. \quad (2.20)$$

This is the equation we will be concerned in most of our work. In the most general case, to solve the Boltzmann equation for our particle of interest χ , we have to consider an equation for each particle species in the Universe interacting with χ . So altogether the Boltzmann equations make a coupled set of integral-partial differential equations for the phase-space distributions of all species present. The solution of this system is very tough, unless we exploit some clever approximations, depending on the specific problem we are dealing with.

2.2 Equilibrium phase-space distributions

We have said that the Boltzmann equation formalism is our tool to study properties of particle species in the Universe and to track their evolution carefully also in the delicate phase of departure from equilibrium. Let us understand what we mean with equilibrium and under which hypothesis we assume a species is in equilibrium.

There are two different types of equilibrium, depending on the processes our considered particle species is involved in:

- *Kinetic equilibrium.* If elastic processes, i.e. ones with the same particles in the initial and final states such as

$$\chi + a \longleftrightarrow \chi + a, \quad (2.21)$$

are efficient, and they can keep the same temperature T between the involved species, we say there is kinetic equilibrium. The efficiency of these processes is measured by a timescale that has to be suitably small. If kinetic equilibrium is assured, particle species are described by Bose-Einstein (BE: $-$) and Fermi-Dirac (FD: $+$) phase-space distributions, which respect the symmetries of our spacetime

$$f(t, E) = \left\{ \exp \frac{E - \mu(t)}{T(t)} \mp 1 \right\}^{-1}. \quad (2.22)$$

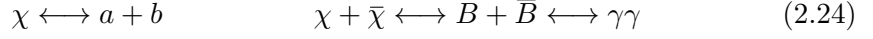
If we neglect the ∓ 1 factor, assuming no quantum degeneracies we obtain

$$f(t, E) \simeq \exp \left\{ \frac{\mu(t) - E}{T(t)} \right\} = f_{\text{MB}}(t, \mu(t), E) \quad (2.23)$$

In this limit the particle species follow the Maxwell-Boltzmann phase-space distribution with non-negligible *chemical potential* $\mu(t)$. In statistical mechanics, μ is the Lagrange multiplier of the number of particles, so it regulates the abundances of

particles according to number-changing reactions.

- *Chemical equilibrium.* If number-changing interactions such as decays, inverse decays and annihilations, e.g.



are efficient, we say chemical equilibrium is assured. In the above processes, B are thermal bath particles and γ are photons. If chemical equilibrium is achieved, we can write linear relations between the chemical potentials of the particle species involved

$$\mu_\chi = \mu_a + \mu_b \qquad \mu_\chi + \mu_{\bar{\chi}} = \mu_B + \mu_{\bar{B}} = \mu_\gamma = 0. \qquad (2.25)$$

The last equality holds since photons can be absorbed or emitted freely.

When we have both chemical and kinetic equilibrium between species we say we have *thermal equilibrium* and particles belong to a thermal bath. If that happens, particles are described only by the thermal bath temperature T and chemical potentials become all negligible: $\mu_i \approx 0$ ². The phase-space distribution of a species α in thermal equilibrium will be

$$f_\alpha^{\text{eq}} = f_\alpha^{\text{eq}}(t, E_\alpha) = \exp \left\{ -\frac{E_\alpha}{T(t)} \right\}. \qquad (2.26)$$

In most cases, kinetic equilibrium is assured, while number-changing processes, such as annihilations, become inefficient earlier on in the thermal history, leading to a departure from chemical equilibrium for species α . In this case, a convenient form of the phase-space distribution throughout the equilibrium and out-of-equilibrium phases is

$$f_\alpha = f(t, E_\alpha) = \exp \left\{ \frac{\mu_\alpha(t)}{T(t)} \right\} f_\alpha^{\text{eq}}, \qquad (2.27)$$

with $\mu(t)$ an unknown function of time.

2.3 Evolution of number density

Sometimes, we are not interested in the full phase-space distribution, but only in its *moments*, i.e. quantities obtained integrating the phase-space distribution over momenta of the considered particle species. For example, the number density of the particle species α is the zeroth moment of the phase-space distribution

$$n_\alpha(t) = \frac{g_\alpha}{(2\pi)^3} \int d^3p f_\alpha, \qquad (2.28)$$

²For asymmetric species in the Universe, such as baryons, it can be verified that $\mu_b/T \simeq \eta_b = n_b/n_\gamma \simeq 10^{-10}$.

while

$$v_\alpha^i(t) = \frac{1}{n_\alpha(t)} \frac{g}{(2\pi)^3} \int d^3p \frac{p \hat{p}^i}{E} f_\alpha \quad (2.29)$$

is the velocity (the dipole) of the species. It is the average of the particle velocity over the distribution, normalized to the density; \hat{p}^i is the direction of momentum. Along this line, one can go for higher moments. Usually, the moment decomposition of the phase-space distribution is exploited for two reasons: to extract physical observables from the quite abstract phase-space distributions and to simplify the solution of the BEs. Indeed the moments are usually hierarchical, that means their importance decreases as one goes to higher moments.

For DM studies, we are interested in reproducing the relic density hence $n_\chi(t)$ is of primary importance. Let us write the BE, from Eq. (2.20) for the zero moment. We integrate over momenta d^3p and multiply both sides by $g_\chi/E(2\pi)^3$: in this way, we reconstruct a $d\Pi_\chi$ at the right-hand side:

$$\begin{aligned} \frac{dn_\chi}{dt} - H(t) \frac{g_\chi}{(2\pi)^3} \int d^3p_\chi \frac{E^2 - m_\chi^2}{E} \frac{\partial f_\chi}{\partial E} &= \int d\Pi_\chi d\Pi_a d\Pi_b \cdots d\Pi_i d\Pi_j d\Pi_k \cdots \\ &\times (2\pi)^4 \delta^{(4)}(p_\chi + p_a + p_b + \cdots - p_i - p_j - p_k - \cdots) |\mathcal{M}|^2 \left[f_i f_j f_k \cdots - f_\chi f_a f_b \cdots \right]. \end{aligned} \quad (2.30)$$

Let us compute the integral on the left-hand side, using $p^2 = E^2 - m^2$ and $pdp = EdE$

$$\int d^3p \frac{E^2 - m^2}{E} \frac{\partial f}{\partial E} = \int d\Omega \int dp p^2 \frac{p^2}{E} \frac{E}{p} \frac{\partial f}{\partial p} = \int d\Omega \left[p^2 f \Big|_0^\infty - \int dp 3p^2 f \right] = -3 \int d^3p f \quad (2.31)$$

The first term in the square brackets vanishes, since we reasonably assume that $f(t, p)$ decays exponentially at infinity. Therefore the Boltzmann equation for the number density gets the form

$$\begin{aligned} \frac{dn_\chi}{dt} + 3H(t)n_\chi(t) &= \int d\Pi_\chi d\Pi_a d\Pi_b \cdots d\Pi_i d\Pi_j d\Pi_k \cdots \\ &\times (2\pi)^4 \delta^{(4)}(p_\chi + p_a + p_b + \cdots - p_i - p_j - p_k - \cdots) |\mathcal{M}|^2 \left[f_i f_j f_k \cdots - f_\chi f_a f_b \cdots \right]. \end{aligned} \quad (2.32)$$

2.4 Standard application: freeze-out production of DM

In this section, we specialize Eq. (2.32) to the famous case of freeze-out production of DM, which we have anticipated in treating the neutrino relic density. We address the problem with a simple model trying to include the two important cases of hot dark matter (HDM) and cold dark matter (CDM) freeze-out production. A very appealing feature of freeze-out is that the DM relic density depends only on masses and couplings assumed in

the model and does not depend on the initial conditions of the Universe or its previous history. This feature is expressed saying that DM freeze-out is “IR-dominated”. Moreover, the aforementioned masses and couplings, giving cross-sections for specific processes, can be in principle measured in a laboratory with a direct detection experiment.

Let us consider a thermal DM candidate, which at very high temperatures is in thermal equilibrium with the primordial plasma. We discuss the simplest case of a single DM particle with no relevant self-interactions. Suppose that the DM candidate χ is stable (or with lifetime $\tau_\chi \gg \tau_H$). If so, the only number-changing interactions are annihilation and inverse annihilation processes, e.g.

$$\chi\bar{\chi} \longleftrightarrow B\bar{B}. \quad (2.33)$$

We denote with B, \bar{B} bath particles in which χ can annihilate; the thermal bath is characterized by a temperature T . Let us assume that m_χ is the relevant energy scale in the process, i.e. that $m_B \ll m_\chi$ otherwise the freeze-out would be determined by the mass scale of bath particles. When in equilibrium, at $m_\chi \ll T$ the reaction proceeds in both directions; however, when $m_\chi \gtrsim T$ the bath particles are not energetic enough to produce χ pairs, hence the DM particles disappear quickly. Bath particles are always more strongly coupled to the thermal bath than χ particles, hence we will safely assume the B species to be in thermal equilibrium, so that

$$f_B = f_B^{\text{eq}} = \exp(-E_B/T), \quad f_{\bar{B}} = f_{\bar{B}}^{\text{eq}} = \exp(-E_{\bar{B}}/T). \quad (2.34)$$

As we show in Appendix A.2, the number density of a particle in thermal equilibrium with the bath is given by

$$n_\chi^{\text{eq}} = \frac{g_\chi T^3}{2\pi^2} \left(\frac{m_\chi}{T}\right)^2 K_2\left(\frac{m_\chi}{T}\right) \simeq \begin{cases} \frac{g_\chi T^3}{\pi^2} & m_\chi \ll T \\ g_\chi \left(\frac{m_\chi T}{2\pi}\right)^{3/2} e^{-m_\chi/T} & m_\chi \gg T \end{cases} \quad (2.35)$$

K_2 is the modified Bessel function of the second kind. Consistently with the above assumptions, we are neglecting the quantum statistics which, as it can be checked, have very little impact on the solution only at $T \gg m_\chi$.

It is useful to scale out from the left-hand side of the Boltzmann equation for the number density Eq. (2.32) the effect of the expansion of the Universe by considering the evolution of the number of particles in a comoving volume. This is usually done introducing the yield or the comoving number density

$$Y_\chi = \frac{n_\chi}{s}. \quad (2.36)$$

Since the entropy of the radiation bath in a comoving volume s is conserved in a FRW

Universe, $sa^3 = \text{const}$, we have that

$$\frac{dn_\chi}{dt} + 3Hn_\chi = \frac{d(sY_\chi)}{dt} + 3HsY_\chi = s\frac{dY_\chi}{dt}. \quad (2.37)$$

The study of Eq. (2.32) is much clearer if we use the temperature as a time variable rather than cosmic time and we make dimensionless its inverse using the other energy scale involved, the mass of the interesting particle species, the DM in our case.

$$x = \frac{m_\chi}{T}. \quad (2.38)$$

To rewrite dY_χ/dt in terms of dY_χ/dT we exploit Eq. (A.80) derived from the conservation of entropy

$$\frac{dY_\chi}{dt} = -\left(1 + \frac{1}{3} \frac{d \log g_{\star s}}{d \log T}\right)^{-1} H \frac{dY_\chi}{d \log T}. \quad (2.39)$$

Then we change variable from T to x simply using the fact that the logarithmic derivative satisfies $dY_\chi/d \log T = -dY_\chi/d \log x$:

$$\frac{dY_\chi}{dt} = \left(1 - \frac{1}{3} \frac{d \log g_{\star s}}{d \log x}\right)^{-1} H \frac{dY_\chi}{d \log x}. \quad (2.40)$$

The dependence of $g_{\star\rho}$ on T , hence on x is given explicitly in Appendix A.2, where we use the formula found by [32]. In these new variables, we can write the BE Eq. (2.32) as

$$\begin{aligned} \frac{dY_\chi}{dx} = & \frac{1}{xs(x)H(x)} \left(1 - \frac{1}{3} \frac{d \log g_{\star s}}{d \log x}\right) \int d\Pi_\chi d\Pi_a d\Pi_b \cdots d\Pi_i d\Pi_j d\Pi_k \cdots \\ & \times (2\pi)^4 \delta^{(4)}(p_\chi + p_a + p_b + \cdots - p_i - p_j - p_k - \cdots) |\mathcal{M}|^2 \left[f_i f_j f_k \cdots - f_\chi f_a f_b \cdots \right]. \end{aligned} \quad (2.41)$$

We can focus on the radiation domination era because it is the epoch in which DM should be already decoupled from the bath, to allow structure formation at lower temperatures. Apart from hot relics, like active neutrinos, we focus on the evolution of the comoving density of DM candidates of mass $m_\chi > 1$ keV and in the interval $x \in [10^{-1}, 10^3]$, hence always safely in radiation domination $T > 1$ eV: in particular, we consider the temperature range $1 \text{ eV} < T < 10^3 \text{ GeV}$. Let us explicit the temperature dependence inside $H(t)$ during radiation domination

$$H(x) = \sqrt{\frac{\rho}{3M_{\text{Pl}}^2}} = 0.33m_\chi^2 g_{\star\rho}^{1/2}(x) \frac{x^{-2}}{M_{\text{Pl}}} \simeq H_1 g_{\star\rho}^{1/2}(x) x^{-2}, \quad (2.42)$$

with $H_1 = 0.33m_\chi^2 M_{\text{Pl}}^{-1}$. We explicit also the dependence in the entropy

$$s(x) = \frac{2\pi^2}{45} g_{\star s}(T) T^3 = s_1 g_{\star s}(x) x^{-3}, \quad (2.43)$$

with $s_1 = 0.439m_\chi^3$. So

$$\begin{aligned} \frac{dY_\chi}{dx} &= \frac{x^4}{s_1 H_1} \left(1 - \frac{1}{3} \frac{d \log g_{\star s}}{d \log x}\right) g_{\star s}^{-1}(x) g_{\star \rho}^{-1/2}(x) \int d\Pi_\chi d\Pi_a d\Pi_b \cdots d\Pi_i d\Pi_j d\Pi_k \cdots \\ &\quad \times (2\pi)^4 \delta^{(4)}(p_\chi + p_a + p_b + \cdots - p_i - p_j - p_k - \cdots) |\mathcal{M}|^2 \left[f_i f_j f_k \cdots - f_\chi f_a f_b \cdots \right]. \end{aligned} \quad (2.44)$$

We can write the yield at equilibrium:

$$Y_\chi^{\text{eq}}(x) = \frac{45}{4\pi^4} \frac{g_\chi}{g_{\star s}} x^2 K_2(x) \simeq \begin{cases} 0.23 \frac{g_\chi}{g_{\star s}} & x \ll 1 \\ 0.145 \frac{g_\chi}{g_{\star s}} x^{3/2} e^{-x} & x \gg 1 \end{cases} \quad (2.45)$$

DM is massive: we know from the above equation that if a massive particle species remained in thermal equilibrium $Y_\chi \simeq Y_\chi^{\text{eq}}$ until now its present abundance will be completely negligible since it was exponentially suppressed. The only way for a candidate to leave a sizeable relic density is to part from equilibrium when the exponential suppression has not washed out the density yet. Now let us write the Boltzmann equation for the species χ in our specific case. From Eq. (2.44) we have, for the considered processes

$$\begin{aligned} \frac{dY_\chi}{dx} &= - \frac{x^4}{s_1 H_1} \left(1 - \frac{1}{3} \frac{d \log g_{\star s}}{d \log x}\right) g_{\star s}^{-1}(x) g_{\star \rho}^{-1/2}(x) \int d\Pi_\chi d\Pi_{\bar{\chi}} \Pi_B \Pi_{\bar{B}} (2\pi)^4 \\ &\quad \times \delta(E_\chi + E_{\bar{\chi}} - E_B - E_{\bar{B}}) \delta^{(3)}(\vec{p}_\chi + \vec{p}_{\bar{\chi}} - \vec{p}_B - \vec{p}_{\bar{B}}) |\mathcal{M}_{\chi\bar{\chi} \rightarrow B\bar{B}}|^2 [f_B^{\text{eq}} f_{\bar{B}}^{\text{eq}} - f_\chi f_{\bar{\chi}}]. \end{aligned} \quad (2.46)$$

Let us focus on the factor $[f_B^{\text{eq}} f_{\bar{B}}^{\text{eq}} - f_\chi f_{\bar{\chi}}]$. Due to energy conservation,

$$f_B^{\text{eq}} f_{\bar{B}}^{\text{eq}} = \exp[-(E_B + E_{\bar{B}})/T] = \exp[-(E_\chi + E_{\bar{\chi}})/T] = f_\chi^{\text{eq}} f_{\bar{\chi}}^{\text{eq}} \quad (2.47)$$

Then we use the fact that the ratio

$$\frac{f_\chi}{f_\chi^{\text{eq}}} = \frac{n_\chi}{n_\chi^{\text{eq}}} = \exp(\mu_\chi/T) \quad (2.48)$$

is independent on momenta, to take this term out of the integral

$$\begin{aligned} \frac{dY_\chi}{dx} &= \frac{x^4}{s_1 H_1} \left(1 - \frac{1}{3} \frac{d \log g_{\star s}}{d \log x}\right) g_{\star s}^{-1}(x) g_{\star \rho}^{-1/2}(x) \int d\Pi_\chi d\Pi_{\bar{\chi}} \Pi_B \Pi_{\bar{B}} (2\pi)^4 \\ &\quad \times \delta(E_\chi + E_{\bar{\chi}} - E_B - E_{\bar{B}}) \delta^{(3)}(\vec{p}_\chi + \vec{p}_{\bar{\chi}} - \vec{p}_B - \vec{p}_{\bar{B}}) |\mathcal{M}_{\chi\bar{\chi} \rightarrow B\bar{B}}|^2 f_\chi^{\text{eq}} f_{\bar{\chi}}^{\text{eq}} \left[1 - \frac{n_\chi}{n_\chi^{\text{eq}}} \frac{n_{\bar{\chi}}}{n_{\bar{\chi}}^{\text{eq}}}\right] \\ &= - \frac{x^4}{s_1 H_1} \left(1 - \frac{1}{3} \frac{d \log g_{\star s}}{d \log x}\right) g_{\star s}^{-1}(x) g_{\star \rho}^{-1/2}(x) [n_\chi n_{\bar{\chi}} - n_\chi^{\text{eq}} n_{\bar{\chi}}^{\text{eq}}] \frac{1}{n_\chi^{\text{eq}} n_{\bar{\chi}}^{\text{eq}}} \\ &\quad \times \int d\Pi_\chi d\Pi_{\bar{\chi}} \Pi_B \Pi_{\bar{B}} (2\pi)^4 \delta^{(4)}(p_\chi + p_{\bar{\chi}} - p_B - p_{\bar{B}}) |\mathcal{M}_{\chi\bar{\chi} \rightarrow B\bar{B}}|^2 f_\chi^{\text{eq}} f_{\bar{\chi}}^{\text{eq}} \end{aligned} \quad (2.49)$$

We assume no DM asymmetry from the beginning $n_\chi(0) = n_{\bar{\chi}}(0) = n_\chi^{\text{eq}}(0) = n_{\bar{\chi}}^{\text{eq}}(0)$, and also, consistently with the thermal candidate hypothesis, that abundances tracked the

equilibrium ones at high temperatures. We introduce the thermally averaged annihilation cross-section

$$\langle \sigma_{\chi\bar{\chi} \leftrightarrow B\bar{B}} |v\rangle = \frac{1}{(n_{\chi}^{\text{eq}})^2} \int d\Pi_{\chi} d\Pi_{\bar{\chi}} \Pi_B \Pi_{\bar{B}} (2\pi)^4 \delta^{(4)}(p_{\chi} + p_{\bar{\chi}} - p_B - p_{\bar{B}}) |\mathcal{M}_{\chi\bar{\chi} \rightarrow B\bar{B}}|^2 f_{\chi}^{\text{eq}} f_{\bar{\chi}}^{\text{eq}}, \quad (2.50)$$

where

$$|v| = \sqrt{1 - \frac{m_{\chi}^4}{(p_{\chi} \cdot p_{\bar{\chi}})^2}} \quad (2.51)$$

is the modulus of the Moeller velocity between the initial state particles. Introducing yields $n = Ys$ and summing over the possible annihilation products B to get the total annihilation cross-section,

$$\langle \sigma_A^{\chi} |v\rangle = \sum_B \langle \sigma_{\chi\bar{\chi} \leftrightarrow B\bar{B}} |v\rangle, \quad (2.52)$$

we can write the Boltzmann equation for particle χ in its final form

$$\frac{dY_{\chi}}{dx} = -\frac{s_1}{H_1} \left(1 - \frac{1}{3} \frac{d \log g_{\star s}}{d \log x}\right) g_{\star s}(x) g_{\star \rho}^{-1/2}(x) \frac{\langle \sigma_A^{\chi} |v\rangle}{x^2} \left[Y_{\chi}^2 - (Y_{\chi}^{\text{eq}})^2 \right]. \quad (2.53)$$

We are interested in the total DM abundance: since we are assuming symmetry between χ and $\bar{\chi}$ particles, eventually we shall multiply the solution Y_{χ} by a factor of 2. We will do this just when we will compute the final relic density. This equation can be solved numerically or semi-analytically under some approximations. First, in general, we should compute the total annihilation cross-section from our model of DM, i.e. a Lagrangian describing all the interactions between the dark sector and the bath particles. In general [20] the annihilation cross-section has velocity dependence $\sigma_A |v| \propto v^{2n}$ with $n = 0$ corresponding to s-wave annihilation, $n = 1$ corresponding to p-wave etc. However, since $\langle v \rangle \sim T^{1/2}$, we have $\langle \sigma_A |v| \rangle \propto T^n$. Therefore we parametrize the thermally average annihilation cross-section as

$$\langle \sigma_A |v| \rangle = \sigma_0 x^{-n}. \quad (2.54)$$

To write the equation in a more compact form, we define

$$\lambda(x) \equiv \frac{s_1}{H_1} \left(1 - \frac{1}{3} \frac{d \log g_{\star s}}{d \log x}\right) \frac{g_{\star s}}{g_{\star \rho}^{1/2}} \sigma_0 = 1.33 m_{\chi} M_{\text{Pl}} \left(1 - \frac{1}{3} \frac{d \log g_{\star s}}{d \log x}\right) \frac{g_{\star s}}{g_{\star \rho}^{1/2}} \sigma_0 \quad (2.55)$$

If we assume that the number of effective degrees of freedom is constant to $g_{\star \rho} = g_{\star s} = 10.75$, which is a good approximation for temperatures $100 \text{ MeV} < T < 1 \text{ MeV}$, then the λ quantity has no x dependence yielding

$$\lambda = 2.7 \times 10^{12} \left(\frac{m_{\chi}}{100 \text{ GeV}} \right) \left(\frac{\sigma_0}{1 \text{ pb}} \right), \quad (2.56)$$

remembering $1 \text{ pb} = 2.57 \times 10^{-9} \text{ GeV}^{-2}$. From now on we say that $\lambda = \text{const}$ we referring to Eq. (2.56). Indeed we can solve the equation semi-analytically in this approximation.

The Boltzmann equation is then

$$\frac{dY_\chi}{dx} = -\frac{\lambda(x)}{x^{n+2}} \left[Y_\chi^2 - (Y_\chi^{\text{eq}})^2 \right]. \quad (2.57)$$

Before numerically and semi-analytically solving this equation, let us understand the qualitative behaviour of the solution. As long as annihilations are efficient, that is $\Gamma_A = sY_\chi^{\text{eq}} \langle \sigma_A |v| \rangle > H$, the yield tracks the equilibrium one $Y_\chi = n_\chi/s \simeq Y_\chi^{\text{eq}}$. When the DM particles become non-relativistic $x < 1$, the annihilation rate drops exponentially with the yielding and, since there are no more relevant number-changing processes, eventually annihilations become inefficient, leading to the *freeze-out* of the yield at a given $x = x_{\text{FO}}$. The general behaviour of the solution will be

$$Y_\chi(x) \simeq \begin{cases} Y_\chi^{\text{eq}}(x) & x < x_{\text{FO}} \\ Y_\chi(x_{\text{FO}}) & x > x_{\text{FO}} \end{cases} \quad (2.58)$$

We can use this fact to define x_{FO} more precisely: we choose it to be the moment when the yield is substantially far from the equilibrium one, i.e.

$$\left. \frac{Y_\chi - Y_\chi^{\text{eq}}}{Y_\chi^{\text{eq}}} \right|_{x_{\text{FO}}} \equiv \left. \frac{\Delta_\chi}{Y_\chi^{\text{eq}}} \right|_{x_{\text{FO}}} = \beta \sim \mathcal{O}(1) \quad \text{freeze out condition} \quad (2.59)$$

with β an order unity numerical constant. The relic density obtained from the solution will be given by

$$\Omega_\chi h^2 = \frac{2m_\chi s_0 Y_\chi^\infty}{\rho_c(t_0) h^{-2}}. \quad (2.60)$$

with $s_0 = 2923 \text{ cm}^{-3}$, $\rho_c(t_0) = 1.1 \times 10^{-5} h^2 \text{ GeV}^{-1}$. The factor of two takes into account an identical evolution of $Y_{\bar{\chi}}$. The quantity to determine is Y_χ^∞ . The details of the solution and, most importantly, the dependences of the relic density on the DM mass and annihilation cross-section depend on the value of x_{FO} . Taking a reference of $x \sim 1$ as the effective moment of transition from relativistic to non-relativistic particles, we distinguish two cases: *hot relics* if $x_{\text{FO}} < 1$ and *cold relics* if $x_{\text{FO}} > 1$.

2.4.1 Hot Relics: $x_{\text{FO}} \lesssim 1$

We have already studied hot relics dealing with Standard Model neutrinos: indeed they are a good example of these thermal candidates. They are extremely hot: with a mass $< 0.12 \text{ eV}$ and an approximate decoupling temperature of $\sim 1 \text{ MeV}$, we obtain roughly $x_{\text{FO}} \sim 10^{-7}$. In general, for a hot relic, the freeze-out occurs when the yield is constant with very good approximation, so the relic yield is the one at equilibrium.

$$\Omega_\chi^{\text{hdm}} h^2 = \frac{2m_\chi s_0 Y_\chi^{\text{eq}}(z_f)}{\rho_c(t_0) h^{-2}} = 2.4 \times 10^{-2} \left(\frac{m_\chi}{1 \text{ eV}} \right) \left(\frac{g_\chi}{2} \right) \left(\frac{10.75}{g_{\star s}(T_{\text{FO}})} \right). \quad (2.61)$$

We have used $s_0 = 2891 \text{ cm}^{-3}$. We see that the relic density depends linearly on the candidate mass. If we increase the mass to $\sim 10 \text{ eV}$, HDM can reproduce the observed abundance. Moreover, notice the dependence on the freeze-out temperature hidden inside g_{*S} : if $T_{\text{FO}} > 300 \text{ GeV}$, $g_{*S} \sim 106.75$ and the relic density will be reduced by an order of magnitude. Nevertheless, we have already discussed in Section 1.4 why the DM cannot be hot: if it accounts for a large part of the observed abundance it spoils structure formation.

2.4.2 Cold Relics: $x_{\text{FO}} > 1$

The case of cold relics is more involved. We have to carefully take into account the evolution of the yield during the freeze-out since it is dropping exponentially. The final relic density will be strongly dependent on the exact moment of freeze-out. We show the numerical solution of the equation in Fig. 2.2 for different values of the candidate mass, resulting in different values for the freeze-out x_{FO} . We see that all these cold relics do reproduce the order of magnitude of the observed abundance. Notice the relic density is very weakly dependent on the mass, while, as we shall see, it is strongly dependent on the annihilation cross-section.

To understand this dependence, let us solve the equation semi-analytically, in the approximation $\lambda = \text{const}$ i.e. λ given by Eq. (2.56). It is easier to consider an equation for the function $\Delta_\chi = Y_\chi - Y_\chi^{\text{eq}}$ rather than for the comoving density Y_χ . The Boltzmann equation in this variable is, denoting $' \equiv d/dx$,

$$\Delta_\chi' = -(Y_\chi^{\text{eq}})' - \frac{\lambda}{z^{n+2}} \Delta_\chi (\Delta_\chi + Y_\chi^{\text{eq}}). \quad (2.62)$$

The idea is to solve this equation in two regimes and extrapolate the solution in the first regime up to x_{FO} to determine the moment of freeze-out.

- *early times solution* $1 < x \lesssim x_{\text{FO}}$: in this period the DM particles are non-relativistic but still coupled to the bath particles so the yield still tracks the equilibrium one $Y_\chi \simeq Y_\chi^{\text{eq}}$. In practice Δ_χ is really small and slowly varying with x : $\Delta_\chi' \simeq 0$. We can approximate the equation exploiting $\Delta_\chi^2, \Delta_\chi' \ll 1$. We have a direct solution

$$\Delta_\chi \simeq \frac{-(Y_\chi^{\text{eq}}(z))' x^{n+2}}{\Delta + 2Y_\chi^{\text{eq}}(x)} \frac{1}{\lambda} \simeq \frac{-(Y_\chi^{\text{eq}}(x))' x^{n+2}}{Y_\chi^{\text{eq}}(x)} \frac{1}{2\lambda} \simeq \frac{x^{n+2}}{2\lambda}. \quad (2.63)$$

The last equality holds since $(Y_\chi^{\text{eq}})' \simeq -Y_\chi^{\text{eq}}$ in the $x \gg 1$ limit (where we can exploit the asymptotic behaviour of Eq. (2.45)) is given by

$$\frac{-(Y_\chi^{\text{eq}}(x \gg 1))'}{Y_\chi^{\text{eq}}(x \gg 1)} = 1 - \frac{3}{2x} \simeq 1. \quad (2.64)$$

- *late times solution* $x > kx_{\text{FO}}$ with $k \sim 1$: now the species is finally decoupled, so Y_χ does not track Y_χ^{eq} (which is decaying exponentially) anymore. So $\Delta_\chi = Y_\chi - Y_\chi^{\text{eq}} \sim$

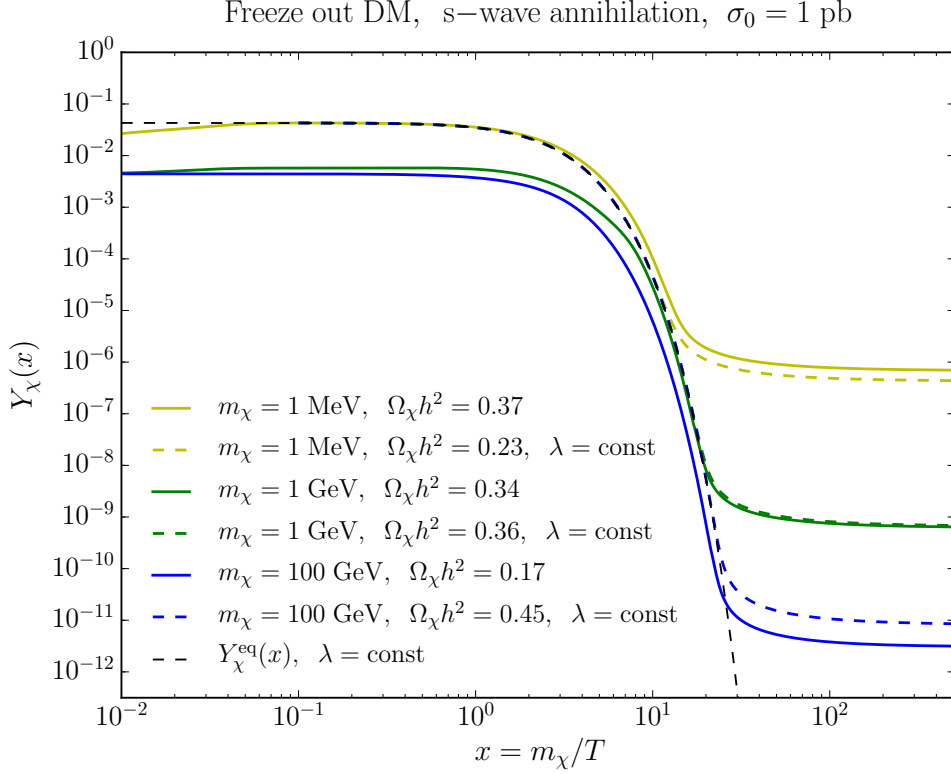


Figure 2.1: The evolution of the yield of cold relics according to the numerical solution of the full Boltzmann equation Eq. (2.57), considering s-wave annihilations $n = 0$ with cross-section $\sigma_0 = 0.1$ pb and different values for the DM candidate mass. For comparison, we show as dashed lines the solutions obtained with the $\lambda = \text{const}$ approximation Eq. (2.56). Notice that in the general case the equilibrium comoving density $Y_\chi^{\text{eq}}(x)$ depends on the DM candidate mass: this has an impact on the relic density since the moment of freeze-out is different.

$Y_\chi \gg Y_\chi^{\text{eq}}$ and $\Delta'_\chi \gg -(Y_\chi^{\text{eq}})'$. Therefore we have

$$\Delta'_\chi \simeq \frac{\lambda}{x^{n+2}} \Delta_\chi^2. \quad (2.65)$$

We can integrate the equation from kx_{FO} to infinity. We have

$$\frac{1}{\Delta_\chi^\infty} - \frac{1}{\Delta_\chi(kx_{\text{FO}})} = \lambda \int_{kx_{\text{FO}}}^\infty x^{-n-2} dx = \frac{\lambda}{n+1} (kx_{\text{FO}})^{-n-1}. \quad (2.66)$$

The decoupling is not instantaneous so Y_χ still decreases after the freeze-out. We have $Y_\chi^{\text{eq}}(kx_{\text{FO}}) = Y_\chi^{\text{eq}}(z_f) k^{3/2} e^{-x_{\text{FO}}(k-1)} \ll 1$. Therefore both $Y_\chi^{\text{eq}}(kz_f)$ and $Y_\chi^{\text{eq}}(\infty)$ can be set to zero³. So, since $Y_\chi(kx_{\text{FO}}) > Y_\chi^\infty$ we are allowed to neglect the $\Delta_\chi(kx_{\text{FO}})$

³Notice that, if we were considering x_{FO} instead of kx_{FO} , we could not neglect $Y_\chi^{\text{eq}}(x_{\text{FO}}) = 0$ since that would imply, from the definition of freeze-out, that $\Delta_\chi(x_{\text{FO}}) = 0$. This is in contradiction with Δ_χ^∞ being negligible with respect to it.

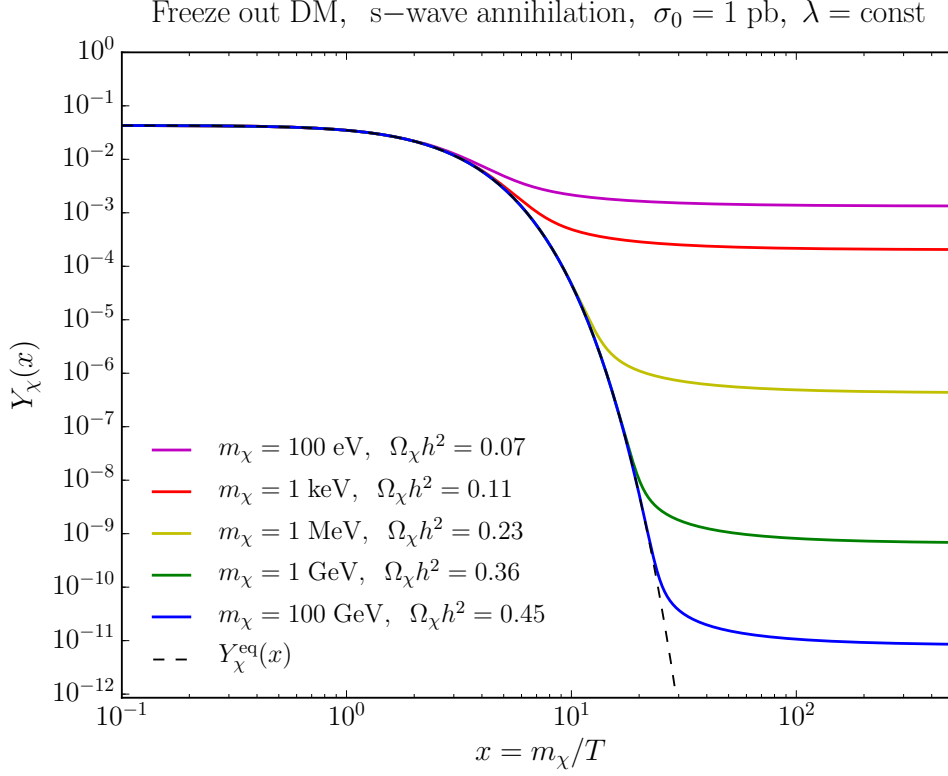


Figure 2.2: The evolution of the yield of cold relics according to the numerical solution of BE Eq. (2.57), using the $\lambda = \text{const}$ approximation, i.e. λ given by Eq. (2.56), considering s-wave annihilations $n = 0$ with cross-section $\sigma_0 = 1$ pb and different values of the DM candidate mass. Notice the relic density which stays of the order of the observed one even with the mass m_χ ranging over nine orders of magnitude. The equilibrium yield $Y_\chi^{\text{eq}}(x)$ is computed using Eq. (2.45) and approximated at large x to speed up the code. The found freeze-out values are, from the hottest to the coldest, $x_{\text{FO}} = 3.6, 5.7, 12.3, 18.9, 23.5$. The dependence on σ_0 is simply $\Omega_\chi h^2 \propto 1/\sigma_0$.

in the above equation, giving the final yield of

$$Y_\chi^\infty \simeq \frac{(n+1)(kx_{\text{FO}})^{n+1}}{\lambda}. \quad (2.67)$$

The approximation works very well, as one can see comparing this estimate with the results obtained numerically.

We still have to find an approximate expression for x_{FO} , in terms of the model parameters, m_χ and σ_0 . We can do that using our defining condition Eq. (2.59) and extrapolating $\Delta_\chi(x)$ at early times up to x_{FO} , where we impose the definition:

$$\Delta_\chi(x_{\text{FO}}) \simeq \frac{x_{\text{FO}}^{n+2}}{\lambda} \frac{(-Y_\chi^{\text{eq}}(x_{\text{FO}}))'}{2Y_\chi^{\text{eq}}(x_{\text{FO}}) + \Delta_\chi(x_{\text{FO}})} \simeq \frac{x_{\text{FO}}^{n+2}}{\lambda(2+\beta)} = 0.145\beta \frac{g_\chi}{g_{\star s}} x_{\text{FO}}^{3/2} e^{-x_{\text{FO}}}. \quad (2.68)$$

We choose $\beta(\beta + 2) \equiv n + 1$ to simplify computations. As stated by [20], this also gives the best fit to the numerical result for the final abundance. We get the equation

$$e^{x_{\text{FO}}} = 0.145\lambda(n + 1) \frac{g_\chi}{g_{\star s}} x_{\text{FO}}^{-n-1/2}. \quad (2.69)$$

This equation can be solved iteratively:

$$x_{\text{FO}} = x_{\text{FO}}^{(1)} + x_{\text{FO}}^{(2)} + \dots \quad (2.70)$$

The first-order solution is

$$x_{\text{FO}}^{(1)} = \log \left[0.145 \frac{g_\chi}{g_{\star s}} \lambda(n + 1) \right] = 25.4 + \log \left[\left(\frac{m_\chi}{100 \text{ GeV}} \right) \left(\frac{\sigma_0}{1 \text{ pb}} \right) \right], \quad (2.71)$$

and the second-order solution $x_{\text{FO}}^{(2)}$ is obtained plugging $x_{\text{FO}}^{(1)}$ in the right-hand side of Eq. (2.69). We find eventually

$$x_{\text{FO}} = x_{\text{FO}}^{(1)} - \left(n + \frac{1}{2} \right) \log x_{\text{FO}}^{(1)} + \dots \quad (2.72)$$

With this formula in mind we can write the relic density substituting the estimate for Y_χ^∞ .

$$\Omega_\chi^{\text{cdm}} h^2 = \frac{2m_\chi s_0 Y_\chi^\infty}{\rho_c(t_0) h^{-2}} = 0.4 \left(\frac{k x_{\text{FO}}}{20} \right)^{n+1} \left(\frac{g_{\star\rho}(m_\chi)}{10.75} \right)^{1/2} \left(\frac{10.75}{g_{\star s}(m_\chi)} \right) \left(\frac{1 \text{ pb}}{\sigma_0} \right). \quad (2.73)$$

Notice the strong dependence on the annihilation cross-section parameters (n and σ_0) and the weak logarithmic dependence on the mass, which barely affects the relic density through the value of x_{FO} . The cross-section dependence is reasonable: the stronger the interaction between the DM particles and the thermal bath, the longer DM particles remain in equilibrium and, thus, the more the abundance gets diluted by Maxwell-Boltzmann suppression.

2.4.3 The fall of the WIMP paradigm

We see that the thermal freeze-out model can reproduce fairly well and easily the observed abundance for the reference values of the parameters, with a weak dependence on the DM mass. Historically, this fact is referred to as the *WIMP miracle*. WIMPs stay for Weakly Interacting Massive Particles [2]: they include a large number of candidates with similar properties, in particular

$$1 \text{ GeV} \lesssim m_{\text{WIMP}} \lesssim 10 \text{ TeV}, \quad (\sigma_A |v|)_{\text{WIMP}} \simeq 10^{-26} \text{ cm}^3 \text{ s}^{-1} \quad (2.74)$$

corresponding to $\sigma_{\text{WIMP}} \simeq 1 \text{ pb}$, a number very similar to the cross-section that arises from the weak interactions. An example of a WIMP could be a stable neutrino with a mass around the GeV, annihilating through the exchange of a Z boson: it would freeze-out with a relic abundance that is roughly equal to the measured density of DM. Such result applies

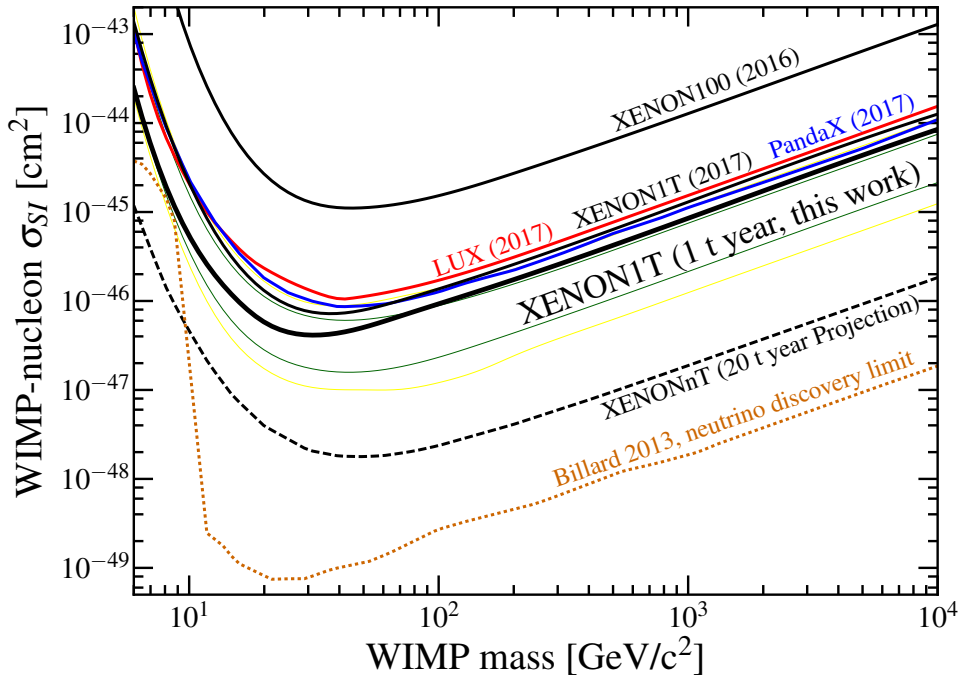


Figure 2.3: Spin-independent (SI) scattering bounds of DM particles with nuclei from direct detection experiments. 90% confidence level upper limits on the SI scattering cross-section from the XENON1T experiment [34] (thick black line) are shown with the 1σ (green) and 2σ (yellow) sensitivity bands. Previous results from LUX [35] and PandaX-II [36] experiments are shown for comparison. The prospect for experiment XENONnt (20 tons) in preparation together with the limit for the neutrino background [37], are also shown. Figure from [34].

also to a broad range of electroweak-scale DM candidates, including any number of stable particles with MeV-TeV masses and interactions that are mediated by the exchange of electroweak-scale particles. This very natural freeze-out model, combined with theoretical arguments in favour of the existence of physics beyond the Standard Model at or around the electroweak scale (mainly to solve the already cited hierarchy problem for the Higgs mass), have led to consider WIMPs the lead DM particle candidates. The prototypical BSM natural theory is the minimal supersymmetric standard model (MSSM), which introduces an additional partner for each SM particle. Also, the superpartners of the electroweak gauge bosons are predicted to be WIMPs, and their superposition, the neutralino, is a natural DM candidate. Indeed a large number of experiments are searching for WIMPs: in particular, they try to detect signals from the elastic scattering of WIMPs off nucleons (direct detection), signals of WIMP pair-annihilation or decay (indirect detection) and the pair-production of WIMPs at colliders, e.g. LHC, in conjunction with detectable Standard Model particles. Some experiments have also claimed detection of a signal that could be related to some particle candidate, however in disagreement with other results in the same parameter space, as reviewed in [2, 3]. In Fig. 2.3 we show the latest bounds obtained by the XENON1T collaboration [34] in the mass and spin-independent elastic scattering

cross-section parameter space: regions above the curves are excluded. Their strongest constraints on DM-nucleon spin-independent (SI) cross-section, following a $1 \text{ tonne} \times \text{year}$ exposure, have reached $\sigma_{\text{SI}} \lesssim 10^{-44} \text{ cm}^{-2}$ for a DM particle mass between 10 and 10^4 GeV , with enhanced sensitivity around 30 GeV. The behaviour of the constraint is reasonable. For light DM the experiment loses sensitivity since the recoil energy of the nucleus lowers below the detection threshold. At large WIMP masses, the constraint goes as $\propto m_\chi$ since, for a given relic density, increasing the mass we are lowering the DM number density and the likelihood of scatterings. We see that the parameter space available for model building around the thermal freeze-out paradigm is shrinking considerably.

As discussed in [33], the absence of evidence for WIMP DM is causing a growing sense of “crisis” in the DM community and a subsequent “fall” of natural WIMPs models. This is leading to a global theoretical effort in proposing new ideas for DM production mechanisms.

Chapter 3

Freeze-in production of Dark Matter

In this chapter, we present the freeze-in paradigm as a simple, but rather rich in model building, DM production mechanism. Then we apply the Boltzmann equation formalism developed in Chapter 2 to study the evolution of DM abundance.

In the general case, the freeze-in scenario involves Feebly Interacting Massive Particles (FIMPs) [1] which are so weakly coupled with the SM visible states, that they never achieve thermal equilibrium. Therefore, in contrast to the usual freeze-out scenario, the DM is produced non-thermally. In literature, many variations of the freeze-in paradigm have been proposed [1, 38], including dynamics and interplay between different DM particles constituting the so-called dark sector. In this chapter, we focus on the simplest model, in which the relic density is made of the frozen-in particles, which are FIMPs themselves. Therefore we will consider only one DM particle candidate χ , feebly coupled to bath particles B_i . In all the cases under consideration, we assume the initial FIMP abundance is negligible.

3.1 General features of freeze-in

Let us describe in general the freeze-in mechanism highlighting analogies and differences with the freeze-out paradigm. Let us assume the FIMP candidate χ is very weakly coupled to the thermal bath particles through interactions described by operators of mass dimension less than four. Let M be the mass of the heaviest particle at the interaction vertex. The coupling of the vertex can be written as

$$\text{coupling} \sim \begin{cases} y & \text{quartic scalar or Yukawa} \\ yM & \text{trilinear scalar} \end{cases} \quad (3.1)$$

in the simple cases considered, with $y \ll 1$ dimensionless. Let us assume the abundance of χ particles is negligible at high temperatures. If so, χ particles are produced only from decays and collisions of thermal bath particles, with rate Γ , given, at $T \gg M$, from dimensional analysis, by

$$\Gamma(T) \sim \begin{cases} y^2 T & \text{quartic scalar or Yukawa} \\ y^2 \frac{M^2}{T} & \text{trilinear scalar} \end{cases} \quad (3.2)$$

The comoving abundance can be estimated in the radiation domination era from the product of this rate and the time $t \sim M_{\text{Pl}}/T^2$ available to processes to populate the FIMP sector.

$$Y(T) \sim t \times \Gamma \sim \begin{cases} y^2 \frac{M_{\text{Pl}}}{T} & \text{quartic scalar or Yukawa} \\ y^2 \frac{M^2 M_{\text{Pl}}}{T^3} & \text{trilinear scalar} \end{cases} \quad (3.3)$$

This means the freeze-in production in this basic scenario is IR dominated, favouring low temperatures, with dominant production at $T \sim M$: after this threshold, the most massive particle's abundance will be exponentially suppressed. Therefore, in this case, the final abundance will be approximately given by

$$Y_{\infty}^{\text{FI}} \sim y^2 \frac{M_{\text{Pl}}}{M}. \quad (3.4)$$

As we have seen in Section 2.4, in the case of the freeze-out DM production, the relic abundance is given by

$$Y_{\infty}^{\text{FO}} \sim \frac{1}{\langle \sigma_A^X |v| \rangle M_{\text{Pl}} M'}. \quad (3.5)$$

In the simplest case where M' is the only relevant mass scale for the annihilation, we have $\langle \sigma_A^X |v| \rangle \sim y'^2/M'^2$ with y' the coupling between bath particles and the DM in the freeze-out scenario. We get

$$Y_{\infty}^{\text{FO}} \sim \frac{1}{y'^2} \frac{M'}{M_{\text{Pl}}} \quad (3.6)$$

Comparing Eqs (3.6) and (3.4), we can say that the freeze-in is indeed the ‘‘opposite’’ mechanism to the freeze-out: the final abundances show opposite dependences concerning both the coupling between visible and dark matter and the relevant energy scale involved. In particular, stronger couplings increase the relic density obtained from freeze-in, while they decrease the final abundance obtained from the freeze-out. We can try to see which are the typical values of the coupling involved to reproduce the observed relic density $\Omega_{\text{DM}} h^2 \sim 0.12$:

$$\begin{aligned} y &\sim 10^{-14} \times \left(\frac{M}{m_{\chi}} \right)^{1/2} \left(\frac{\Omega_{\chi} h^2}{0.12} \right)^{1/2} && \text{freeze in} \\ y' &\sim 10^{-3} \times \frac{(m_{\chi} M')^{1/2}}{100 \text{ GeV}} \left(\frac{0.12}{\Omega_{\chi} h^2} \right)^{1/2} && \text{freeze out} \end{aligned} \quad (3.7)$$

We are neglecting important factors such as the effective number of degrees of freedom, but this estimate should already give the flavour of the difference in the order of magnitude of the parameters involved in the two scenarios. Despite these differences, freeze-out and freeze-in have a crucial common feature: the final out-of-equilibrium abundance, given the relevant mass scales and couplings, can be computed solely knowing the initial state of particles in thermal equilibrium. The resulting abundance is dominated by IR, low-temperature physics.

3.2 Evolution of FIMP abundance

As well as freeze-out, the freeze-in mechanism can reproduce the observed DM abundance in a simple and predictive way. The scenario can also be complicated at will, adding an interplay between dark particles, e.g. letting the frozen-in particle decay at a later stage into the actual DM particles, or between the dark and visible sectors.

In this Section we will stick to the simplest model with only one stable FIMP DM candidate χ to reproduce the relic DM density, making general assumptions on the type of processes involved in the DM production. We can start considering the Boltzmann equation for the number density Eq. (2.32) and exploit dimensionless variables, to recast it in the following compact form

$$\frac{dY_\chi}{dx} = \frac{1}{x} \left(1 - \frac{1}{3} \frac{d \log g_{*s}}{d \log x} \right) \frac{\mathcal{C}(x)}{s(x)H(x)}. \quad (3.8)$$

In this case, $x = M/T$ with M a relevant mass scale, which is not, in general, the mass of the FIMP candidate. The definition of x clearly can change case by case when writing in its explicit form the collision term $\mathcal{C}(x) \equiv 2 \int d\Pi_\chi C[f_\chi](x)$, which includes all relevant interactions for χ . Again, as we did in the case of the freeze-out in Section 2.4, we assume that the thermal bath is described by its number of effective degrees of freedom, evolving with temperature as described in Appendix A.2. Trying to be as much general as possible, we consider the following freeze-in processes to produce dark particles χ through reactions involving bath particles in the initial state B_i :

1. **Decays** $B_1 \rightarrow \chi B_2 \cdots B_{n-2}$. In the general n -body decay framework, the heavy bath particle B_1 decays to a final state involving the DM particle χ and other bath particles $B_2 \dots B_{n-2}$. For simplicity we will consider only two-body decays $B_1 \rightarrow B_2 \chi$ but, as far as we are interested in the final abundance only, our results are valid in general. When dealing with the full phase-space distribution or higher moments, however, the kinematics of e.g. three-body decays is sensibly different from the one of two-body decays and can have an impact on the quantities we want to track: remember, e.g. that a particle in the final state of a three-body decay is produced with an energy spectrum rather than definite energy. The case of decay channels involving more than one DM particle in the final state, e.g. $B_1 \rightarrow \chi \chi$ is analogous.

2. **Collisions** $B_1 B_2 \rightarrow B_3 \chi$ or $B_1 B_2 \rightarrow \chi \chi$. Scatterings between two bath particles produce one (or two) DM particle(s) χ in the final state. The first case is called *single production* and happens if one of the two initial state bath particles has the same discrete quantum number as χ . The second case is called *pair production*: now, being the DM particle pair-produced, there is no symmetry constrain on these processes.

Let us write and solve the BE Eq. (3.8) in these different cases.

3.2.1 Freeze-in from decays

Let us consider the toy model interaction Lagrangian

$$\mathcal{L}_{\text{FI}}^d = \lambda_d m_{B_1} B_1 B_2 \chi, \quad (3.9)$$

with a trilinear scalar coupling. In the case of $m_{B_1} \geq m_{B_2} + m_\chi$, the Lagrangian allows two-body decays of B_1 to take place

$$B_1 \rightarrow \chi B_2 \quad (3.10)$$

The relevant mass scale for these decays is m_{B_1} hence we anticipate it will be the suitable mass scale for the definition of x in Eq. (3.8). All the particles involved are real scalars fields hence $g_{B_1} = g_{B_2} = g_\chi$ at the end. Let us write the collision term $\mathcal{C}_{B_1 \rightarrow \chi B_2}$. In this simplest model, we assume a completely negligible FIMP abundance at very high temperatures. Since the thermal equilibrium between DM and the bath is never attained, inverse decays do not play any role. Instead, the decaying bath particles B_1 are in thermal equilibrium. As usual, we are neglecting the quantum statistics. Under these assumptions, the collision term reads

$$\mathcal{C}_{B_1 \rightarrow \chi B_2} = \int d\Pi_{B_1} d\Pi_{B_2} d\Pi_\chi (2\pi)^4 \delta^{(4)}(p_{B_1} - p_{B_2} - p_\chi) |\mathcal{M}_{B_1 \rightarrow \chi B_2}|^2 f_{B_1}^{\text{eq}}. \quad (3.11)$$

We introduce the partial decay width for the considered channel computed in the B_1 rest frame:

$$\Gamma_{B_1 \rightarrow \chi B_2} = \frac{1}{2m_{B_1}} \int d\Pi_{B_2} d\Pi_\chi (2\pi)^4 \delta^{(4)}(p_{B_1} - p_{B_2} - p_\chi) |\mathcal{M}_{B_1 \rightarrow \chi B_2}|^2, \quad (3.12)$$

and rewrite the collision term in the form

$$\mathcal{C}_{B_1 \rightarrow \chi B_2} = g_{B_1} \Gamma_{B_1 \rightarrow \chi B_2} \int \frac{d^3 p_{B_1}}{(2\pi)^3} \frac{m_{B_1}}{E_{B_1}} f_{B_1}^{\text{eq}}(E_{B_1}, T). \quad (3.13)$$

We perform the integral similarly to we did in Section 2.4, defining $x = m_{B_1}/T$ and $q = E/T$

$$\begin{aligned} \int \frac{d^3 p_{B_1}}{(2\pi)^3} \frac{m_{B_1}}{E_{B_1}} f_{B_1}^{\text{eq}}(E_{B_1}, T) &= \frac{1}{2\pi^2} \int_{m_{B_1}}^{\infty} E dE \sqrt{E^2 - m_{B_1}^2} \frac{m_{B_1}}{E} e^{-E/T} \\ &= \frac{1}{2\pi^2} T^2 m_{B_1} \int_x^{\infty} dq \sqrt{q^2 - x^2} e^{-q} = \frac{1}{2\pi^2} m_{B_1}^3 x^{-1} K_1(x), \end{aligned} \quad (3.14)$$

with $K_1(x)$ the modified Bessel function of the second kind. Remembering that the equilibrium density for a particle species is given by

$$n_{B_1}^{\text{eq}} = \frac{g_{B_1}}{2\pi^2} m_{B_1}^3 x^{-1} K_2(x), \quad (3.15)$$

we can finally write the collision term in the compact form

$$\mathcal{C}_{B_1 \rightarrow \chi B_2} = n_{B_1}^{\text{eq}} \Gamma_{B_1 \rightarrow \chi B_2} \frac{K_1(x)}{K_2(x)}. \quad (3.16)$$

Inserting this expression in Eq. (3.8), we get

$$\frac{dY_\chi}{dx} = \frac{1}{x} \left(1 - \frac{1}{3} \frac{d \log g_{\star s}}{d \log x} \right) \frac{Y_{B_1}^{\text{eq}}}{H(x)} \Gamma_{B_1 \rightarrow \chi B_2} \frac{K_1(x)}{K_2(x)}. \quad (3.17)$$

Remembering

$$Y_{B_1}^{\text{eq}}(x) = \frac{45}{4\pi^4} \frac{g_{B_1}}{g_{\star s}(x)} x^2 K_2(x), \quad (3.18)$$

and substituting into Eq. (3.17), we can solve for the comoving abundance of DM

$$Y_\chi(x) = \frac{45}{4\pi^4} g_{B_1} \Gamma_{B_1 \rightarrow \chi B_2} \int_0^x dx' \left(1 - \frac{1}{3} \frac{d \log g_{\star s}}{d \log x'} \right) \frac{x' K_1(x')}{g_{\star s}(x') H(x')}. \quad (3.19)$$

Here we can take $x' = 0$ as lower integration extremum, since, as we have shown, the FIMP DM is IR-produced. The final abundance is given by taking $x \rightarrow \infty$ in the above equation. We can compute the above integral in the radiation domination epoch, in which

$$H(x) = \sqrt{\frac{\pi^2}{90} g_{\star \rho}^{1/2}(x)} \frac{m_{B_1}^2}{M_{\text{Pl}}} x^{-2}. \quad (3.20)$$

The partial decay width in the B_1 rest frame is given by

$$\Gamma_{B_1 \rightarrow B_2 \chi} = \frac{p_\star}{32\pi^2 m_{B_1}^2} \int |\mathcal{M}_{B_1 \rightarrow B_2 \chi}|^2 d\Omega, \quad (3.21)$$

with p_\star the momentum of decay products in the B_1 rest frame, which from energy conservation is given by:

$$m_{B_1} = \sqrt{m_{B_2}^2 + p_\star^2} + \sqrt{m_\chi^2 + p_\star^2} \implies p_\star = \sqrt{\frac{(m_{B_1}^2 + m_{B_2}^2 - m_\chi^2)^2 - 4m_{B_1}^2 m_{B_2}^2}{4m_{B_1}^2}} \quad (3.22)$$

Since $|\mathcal{M}_{B_1 \rightarrow B_2 \chi}|^2 = \lambda_d^2 m_{B_1}^2$, the partial decay width reads

$$\Gamma_{B_1 \rightarrow B_2 \chi} = \frac{\lambda_d^2}{8\pi} \sqrt{\frac{(m_{B_1}^2 + m_{B_2}^2 - m_\chi^2)^2 - 4m_{B_1}^2 m_{B_2}^2}{4m_{B_1}^2}}. \quad (3.23)$$

We can assume a simple parametrization for the partial decay width to have a dependence only on the relevant mass scale m_{B_1} :

$$\Gamma_{B_1 \rightarrow \chi B_2} = \frac{\tilde{\lambda}_d^2}{8\pi} m_{B_1}. \quad (3.24)$$

We have properly defined a new coupling $\tilde{\lambda}_d^2$. Notice that for $m_{B_1} \gg m_{B_2}, m_\chi$, one has $\tilde{\lambda}_d^2 \rightarrow \lambda_d^2/2$. We can finally write the solution for the comoving abundance of χ particles:

$$Y_\chi(x) = \frac{45}{4\pi^4} \sqrt{\frac{90}{\pi^2}} \frac{\tilde{\lambda}_d^2 M_{\text{Pl}}}{8\pi m_{B_1}} g_{B_1} \int_0^x dx' \left(1 - \frac{1}{3} \frac{d \log g_{*s}}{d \log x'}\right) \frac{x'^3 K_1(x')}{g_{*s}(x') g_{*p}^{1/2}(x')}. \quad (3.25)$$

We define¹

$$J_\infty^d(m_{B_1}) \equiv \int_0^\infty dx' \left(1 - \frac{1}{3} \frac{d \log g_{*s}(m_{B_1}/x')}{d \log x'}\right) \frac{x'^3 K_1(x')}{g_{*s}(m_{B_1}/x') g_{*p}^{1/2}(m_{B_1}/x')}. \quad (3.26)$$

If we choose $m_{B_1} = 1$ TeV, we obtain $J_\infty^d(1 \text{ TeV}) \simeq 4.4 \times 10^{-3}$. For reference, we show in Fig. 3.1 the dependence of J_∞^d on m_{B_1} . We can finally obtain the relic density:

$$\Omega_\chi h^2 = 0.014 \times g_{B_1} \tilde{\lambda}_d^2 \frac{s(t_0) M_{\text{Pl}}}{\rho_c(t_0)} \left(\frac{m_\chi}{m_{B_1}}\right) J_\infty^d(m_{B_1}), \quad (3.27)$$

from which one can get the value of $\tilde{\lambda}_d$ needed to reproduce the observed relic density

$$\tilde{\lambda}_d = 1.22 \times 10^{-11} \left(\frac{m_{B_1}/m_\chi}{100}\right)^{1/2} \left(\frac{4.4 \times 10^{-3}}{J_\infty^d(1 \text{ TeV})}\right)^{1/2} \left(\frac{1}{g_{B_1}}\right)^{1/2} \left(\frac{\Omega_\chi h^2}{0.12}\right)^{1/2}. \quad (3.28)$$

We have chosen, as a reference, $m_{B_1} = 1$ TeV and $m_\chi = 10$ GeV. In Fig. 3.2, we show the results of Eq. (3.25) for four reference choices of the masses involved, changing $\tilde{\lambda}_d$ to reproduce the relic abundance. The dependence on the mass m_{B_2} is hidden inside the value of $\tilde{\lambda}_d$ because of the chosen parametrization of the partial decay width. Notice the freeze-in happens at $x_{\text{FI}} \sim 1 \div 10$ and that the process is clearly IR-dominated, since most of the final abundance freezes-in around x_{FI} .

¹The effective degrees of freedom depend on temperature so their dependence on x implies a dependence on m_{B_1}

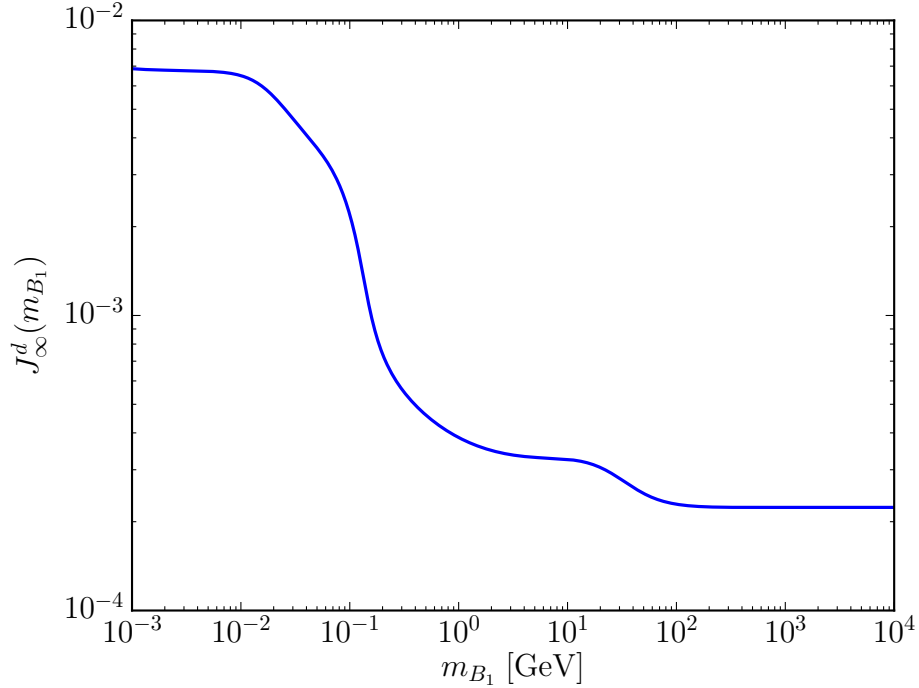


Figure 3.1: The behaviour of the factor J_∞^d defined in Eq. (3.26) as a function of the mass of the decaying particle m_{B_1} in the range of interest.

3.2.2 Freeze-in from collisions

For simplicity, let us consider the following toy models described by the interaction Lagrangians

$$\mathcal{L}_{\text{FI}}^{\text{sp}} = \lambda_{sp} B_1 B_2 B_3 \chi \quad (3.29)$$

$$\mathcal{L}_{\text{FI}}^{\text{pp}} = \frac{1}{2} \lambda_{pp} B_1 B_2 \chi^2 \quad (3.30)$$

These Lagrangians model the interaction between the FIMP DM and the bath particles, all considered as scalars $g_{B_i} = g_\chi = 1$. The first case models the single production, while the second models the pair production. In this way, the scattering amplitudes of the considered processes will be a dimensionless constant. We will take advantage of this fact when explicitly computing the frozen-in abundance from scatterings. However, we will write a general expression for the collision term in both cases. Notice that the above Lagrangians also allow three-body decays to take place, for a suitable choice of the mass spectrum of the theory. Nevertheless, at this stage, we focus on scatterings: the three-body decays will be interesting when studying the full phase-space distribution with the Boltzmann equation. Let us consider the two processes of single and pair production separately, following the approach of [39].

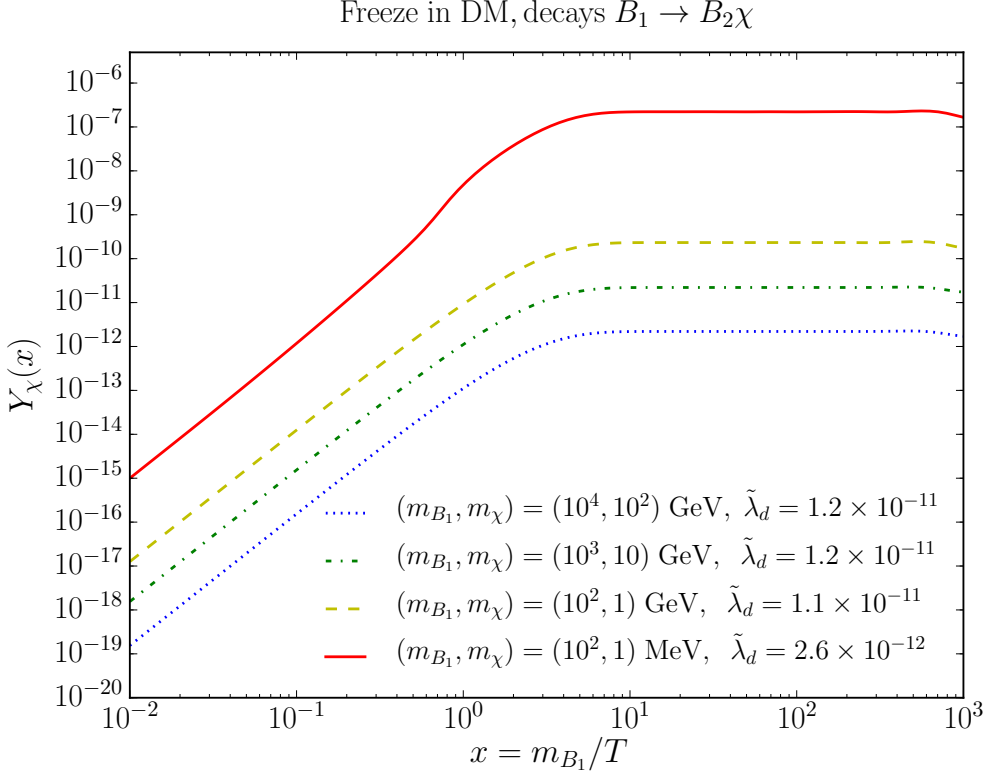


Figure 3.2: The evolution of the yield Y_χ of the FIMP DM candidate for the case of freeze-in from decays. We plot the solution for four reference models leaving constant the ratio $m_{B_1}/m_\chi = 100$ and changing the coupling responsible for the decay $\tilde{\lambda}_d$ to reproduce the observed relic density $\Omega_{\text{DM}}h^2 = 0.12$. In the case of the lightest particle, notice the effect on the shape of the Y_χ curve, due to the change in the number of degrees of freedom during the radiation domination period.

Single production

With single production we mean the general process

$$B_i B_j \longrightarrow B_k \chi, \quad (3.31)$$

for $i, j, k = 1, 2, 3$ and $i \neq j \neq k$. We have three possible processes: $B_1 B_2 \rightarrow B_3 \chi$, $B_1 B_3 \rightarrow B_2 \chi$ and $B_2 B_3 \rightarrow B_1 \chi$, all contributing to the production of χ . For the general process, the collision term reads

$$\mathcal{C}_{B_i B_j \rightarrow \chi B_k}^{\text{light}} = \int d\Pi_{B_i} d\Pi_{B_j} \Pi_{B_k} d\Pi_\chi (2\pi)^4 \delta^{(4)}(p_{B_i} + p_{B_j} - p_{B_k} - p_\chi) |\mathcal{M}_{B_i B_j \rightarrow \chi B_k}|^2 f_{B_i}^{\text{eq}} f_{B_j}^{\text{eq}}. \quad (3.32)$$

Again, the inverse process is strongly suppressed by the negligible initial abundance of FIMP particles. Exploiting the conservation of energy $f_{B_i}^{\text{eq}} f_{B_j}^{\text{eq}} = f_{B_k}^{\text{eq}} f_\chi^{\text{eq}}$, and assuming CP invariance $|\mathcal{M}_{B_i B_j \rightarrow \chi B_k}|^2 = |\mathcal{M}_{\chi B_k \rightarrow B_i B_j}|^2$, we can rewrite the collision term in the

following equivalent way:

$$\mathcal{C}_{B_i B_j \rightarrow \chi B_k}^{\text{heavy}} = \int d\Pi_{B_i} d\Pi_{B_j} \Pi_{B_k} d\Pi_{\chi} (2\pi)^4 \delta^{(4)}(p_{B_i} + p_{B_j} - p_{B_k} - p_{\chi}) |\mathcal{M}_{\chi B_k \rightarrow B_i B_j}|^2 f_{B_k}^{\text{eq}} f_{\chi}^{\text{eq}}. \quad (3.33)$$

Despite being equivalent, it is computationally advantageous to use the expression for the reaction allowed at zero kinetic energy: in other words, if $m_{B_k} + m_{\chi} < m_{B_i} + m_{B_j}$ (lighter final state), we use Eq. 3.32), otherwise (heavier final state) Eq. (3.33). As pointed out in Appendix A of [39], this strategy isolates thermal suppressions in the equilibrium distribution functions rather than phase-space integrals when reaching mass thresholds. To write the collision term in a more compact form, we would like to isolate the cross-section for the above process. First, we define the Lorentz-invariant relative velocity between the initial state particles B_i, B_j [40]

$$v_{B_i, B_j} = -\frac{1}{(p_{B_i} \cdot p_{B_j})} \sqrt{(p_{B_i} \cdot p_{B_j})^2 - m_{B_i}^2 m_{B_j}^2}, \quad (3.34)$$

with p_{B_ℓ} the physical four-momentum of B_ℓ , $\ell = i, j$ and Lorentz-invariant products defined with the FRW metric (with scale factor absorbed in the spatial components $|\vec{p}|^2 \equiv a^2 \delta_{ij} p^i p^j$). If we introduce the centre-of-mass energy (Mandelstam variable) $s = -(p_{B_i} + p_{B_j})^2 = -(p_{\chi} + p_{B_k})^2$ and put the particles on-shell $p_{B_\ell}^2 = -m_{B_\ell}^2$ ², we can rewrite the relative velocity as

$$v_{B_i, B_j} = -\frac{k^{1/2}(\sqrt{s}, m_{B_i}, m_{B_j})}{2(p_{B_i} \cdot p_{B_j})}, \quad (3.35)$$

having defined the function

$$k(b, c, d) = [b^2 - (c + d)^2][b^2 - (c - d)^2]. \quad (3.36)$$

Now we can try to isolate the Lorentz-invariant cross-section [40] in the collision term

$$\sigma_{B_i B_j \rightarrow \chi B_k}(s) = -\frac{1}{4(p_{B_i} \cdot p_{B_j}) v_{B_i, B_j}} \int d\Pi_{B_k} d\Pi_{\chi} (2\pi)^4 \delta^{(4)}(p_{B_i} + p_{B_j} - p_{B_k} - p_{\chi}) |\mathcal{M}_{B_i B_j \rightarrow \chi B_k}|^2, \quad (3.37)$$

so that our ‘‘light final state’’ collision term reads

$$\mathcal{C}_{B_1 B_2 \rightarrow \chi B_3}^{\text{light}} = 2 \int d\Pi_{B_1} d\Pi_{B_2} k^{1/2}(\sqrt{s}, m_{B_1}, m_{B_2}) \sigma_{B_1 B_2 \rightarrow \chi B_3}(s) f_{B_1}^{\text{eq}} f_{B_2}^{\text{eq}}. \quad (3.38)$$

Now we have to perform the phase-space integration. The integrand depends only on the energies E_{B_i} and E_{B_j} and on s . Thus, the only non-trivial angular integration is the one over the angle between the initial momenta because s depends on it. Here we report the final result of the integration (see [39] for details)

$$\mathcal{C}_{B_i B_j \rightarrow \chi B_k}^{\text{light}} = \frac{T}{16\pi^4} \int_{\sqrt{s_{ij}^{\text{min}}}}^{\infty} d\sqrt{s} k(\sqrt{s}, m_{B_i}, m_{B_k}) \sigma_{B_i B_j \rightarrow \chi B_k}(\sqrt{s}) K_1(\sqrt{s}/T), \quad (3.39)$$

²The signs are due to our coherent mostly-plus choice for the FRW metric.

having defined $s_{ij}^{\min} = (m_{B_i} + m_{B_j})^2$. If we introduce the variables $x_{ij} = (m_{B_i} + m_{B_j})/T$ and $w = \sqrt{s}/T$, we can rewrite the integral in a dimensionless form, for computational convenience,

$$\mathcal{C}_{B_i B_j \rightarrow \chi B_k}^{\text{light}} = \frac{T^4}{16\pi^4} \int_{x_{ij}}^{\infty} dw k\left(w, \frac{m_{B_i}}{T}, \frac{m_{B_j}}{T}\right) \tilde{\sigma}_{B_i B_j \rightarrow \chi B_k}(w) K_1(w), \quad (3.40)$$

where now $\tilde{\sigma} = \sigma T^2$ has no mass dimension. In the ‘‘heavy final state’’ case, instead, it is more convenient to use the other form for the collision term, which reads

$$\mathcal{C}_{B_i B_j \rightarrow \chi B_k}^{\text{heavy}} = \frac{T^4}{16\pi^4} \int_{x_{k\chi}}^{\infty} dw k\left(w, \frac{m_{B_k}}{T}, \frac{m_{\chi}}{T}\right) \tilde{\sigma}_{\chi B_k \rightarrow B_i B_j}(w) K_1(w), \quad (3.41)$$

with $x_{k\chi} = (m_{B_k} + m_{\chi})/T$. Depending on the case we will choose the proper collision term to compute. So far, we did not rely upon any approximation. However, if we consider the toy model in Eq. (3.29), we can write explicitly the expression for the cross-sections above. The matrix elements for the collisions are independent on the kinematics and read

$$|\mathcal{M}_{B_i B_j \rightarrow \chi B_k}|^2 = |\mathcal{M}_{\chi B_k \rightarrow B_i B_j}|^2 = \lambda_{sp}^2. \quad (3.42)$$

Being the particles scalars, there is no need to average over initial or final degrees of freedom. Therefore our dimensionless cross-sections are simply

$$\tilde{\sigma}_{B_i B_j \rightarrow \chi B_k}(\sqrt{s}/T) = \frac{T^2}{16\pi s} |\mathcal{M}_{B_i B_j \rightarrow \chi B_k}|^2 \frac{k^{1/2}(\sqrt{s}, m_{B_k}, m_{\chi})}{k^{1/2}(\sqrt{s}, m_{B_i}, m_{B_j})} \quad (3.43)$$

$$\tilde{\sigma}_{\chi B_k \rightarrow B_i B_j}(\sqrt{s}/T) = \frac{T^2}{16\pi s} |\mathcal{M}_{\chi B_k \rightarrow B_i B_j}|^2 \frac{k^{1/2}(\sqrt{s}, m_{B_i}, m_{B_j})}{k^{1/2}(\sqrt{s}, m_{B_k}, m_{\chi})} \quad (3.44)$$

Substituting in the collision terms we get

$$\mathcal{C}_{B_1 B_2 \rightarrow \chi B_3}^{\text{light}} = \frac{\lambda_{sp}^2 T^4}{256\pi^5} \int_{x_{ij}}^{\infty} \frac{dw}{w^2} k^{1/2}\left(w, \frac{m_{B_i}}{T}, \frac{m_{B_j}}{T}\right) k^{1/2}\left(w, \frac{m_{B_k}}{T}, \frac{m_{\chi}}{T}\right) K_1(w) \quad (3.45)$$

and

$$\mathcal{C}_{B_i B_j \rightarrow \chi B_k}^{\text{heavy}} = \frac{\lambda_{sp}^2 T^4}{256\pi^5} \int_{x_{k\chi}}^{\infty} \frac{dw}{w^2} k^{1/2}\left(w, \frac{m_{B_i}}{T}, \frac{m_{B_j}}{T}\right) k^{1/2}\left(z, \frac{m_{B_k}}{T}, \frac{m_{\chi}}{T}\right) K_1(w) \quad (3.46)$$

As we can see, only the extremum of integration (the useful time variable for the Boltzmann equation) changes in the two cases. Let us write the collision term in a very general and compact way, exploiting some definitions. We define the relevant mass scale

$$M = \max(m_{B_1}, m_{B_2}, m_{B_3}, m_{\chi}), \quad (3.47)$$

useful to define the time variable $x = M/T$ in the Boltzmann equation. Then, we introduce

$$I_{sp}(x, m_{B_i}, m_{B_j}, m_{B_k}, m_\chi) \equiv \int_{r_{ijk}x}^{\infty} \frac{dw}{w^2} k^{1/2}\left(w, \frac{m_{B_i}}{M}x, \frac{m_{B_j}}{M}x\right) k^{1/2}\left(w, \frac{m_{B_k}}{M}x, \frac{m_\chi}{M}x\right) K_1(w), \quad (3.48)$$

where $r_{ijk} = m_{ijk}/M$ with m_{ijk} defined as

$$m_{ijk} = \begin{cases} m_{B_i} + m_{B_j} & \text{if } m_{B_i} + m_{B_j} > m_{B_k} + m_\chi & \text{light final state} \\ m_{B_k} + m_\chi & \text{if } m_{B_i} + m_{B_j} < m_{B_k} + m_\chi & \text{heavy final state} \end{cases} \quad (3.49)$$

With these definitions we can write the single-process collision term as

$$\mathcal{C}_{B_i B_j \rightarrow \chi B_k}(x) = \frac{\lambda_{sp}^2 T^4}{256\pi^5} I_{sp}(x, m_{B_i}, m_{B_j}, m_{B_k}, m_\chi). \quad (3.50)$$

The total collision term is given by the sum over the three processes,

$$\mathcal{C}_{sp}(x) = \sum_{i \neq j \neq k} \mathcal{C}_{B_i B_j \rightarrow \chi B_k}(x) = \frac{\lambda_{sp}^2 T^4}{256\pi^5} \sum_{i \neq j \neq k} I_{sp}(x, m_{B_i}, m_{B_j}, m_{B_k}, m_\chi). \quad (3.51)$$

So we can write the Boltzmann equation as

$$\frac{dY_\chi}{dx} = \frac{\lambda_{sp}^2 M^4}{256\pi^5} \frac{1}{x^5 s(x) H(x)} \left(1 - \frac{1}{3} \frac{d \log g_{\star s}}{d \log x}\right) \sum_{i \neq j \neq k} I_{sp}(x, m_{B_i}, m_{B_j}, m_{B_k}, m_\chi). \quad (3.52)$$

During radiation domination, we have expressions for both $s(x)$ and $H(x)$: substituting them we can write the general solution

$$Y_\chi(x) = \frac{45\sqrt{90}}{512\pi^8} \frac{\lambda_{sp}^2 M_{\text{Pl}}}{M} \int_0^x dx' \left(1 - \frac{1}{3} \frac{d \log g_{\star s}(M/x')}{d \log x}\right) \frac{\sum_{i \neq j \neq k} I_{sp}(x', m_{B_i}, m_{B_j}, m_{B_k}, m_\chi)}{g_{\star \rho}^{1/2}(M/x') g_{\star s}(M/x')}, \quad (3.53)$$

Now we can obtain numerically the solution and the final abundance assuming a specific mass spectrum for our toy model. The final abundance is given by the above expression for $x \rightarrow \infty$.³ As we did in the case of decays, we define the integral

$$J_\infty^{sp}(m_{B_1}, m_{B_2}, m_{B_3}, m_\chi) \equiv \sum_{i,j,k} \int_0^\infty dx' \left(1 - \frac{1}{3} \frac{d \log g_{\star s}(m/x')}{d \log x}\right) \frac{I_{sp}(x', m_{B_i}, m_{B_j}, m_{B_k}, m_\chi)}{g_{\star \rho}^{1/2}(m/x') g_{\star s}(m/x')} \quad (3.54)$$

which takes into account all the history of our FIMP candidate interacting with the bath particle, for a given mass spectrum. We will consider the spectra reported in the following table, where we also show the correspondent value of the integral J_∞^{sp} . We obtain a scaling for the coupling λ_{sp} to reproduce the observed relic density

$$\lambda_{sp} = 1.5 \times 10^{-10} \left(\frac{M/m_\chi}{100}\right)^{1/2} \left(\frac{10^{-2}}{J_\infty^{sp}}\right)^{1/2} \left(\frac{\Omega_\chi h^2}{0.12}\right)^{1/2} \quad (3.55)$$

³In practice, when computing the integral numerically, we set $x \rightarrow 10^3$, implying $T_0 = 10^{-3}M$. This is sufficient to obtain the relic density today, as Y_χ is constant after the freeze-in, happening at $T \sim M$.

Model	m_{B_1}	m_{B_2}	m_{B_3}	m_χ	M	m_{ijk}	J_∞^{sp}
Spectrum (a)	0	0	1 TeV	10 GeV	1 TeV	1 TeV	0.00887
Spectrum (b)	0	0	100 GeV	1 MeV	100 GeV	100 GeV	0.00977
Spectrum (c)	1 TeV	1 TeV	100 GeV	100 GeV	1 TeV	2 TeV	0.00638
Spectrum (d)	100 GeV	100 GeV	100 GeV	10 keV	100 GeV	200 GeV	0.00504
Spectrum (e)	1 TeV	0	0	10 keV	1 TeV	1 TeV	0.00887

In Fig. 3.3 we show the solution Eq. (3.53) for the considered spectra, tuning λ_{sp} to reproduce the observed relic density. Notice that the freeze-in happens at $x = M/T \simeq 1 \div 10$ as usual.

Pair production

The case of pair production, i.e. processes of type

$$B_1 B_2 \longrightarrow \chi \chi, \quad (3.56)$$

is very similar to the single production case considered above, apart from a factor of two, since each event produces two χ particles. As before, depending on the considered mass hierarchy, it is more convenient to use different expressions for the collision term. The matrix elements for our simple model are

$$|\mathcal{M}_{B_1 B_2 \rightarrow \chi \chi}|^2 = |\mathcal{M}_{\chi \chi \rightarrow B_1 B_2}|^2 = \lambda_{pp}^2. \quad (3.57)$$

The cross-sections for pair production are given by

$$\begin{aligned} \tilde{\sigma}_{B_1 B_2 \rightarrow \chi \chi}(\sqrt{s}/T) &= \frac{T^2}{16\pi s} |\mathcal{M}_{B_1 B_2 \rightarrow \chi \chi}|^2 \frac{k^{1/2}(\sqrt{s}, m_\chi, m_\chi)}{k^{1/2}(\sqrt{s}, m_{B_1}, m_{B_2})}, \\ \tilde{\sigma}_{\chi \chi \rightarrow B_1 B_2}(\sqrt{s}/T) &= \frac{T^2}{16\pi s} |\mathcal{M}_{\chi \chi \rightarrow B_1 B_2}|^2 \frac{k^{1/2}(\sqrt{s}, m_{B_1}, m_{B_2})}{k^{1/2}(\sqrt{s}, m_\chi, m_\chi)}, \end{aligned} \quad (3.58)$$

with $s = -(p_{B_1} + p_{B_2})^2 = -(p_\chi + p'_\chi)^2$. Defining the following integral, as in the previous case

$$I_{pp}(x, m_{B_1}, m_{B_2}, m_\chi) \equiv \int_x^\infty \frac{dw}{w^2} k^{1/2}\left(w, \frac{m_{B_1}}{T}, \frac{m_{B_2}}{T}\right) k^{1/2}\left(w, \frac{m_\chi}{T}, \frac{m_\chi}{T}\right) K_1(w), \quad (3.59)$$

we can write

$$\mathcal{C}_{B_1 B_2 \rightarrow \chi \chi}(x) = \frac{\lambda_{pp}^2 T^4}{128\pi^5} I_{pp}(x, m_{B_1}, m_{B_2}, m_\chi), \quad (3.60)$$

with $x = m/T$ and

$$m = \begin{cases} m_{B_1} + m_{B_2} & \text{if } m_{B_1} + m_{B_2} > 2m_\chi & \text{light final state} \\ 2m_\chi & \text{if } m_{B_1} + m_{B_2} < 2m_\chi & \text{heavy final state} \end{cases} \quad (3.61)$$

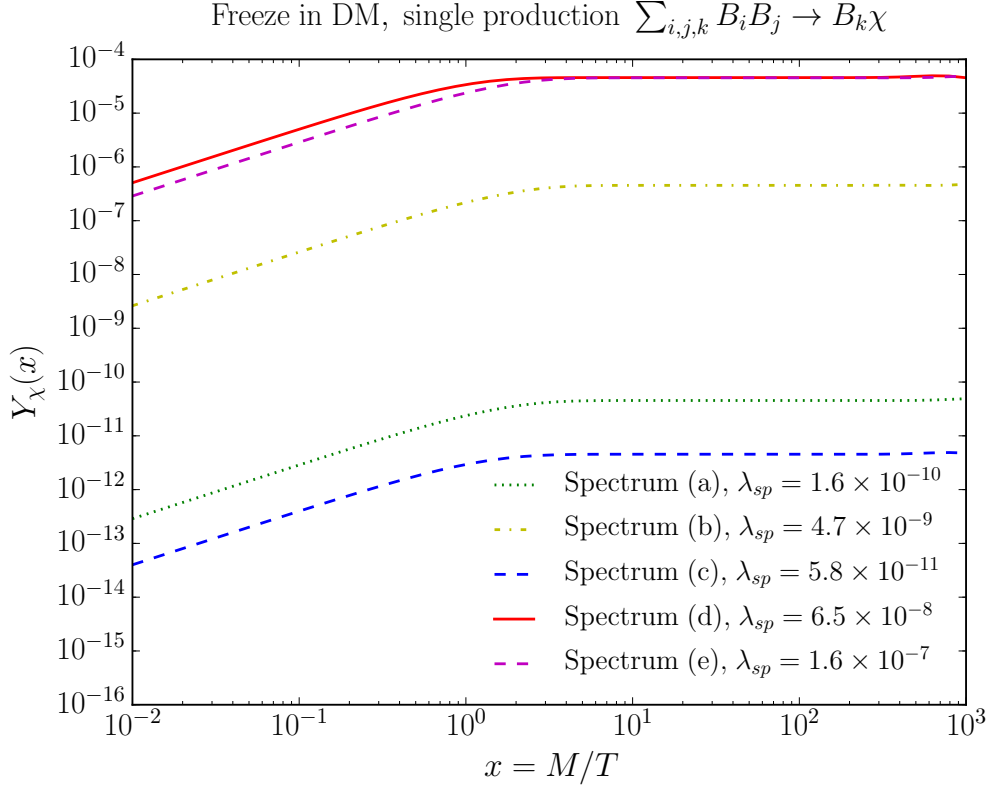


Figure 3.3: The evolution of the comoving density of FIMP DM Y_χ for the case of freeze-in from the sum of the three single production processes $B_1 B_2 \rightarrow B_3 \chi$, $B_1 B_3 \rightarrow B_2 \chi$ and $B_3 B_2 \rightarrow B_1 \chi$. We plot the solution for the simple scalar model in Eq. (3.29) and five choices of spectra. The coupling λ_{sp} was tuned to reproduce the observed relic density $\Omega_{\text{DM}} h^2 = 0.12$. The time variable is the inverse temperature normalized to the relevant mass scale $M = \max(m_{B_1}, m_{B_2}, m_{B_3}, m_\chi)$.

We can directly write the solution of the Boltzmann equation in radiation domination, which is analogous to the one for single FIMP production

$$Y_\chi(x) = \frac{45\sqrt{90} \lambda_{pp}^2 M_{\text{Pl}}}{256\pi^8 m} \int_0^x dx' \left(1 - \frac{1}{3} \frac{d \log g_{*s}(m/x')}{d \log x} \right) \frac{I_{pp}(x', m_{B_1}, m_{B_2}, m_\chi)}{g_{*\rho}^{1/2}(m/x') g_{*s}(m/x')}. \quad (3.62)$$

The final abundance is given by the above expression for $x \rightarrow \infty$. Again we define the integral

$$J_\infty^{pp}(m_{B_1}, m_{B_2}, m_\chi) \equiv \int_0^\infty dx' \left(1 - \frac{1}{3} \frac{d \log g_{*s}(m/x')}{d \log x} \right) \frac{I_{pp}(x', m_{B_1}, m_{B_2}, m_\chi)}{g_{*\rho}^{1/2}(m/x') g_{*s}(m/x')}. \quad (3.63)$$

For reference, we show in Fig. 3.4 the dependence of J_∞^{pp} on m_χ having set B_1 and B_2 to be massless.

Let us consider the spectra reported in the following table together with the correspondent value of the integral J_∞^{sp} . We obtain the following scaling for the coupling λ_{pp} to

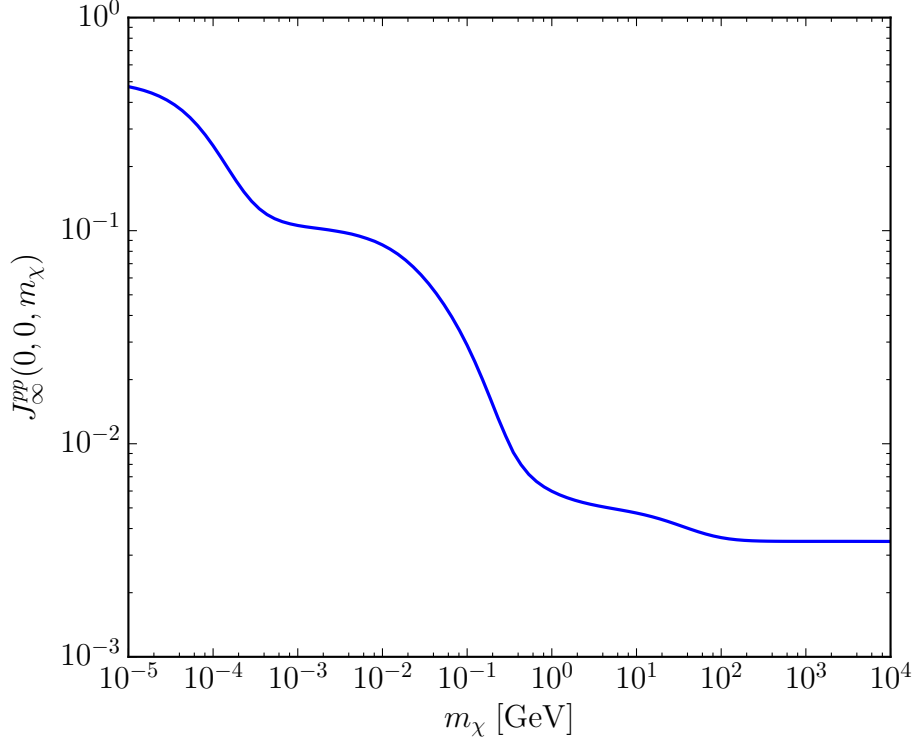


Figure 3.4: The behaviour of the factor J_∞^{pp} defined in Eq. (3.63) as a function of the mass of the FIMP candidate in the range of interest. We have considered the bath particles B_1 and B_2 to be massless.

Model	m_{B_1}	m_{B_2}	m_χ	m	J_∞^{pp}
Spectrum (a)	0	0	10 GeV	20 GeV	0.00473
Spectrum (b)	0	0	1 MeV	2 MeV	0.10579
Spectrum (c)	1 TeV	1 TeV	100 GeV	2 TeV	0.00348
Spectrum (d)	100 GeV	100 GeV	10 keV	200 GeV	0.00363

reproduce the observed relic density

$$\lambda_{pp} = 2.7 \times 10^{-11} \left(\frac{m/m_\chi}{2} \right)^{1/2} \left(\frac{3 \times 10^{-3}}{J_\infty^{pp}} \right)^{1/2} \left(\frac{\Omega_\chi h^2}{0.12} \right)^{1/2}. \quad (3.64)$$

We have normalized the ratio m/m_χ to 2, which is the case for the heavy final state pair production. In Fig. 3.5 we show the solution Eq. (3.62) for the considered spectra, as usual tuning λ_{pp} to reproduce the observed relic density. We note that if χ is light, λ_{pp} gets enhanced. The freeze-in still happens at $x = m/T \simeq 1 \div 10$ with m the relevant mass scale in the process defined in Eq. (3.61).

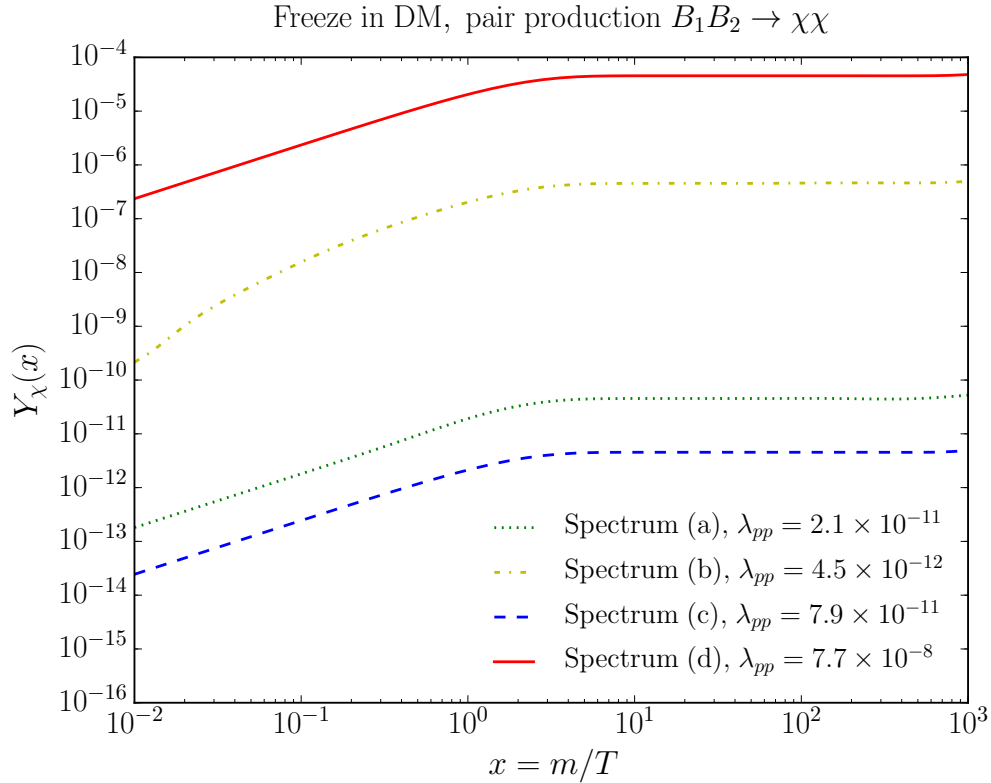


Figure 3.5: The evolution of the comoving density of FIMP DM Y_χ for the case of freeze-in from pair production processes. We plot the solution for the simple scalar model in Eq. (3.30) and four choices of spectra. The coupling λ_{pp} was tuned to reproduce the observed relic density $\Omega_{\text{DM}} h^2 = 0.12$. The time variable is the inverse temperature normalized to the relevant mass scale, defined in Eq. (3.61). The unusual behaviour of the solution relative to spectrum (b) is due to the particular relevant mass scale of the process and the change in the number of relativistic degrees of freedom, as evident from the anomalous value of J_∞^{pp} .

3.3 Observational features of frozen-in Dark Matter

As we have seen in the previous Sections 3.1 and 3.2, the main feature of frozen-in DM candidates is the smallness of their coupling with the visible Standard Model (SM) particles, which constitute the thermal bath in the early Universe. The extreme weakness of this coupling is such that FIMPs never attain thermal equilibrium with the SM particles, and this is crucial for DM production. If we compare the freeze-in scenario with the standard freeze-out mechanism we reviewed in Section 2.4, we could be led to think that the smallness of the couplings between dark and visible sectors in the former case forbids any experimental observation of the non-gravitational interactions between dark and visible particles. On one side, this can make FIMPs more appealing, since the unconstrained parameter space is way larger than in the case of WIMPs, while, on the other side, the

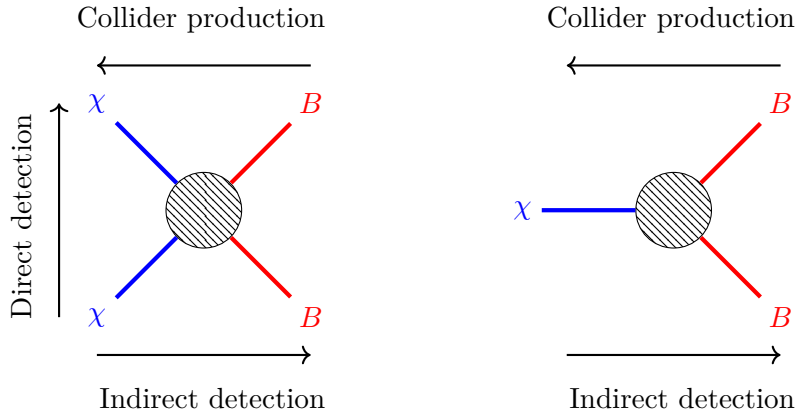


Figure 3.6: Schematic representation of the ways to observe DM particles. We show scattering-like and decay-like diagrams implying some interactions between DM particles χ and Standard Model states B . Depending on the considered direction of the arrow of time, the diagrams represent different processes, which are studied in detection experiments: DM annihilation and decay (indirect detection), scattering of DM and nuclei (direct detection), DM production (collider production).

inability to experimentally test the model can rightly concern the physicist. However, as we shall see in this section, the freeze-in scenario can be tested in many ways and the features of the frozen-in dark sector can be unveiled by laboratory experiments and by observations on astrophysical and cosmological scales. In the next chapter, we will focus on a specific method to constrain freeze-in models: the observation of structure formation.

In general, searches of DM look for signatures of their interactions with SM particles through different kind of processes. We show in Fig. 3.6 a schematic representation of the possible processes involving DM particles χ and SM states B , through Feynman-like diagrams. We briefly review, with some specific examples, the possible signatures of frozen-in DM in three different types of searches: direct detection experiments, indirect detection observations, colliders searches.

3.3.1 Direct detection signatures

Direct detection experiments search for processes of the type

$$\chi B \longrightarrow \chi B, \quad (3.65)$$

where B is usually a large nucleon, to enhance the interaction cross-section. We have shown in Fig. 2.3 the tightest constraints obtained by the XENON1T collaboration on WIMP DM-nucleon spin-independent cross-section. Given the fact that FIMPs are much more weakly coupled with the visible sector, freeze-in models are very challenging to test in fixed-target experiments. However, due to its non-thermal nature, FIMP DM can be lighter than WIMP DM, allowing for a larger number density n_χ that can drastically enhance

detection rates. Recently, a large number of ideas for new experimental setups to detect DM in the keV - MeV mass range has been developed and next-generation experiments will explore this path.

Instead, for super-GeV DM, direct detection experiments, e.g. XENON1T, have recently already achieved the needed sensitivity to test freeze-in mechanisms. In particular, this applies to a class of FIMP models in which the dark χ and SM N states are connected through a light mediator, with mass $\lesssim 10$ MeV. In this case, elastic scatterings with nuclei can proceed through a t-channel, in which the cross-section can be boosted compensating the smallness of the FIMP coupling required for the freeze-in mechanism. Following [38,41], we review this interesting possibility focusing on a particular scenario, the millicharged freeze-in DM coupled with SM through a kinetic mixing portal. In the minimal model, the fermionic DM particle χ and its antiparticle $\bar{\chi}$ are charged under a dark $U(1)_d$ gauge symmetry with fine structure constant $\alpha_d = e_d^2/(4\pi)$. Decays of DM are forbidden by gauge symmetry, as for the electron in QED. The coupling to the SM is obtained through a mixing of the gauge field strength tensors of $U(1)_d$ and of the hypercharge $U(1)_Y$ gauge field i.e. through the gauge-invariant term

$$\mathcal{L} \supset -\frac{\varepsilon}{2} V^{\mu\nu} B_{\mu\nu}. \quad (3.66)$$

This term can be originated by loop interactions between heavy fermions charged under both gauge fields, resulting in effective interaction between the gauge fields at low energies [42]. If $U(1)_d$ is broken, the two sectors feebly interact with the exchange of massive gauge bosons: the ordinary Z field and the so-called dark photon V , here we consider light $m_V \lesssim 10$ MeV. To understand the interaction between the dark and the visible sectors, for simplicity, let us neglect the Z -boson component in the B_μ field and focus on the unbroken gauge group of $SU(2)_L \times U(1)_Y$, the $U(1)_{em}$. The relevant Lagrangian is, before symmetry breaking,

$$\mathcal{L} \supset -\frac{1}{4} F_{\mu\nu} F^{\mu\nu} - \frac{1}{4} V_{\mu\nu} V^{\mu\nu} - \frac{\varepsilon}{2} V^{\mu\nu} F_{\mu\nu} + i\bar{f}\not{D}f + i\bar{\chi}\not{D}\chi, \quad (3.67)$$

with the covariant derivative,

$$D_\mu = \partial_\mu - ieQA_\mu - ie_d Q_d V_\mu. \quad (3.68)$$

Here $F_{\mu\nu}$ is the photon field strength tensor $V_{\mu\nu}$ is the dark photon strength tensor, χ is the DM particle and f an electrically charged SM state, e.g. the electron. We have $(Q_f, Q_f^d) = (1, 0)$ and $(Q_\chi, Q_\chi^d) = (0, 1)$. We can apply a field redefinition to diagonalize the kinetic sector. In the $X_{\mu\nu} = (F_{\mu\nu}, V_{\mu\nu})$ vector space, we can write the kinetic sector as

$$\mathcal{L}_{\text{kin}} = -\frac{1}{4} X_{\mu\nu} K X^{\mu\nu}, \quad (3.69)$$

with

$$K = \begin{pmatrix} 1 & \varepsilon \\ \varepsilon & 1 \end{pmatrix}. \quad (3.70)$$

This matrix can be diagonalized $K = ODO^T$ with the orthogonal transformation

$$O = \frac{1}{\sqrt{2}} \begin{pmatrix} 1 & 1 \\ -1 & 1 \end{pmatrix}, \quad (3.71)$$

giving $D = \text{diag}(1 - \varepsilon, 1 + \varepsilon)$. Therefore to obtain the canonical normalization in the diagonal kinetic term, we have to perform the field redefinition $X'_\mu = D^{1/2}O^T X_\mu$, i.e.

$$\begin{cases} A'_\mu = \sqrt{\frac{1-\varepsilon}{2}}(A_\mu - V_\mu) \\ V'_\mu = \sqrt{\frac{1+\varepsilon}{2}}(A_\mu + V_\mu) \end{cases} \quad (3.72)$$

Hence these gauge fields are two non-orthogonal combinations of the primed fields. This implies that the gauge field radiated by f has a component of the gauge field which is radiated by χ , and vice versa. We can still consider a more suitable basis, which is the most physically intuitive one. Any orthonormal combination of the primed fields will conserve the form of the kinetic sector. Let us indeed introduce the fields A''_μ and V''_μ as the orthonormal combinations of primed fields, which are not and are coupled to the DM field χ , respectively. We work at the lowest order in the mixing parameter ε . Let us rewrite the interesting pieces in the covariant derivative in terms of A''_μ and V''_μ , inverting Eq. (3.72)

$$e_d V_\mu = \frac{e_d}{\sqrt{2}} \left(\frac{V'_\mu}{\sqrt{1+\varepsilon}} - \frac{A'_\mu}{\sqrt{1-\varepsilon}} \right) = \frac{e_d}{\sqrt{2}} (V'_\mu - A'_\mu) + \mathcal{O}(\varepsilon) \equiv e_d V''_\mu \quad (3.73)$$

and

$$\begin{aligned} e A_\mu &= \frac{e}{\sqrt{2}} \left(\frac{V'_\mu}{\sqrt{1+\varepsilon}} + \frac{A'_\mu}{\sqrt{1-\varepsilon}} \right) = \frac{e}{\sqrt{2}} \left[(V'_\mu + A'_\mu) + \frac{\varepsilon}{2} (V'_\mu - A'_\mu) + \mathcal{O}(\varepsilon^2) \right] \\ &\equiv e (A''_\mu + \frac{\varepsilon}{2} V''_\mu) \end{aligned} \quad (3.74)$$

Therefore, suppressing primes, at lowest order in ε , the covariant derivative is

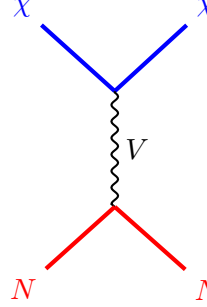
$$D_\mu = \partial_\mu - ieQ \left(A_\mu + \frac{\varepsilon}{2} V_\mu \right) - ie_d Q_d V_\mu \quad (3.75)$$

The electromagnetic current $J_{em}^\mu = Q \bar{f} \gamma^\mu f$ couples also to the dark photon V_μ with strength $e' = e\varepsilon/2$: the dark photon can mediate interactions between dark and visible states. In the general case, after electroweak symmetry breaking and diagonalising the terms containing the field strength tensors with suitable field redefinitions, the relevant terms in the Lagrangian are

$$\mathcal{L} \supset -\frac{1}{4} V_{\mu\nu} V^{\mu\nu} + \frac{1}{2} m_V^2 V_\mu V^\mu + e' V_\mu J_{em}^\mu + e_d V_\mu J_\chi^\mu, \quad (3.76)$$

where $J_\chi^\mu = Q_d \bar{\chi} \gamma^\mu \chi$ is the dark current. We have also introduced a mass term for the dark photon, originated from the breaking of $U(1)_d$ with a Higgs mechanism. We define

$\kappa = e'e_d/e^2$: it is the small coupling between dark and visible sectors and determines the freeze-in mechanism. In [41] the authors show how to recast the XENON1T limits on WIMPs, derived assuming a very short-range interaction due to a heavy mediator, in limits on FIMPs in which the interaction is long-ranged, due to the small m_V , with a t-channel propagator



The diagram shows a t-channel exchange of a mediator V between two incoming particles χ (blue lines) and N (red lines), resulting in two outgoing particles χ and N . The propagator is a wavy line labeled V . The equation (3.77) is:

$$\simeq \frac{e'e}{t - m_V^2} \simeq -\frac{\kappa e^2}{2m_B E_R + m_{\gamma'}^2} \quad (3.77)$$

where m_N is the nucleus mass, E_R the nucleus recoil energy. If $m_V^2 < 2m_N E_R$ the differential cross-section for the process will scale as $\propto \kappa^2 \alpha^2 / E_R^2$. Under this light mediator assumption, the XENON1T constraints in the $(\sigma_{\text{SI}}, m_{\text{WIMP}})$ plane can be mapped onto (κ, m_χ) , with some error, less than 30 %. The results obtained by [41] are shown in Fig. 3.7: we see that XENON1T is already testing FIMPs coupled through the kinetic mixing portal with masses 50 – 100 GeV and couplings with values in agreement with the ones we found in Section 3.2 to reproduce the relic density. Future longer-lasting experiments such as XENON1T4y and LZ will be able to explore in detail the relevant parameter space of this model, shown with a green solid line, for masses $m_\chi \gtrsim 50$ GeV. As pointed out in the same work, XENON1T bounds can also be exploited to constrain DM self-interactions that are relevant in the considered model of millicharged DM.

3.3.2 Indirect detection signatures

With indirect detection, we refer to the observation of signatures of decay or DM annihilation

$$\chi \longrightarrow BB, \quad \chi\chi \longrightarrow BB \quad (3.78)$$

Decaying DM can be embedded easily in the freeze-in scenario, for suitable choices of the mass spectrum of the theory; the smallness of the coupling between SM and dark states allows very long lifetimes, which do not spoil BBN or CMB constraints, we reported in Section 1.5: $\tau_\chi \gtrsim 10^{28}$ s. Since the freeze-in mechanism requires completely negligible decay rates of FIMPs into visible states, a simple estimate based on a trilinear scalar operator describing the decay

$$\mathcal{L} \supset \lambda_\chi m_\chi \chi BB, \quad (3.79)$$

with $m_B \ll m_\chi$, leads to the estimate

$$\tau_\chi \simeq \frac{16\pi}{\lambda_\chi^2 m_\chi} \sim 10^{28} \text{ s} \left(\frac{10^{-26}}{\lambda_\chi} \right)^2 \left(\frac{1 \text{ GeV}}{m_\chi} \right). \quad (3.80)$$

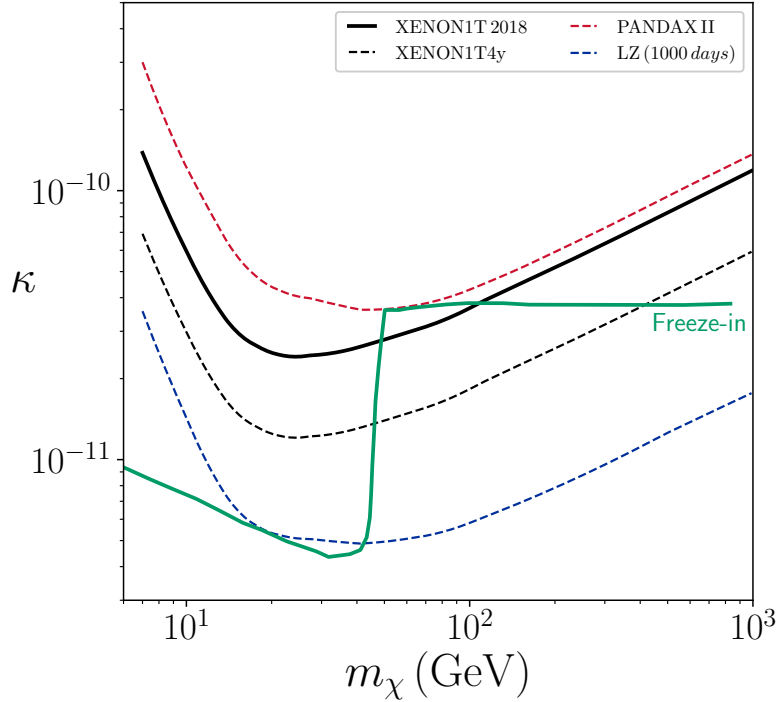


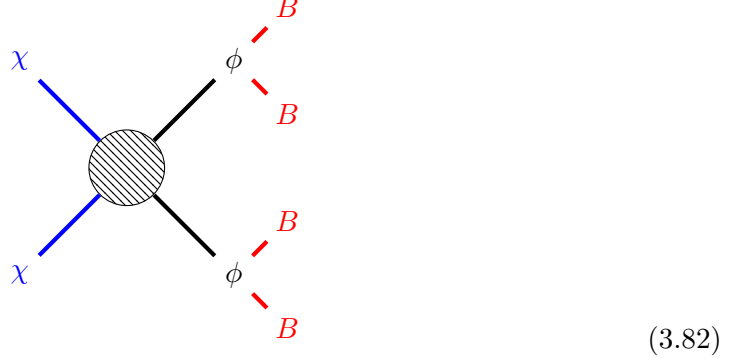
Figure 3.7: Constraints from XENON1T (black), forecast for XENON1T for 4 years (black, dashed), PANDAXII (red, dashed) and forecast for LZ for 1000 days (blue, dashed). Regions above the lines are excluded. The solid green line corresponds to the κ needed to reproduce the observed relic density through the freeze-in mechanism. Figure from [41].

Indeed $\lambda_\chi \ll \lambda_d \sim 10^{-11}$: this process is much more suppressed with respect to the FIMP production via decays of SM states. In the case in which the FIMP is a sterile neutrino, its decay products can be active SM neutrinos, that can be observed in IceCube, as explored by the authors of [43], who consider models with 6-dimensional operators to avoid unnaturally small couplings such as λ_χ . In general, one may expect also decays into photons, in the gamma-ray or X-ray band. There are plenty of satellites and observatories probing the interesting frequency band for decays of light DM, with couplings and masses suitable for the freeze-in mechanism [44]. In particular, recently, much attention was raised by the observation of a 3.55 keV line from DM-dominated systems [45] and this has motivated many theoretical studies to explain it in a freeze-in DM framework.

DM annihilation in standard freeze-in context with only a dark candidate χ is usually not observable, being the coupling between visible and dark particles suppressed by more than 6 orders of magnitudes with respect to the WIMP case. However, one can consider variations of the standard freeze-in paradigm, introducing a mediator ϕ , which is the one interacting with the SM [38]. So one can consider an unsuppressed dark annihilation

$$\chi\chi \longrightarrow \phi\phi \longrightarrow BB, BB, \quad (3.81)$$

followed by decays into visible particles. Schematically,



Since ϕ decays into SM states, these processes can be observed in the same way we have discussed above, resulting in an effective annihilation of DM into visible particles. Remarkably, this idea was implemented in a natural freeze-in scenario to fit the gamma-ray GeV excess in the centre of the Milky Way [46].

3.3.3 Collider signatures

Colliders can have luminosity and centre-of-mass energy high enough to produce DM with the following processes

$$BB \longrightarrow B'B' \longrightarrow \chi\chi, \quad BB \longrightarrow B'B' \longrightarrow B''\chi. \quad (3.83)$$

Typically searches at colliders focus on signals of mono-jets with missing energy, due to production of invisible WIMP DM. At the moment these experiments are not sensitive to standard FIMP DM, due to the small production cross-section, be it pair production, single production or decay of visible particles, since this processes are, by construction, suppressed by the small couplings $\lambda \sim 10^{-11}$, we have seen in Section 3.2 are needed to reproduce the relic abundance of DM. As an example, we can exploit Eq. (3.28) with the relic density given by decays of SM in FIMP DM, remembering the parametrization $\Gamma_{B_1 \rightarrow B_2 \chi} = \tilde{\lambda}_d^2 m_{B_1} / (8\pi)$, to write the so-called decay length $\tau_{B_1} \simeq 1/\Gamma_{B_1}$, in agreement with [1, 39]⁴

$$\tau_{B_1} \simeq \frac{1}{\Gamma_{B_1 \rightarrow B_2 \chi}} \simeq 3.3 \times 10^6 \text{ cm} \left(\frac{m_\chi}{10 \text{ GeV}} \right) \left(\frac{1 \text{ TeV}}{m_{B_1}} \right)^2 \left(\frac{0.12}{\Omega_\chi h^2} \right) \left(\frac{J_\infty^d(1 \text{ TeV})}{4.4 \times 10^{-3}} \right). \quad (3.84)$$

We have approximated the total decay width of B_1 with its partial decay rate. This corresponds to $\tau_{B_1} \sim 10^{-4}$ s. Therefore the detection of visible particles with macroscopic lifetimes is a unique signature of FIMPs. These events produce so-called displaced signals in the detector, i.e. disappearing tracks, tracks displaced from the collision axis, particles decaying in the calorimeter. However, the value of $\tau_{B_1} \sim 10^6$ cm is far beyond the size

⁴We are accounting for changes in the effective number of degrees of freedom during the expansion of the Universe, while in the estimate in [1, 39] the authors do not, so we get a order of magnitude of difference.

of any detector L , which has to be compatible with $\beta\gamma\tau_{B_1}$, where $\beta\gamma = |\vec{p}_{B_1}|/m_{B_1}$ is the time dilation factor times the velocity of the decaying particle. In practice, in the standard freeze-in scenario, DM is produced by decays of a stable, for collider purposes, particle B_1 . Nevertheless, as explored in [39, 47], if the freeze-in happens during an early matter-dominated era after inflation, or in general during an era of a fast expansion of the Universe, the resulting $\tau_{B_1} \propto \lambda_d^{-2}$ can be reduced to values in the band $10^{-2} \text{ cm} < \tau_\chi < 10^4 \text{ cm}$, which is accessible to future and present colliders. Briefly, for an early matter-dominated era, entropy production at the beginning of the standard cosmological history dilutes the frozen-in FIMP abundance, and this has to be compensated by a stronger coupling λ_d to give the correct final relic density. Finally, we have to mention that in many freeze-in scenarios, the DM is coupled to SM via a mediator particle, as we have discussed above for indirect detection. However, in this case, one can request that the coupling between the mediator and SM is not that feeble so that the mediator can be observed at colliders from its decay products.

3.3.4 Large-scales signatures

As we have said regarding indirect detection, the standard freeze-in paradigm allows the presence of long-lived dark particles that can decay feebly into the SM states, due to the small coupling between visible and dark sector. If these decays happen during the thermal history between BBN ($T \sim 0.1 \text{ MeV}$) and photon decoupling ($T \sim 0.1 \text{ eV}$) the energy released from the dark sector into the photon bath can leave a significant imprint into cosmological observables like primordial abundances and the CMB power spectrum. In [61] the authors constrain decaying millicharged freeze-in DM, while in [30] the authors obtain model-independent cosmological bounds on DM lifetimes. Another window on the physics of the early Universe can come from the observation of gravitational waves produced in phase transitions in the visible but also a possible dark sector. In particular, these observations could be possible with the upcoming LISA mission. Gravitational waves can allow us to explore the features and structure of the dark sector, without relying on its non-gravitational interactions with the SM.

Another compelling feature of freeze-in models is that they can be dependent on the initial conditions after inflation or also on the details of inflation themselves, unlike thermal DM. While the standard scenario is IR dominated, since one assumes a negligible FIMP abundance, in the more general case the FIMP particle can couple to the inflaton or be a spectator scalar field during inflation. Therefore freeze-in DM can be sensitive to very high energy physics. In the first case, the decay of the inflaton during reheating can lead to a DM overproduction, so the inflaton-FIMP coupling is tightly constrained. In the second case instead, quantum fluctuations of the FIMP field would be amplified and conserved throughout the FRW history leaving imprints in the CMB: this scenario can be constrained by the CMB power spectrum and possibly by a future observation of gravitational waves from inflation.

3.3.5 Small-scales signatures

As we have discussed talking about active neutrinos, and in general about the “coldness” of DM, the mechanism through which DM is produced and the non-gravitational interactions it is involved in can have a significant impact on the formation of structures we observe in the Universe, in particular small-scale structures. While on very large scales DM can be modelled as a perfect pressureless and cold fluid, on small scales the particle nature of DM is relevant to characterize the properties of halos and small clusters. We have seen in Section 1.5 that fermionic DM cannot be lighter than ~ 0.1 keV (Tremaine-Gunn bound) just because of the existence of dwarf spheroidal galaxies of size < 10 kpc. Other more accurate bounds can be obtained with realistic models of the DM density profile in these systems.

As we discuss in detail in Appendix B, the collisionless cold DM (CDM) paradigm is not always consistent with the observation of the small scale structures of the Universe. The main problem is an overabundance of power on small scales, producing massive and numerous small structures in N -body simulations, but that are not observed. A proposed solution we discuss in Appendix B is warm DM (WDM), where thermal DM is light $m_{\text{WDM}} \sim 1 - 10$ keV, hence possessing a relatively large free-streaming scale, below which structure formation is suppressed. The free-streaming scale produces a cut-off in the power spectrum, alleviating the small-scale shortcomings. However, thermal WDM is strongly constrained by the Lyman- α forest data, which give a lower bound on its mass $m_{\text{WDM}} > 5.3$ keV [56], or in general, depending on the assumptions, in the range $1 - 10$ keV, exactly where the mass should lie to alleviate the excess of power on small scales. Nonetheless, these tight constraints apply only if the DM phase-space distribution is thermal, so the tension with Lyman- α data might be alleviated within scenarios in which DM is produced non-thermally, such as in the freeze-in. Many studies explored this possibility and tried to map Lyman- α constraints on m_{WDM} onto constraints on the mass of FIMP DM. The starting point of the procedure is always the DM phase-space distribution, which can deviate from the Fermi-Dirac or Bose-Einstein equilibrium one. It is computed exploiting the Boltzmann equation formalism, when possible in its complete form, otherwise, moment by moment. From the phase-space distribution, one can extract physical quantities that can be compared to observables. The comparison is usually done exploiting three different techniques. Let us review them from the less to the most involved one.

1. **The free-streaming scale or horizon.** The simplest quantity one can rely on to compare theoretical predictions with structure formation is the so-called free-streaming horizon λ_{fs} , which we have already encountered treating HDM in Section 1.4. Defining the average velocity of DM particles

$$\langle v(t) \rangle = \frac{1}{m_\chi} \sqrt{\langle p^2 \rangle} = \sqrt{\frac{g_\chi}{n_\chi} \int \frac{d^3 p}{(2\pi)^3} \frac{p^2}{m_\chi^2} f_\chi(t, p)}, \quad (3.85)$$

the free-streaming horizon is

$$\lambda_{\text{fs}} = \int_{t_{\text{prod}}}^{t_0} dt \frac{\langle v(t) \rangle}{a(t)}. \quad (3.86)$$

This quantity gives an estimate of the average length scale (now) that the DM particle has travelled from production until today if it was not gravitationally trapped. The greater the free-streaming horizon, the tighter the constraints from structure formation. As we have seen, for DM, the scale of 0.1 Mpc, which is typical of dwarf galaxies, marks the border between HDM, which suppresses too much power on small-scales (compared to CDM) and models which are in only tension with data on structure formation like WDM. Therefore one can compute the phase-space distribution from the chosen model and test the warmness of its DM candidate. The authors of [62] applied this methodology to the case the freeze-in production of a DM candidate in the $U(1)_{B-L}$ gauge symmetry framework, involving substantially non-thermal distributions. They find indeed $\lambda_{\text{fs}} \ll 0.01$ Mpc, giving safely a cold candidate. However, in [63] the authors showed explicitly that the free-streaming horizon may be an inadequate quantity to carefully characterize cases in which the distribution function is non-thermal, as it is in the freeze-in mechanism: in fact, λ_{fs} takes into account only the momentum dispersion of the DM particles, rather than the full form of the distribution. This can lead us to discard non-thermal models which, under a more careful study are instead in agreement with data. Therefore λ_{fs} can only provide an order of magnitude estimate of the coldness of DM.

2. **A warmness quantity.** A simple way, but slightly more precise than the previous one, to constrain freeze-in dark model exploiting bounds on WDM parameters is to introduce a warmness quantity, defined from the phase-space distribution. The idea is to compare the warmness quantity in the FIMP and WDM models. In [58, 64] the authors apply this method to see if a 7 keV mass DM candidate in some benchmark model is compatible with constraints on m_{WDM} from Lyman- α [56]. The warmness quantity is defined as

$$\sigma = \frac{1}{m_{\text{DM}}} \sqrt{\langle p^2 \rangle} = \tilde{\sigma} \frac{T_{\text{DM}}}{m_{\text{DM}}}, \quad (3.87)$$

where the DM temperature is defined as

$$T_{\text{DM}} = \left(\frac{g_{\star s}(T)}{g_{\star s}(T_{\text{dec}})} \right)^{1/3} T, \quad (3.88)$$

with T the temperature of the radiation bath and T_{dec} is the decoupling temperature from the bath. The quantity $\tilde{\sigma}$ is defined as

$$\tilde{\sigma}^2 T_{\text{DM}}^2 = \frac{\int d^3 p p^2 f}{\int d^3 p f}. \quad (3.89)$$

The map between FIMP parameters and m_{WDM} is obtained from the equation

$$\sigma_\chi = \sigma_{\text{WDM}} \implies \tilde{\sigma} \frac{T_\chi}{m_\chi} = \tilde{\sigma}_{\text{WDM}} \frac{T_{\text{WDM}}}{m_{\text{WDM}}}, \quad (3.90)$$

where T_{WDM} is fixed to reproduce the relic density with mass m_{WDM} and, for a thermal fermion candidate, $\tilde{\sigma}_{\text{WDM}} \simeq 3.6$. Then, the problem is to compute $\tilde{\sigma}_\chi$ from the model-dependent phase-space distribution. Finally, the bound on m_χ reads

$$m_\chi > 7 \text{ keV} \left(\frac{m_{\text{WDM}}}{2.5 \text{ keV}} \right)^{4/3} \left(\frac{\tilde{\sigma}_\chi}{3.6} \right) \left(\frac{106.75}{g_{\star s}(T_{\text{dec}})} \right)^{1/3}, \quad (3.91)$$

for a Lyman- α constraint of $m_{\text{WDM}} > 2.5 \text{ keV}$. This method can be exploited efficiently in simple scenarios in which, under some approximations, one can compute analytically the phase-space distribution [58]. So it is a method to obtain rather quickly some bounds on the FIMP mass, within a 10 % accuracy, with respect to the following, more reliable, method.

3. **Linear matter power spectrum.** The linear matter power spectrum $P(k)$ encodes almost all the relevant information about the process of structure formation. The peculiar behaviour of the power spectrum at small scales, with respect to the standard $P_{\text{CDM}}(k)$ one, characterizes the warmness of the DM candidate. One can define the squared transfer function

$$\mathcal{T}^2(k) = \frac{P(k)}{P_{\text{CDM}}(k)}, \quad (3.92)$$

giving information about the small-scale power suppression for our non-thermal relic with respect to the perfectly cold thermal DM. Indeed Lyman- α bounds are usually expressed in terms of the limiting transfer function for thermal WDM $\mathcal{T}_{\text{lim}}^2(k)$. In principle, as stated by [58,63] the most suitable approach would be to analyse Lyman- α data using the computed model-dependent phase-space distribution; however, this is highly time-consuming, hence is not a viable approach. What is usually done is to compute the transfer function for every point in parameter space using a Boltzmann-solver code optimized for non-cold DM and compare the result to the result of WDM. In general, if $\mathcal{T}^2(k) \geq \mathcal{T}_{\text{lim}}^2(k)$ for all modes k the model for the chosen point in parameter space is in agreement with the Lyman- α bound. However one has to take into account the shape of the transfer function itself since, in particular for non-thermal distribution, the behaviour of the transfer function around the cutoff can be highly modified. To use the criterion also for freeze-in models, another procedure is applied. As a fair compromise for a reference mode, one computes the half-mode $k_{1/2}$ at which $\mathcal{T}^2(k_{1/2}) = 1/2$ for both the model and the limiting transfer function. In [63] it is shown that the choice of $k_{1/2}$ as a reference mode is robust and does not change the results much. Then two criteria can be exploited:

- In [58,64] the authors assume a model is in agreement with Lyman- α if $k_{1/2} > k_{1/2}^{\text{lim}}$.

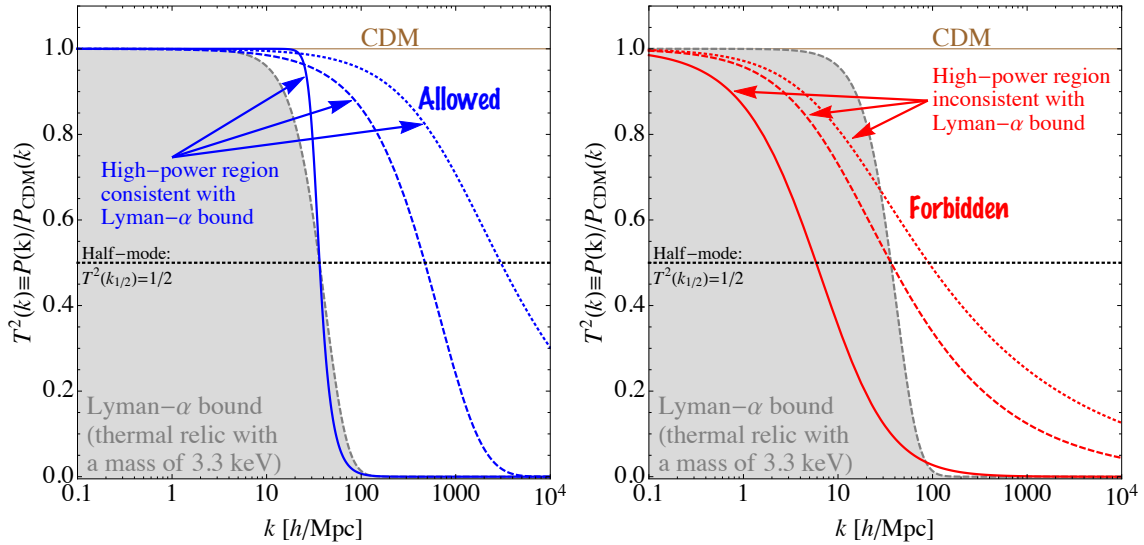


Figure 3.8: Representation of the criterion of [63] to establish which models are in agreement (left) with some bound and which are not (right). Figure from [63].

- Instead in [63], the authors check if the condition $\mathcal{T}^2(k) \geq \mathcal{T}_{\text{lim}}^2(k)$ is fulfilled for all $k \leq k_{1/2}$: if so the model is consistent with the Lyman- α bound.

The last choice seems to be the more consistent with the idea that Lyman- α bounds have to stay untouched on scales $k < k_{1/2}$: the modified slope of the cutoff for a non-thermal relic can lead to suppression at scales $k < k_{1/2}$ and this has to be avoided. This idea is illustrated in Fig. 3.8 from [63]. There we see that the two methods of [58, 64] and [63] may lead to different conclusions since for the former authors the dotted and dashed transfer functions in the right panel are allowed as the ones on the left panel. In [66] the authors provide an analytical fit formula for the transfer function of a given thermally distributed WDM species of mass m_{WDM} , which has been exploited to draw $\mathcal{T}_{\text{lim}}^2$ for $m_{\text{WDM}} = 3.3$ keV.

Basing on the last and most reliable method, in this work we will develop a general procedure to constrain the parameter space of freeze-in scenarios, once a model is given. Then we will apply the methodology to the simple four-dimensional scalar operators already considered in Section 3.2.

Study of small-scale structures can also give insights on DM self-interactions, i.e. self-couplings between χ particles. As we discuss in Appendix B, self-interacting DM (SIDM) can be a solution to the aforementioned shortcomings of the CDM paradigm since it has an impact on structure formation and DM halo density profiles. As we have seen above with the millicharged DM model [41], self-interacting DM can be produced via freeze-in, and we can get bounds on the couplings responsible for self-interactions in specific models as we have discussed above focusing more on the DM mass m_χ .

Other important bounds on FIMPs models and, more generally, on the dark sector,

come from the study of stellar energy losses for particles in the range $0.01 - 100$ keV and supernovae explosions in the mass range $1 - 100$ MeV. These two possibilities are respectively explored by [59] and [60] in the case of models involving dark photons similar to the one outlined above.

Chapter 4

Constraints on FIMP parameters: methodology

In this chapter we will illustrate our new methodology to obtain constraints on parameters of FIMP models in the freeze-in standard scenario. We intend to develop a very general procedure to constrain the parameters of any given Lagrangian describing the freeze-in DM production. A given model can always be decomposed into single operators, each one contributing to the freeze-in production with some processes. In general, a model can be written in the form

$$\mathcal{L}_{\text{FI}} = \sum_{k=1}^n C_k^{(4-\Delta_k)} \mathcal{O}_{\Delta_k}^{(k)}(\phi, \psi, A_\mu, \chi, \dots). \quad (4.1)$$

Each term in the freeze-in Lagrangian is characterized by a coupling $C_k^{(4-\Delta_k)} = \lambda_k \Lambda_k^{4-\Delta_k}$ which can be dimensionful, depending on the dimension Δ_k of the operator $\mathcal{O}_{\Delta_k}^{(k)}$. The coupling strength is determined by a dimensionless small coupling $\lambda \sim 10^{-7} - 10^{-12}$ between the N_k involved particles: scalars ϕ , spin 1/2 fields ψ , vector spin 1 fields A_μ and the DM candidate χ , each with its mass. Since the general operator can have mass dimension Δ_k , the coupling is multiplied by a relevant mass scale $\Lambda_k^{4-\Delta_k}$: Λ_k can be the mass of the heaviest particle involved in the k -th term, or, in the case of higher-than-four dimensional operators, it is set by the mass scale of some heavy particle state which has been integrated out, in an effective theory framework. To sum up, we have only four ingredients for the k -th term in the freeze-in model:

1. the value of the coupling $C_k^{(4-\Delta_k)}$;
2. the particle content of the operator, thus the nature of the DM particle χ ;
3. the functional form of \mathcal{O}_k , determining the mass dimension Δ_k of the operator;
4. the mass spectrum of the particles involved, determining the relevant mass scale if

$$\Delta_k \neq 4.$$

The free parameters of the theory will be the values of the n couplings and of the masses involved, which are less than $n \times N_k$. In the first part of the chapter, we present the general procedure to be applied for any given model and we obtain a general result for the DM phase-space distribution. In the second part of the chapter, we apply the methodology to three simple scalar toy models. We rely on the calculations carried out in Appendix D, where we find collision terms for various processes.

4.1 General procedure

In this section, we outline the general procedure to constrain the parameters of a freeze-in model. We want to constrain mainly the coupling λ and the FIMP mass m_χ . The other values of the mass spectrum m_i will be of secondary importance. We can proceed as follows:

1. We choose a mass spectrum. We fix the global relevant mass scale M to be the mass of the heaviest particle involved in the model. The other masses will be parameters to be constrained, and, among them, m_χ will be of primary importance for our studies.
2. We redefine all the dimensionless couplings

$$\lambda_k \longrightarrow \lambda_k \left(\frac{\Lambda_k}{M} \right)^{4-\Delta_k} \quad (4.2)$$

to get rid of the dependence on Λ_k and to write the model as

$$\mathcal{L}_{\text{FI}} = \sum_{k=1}^n \lambda_k M^{4-\Delta_k} \mathcal{O}_{\Delta_k}^{(k)}(\phi, \psi, A_\mu, \chi, \dots). \quad (4.3)$$

Then we choose the values of these new λ_k .

3. For a given mass spectrum we list all the possible processes allowed by each operator and kinematics. Broadly, the processes can be classified as n -body decays (mainly two and three-body ones) and $n \rightarrow m$ scatterings (mainly $2 \rightarrow 2$ ones). We compute the collision terms for each allowed process.
4. We write the Boltzmann equation for all the particles species involved in the model which are out-of-equilibrium and therefore can have a non-thermal phase-space distribution. Each Boltzmann equation takes into account all the processes in which the particle species is involved. Of primary importance is the DM distribution function f_χ .
5. We solve the set of (possibly coupled) Boltzmann equations to find the unknown

phase-space distributions. If necessary, one can rely on a perturbative expansion in some suitable quantity.

6. We impose a first constraint on the parameters requiring that the relic DM abundance reproduces a given fraction $F \equiv \Omega_\chi/\Omega_{\text{DM}}$ of the observed one. This constraint fixes a combination of the values of the couplings λ_k .
7. We use the obtained DM phase-space distribution to compute the linear matter power spectrum $P(k)$ with a Boltzmann solver code, like CLASS [68, 69].
8. We compare the (squared) transfer function $\mathcal{T}^2 \equiv P/P_{\text{CDM}}$ obtained from our model with the limit one $\mathcal{T}_{\text{lim}}^2$ obtained from observational constraints. With a suitable criterion to do that, we see whether the model for the chosen mass spectrum agrees with observations or not. One can exploit more than one criterion to double-check the robustness of the results, e.g. the two illustrated in Section 3.3. Defining $k_{1/2}$ such that $\mathcal{T}^2(k_{1/2}) = 1/2$, the criteria are:
 - If $k_{1/2} \geq k_{1/2}^{\text{lim}}$ the model is in agreement with the bound.
 - If $\mathcal{T}_{\text{lim}}^2(k) \leq \mathcal{T}^2(k)$ for all $k \leq k_{1/2}$ the model respects the imposed bound.

The two criteria can give different outputs, so we record them separately.

9. We repeat the procedure from step 1, exploring the available parameter space.

In this scheme, the model is characterized by the following input parameters

$$(M, \lambda_k, m_i, \dots, m_\chi; F^*), \quad (4.4)$$

with F^* fixed once for all. The output of the procedure is a region of parameter space that is in agreement with the bounds. The procedure can be slightly modified changing point 5.: in particular, one can leave F as a free (output) parameter and discard the model if $F < F^*$ or $F > 1$, going back to point 1. In this case, the methodology amounts to check whether a model is globally in agreement with both the information on structure formation and the relic density.

In any case, with our methodology, the analysis will be possible both for every single operator in the Lagrangian, assuming it is the only one contributing to the freeze-in relic density, and for multiple operators organized in a more involved model. If we consider models with one operator only, like

$$\mathcal{L}_{\text{FI}} = \lambda M^{4-\Delta} \mathcal{O}_\Delta(\phi, \psi, A_\mu, \chi, \dots), \quad (4.5)$$

we can easily constrain the parameter space by fixing the coupling λ to reproduce the relic density in point 5. As we have seen in Section 3.2, focusing on some particular cases, this fixes the coupling λ once the mass spectrum is fixed. In general, if there are more terms

in the Lagrangian, each with its coupling, the constraint is also possible but less efficient since only a combination of the couplings is fixed. Then we may further constrain the mass spectrum of the theory using structure formation. We focus on dimension $\Delta = 3$ or 4 operators on simple scalar models we have already introduced in Section 3.2 and on mass spectra involving a light $m_\chi \simeq 1 - 10$ keV FIMP candidate. Considering higher dimension operators, e.g. dimension 5 or 6, one has to take into account dependences on the final stages of inflation. This can be done within our formalism but this possibility is beyond the scope of this work.

In the simplest scenario, which is the one we will consider in this work, the FIMP DM candidate is the only particle species which is characterized by a non-thermal phase-space distribution f_χ . Therefore we need to solve only one Boltzmann equation to obtain its expression. The solution can be written analytically as an integral which, as we shall see, is usually computed numerically. However, some analytical expressions are possible under some approximations. As we have seen in Section 2.1, the Boltzmann equation for the particle species χ phase-space distribution $f_\chi(t, p)$ can be written in the form

$$g_\chi \frac{df_\chi}{dt} = g_\chi \frac{C}{E}. \quad (4.6)$$

We assume, reasonably, that the collision term C is not a functional of the DM distribution: this amounts to neglect all possible processes involving χ particles in the initial state and any possible quantum Pauli-blocking or Bose-enhancement effects for the DM species. This is a very good approximation throughout the freeze-in production. Hence C can only depend on all the other particles' distributions and allows the above equation to be directly integrated. The number of internal degrees of freedom of χ is introduced in the Boltzmann equation for later convenience. It is useful to change the time variable from cosmic time t to temperature T using Eq. (A.80) and then, as usual, to the dimensionless variable $x \equiv M/T$. Hence, we recast the Boltzmann equation in the form

$$g_\chi \frac{df_\chi}{dx} = \frac{1}{xH(x)} \left(1 - \frac{1}{3} \frac{d \log g_{*s}}{d \log x} \right) g_\chi \frac{C}{E}. \quad (4.7)$$

We can integrate this equation in the interval $[x_i, x]$ to obtain the distribution at time x . However, we have to take into account the fact that the physical momentum is always redshifted in time as $p \propto 1/a$, so, even after a χ particle is produced, its momentum is redshifted and the phase-space distribution changes. We can get rid of this residual time dependence in the phase-space distribution introducing a dimensionless comoving momentum $q = (pa)/(a_{\text{FI}}T_{\text{FI}})$ where a is the scale factor. Exploiting the conservation of entropy $aTg_{*s}^{1/3} = a_{\text{FI}}T_{\text{FI}}g_{*s}^{1/3}(T_{\text{FI}})$ we can rewrite the comoving momentum in the form [58, 63, 64, 67]

$$q = \frac{p}{T_\chi}, \quad (4.8)$$

where T_χ is given by

$$T_\chi(x) = \left(\frac{g_{\star s}(T)}{g_{\star s}(T_{\text{FI}})} \right)^{1/3} T = \left(\frac{g_{\star s}(M/x)}{g_{\star s}(M)} \right)^{1/3} \frac{M}{x}. \quad (4.9)$$

This formula can be seen as a definition of a temperature of relativistic decoupled χ particles and provides a scale of momentum to convert comoving momenta into physical ones. This definition is also exploited in the CLASS code [69], so it is convenient to provide the phase-space distribution as a function of comoving momenta. The freeze-in temperature is chosen as a reference and taken to be the relevant mass scale $T_{\text{FI}} = M$. With this definition, we can write the phase-space distribution after the removal of the time dependence inside the momentum

$$g_\chi f_\chi(x, q) = \int_{x_i}^x dx' \frac{1}{x' H(x')} \left(1 - \frac{1}{3} \frac{d \log g_{\star s}(x')}{d \log x'} \right) g_\chi \frac{C(x', q)}{E(x', q)}. \quad (4.10)$$

Notice that the energy is dependent both on time and on comoving momentum $E(x, q) = \sqrt{q^2 T_\chi^2(x) + m_\chi^2}$. To obtain the phase-space distribution relevant for structure formation, we can take $x_i = 0$ and $x \rightarrow \infty$, since the freeze-in is an IR-dominated mechanism, i.e. the production is most efficient at $x \sim 1 - 10$ and not beyond.

$$g_\chi f_\chi(q) = \int_0^\infty dx' \frac{1}{x' H(x')} \left(1 - \frac{1}{3} \frac{d \log g_{\star s}(x')}{d \log x'} \right) g_\chi \frac{C(x', q)}{E(x', q)}. \quad (4.11)$$

This solution is completely general and holds for every freeze-in model with only one FIMP DM candidate and any FRW-like cosmology. The dependence on the considered model enters the explicit form of the collision term and the processes to be considered, while the role of cosmology enters through $H(x)$. Usually, the Boltzmann equation is solved during a radiation dominated era, but one can also consider freeze-in during, e.g., an early matter domination era or a fast-expanding Universe, by simply introducing the suitable explicit form of $H(x)$. Once one has obtained the DM phase-space distribution, he can write the number density of DM and use it to require that the model reproduces the relic density $\Omega_\chi h^2 = m_\chi n_\chi / \rho_c(t_0)$:

$$n_\chi = \frac{T_\chi^3(T_0)}{2\pi^2} \int_0^\infty dq q^2 g_\chi f_\chi(q), \quad (4.12)$$

with $x_0 = M/T_0$ and $T_0 = 2.35 \times 10^{-4}$ eV, the CMB temperature today.

4.2 Phase-space distribution for our models

Once we have chosen a model, we can find the phase-space distribution using Eq. (2.20): to do so, we have to explicit the processes that contribute to DM production and write the corresponding collision terms. In Appendix D, we find the expressions of the collision terms, first in general and then under some approximations that can be useful to simplify

the problem, even at the level to solve it analytically. The approximated found formulae are in agreement with the results of [63, 64].

In this work we consider three very simple operators, making up three different models. All models involve only scalar particles for simplicity: they are meant to be toy models to illustrate and apply our procedure in practice. Our concern is on the methodology itself, which can be applied to more involved and concrete examples.

4.2.1 Trilinear scalar interaction

Our first model is a trilinear scalar interaction between the DM particle χ and two different particles B_1 and B_2 belonging to the thermal bath.

$$\mathcal{L}_{\text{FI}}^{(3)} = \lambda_3 m_{B_1} \chi B_1 B_2. \quad (4.13)$$

We assume B_1 is the heaviest particle, hence the relevant mass scale is given by m_{B_1} . All the considered mass spectra will satisfy the inequality

$$m_{B_1} \leq m_{B_2} + m_\chi. \quad (4.14)$$

If so, the only DM number-changing process allowed by this model at order λ_3 in amplitude is the two-body decay of B_1 into B_2 and the DM candidate. The process has an amplitude

$$\mathcal{M}_{B_1 \rightarrow B_2 \chi} = \begin{array}{c} \begin{array}{c} B_2 \\ \nearrow p_{B_2} \\ \text{---} \\ \text{---} \\ \searrow p \\ \chi \end{array} \\ B_1 \text{---} \xrightarrow{p_{B_1}} \end{array} = i\lambda_3 m_{B_1}. \quad (4.15)$$

We are interested in the squared amplitude, in particular in the combination summed over initial and final spins, in our notation

$$g_{B_1} g_{B_2} g_\chi |\mathcal{M}_{B_1 \rightarrow B_2 \chi}|^2 = \lambda_3^2 m_{B_1}^2. \quad (4.16)$$

We can substitute this expression in Eq. (D.18) to obtain the collision term of this process

$$\frac{g_\chi C(T, p)}{E} = \frac{\lambda_3^2 m_{B_1}^2}{16\pi} \frac{T}{Ep} h_{\text{eq}}(T, p). \quad (4.17)$$

Introducing the dimensionless variables

$$x = \frac{m_{B_1}}{T}, \quad q = \frac{px}{m_{B_1}} \left(\frac{g_{*s}(m_{B_1})}{g_{*s}(m_{B_1}/x)} \right)^{1/3} \equiv \frac{p}{T_\chi(x)}, \quad (4.18)$$

we rewrite the collision term in the form

$$\frac{g_\chi C(x, q)}{E} = \frac{\lambda_3^2 m_{B_1}^3}{16\pi} \frac{h_{\text{eq}}(x, q)}{xqT_\chi(x)E(x, q)}, \quad (4.19)$$

with $E(x, q) \equiv \sqrt{q^2 T_\chi^2(x) + m_\chi^2}$. Finally we write the phase-space distribution

$$g_\chi f_\chi(q) = \frac{\lambda_3^2 m_{B_1}^3}{16\pi} \frac{1}{q} \int_0^\infty dx \frac{1}{x^2 H(x)} \left(1 - \frac{1}{3} \frac{d \log g_{*s}(x)}{d \log x} \right) \frac{h_{\text{eq}}(x, q)}{T_\chi(x)E(x, q)}. \quad (4.20)$$

In Appendix D we have derived the general form for the function h_{eq} in the approximation where we neglect Pauli-blocking and Bose-enhancement factors. We quote the result applied to our specific case, in which the particles are all scalars, hence bosons

$$h_{\text{eq}}(x, q) = -\log \left[\frac{1 - \exp\left(\frac{-x(E+E_2^-)(x, q)}{m_{B_1}}\right)}{1 - \exp\left(\frac{-x(E+E_2^+)(x, q)}{m_{B_1}}\right)} \right]. \quad (4.21)$$

The functions $E_2^\pm(x, q)$ are defined in Eq. (D.15) from Eq. (D.13), where we perform the following substitutions:

$$p \rightarrow qT_\chi(x), \quad T \rightarrow \frac{m_{B_1}}{x}, \quad (m_1, m_2, m_\chi) \rightarrow (m_{B_1}, m_{B_2}, m_\chi). \quad (4.22)$$

We find the phase-space distribution computing the integral in Eq. (4.20) numerically, once both a suitable mass spectrum and a cosmological history $H(x)$ are chosen. We focus on the case in which the production occurs during the radiation dominated era, where

$$H(x) = \sqrt{\frac{\pi^2}{90} g_{*\rho}(m_{B_1}/x)} \frac{m_{B_1}^2}{x^2 M_{\text{Pl}}}. \quad (4.23)$$

However, under some approximations, the phase-space distribution can be found analytically, as done in [58] for another model.

- We neglect the dependence on temperature of the number of effective degrees of freedom g_{*s} and $g_{*\rho}$, which can only be treated numerically.
- we assume $T_\chi = T$, neglecting entropy production during the thermal history.
- We assume always $m_\chi \ll m_{B_1}, m_{B_2}$. This implies $E = qT$. Moreover, we need to exploit the limiting expressions for p_2^\pm provided in Appendix D that give, under our assumptions

$$p_2^+ = \infty, \quad p_2^- = qT \frac{r^2}{1-r^2} - \frac{m_{B_1}^2(1-r^2)}{4qT}, \quad (4.24)$$

having defined $r \equiv m_{B_2}/m_{B_1}$. We obtain

$$E_2^+ = \infty, \quad E_2^- = \sqrt{m_{B_1}^2 r^2 + (p_2^-)^2} = \frac{m_{B_1}^2}{4qT} (1 - r^2) + qT \frac{r^2}{1 - r^2}. \quad (4.25)$$

- We neglect all quantum corrections and assume a classical Maxwell-Boltzmann statistics for all the particles involved. As shown in Appendix D, this amounts to consider

$$h_{\text{eq}}(x, q) = \exp \left\{ - \frac{x(E + E_2^-)(x, q)}{m_{B_1}} \right\} - \exp \left\{ - \frac{x(E + E_2^+)(x, q)}{m_{B_1}} \right\} \quad (4.26)$$

that, under the above assumptions, is a Gaussian function in x :

$$h_{\text{eq}}(x, q) = \exp \left\{ - x^2 \left[\frac{1 - r^2}{4q} \right] - \frac{q}{1 - r^2} \right\}. \quad (4.27)$$

Exploiting all these approximations, the phase-space distribution becomes

$$g_\chi f_\chi(q) \simeq \lambda_3^2 \frac{\sqrt{90}}{16\pi^2} \frac{M_{\text{Pl}}}{g_{\star\rho}^{1/2}(m_{B_1})m_{B_1}} \frac{1}{q^2} \exp \left(- \frac{q}{1 - r^2} \right) \int_0^\infty dx x^2 \exp \left\{ - x^2 \left[\frac{1 - r^2}{4q} \right] \right\}, \quad (4.28)$$

which reads

$$g_\chi f_\chi(q) \simeq \lambda_3^2 \frac{\sqrt{90}}{8\pi^{3/2}} \frac{M_{\text{Pl}}}{g_{\star\rho}^{1/2}(m_{B_1})m_{B_1}} \frac{(1 - r^2)^{-3/2}}{\sqrt{q}} \exp \left(- \frac{q}{1 - r^2} \right). \quad (4.29)$$

We use this analytic result to compare the actual numerical outcome with the equilibrium phase-space distribution. In this way, we can understand the impact of the various approximations.

In Fig. 4.1 we show the results of our calculations for various values of the parameters. We have chosen different mass spectra, all with $m_{B_1} = 1$ TeV while varying the mass of the FIMP and the other bath particle. We focus on light DM candidates. In the upper plot we consider $m_\chi = 10$ MeV while in the lower one $m_\chi = 10$ keV. Then we plot the analytical approximation Eq. (4.29) together with the simple thermal distribution and numerical results for various masses $m_{B_2} = r m_{B_1}$ with $r = 10^{-4}, 0.1, 0.5$. In all cases the coupling λ_3 is fixed so that the model reproduces the observed relic density $F = 1$ at $T_0 = 2.35 \times 10^{-4}$ eV. The thermal BE distribution for massless χ ,

$$f_\chi^{\text{eq}} = \frac{1}{e^q - 1}, \quad (4.30)$$

has been normalized in order to obtain the observed relic density. Notice that the analytic approximation reproduces almost exactly the full numerical result. The non-thermal FIMP phase-space distributions are slightly colder than the equilibrium Bose-Einstein one,

meaning that the peak is at higher comoving momentum and they have a larger width, which is associated to the “dispersion” of comoving momentum. This parameter measures the warmness of the particle species and is described effectively by the quantity

$$\tilde{\sigma}^2 = \frac{\int dq q^4 f_\chi(q)}{\int dq q^2 f_\chi(q)}, \quad (4.31)$$

which characterizes the sound speed and hence the Jeans scale of our DM model. We compute this value for each distribution and show it in the plot legend: in the case of equilibrium, for bosonic DM, $\tilde{\sigma}_{\text{eq}} \simeq 3.2$. We can use the warmness constraint, described in Section 3.3, to give raw bound on the FIMP mass, similarly to what was done in [58],

$$m_\chi > 7.4 \text{ keV} \left(\frac{m_{\text{WDM}}}{3 \text{ keV}} \right)^{4/3} \left(\frac{\tilde{\sigma}}{3} \right) \left(\frac{106.75}{g_{*s}(m_{B_1})} \right)^{1/3}, \quad (4.32)$$

for a constraint on the structure formation of $m_{\text{WDM}} > 3 \text{ keV}$. A more complete analysis will be done in the next chapter. Comparing the two plots of $f_\chi(q)$, we notice that, in this very simple model, varying the mass of the DM particle, if $m_\chi \ll m_{B_1}$, change neither the shape of the distribution nor $\tilde{\sigma}$, but only the value of the coupling required to reproduce the relic density. The same happens for fixed values of m_χ if we change m_{B_2} below the value of $0.1 \times m_{B_1}$. Instead, if $m_{B_2} > 0.1 \times m_{B_1}$ the distribution of χ gets colder, as one may expect since less centre-of-mass energy is available. From $f_\chi(q)$ one can get the velocity distribution of the particle species, which is of physical interest. The comoving momentum is written in terms of velocity as

$$q = \frac{p}{T_\chi} = \frac{m_\chi \gamma \beta}{T_\chi(T)} = \frac{m_\chi}{T_\chi(T)} \frac{\beta}{\sqrt{1 - \beta^2}}, \quad (4.33)$$

with $\beta = v/c$. From this definition we see that the velocity distribution $f_\chi(\beta, T)$ is temperature or x -dependent. If we evaluate the distribution for $T \ll m_{B_1}$, e.g. $T < 10^{-3} \times m_{B_1}$, the production of χ particle is surely exhausted and we can safely take $x \rightarrow \infty$ to compute the integral in Eq. (4.11). Then we obtain simply $g_\chi f_\chi(q(\beta, T))$ where the temperature dependence has to be considered only considered in the q dependence of the distribution. In Fig. 4.2 we show the velocity distributions for the two mass spectra considered above at reference temperatures $T = (10^2, 10, 0.1) \times m_\chi$. We see the transition from relativistic to the non-relativistic regime in the shape of the velocity distribution. In particular, in the lower plot, for $m_\chi = 10 \text{ keV}$, the velocity distribution is computed at $T = 1 \text{ keV}$, a temperature that is always taken as a reference to constrain WDM models with observational data from structure formation. The distributions are normalized to 1, that is

$$\int_0^1 d\beta \beta^2 g_\chi f_\chi(\beta, T) = 1. \quad (4.34)$$

We also compute the velocity dispersion $\tilde{\sigma}_\beta$ as

$$\tilde{\sigma}_\beta(T) = \frac{\int d\beta \beta^4 f_\chi(\beta, T)}{\int d\beta \beta^2 f_\chi(\beta, T)}. \quad (4.35)$$

To get an idea of how this quantity evolves with temperature, we plot it in Fig. 4.3 for the model $(m_{B_1}, m_{B_2}, m_\chi) = (10^3 \text{ GeV}, 10^2 \text{ GeV}, 10 \text{ keV})$ in the temperature range 1 MeV - 0.1 keV, and compare it with the dispersion velocity obtained exploiting the thermal BE distribution. We see that at high temperatures the dispersion velocity is significantly higher than the equilibrium one, while they become very similar after the DM particles have become non-relativistic.

4.2.2 Quadrilinear scalar interaction for single production

The second model we consider is a quadrilinear scalar interaction between a DM particle χ and three different bath particles B_1 , B_2 and B_3 described by the Lagrangian term

$$\mathcal{L}_{\text{FI}}^{(4),\text{sp}} = \lambda_4 \chi B_1 B_2 B_3. \quad (4.36)$$

If the DM is not the heaviest particle involved, we can assume, without loss of generality, B_1 to be the heaviest particle providing the relevant mass scale m_{B_1} . Unlike the trilinear model, this example allows for multiple processes to contribute to FIMP DM production. We have three different scatterings of the type

$$\mathcal{M}_{B_i B_j \rightarrow B_k \chi} = \begin{array}{c} B_j \text{---} p_{B_k} \text{---} B_k \\ \text{---} p_{B_j} \text{---} \\ B_i \text{---} p_{B_i} \text{---} \chi \\ \text{---} p \text{---} \end{array} = i\lambda_4 \implies g_\chi g_{B_1} g_{B_2} g_{B_3} |\mathcal{M}_{B_i B_j \rightarrow B_k \chi}|^2 = \lambda_4^2 \quad (4.37)$$

with $i \neq j \neq k$ varying from 1 to 3. The scatterings have a different phase-space so we have a different collision term for each process. If the mass spectrum satisfies the relation

$$m_{B_1} \geq m_{B_2} + m_{B_3} + m_\chi, \quad (4.38)$$

then the three-body decay channel is allowed:

$$\mathcal{M}_{B_1 \rightarrow B_2 B_3 \chi} = \begin{array}{c} B_2 \\ \text{---} \\ B_1 \text{---} \chi \\ \text{---} \\ B_3 \end{array} = i\lambda_4 \implies g_\chi g_{B_1} g_{B_2} g_{B_3} |\mathcal{M}_{B_1 \rightarrow B_2 B_3 \chi}|^2 = \lambda_4^2. \quad (4.39)$$

This process is characterized by different kinematics to scatterings and again has to be considered separately. Therefore the collision term is the sum of all the processes' collision

terms:

$$\frac{g_\chi C(x, q)}{E} = \Theta(m_{B_1} - m_{B_2} - m_{B_3} - m_\chi) \frac{g_\chi C_{3d}(x, q)}{E} + \sum_{i \neq j \neq k} \frac{g_\chi C_s^{ijk}(x, q)}{E}, \quad (4.40)$$

with Θ the Heaviside function imposing the kinematical condition allowing the three-body decay.

Let us start from scatterings:

$$B_i B_j \longrightarrow B_k \chi. \quad (4.41)$$

In Appendix D we find the general expression of the collision term neglecting Pauli-blocking and Bose-enhancement factors for bosons. Using our notation, from Eq. (D.44) and substituting the expression of the amplitude squared, we obtain

$$\frac{g_\chi C_s^{ijk}(T, p)}{E} = -\frac{\lambda_4^2}{512\pi^3} \frac{T}{pE} \frac{1}{e^{E/T} - 1} \int_{s_{\min}}^{s_{\max}} \frac{ds}{p_{k\chi}(s)\sqrt{s}} \log \left(\frac{1 - e^{-E_{B_k}^-(s)/T}}{1 - e^{-E_{B_k}^+(s)/T}} \right) \int_{t_{\min}(s)}^{t_{\max}(s)} dt. \quad (4.42)$$

The expressions for $E_{B_k}^\pm$ are reported as E_3^\pm in Eq. (D.38) with momenta p_3^\pm from Eq. (D.36). The momentum in the centre-of-mass in the initial and final state is given by

$$p_{ij}(s) = \frac{k^{1/2}(\sqrt{s}, m_{B_i}, m_{B_j})}{2\sqrt{s}}, \quad p_{k\chi}(s) = \frac{k^{1/2}(\sqrt{s}, m_{B_k}, m_\chi)}{2\sqrt{s}}. \quad (4.43)$$

The integration bounds over s and t are found in Appendix D.:

$$s \in [M_{ijk}^2, +\infty[\equiv \left[\max \left\{ (m_{B_i} + m_{B_j})^2, (m_{B_k} + m_\chi)^2 \right\}, +\infty[\right], \quad (4.44)$$

$$\begin{aligned} t_{\max}(s) &\equiv m_{B_i}^2 + m_\chi^2 - E_{B_i}^{\text{cm}}(s)E^{\text{cm}}(s) + 2p_{ij}(s)p_{k\chi}(s), \\ t_{\min}(s) &\equiv m_{B_i}^2 + m_\chi^2 - E_{B_i}^{\text{cm}}(s)E^{\text{cm}}(s) - 2p_{ij}(s)p_{k\chi}(s). \end{aligned} \quad (4.45)$$

Performing the integral over t , we get

$$\frac{g_\chi C_s^{ijk}(T, p)}{E} = \frac{\lambda_4^2}{128\pi^3} \frac{T}{pE} \frac{1}{e^{E/T} - 1} \int_{M_{ijk}^2}^{\infty} \frac{ds}{\sqrt{s}} p_{ij}(s) \log \left(\frac{1 - e^{-E_{B_k}^+(s)/T}}{1 - e^{-E_{B_k}^-(s)/T}} \right). \quad (4.46)$$

The total scattering collision term in our dimensionless variables reads

$$\frac{g_\chi C_s(x, q)}{E} = \frac{\lambda_4^2}{128\pi^3} \frac{m_{B_1}}{xqT_\chi(x)E(e^{xE/m_{B_1}} - 1)} \sum_{i \neq j \neq k} \int_{M_{ijk}^2}^{\infty} \frac{ds}{\sqrt{s}} p_{ij}(s) \log \left(\frac{1 - e^{-xE_{B_k}^+(s)/m_{B_1}}}{1 - e^{-xE_{B_k}^-(s)/m_{B_1}}} \right). \quad (4.47)$$

Now let us treat three-body decays. The analysis is very similar to the one for scatterings, but, as explained in Appendix D, the Mandelstam variables for three-body decays are

defined differently.

$$\begin{aligned} s &= -(p_{B_2} + p_{B_3})^2 = -(p_{B_1} - p)^2, \\ t &= -(p_{B_3} + p)^2 = -(p_{B_1} - p_{B_2})^2. \end{aligned} \quad (4.48)$$

The collision term is, similarly to the previous case,

$$\frac{g_\chi C_{3d}(T, p)}{E} = -\frac{\lambda_4^2}{512\pi^3} \frac{T}{pE} \int_{s_{\min}}^{s_{\max}} \frac{ds}{p_{1\chi}(\sqrt{s})\sqrt{s}} \log \left(\frac{1 - e^{-E_{B_1}^-(s)/T}}{1 - e^{-E_{B_1}^+(s)/T}} \right) \int_{t_{\min}(s)}^{t_{\max}(s)} dt. \quad (4.49)$$

Here the expressions for $E_{B_1}^\pm$ are reported as E_1^\pm in Eq. (D.67) with momenta p_1^\pm from Eq. (D.65). The momenta in the centre-of-mass of particles B_1 and χ are given by

$$p_{23}(s) = \frac{k^{1/2}(\sqrt{s}, m_{B_2}, m_{B_3})}{2\sqrt{s}}, \quad p_{1\chi}(s) = \frac{k^{1/2}(\sqrt{s}, m_{B_1}, m_\chi)}{2\sqrt{s}}. \quad (4.50)$$

The integration limits are

$$s \in [(m_{B_2} + m_{B_3})^2, (m_{B_1} - m_\chi)^2], \quad (4.51)$$

$$\begin{aligned} t_{\max}(s) &\equiv m_{B_3}^2 + m_\chi^2 + E_{B_3}^{\text{cm}}(s)E^{\text{cm}}(s) + 2p_{23}(s)p_{1\chi}(s), \\ t_{\min}(s) &\equiv m_{B_3}^2 + m_\chi^2 + E_{B_3}^{\text{cm}}(s)E^{\text{cm}}(s) - 2p_{23}(s)p_{1\chi}(s). \end{aligned} \quad (4.52)$$

Performing the integral over t , we obtain

$$\frac{g_\chi C_{3d}(T, p)}{E} = -\frac{\lambda_4^2}{128\pi^3} \frac{T}{pE} \int \frac{ds}{\sqrt{s}} p_{23}(s) \log \left(\frac{1 - e^{-E_{B_1}^-(s)/T}}{1 - e^{-E_{B_1}^+(s)/T}} \right). \quad (4.53)$$

In dimensionless variables,

$$\frac{g_\chi C_{3d}(x, q)}{E} = \frac{\lambda_4^2}{128\pi^3} \frac{m_{B_1}}{xqT_\chi E} \int_{(m_{B_2}+m_{B_3})^2}^{(m_{B_1}-m_\chi)^2} \frac{ds}{\sqrt{s}} p_{23}(s) \log \left(\frac{1 - e^{-xE_{B_1}^+(s)/m_{B_1}}}{1 - e^{-xE_{B_1}^-(s)/m_{B_1}}} \right). \quad (4.54)$$

Finally, we can write the DM phase-space distribution summing the two contributions:

$$\begin{aligned} g_\chi f_\chi(q) &= \Theta(m_{B_1} - m_{B_2} - m_{B_3} - m_\chi) g_\chi f_\chi^{3d}(q) + g_\chi f_\chi^s(q) \\ &= \int_0^\infty dx \frac{1}{xH(x)} \left(1 - \frac{1}{3} \frac{d \log g_{*s}(x)}{d \log x} \right) \\ &\quad \times \left[\Theta(m_{B_1} - m_{B_2} - m_{B_3} - m_\chi) g_\chi \frac{C_{3d}}{E}(x, q) + g_\chi \frac{C_s}{E}(x, q) \right]. \end{aligned} \quad (4.55)$$

We perform the double integration numerically for two reference spectra, both also allowing three-body decays: $(m_{B_1}, m_{B_2}, m_{B_3}, m_\chi) = (1 \text{ TeV}, 100 \text{ GeV}, 0, 10 \text{ MeV})$ and $(m_{B_1}, m_{B_2}, m_{B_3}, m_\chi) = (1 \text{ TeV}, 0, 0, 10 \text{ keV})$. In both cases we fix the coupling λ_4 , so that the total phase-space distribution $f_\chi(q)$ reproduces the observed relic density, i.e. $F = 1$. In Fig. 4.4 we show the results of the computations. As we can see, the three-body decay

is relevant in the case in which we have a heavy mother particle m_{B_1} and products are very light, but is always subdominant with respect to the contribution from scatterings, also because three different scattering processes are always allowed and they sum. For the mass of one of the decay products, say m_{B_2} lower than 10% of the mother particle's mass m_{B_1} , the relevance of three-body decays is constant. Instead, reasonably, if we increase m_{B_2} , the three-body decay channel gets more and more disfavoured, until it becomes forbidden. In both choices of spectra, we see that the final phase-space distribution is colder than the thermal one, having a smaller width and a peak at lower momenta. The raw warmness constraint on the FIMP mass are milder than in the trilinear model:

$$m_\chi > 6.8 \text{ keV} \left(\frac{m_{\text{WDM}}}{3 \text{ keV}} \right)^{4/3} \left(\frac{\tilde{\sigma}}{2.74} \right) \left(\frac{106.75}{g_{*s}(m_{B_1})} \right)^{1/3}. \quad (4.56)$$

As we did for the trilinear model, it is interesting to see the time evolution of the velocity dispersion. As we see in Fig. 4.5, in this model its evolution with temperature is more similar to the equilibrium one. The DM produced with this model has a lower velocity dispersion with respect to the one obtained from the thermal distribution so that this FIMP candidate is indeed colder.

4.2.3 Quadrilinear scalar interaction for pair production

The last model under study is a quadrilinear scalar interaction between two DM particles χ and two different bath particles B_1, B_2 described by the Lagrangian term

$$\mathcal{L}_{\text{FI}}^{(4),\text{pp}} = \frac{1}{2} \lambda_{2\chi} \chi^2 B_1 B_2. \quad (4.57)$$

The analysis of this model is very similar to the previous one. However, in this case, we are modelling pair production processes instead of single production ones. For the calculations, this implies the presence of a factor of 2 in the expression of the collision operator and a different phase-space integration. This model can be seen as a particular case of the previous one with $B_3 = \chi$: we have less freedom in choosing the mass spectrum of the model. As usual, we assume B_1 to be the heaviest particle involved and that DM never gives the relevant mass scale for its production, which is a good assumption to study light DM. Since we are constrained to have DM particles only in the final state, unlike the single production case, we have only one allowed scattering process

$$B_1 B_2 \longrightarrow \chi \chi, \quad (4.58)$$

with amplitude

$$\mathcal{M}_{B_1 B_2 \rightarrow \chi \chi} = i\lambda_{2\chi} \implies g_\chi^2 g_{B_1} g_{B_2} |\mathcal{M}_{B_1 B_2 \rightarrow \chi \chi}|^2 = \lambda_{2\chi}^2. \quad (4.59)$$

If the mass spectrum satisfies the relation

$$m_{B_1} \geq m_{B_2} + 2m_\chi, \quad (4.60)$$

then the three-body decay channel is allowed:

$$\mathcal{M}_{B_1 \rightarrow B_2 \chi \chi} = i\lambda_{2\chi} \implies g_\chi^2 g_{B_1} g_{B_2} |\mathcal{M}_{B_1 \rightarrow B_2 \chi \chi}|^2 = \lambda_{2\chi}^2. \quad (4.61)$$

The final result for the phase-space distribution is written in the form

$$\begin{aligned} g_\chi f_\chi(q) &= \Theta(m_{B_1} - m_{B_2} - 2m_\chi) g_\chi f_\chi^{3d}(q) + g_\chi f_\chi^s(q) \\ &= \int_0^\infty dx \frac{1}{xH(x)} \left(1 - \frac{1}{3} \frac{d \log g_{*s}(x)}{d \log x} \right) \\ &\quad \times \left[\Theta(m_{B_1} - m_{B_2} - 2m_\chi) g_\chi \frac{C_{3d}}{E}(x, q) + g_\chi \frac{C_s}{E}(x, q) \right], \end{aligned} \quad (4.62)$$

where the two collision terms for the allowed processes are the following: for scatterings, (assuming $m_{B_1} > 2m_\chi$ as it will always be the case)

$$\frac{g_\chi C_s(x, q)}{E} = \frac{\lambda_{2\chi}^2}{64\pi^3} \frac{m_{B_1} e^{-xE/m_{B_1}}}{xqT_\chi(x)E} \int_{(m_{B_1}+m_{B_2})^2}^\infty \frac{ds}{\sqrt{s}} p_{12}(s) \left(e^{-xE_\chi^-(s)/m_{B_1}} - e^{-xE_\chi^+(s)/m_{B_1}} \right), \quad (4.63)$$

and three body decays,

$$\frac{g_\chi C_{3d}(x, q)}{E} = \frac{\lambda_{2\chi}^2}{64\pi^3} \frac{m_{B_1}}{xqT_\chi(x)E} \int_{(m_{B_2}+m_\chi)^2}^{(m_{B_1}-m_\chi)^2} \frac{ds}{\sqrt{s}} p_{2\chi}(s) \log \left(\frac{1 - e^{-xE_{B_1}^+(s)/m_{B_1}}}{1 - e^{-xE_{B_1}^-(s)/m_{B_1}}} \right). \quad (4.64)$$

Using these expressions, we can compute numerically the phase space distribution and repeat the analysis we have done in the case of the single production. We choose two reference spectra, both allowing also three-body decays: $(m_{B_1}, m_{B_2}, m_\chi) = (1 \text{ TeV}, 100 \text{ GeV}, 10 \text{ MeV})$ and $(m_{B_1}, m_{B_2}, m_{B_3}, m_\chi) = (1 \text{ TeV}, 0, 10 \text{ keV})$. In both cases we fix the coupling $\lambda_{2\chi}$, so that the total phase-space distribution $f_\chi(q)$ reproduces the observed relic density, i.e.

$F = 1$. In Fig. 4.6 we show the results of the computations. With respect to the case of the single production, we see that three-body decays, when allowed, are much more relevant in determining the coldness of the final distribution. We clearly see that the contribution from decays moves the peak of the distribution from the equilibrium one towards smaller momenta, much more than the contribution from scattering does. In this case, since there is only one allowed scattering process, both scattering and decays are relevant. The raw warmness constraint on the FIMP mass gives the same result we found for the single production. Finally, we show in Fig. 4.7 the evolution of the velocity dispersion with temperature. Again it is clear that our non-thermal distribution is colder than the equilibrium one.

4.3 The linear matter power spectrum from CLASS

Once we have computed the phase-space distributions from our specific model, we can link theory to observations by computing the linear matter power spectrum at redshift $z = 0$ in a given cosmological framework. In our basic scenario, the standard Λ CDM model is modified only by the replacement of a significant fraction F of CDM with our non-CDM, FIMP dark matter produced via freeze-in.

4.3.1 The CLASS code

The accurate computation of the power spectrum, in this case, is highly non-trivial and it is usually performed relying on pre-made and publicly available codes like CAMB or CLASS [68]. In particular, the Cosmological Linear Anisotropy Solving System (CLASS) was developed in 2011 on request of the Planck collaboration to have an independent Boltzmann solver from CAMB, developed in 1999, which was the most accurate at the time. The CLASS-CAMB comparison was useful both to check for possible code-induced biases in the extraction of cosmological parameters from the CMB spectrum and to improve the accuracy in both codes. At highest precision, both codes were able to reach a 0.01% accuracy for CMB observables. Nevertheless CLASS is meant to be more modern, friendly and equally if not more accurate and fast than its competitors. It is written in `C`, but has a wrapper for `python` and `C++`, so that CLASS can be imported as a class in other codes; moreover, its modular and flexible structure is easy to modify in order to introduce additional models, e.g. our non-CDM FIMP DM model. The code is also very general and versatile and can be used to compute a large number of quantities and observables.

The implementation of non-CDM relics, such as sterile neutrinos or WDM, in CLASS, is particularly easy and fast. The developers have introduced an approximate viscous fluid description inside the Hubble radius to integrate the perturbations throughout the cosmological history [69], increasing substantially the performance of the code, by more than a factor of 3. Therefore CLASS is suitable to derive bounds on FIMP models due to

its flexibility, accuracy and speed. The code requires three main input quantities, which are read through a specific function of the source module `background.c`:

- an array of cosmological parameters for the standard flat Λ CDM model. We stick to the default values obtained through the analysis of CMB temperature anisotropies by the Planck collaboration [17]. The only modification is the CDM relic density we parametrize as $\Omega_{\text{CDM}}h^2 \equiv (1 - F)\Omega_{\text{DM}}h^2$;
- an array of properties of the non-CDM sector: the number of non-CDM species, their degeneracies, their masses, the value of $\Omega_{\text{NCDM}}h^2 \equiv F\Omega_{\text{DM}}h^2$, temperature $T_\chi(T_0)$ used to define physical momenta $p = qT_\chi$, possible chemical potentials, to mention the main ones;
- the phase-space distribution $g_\chi f_\chi(q)$ as a function of comoving momentum $q = p/T_\chi$ for each species. We can provide this function in two ways: (i) we can write an analytic expression dependent on some parameters to be read from the input, replacing the default Fermi-Dirac thermal distribution appearing in the code; (ii) we can provide a two-columns $(q, g_\chi f_\chi(q))$ data file where the phase-space distribution is written discretely. In the latter case, the CLASS module will proceed to interpolate the distribution. In any case, the distribution can be even non-normalized: giving values of masses and Ω_{NCDM} to the code assures it will renormalise the $g_\chi f_\chi(q)$ in order to fulfil both conditions.

After some trial runs with thermal Bose-Einstein distribution for DM candidates of mass m_χ with same cosmological and non-CDM parameters, we reached the conclusion that introducing an analytic, parameter-dependent function in the CLASS module is better than making CLASS read and interpolate data points, both for the accuracy and the speed of the code. However, since in general, we do not have analytic expressions for our non-thermal distribution, we have to rely on a fit function to interpolate the computed discrete values of $g_\chi f_\chi(q)$. In particular we choose the general form dependent on six parameters a, b, c, d, h, n :

$$g_\chi f_\chi(q; a, b, c, d, h; n) = a \left(\frac{q^{2+b} + d}{q^2} \right) \left\{ \exp(cq + hq^2) + n \right\}^{-1} \quad a > 0, c > 0, h \geq 0. \quad (4.65)$$

The n parameter is introduced to parametrize the thermal Bose-Einstein and Fermi-Dirac thermal distributions, which are obtained by setting $b, d, h = 0$ and $n = -1, +1$, respectively. For a general non-thermal distribution the best fit is obtained setting $n = 0$ and leaving a, b, c, d, h free. With this method, for each model and species considered, we can compute the phase-space distribution numerically (in a discrete way), as we have done in the previous section, and then fit the result with this general function. This provides the values of the parameters directly to CLASS, where we coded the form in Eq. (4.65). If CLASS is provided both the mass of the non-CDM candidate m_χ and the fraction of DM to reproduce, it will normalize the distribution on its own, so the normalization parameter a does not need to be passed. Therefore we do not need to compute the normalization of the

phase-space distribution, which is time-consuming; the value of a is only relevant to know the value of the coupling (λ_3 , λ_4 or $\lambda_{2\chi}$) which, in our case involving a single operator at the time, is fixed by the choice of F . The specific values of the fit parameters depend also on the number of points N_q we exploit to discretize the phase-space distribution. One can verify that the results are robust varying the number of fit points: a good choice is to consider 50 - 100 points. To check the goodness of the fit we can introduce a sort of $\chi^{(2)}$ test, defining

$$\chi^{(2)} = \frac{1}{N_q - 5} \sum_{i=1}^{N_q} \left(\frac{(g_\chi f_\chi(q_i) - g_\chi f_\chi(q_i; a, b, c, d, h))}{g_\chi f_\chi(q_i; a, b, c, d, h)} \right)^2. \quad (4.66)$$

The fit is good if the $\chi^{(2)}$ is not much larger than 1. As a reference, we show in the following table the results of the fit for the non-thermal distribution obtained from the models we considered in the previous Section, with $F = 1$. We choose $N_q = 100$. In these simple cases, the error on the computed parameters is always below 10^{-2} %. We do not show the parameter a , which is only a normalization that is set by CLASS, eventually.

Model	$(m_{B_1}, m_{B_2}, m_{B_3}, m_\chi)$	$-b$	c	d	h	$\chi^{(2)}$
Tril.	$(10^3, 10^2, -, 10^{-2})$ GeV	0.604	0.982	-7.58×10^{-4}	5.54×10^{-9}	0.01
Tril.	$(10^3, 0, -, 10^{-5})$ GeV	0.605	0.973	-7.85×10^{-4}	8.46×10^{-10}	0.01
Quad. s.p.	$(10^3, 10^2, 0, 10^{-2})$ GeV	0.887	0.881	1.16×10^{-3}	7.86×10^{-3}	0.13
Quad. s.p.	$(10^3, 0, 0, 10^{-5})$ GeV	0.886	0.880	1.16×10^{-3}	7.81×10^{-3}	0.12
Quad. p.p.	$(10^3, 10^2, 0, 10^{-2})$ GeV	1.014	0.801	1.26×10^{-3}	1.30×10^{-3}	0.45
Quad. p.p.	$(10^3, 0, 0, 10^{-5})$ GeV	1.002	0.806	1.31×10^{-3}	1.26×10^{-2}	0.41

We show the fits in Fig. 4.8. We have also visually checked that our fit function is suitable for all the considered models and any possible choice of the mass spectrum, for $m_{B_1} \in [10^{-3}, 10^3]$ GeV, even in peculiar cases in which the spectrum is degenerate.

After reading all the input parameters and the phase-space distribution(s), CLASS proceeds automatically to compute the mass-density relation and the optimal momentum sampling to run the module which solves Boltzmann perturbation equations and computes requested output quantities. In [69] it is shown that the approximations and sampling algorithms exploited by CLASS work very well for realistic active neutrinos (with a total mass smaller than the eV), and WDM candidates, becoming non-relativistic during radiation domination $m > \text{few keV}$. In between these two limits, however, there is a range in which the accuracy of the fluid approximation is not well tested, and in which one might turn off this approximation at expense of the speed of the code.

4.3.2 WDM and Lyman- α bounds

We are interested in comparing linear matter power spectra obtained from our FIMP phase-space distributions with spectra denoting observational limits on WDM from structure formation. The strongest constraints come from the Lyman- α forest, which probes structure

formation at medium and small scales. It is an absorption feature in the observed spectra of light from distant background sources scattered on the neutral hydrogen atoms in the intergalactic medium (IGM). Along the observer's line of sight, the low-density IGM at high redshift shows a filamentary structure on small-medium scales, which is traced by the Lyman- α lines. The observable is the flux power spectrum, which can be computed from models exploiting a suitable hydrodynamical simulation and then compared to data in a Markov Chain Monte Carlo (MCMC). The results of this procedure are extremely useful and can put tight constraints on small scale properties of dark matter.

However, this procedure is complicated and time-consuming, because, in principle, each DM model would require a hydrodynamical simulation and a MCMC fit to flux data. To help the theoretical community in putting bounds on their models, the Lyman- α constraints are reported in terms of the equivalent mass of thermal relic WDM particles, in particular, a model in which all the DM is made of WDM ($F = 1$): in [56], depending on the assumptions and exploited datasets, the tightest bound is $m_{\text{WDM}} > 5.3$ keV and a milder one is $m_{\text{WDM}} > 3.5$ keV. This allows taking the power spectra $P_{\text{WDM}}(k)$ computed in these models as references of the Lyman- α bounds. So one can directly compare them with the power spectra obtained from any other model one may consider. This procedure is much simpler and faster than reanalysing all the Lyman- α data with each model and it is enough accurate to put constraints on those models. In these work, the models will be characterized by a different Lagrangian, mass spectrum and FIMP DM fraction F . For any choice of these quantities, the obtained power spectra from CLASS must never show features different from the WDM limit spectra, as we have described in Section 3.1. For each bound (the conservative for $m_{\text{WDM}} = 3.5$ keV and the stronger $m_{\text{WDM}} = 5.3$ keV), to be completely allowed by structure formation, our models' power spectra must have a higher cutoff scale (the half mode $k_{1/2}$) and a transfer function that never goes below the limit one for any $k < k_{1/2}$. If none of these criteria is satisfied the model is rejected, while if only one of the two is satisfied, we have tension with Lyman- α . To sum up, we will apply these two criteria to our two limit WDM models for complete and safe constraints for our models.

We conclude defining the properties of a WDM model, which will incorporate the Lyman- α constraints. Thermal WDM particles are, by definition, thermally distributed fermions, i.e. characterized by the phase-space distribution

$$g_{\text{WDM}} f_{\text{WDM}}(q) = \frac{2}{e^q + 1}. \quad (4.67)$$

Being thermal relics, they can be fully characterized by their mass and the decoupling temperature, in analogy with the case of active neutrino HDM. Therefore the relic density is parametrized by mass and temperature normalized to the ones from neutrinos

$$\Omega_{\text{WDM}} h^2 = F \left(\frac{m_{\text{WDM}}}{93.14 \text{ eV}} \right) \left(\frac{T_{\text{WDM}}(t_0)/T_0}{T_\nu(t_0)/T_0} \right)^3. \quad (4.68)$$

For neutrinos the value implemented in CLASS is $T_\nu(t_0)/T_0 = 0.71611$ [68, 69], which is slightly larger than the instantaneous decoupling value $(4/11)^{1/3}$ as predicted by precise studies of active neutrino decoupling [70]. Once one requires WDM to reproduce a given fraction F of the DM relic density, $T_{\text{WDM}}(t_0)/T_0$ is fixed for every value of the mass m_{WDM} , which is indeed the only free parameter of the model. As a reference, the temperature for $F = 1$ and $m_{\text{WDM}} = 5.3$ keV is

$$\frac{T_{\text{WDM}}(t_0)}{T_0} = \left(\frac{5.3 \text{ keV}}{m_{\text{WDM}}} \right)^{1/3} F^{1/3} = 0.09. \quad (4.69)$$

Such a low temperature is associated with significant entropy production. If we apply the conservation of entropy,

$$\frac{T_{\text{WDM}}(t_0)}{T_0} = \left(\frac{g_{*s}(T_0)}{g_{*s}(T_{\text{WDM}}^{\text{dec}})} \right)^{1/3}, \quad (4.70)$$

we find out that $g_{*s}(T_{\text{WDM}}^{\text{dec}}) \simeq 5000$, which is much higher than the maximum number of effective degrees of freedom obtained from the SM.

The Lyman- α bounds from [56] are implemented in CLASS computing the power spectrum for a WDM candidate of mass between 3.5 and 5.3 keV, with temperature fixed by the choice $F = 1$. We use Eq. (4.65) with $(a, b, c, d, h, n) = (2, 0, 1, 0, 0, 1)$. Then we compute the transfer function $\mathcal{T}_{\text{lim}}^2(k) = P_{\text{WDM}}(k)/P_{\text{CDM}}(k)$ and compare it to the one obtained from our models, $\mathcal{T}^2(k)$. In Fig. 4.9 we show the outcome of CLASS for the two WDM Lyman- α bounds and our FIMP candidate of mass 10 keV in the trilinear and two quadrilinear models. We see that the models are in tension with the Lyman- α bounds: they are barely in agreement with the conservative bound for $m_{\text{WDM}} = 3.5$ keV but are not with the stringent one of $m_{\text{WDM}} = 5.3$ keV. This motivates a careful and systematic study of the constraint we can derive from structure formation on our toy models. We will carry on the analysis and show its results in the next chapter, exploiting different criteria to test the robustness of the evinced bounds.

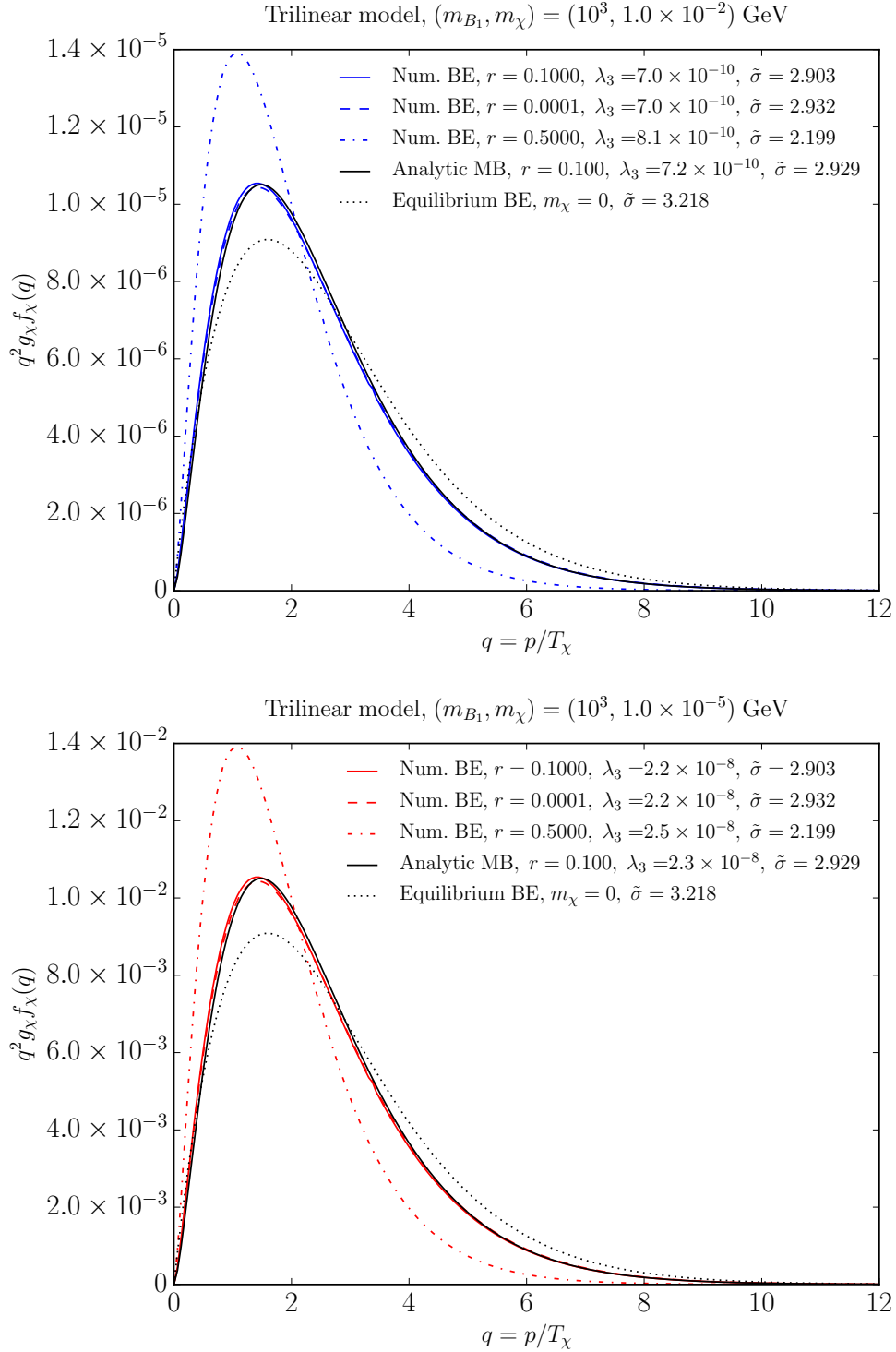


Figure 4.1: Phase-space distributions for different mass spectra in the trilinear model, where the only DM production mechanism is given by two-body decays. We focus on two cases, $m_\chi = 10$ MeV (upper plot) and $m_\chi = 10$ keV (lower plot) and for each case we vary $r = m_{B_2}/m_{B_1}$. We also show the analytic approximation obtained under the assumptions listed in the main text and the equilibrium thermal distribution. Furthermore, we compute the coupling λ_3 necessary to reproduce the observed relic density and the dispersion $\tilde{\sigma}$.

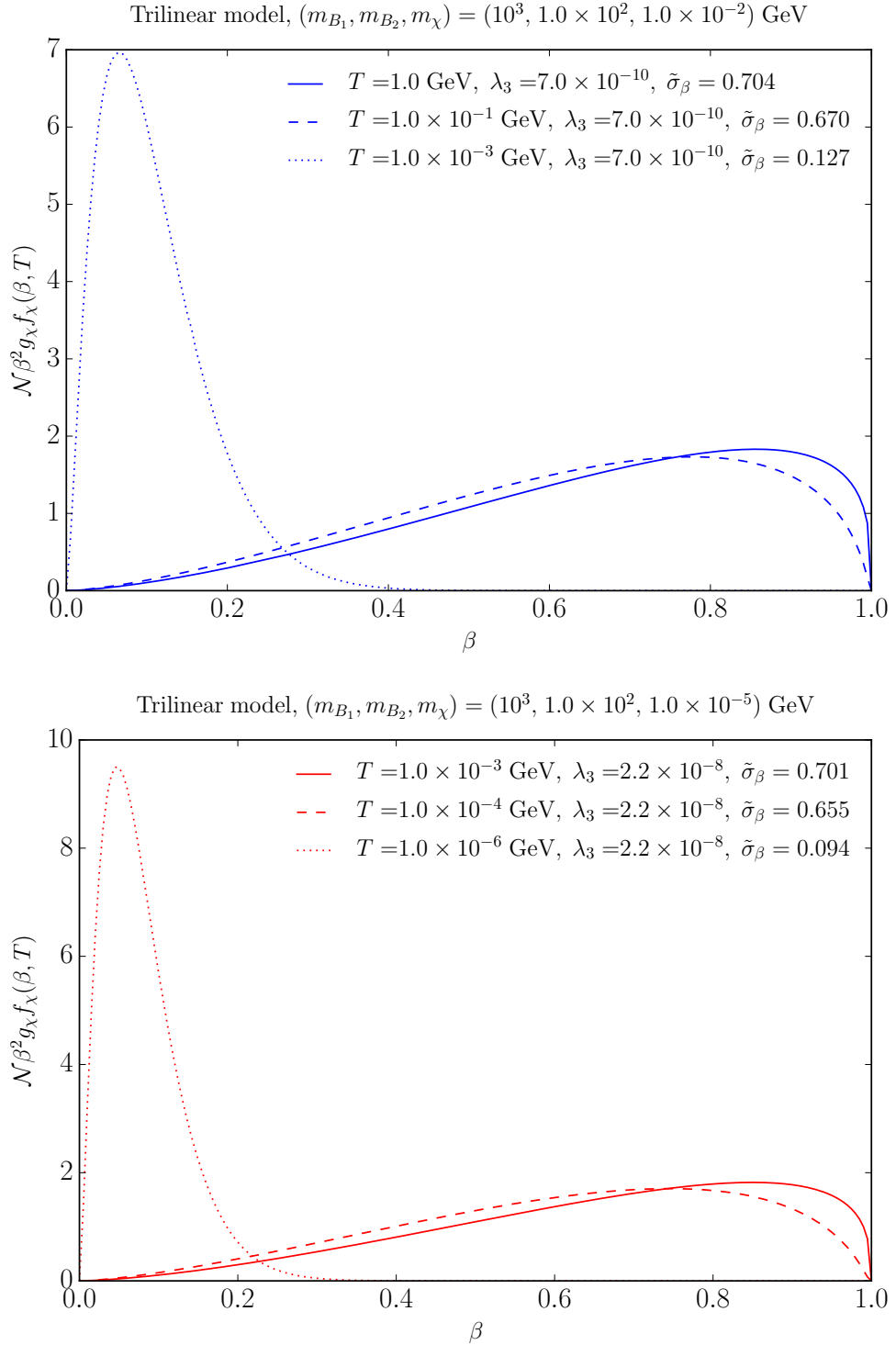


Figure 4.2: Velocity distributions for different mass spectra in the trilinear model, where the only DM production mechanism is given by two-body decays. We look at the distribution at three reference temperatures, to observe the transition from relativistic to non-relativistic DM.

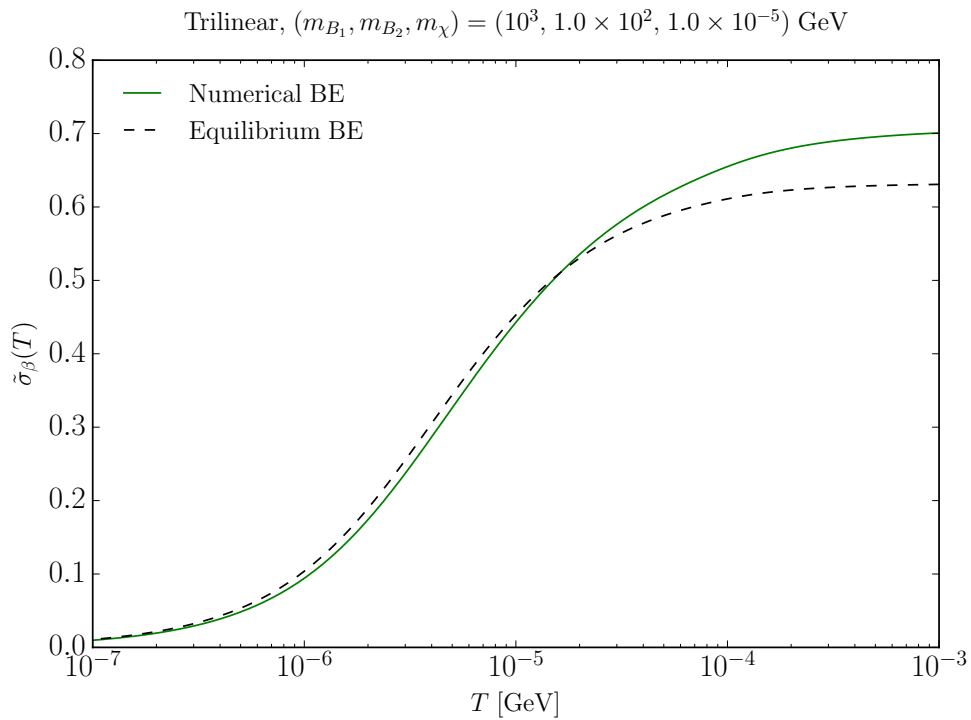


Figure 4.3: The evolution of the velocity dispersion (solid) for the trilinear model with $(m_{B_1}, m_{B_2}, m_\chi) = (1 \text{ TeV}, 10^2 \text{ GeV}, 10 \text{ keV})$ in the temperature range 1 MeV - 0.1 keV, compared to the equilibrium one (dashed).

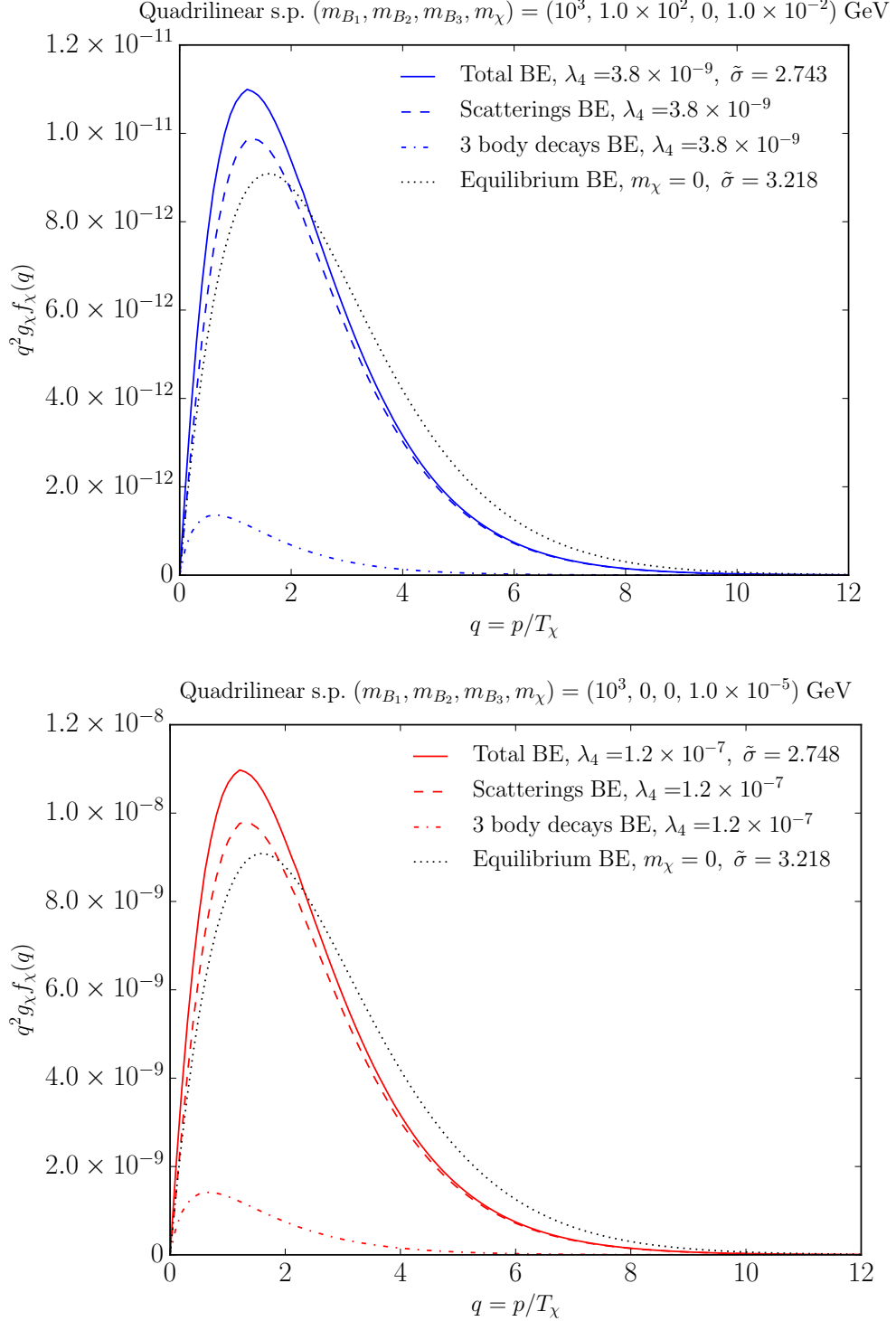


Figure 4.4: Phase-space distributions for different mass spectra in the quadrilinear model for single production, where both scatterings and three-body decays contribute to the DM production. We focus on two cases, $(m_{B_1}, m_{B_2}, m_{B_3}, m_\chi) = (1 \text{ TeV}, 100 \text{ GeV}, 0, 10 \text{ MeV})$ (upper plot) and $(m_{B_1}, m_{B_2}, m_{B_3}, m_\chi) = (1 \text{ TeV}, 0, 0, 10 \text{ keV})$ (lower plot). We plot separately the contribution from scatterings and the one from three-body decays together with the sum of the two. We also show the equilibrium thermal distribution and compute the coupling λ_4 necessary to reproduce the observed relic density, together with the computed dispersion $\tilde{\sigma}$ for the distribution.

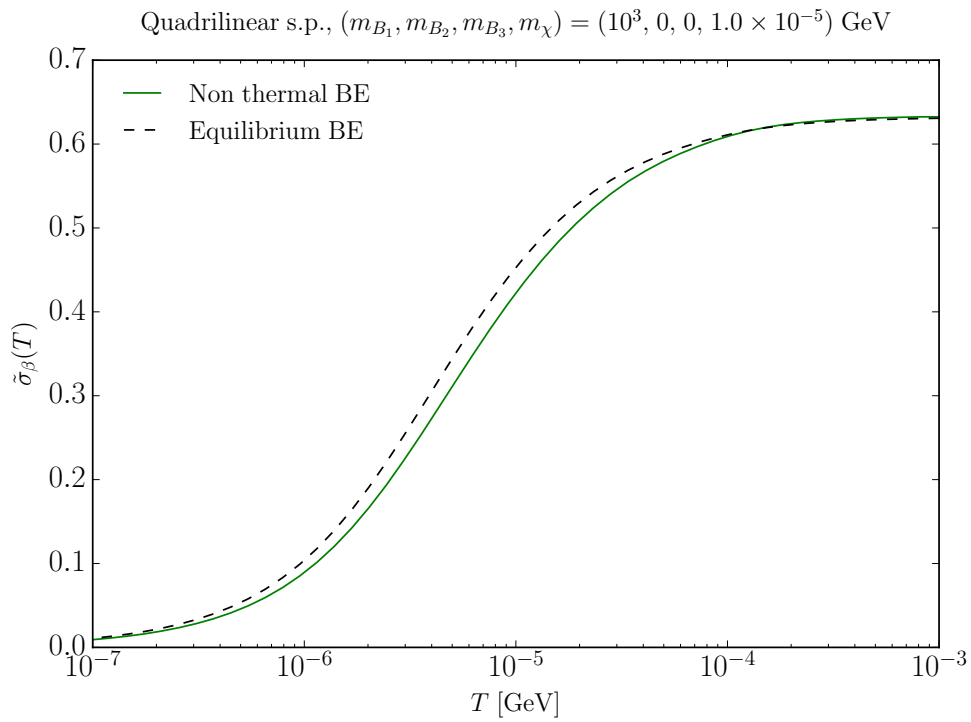


Figure 4.5: The evolution of the velocity dispersion (solid) for the quadrilinear model for single production with $(m_{B_1}, m_{B_2}, m_{B_3}, m_\chi) = (1 \text{ TeV}, 0, 0, 10 \text{ keV})$ in the temperature range 1 MeV - 0.1 keV, compared to the equilibrium one (dashed).

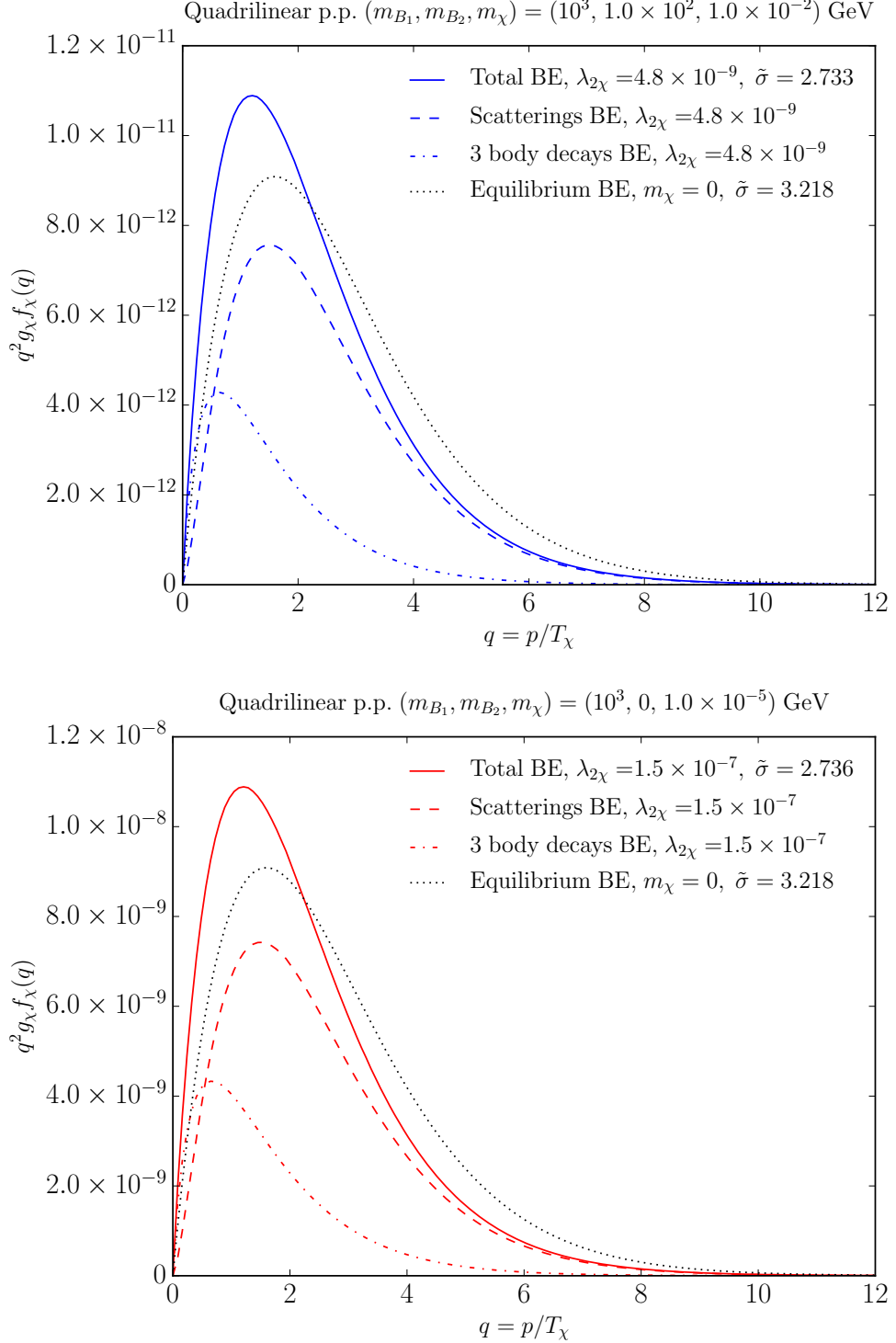


Figure 4.6: Phase-space distributions for different mass spectra in the quadrilinear model for pair production, where both scatterings and three-body decays contribute to the DM production. We focus on two cases, $(m_{B_1}, m_{B_2}, m_\chi) = (1 \text{ TeV}, 100 \text{ GeV}, 10 \text{ MeV})$ (upper plot) and $(m_{B_1}, m_{B_2}, m_\chi) = (1 \text{ TeV}, 0, 10 \text{ keV})$ (lower plot). We plot separately the contribution from scatterings and the one from three-body decays together with the sum of the two. We also show the equilibrium thermal distribution and compute the coupling $\lambda_{2\chi}$ necessary to reproduce the observed relic density, together with the computed dispersion $\tilde{\sigma}$ for the distribution.

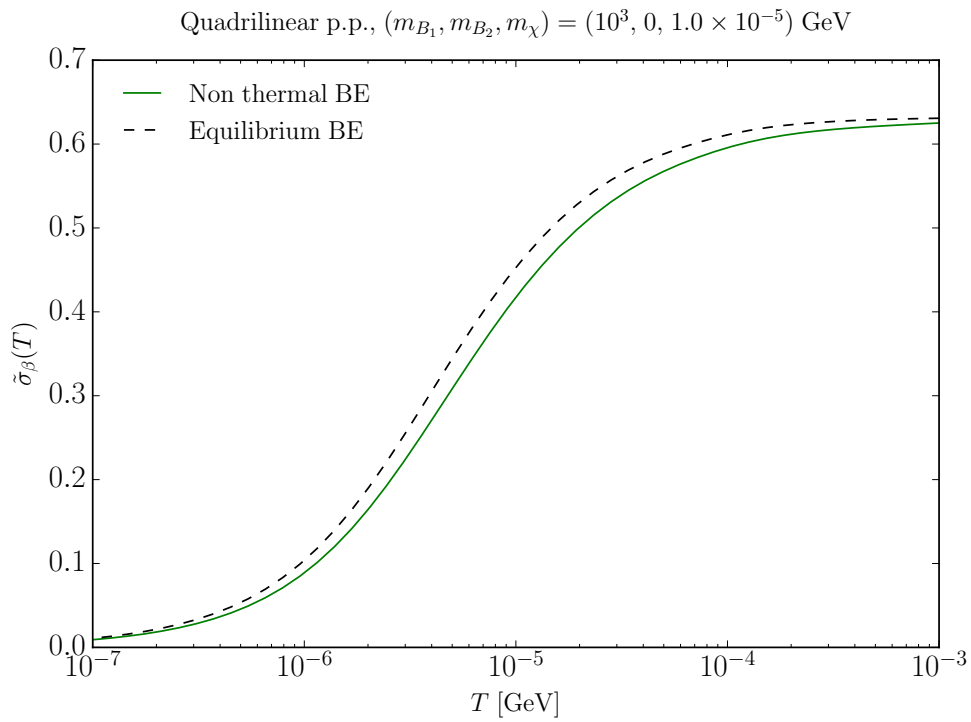


Figure 4.7: The evolution of the velocity dispersion (solid) for the quadrilinear model for pair production with $(m_{B_1}, m_{B_2}, m_\chi) = (1 \text{ TeV}, 0, 10 \text{ keV})$ in the temperature range 1 MeV - 0.1 keV, compared to the equilibrium one (dashed).

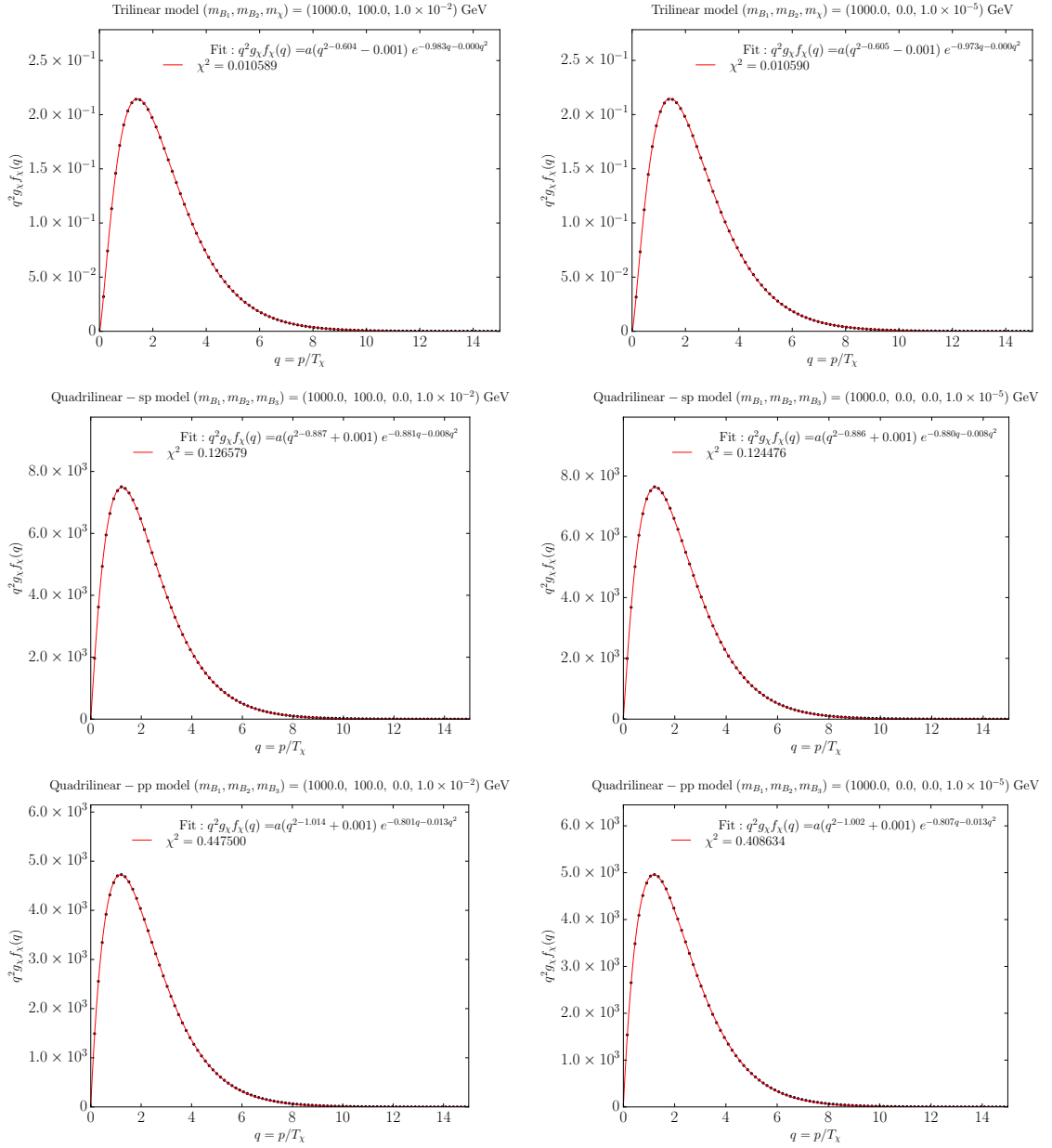


Figure 4.8: The fits of the phase space distributions $q^2 g_\chi f_\chi$ for the cases shown in the above table.

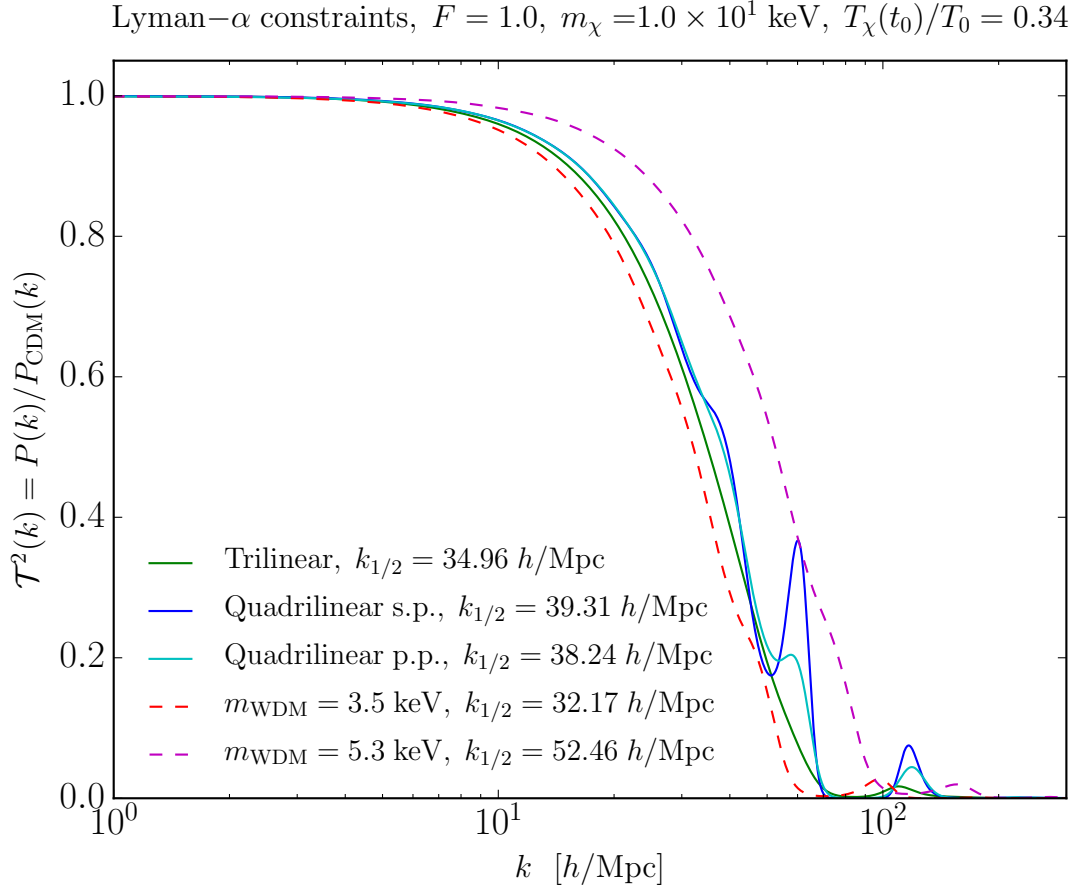


Figure 4.9: The transfer function between power spectra computed from various models (FIMP trilinear, FIMP quadrilinear for the single production and pair production, WDM with different masses) and the standard CDM linear matter power spectrum. We also show the value of the mode where $\mathcal{T}^2 = 1/2$. We have used $F = 1$ and the above-mentioned fit values for models with $m_\chi = 10$ keV.

Chapter 5

Constraints on FIMP parameters: results

In this chapter, we apply the methodology developed so far to constrain the free parameters of the scalar FIMP toy models we have considered throughout our work. The procedure has been implemented in a `python` code which is used to extract all the cosmological consequences of the considered FIMP model and to set constraints, based on structure formation, on its parameters. In the first part of the chapter we present the structure of the code and the implementation of the methodology explained in the previous chapter. Then, we show the outcome of the analysis and comment on the results.

5.1 Our code

We perform our calculations exploiting a `python3.5` code. This language is particularly suitable for our needs, since it includes various libraries for fast and reliable evaluation of integrals – such as the `scipy.integrate` module, containing the `quad` function which uses a technique from the `fortran` library `QUADPACK` – as well as for parallelization of the computation on multi-CPU machines and powerful visualization tools. In particular, we can use `CLASS` inside our code simply importing the `Class` class from the `classy` module. We have exploited the latest version of `CLASS` in its original form, apart from the introduction of the analytic form of the phase-space distribution $g_\chi f_\chi(q)$ written in Eq. (4.65). It is implemented in the `CLASS` `background_ncdm_distribution` function inside the `background.c` module as

```
double A0=param[0];    #a
double A1=param[1];    #b
double A2=param[2];    #c
double A3=param[3];    #d
double A4=param[4];    #h
double A5=param[5];    #n
```

```
*f0 = A0*(pow(q,2+A1)+A3)*pow(exp(A2*q+A4*q*q)+A5,-1)/q/q; #gXfX(q)
```

We have written the code in a way that it can be easily generalized for any other model. While presenting its structure, we shall remark where the code can be improved to include more general scenarios.

5.1.1 Structure

The code is structured in three sections.

1. **Cosmology.** The first includes the definition of thermodynamical quantities and the cosmological history during DM production: according to the formulae given in Appendix A.2.2, we introduce the number of effective degrees of freedom $g_{\star\rho}(T)$ and $g_{\star s}(T)$ with the functions `gstar(T)` and the log derivative of $g_{\star s}$ with `dloggstslogx(T)`. The cosmological history during FIMP production is parametrized by the Hubble parameter function `H(T)`: we have exploited the standard formula for a radiation-dominated era, but it can be modified to include other scenarios. All these quantities are used throughout the code, e.g. to define the reference temperature T_χ , i.e. `TX(T,TFI)`.
2. **Kinematics.** The second section includes the definition of all functions useful to compute the phase-space distribution of the FIMP candidate through the Boltzmann equation, following the procedure we have seen in the previous chapter. We define the squared amplitudes $|\mathcal{M}|^2$ (averaged over both initial and final degrees of freedom) of the process allowed in the range of operators considered in the model Lagrangian. The general squared amplitude is a function of the Mandelstam variables s and t , of the mass spectrum of the theory and the coupling of the operator. One can consider other cases simply including them as an `if` statement in the `amplitude_sq` function and add that condition in the subsequent functions. Next, we define the functions relevant for the kinematics of the considered processes (two-body decays, two-two scatterings and three-body decays), i.e. momenta in the centre-of-mass frame and maximum and minimum energy available for certain particles as functions of the mass spectrum, Mandelstam variables and the FIMP momentum p . Then we compute collision terms $g_\chi C/E_\chi$ in the function `gXCXEX` and integrate them in the function `q2gXfX`. This function is called a number `Nq` of times by another one, `phase_space_q`, to compute the phase-space distribution for a discrete array of values of q ; finally, the discrete distribution is fit with Eq. (4.65) with $n = 0$ and `phase_space_q` returns the values of the parameters. The function also includes the possibility to plot the phase-space distribution and check the goodness of the fit.
3. **Routine.** The third section is the core of the code containing the routine to obtain bounds from structure formation. After the acquisition of input parameters, the code calls `CLASS` to compute the power spectrum for the standard Λ CDM model with cosmological parameters from the Planck satellite [17] and the power spectra for the two WDM models considered, for $m_{\text{WDM}} = 3.5$ keV and $m_{\text{WDM}} = 5.3$ keV.

to see whether our model satisfies (`return 1`) or not (`return 0`) the two criteria for the two Lyman- α constraints. We give to each criterion a score describing the difficulty in satisfying it and how much it is robust: scores of 1 and 2 are given for the half-modes criteria, respectively for $m_{\text{WDM}} = 3.5$ keV and 5.3 keV, while scores of 4 and 8 are given to the $\mathcal{T}_{\text{lim}}^2$ criteria. As we shall see, this choice allows us to take the sum of the scores as a level of confidence, on a scale from 0 to 15, that the Lyman- α bounds are satisfied. At the same time, from the value of the sum, we can tell which criteria have been satisfied, since each number between 1 and 15 can be written uniquely as a sum of two or more powers of 2. For example, if the sum is 12, we know that the point in the grid satisfies only the two $\mathcal{T}_{\text{lim}}^2$ criteria and not the half mode ones, while a total score of 5 flags that only the $m_{\text{WDM}} = 3.5$ keV criteria (both half-mode and transfer function) are satisfied. The criteria exploited and their scores are summarized in the following table:

Lyman- α bound	m_{WDM} [keV]	$k_{1/2}$ criterion score	$\mathcal{T}_{\text{lim}}^2$ criterion score
conservative	3.5 keV	1	4
stringent	5.3 keV	2	8

iv) The code prints the output and the routine goes on.

5.1.2 Input

The code needs a fair number of input parameters to run; if a parameter is not given, its default value will be considered. We can divide the parameters in three groups: physical, discretization and execution parameters. The last group includes parameters which control the output, visualization or execution of tests and we do not treat them here, since they are explained in the code itself.

- **Physical parameters.** This set consists of parameters that characterize the model we are treating, apart from the ones we are keeping free in order to constrain them. For example, if we consider the FIMP particle mass `mX` and FIMP DM fraction `FF` as free parameters, the set of physical input parameters includes the mass spectrum `m1,r2,(r3)`, i.e. m_{B_1} , m_{B_2}/m_{B_1} , (m_{B_3}/m_{B_1}) and the operator considered (e.g. "trilinear", "quadrilinear-sp", "quadrilinear-pp"), together with the statistics of the particles involved ("MB", "BE", "FD"). In a more general case, instead, we can treat each of the entry of the mass spectrum as a free parameter, varying over some interval we want to constrain.
- **Discretization parameters.** This set of parameters determines the resolution of our computations and directly affects the execution time of the code. Let us see them one by one.

1. `N_q`. The first important parameter is the number of values of the dimensionless

comoving momentum we exploit to fit the phase-space distribution. The default value is 50: for this choice, the code takes about 0.02 seconds of CPU time to compute the points.

2. `N_mB1, N_mB2, N_mB3, N_mX, N_F`... These parameters set the number of points along each axis of the grid over which the routine is performed and set the resolution on the DM fraction, the FIMP mass etc. The total number of iterations will be given by the product of these numbers. In the simplest case the grid will be made of `N_F*N_mX`. To give an idea, a `40*40` grid will take about 33 CPU hours to be computed.
3. The boundaries of the free parameters. The to-be-discretized region of parameter space must have finite and clear boundaries. In the simplest case in which the routine is over the DM fraction and the FIMP particle mass, we vary `FF` between 0.1 and 1, and `mX` between 1 and 100 keV.
4. `maxk`. This value is the mode in units of $h\text{Mpc}^{-1}$ up to which the power spectra are computed by CLASS. ΛWDM and ΛFIMP DM models are characterized by a small-scale power suppression with respect to a ΛCDM model. For example, the half modes for WDM models with $m_{\text{WDM}} = 3.5$ keV and 5.3 keV are $k_{1/2} \simeq 32$ $h\text{Mpc}^{-1}$ and 52 $h\text{Mpc}^{-1}$, respectively. Therefore `maxk` should be much higher than these values to allow for a precise evaluation of the transfer function at those small scales. Increasing `maxk` slows down the code since the computation of the observables by CLASS is more expensive. A good compromise for our purposes is to take `maxk=1e3`. Therefore the values of $k_{1/2}$ will be capped at 1000 $h\text{Mpc}^{-1}$.

5.1.3 Output

The output of the code is a text file `.dat` containing all the relevant information to produce plots illustrating the bounds on the free parameters. For reference, at the beginning of the file one finds the values of the input parameters exploited in the computation. Then a table of the following form is shown

```
#(fixed & free params) T2kmax kh_Ly1 kh_Ly2 khalf (criteria) (diagnostics)
```

The columns `(fixed & free params)` include all the physical parameters defining the model at the specific iteration. The column `T2kmax` is for diagnostic purposes: this value has to be as close to 1 as possible – usually less than 1.001 for the point to be considered in the analysis. Otherwise, it is rejected, meaning that the criteria outputs are all read as 0. The columns `kh_Ly1, kh_Ly2, khalf` include the results for the half-mode in the two WDM models considered and the FIMP one, respectively. The columns `(criteria)` show the results of the four criteria outputs to determine if the model agrees with the Lyman- α bounds. Finally, the last columns show diagnostics outputs. For example, in the simplest case in which we only let the DM mass and the DM fraction vary, we have something like

```
#(fixed params) mX[eV]  F      T2kmax  kh_Ly1  kh_Ly2  khalf  criteria (diagn.)
( . . . )          8.377e+03  0.663  1.0001  32.17   52.29   39.50   1 0 4 0  ( . . . )
```

5.2 Constraints on m_χ

We focus our analysis on the determination of the bounds on the allowed values of the FIMP DM mass m_χ for the three considered toy models, depending on the free parameters: the values of the involved masses m_{B_1} , m_{B_2} (and m_{B_3} for the quadrilinear for single production model) and the fraction F of the observed relic density one wants to reproduce. We know light FIMP models are constrained by Lyman- α bounds, similarly to thermal WDM models. Therefore, in practice, we want to answer the following question: “given a mass spectrum and the fraction of relic density to reproduce, what is the *minimum* value of the mass m_χ that puts the model in agreement with Lyman- α constraints?” As we shall see, the answer is not straightforward and may depend also on the criteria exploited to impose the bounds from structure formation. Let us consider each operator independently.

5.2.1 Trilinear model

We can split the analysis of the parameter space of the trilinear model in two parts. In the first part, we fix all the masses involved in the model apart from m_χ , i.e. we choose m_{B_1} and m_{B_2} and we let F vary from a minimum value to 1. We want to find, for each value of F , which is the minimum m_χ allowed by the structure formation and show the constraints in the (m_χ, F) plane. In the second part we can fix a required relic density F and explore the mass parameter space (m_{B_1}, m_{B_2}) (or better (m_{B_1}, r_{B_2})), to always take into account the kinematical constraint $m_{B_1} > m_{B_2} + m_\chi$) and eventually find the minimum allowed DM mass for each point in this plane.

The (m_χ, F) plane

To perform the first analysis, we fix $m_{B_1} = 1$ TeV and $m_{B_2} = 0$ and we let m_χ vary in the interval $[1, 100]$ keV, while F in the interval $[F_{\min}, 1]$. Naively, we expect that at $F = 1$ the strongest constraints apply on m_χ , while, below a certain fraction F_{free} , all the considered values m_χ are allowed. So we are interested in the shape of the constraint in the (m_χ, F) plane and in the value of F_{free} . We exploited our code to compute a 42×42 grid in the (m_χ, F) plane in the region $[1, 100]$ keV \times $[F_{\min}, 1]$, choosing $F_{\min} = 0.1$. As presented in the previous section, the code’s crucial output is the result of the four criteria exploited to see whether the model agrees with the stringent $m_{\text{WDM}} = 5.3$ keV and the conservative $m_{\text{WDM}} = 3.5$ keV Lyman- α bounds. We have the so-called $k_{1/2}$ criteria which, if passed, output 1 and 2, and the so-called $\mathcal{T}_{\text{lim}}^2$ criteria which, if passed, output 4 and 8 for the conservative and stringent bounds, respectively. When a test is not passed, the output in the respective column is 0. In Fig. 5.1 we show separately the output of the $k_{1/2}$ criteria and $\mathcal{T}_{\text{lim}}^2$ criteria separately. In each plot, we have three different regions: a dark

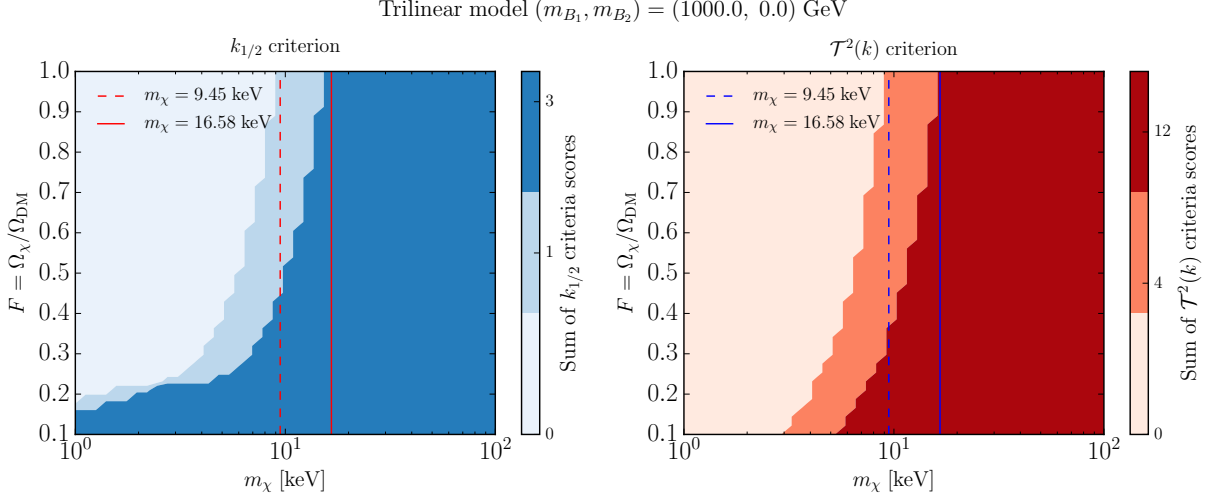


Figure 5.1: Plot of the results of the $k_{1/2}$ criteria (left) and $\mathcal{T}_{\text{lim}}^2$ criteria (right) scores in the (m_χ, F) plane with $F_{\text{min}} = 0.1$ in the trilinear model, where FIMPs are produced via two-body decays. The vertical lines show the value of the minimum m_χ allowed by the stringent (solid) and conservative (dashed) bounds at $F = 1$.

region where both the stringent and the conservative bounds are satisfied, a lighter region in which only the conservative bound is satisfied and a blank region where no bounds are satisfied. In practice the three regions can be labelled as *allowed*, *in tension*, *excluded*. We notice that for $F > 0.3$ the $k_{1/2}$ and $\mathcal{T}_{\text{lim}}^2$ criteria agree, while for $F < 0.3$ their behaviour is different. In particular the $\mathcal{T}_{\text{lim}}^2$ criteria are more stringent: while the $k_{1/2}$ are always satisfied for $F \lesssim 0.15$, the $\mathcal{T}_{\text{lim}}^2$ criteria still give a minimum mass m_χ up to $F = 0.1$ and below. This is because at such low values of F the effect of FIMP DM in the matter power spectrum is to introduce a different shape producing a slight suppression of power at scales larger than the cutoff. From the analysis, we evince that all the criteria agree that, for a FIMP candidate produced by decays of a 1 TeV particle in a massless one, and DM reproducing all the observed relic density, the conservative and stringent bounds on the minimum mass are 9.45 keV and 16.58 keV.

We can see the bounds in the (m_χ, F) plane in a comprehensive way considering, for each point, the sum of all the criteria scores. The values 1, 2, 4 and 8 for the criteria are chosen so that the sum of all criteria gives a total score which represents a degree of confidence that the model respects the bounds, but also such that one can evince uniquely which tests were passed. In Fig. 5.2 we show the resulting plot. The colour palette is chosen to resemble a traffic light, to tell whether a point in parameter space is allowed or not. We see six regions, coloured in different ways:

1. Dark red region, score 0: none of the criteria is satisfied so this region of parameter space is excluded by Lyman- α data.
2. Light red region, score 1: only the conservative $k_{1/2}$ criterion is satisfied, so this

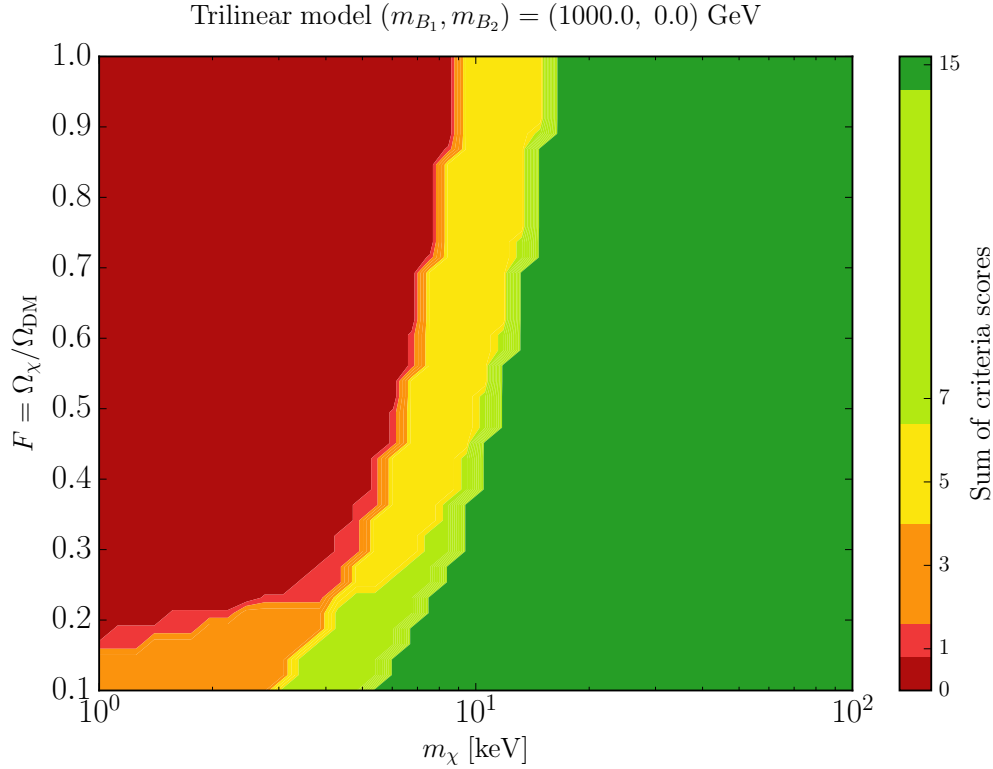


Figure 5.2: Plot of the sum of the resulting scores of the four criteria exploited to determine the allowed region in the (m_χ, F) space in the trilinear model, where FIMPs are produced via two-body decays. The use of colours is described in the text.

region is practically excluded.

3. Orange region, score 3: only the two $k_{1/2}$ criteria are satisfied, hence this region is in tension with structure formation.
4. Yellow region, score 5: only the two conservative criteria are satisfied, hence this region is in tension with structure formation, but for a different reason than the previous one.
5. Light green region, score 7: the criteria are all satisfied apart from the stringent $\mathcal{T}_{\text{lim}}^2$ one, hence this region can be considered nearly allowed by Lyman- α bounds.
6. Dark green region, score 15: all the criteria are satisfied, so the region of parameter space is fully allowed by structure formation.

We notice that, as mentioned above, the fact that $\mathcal{T}_{\text{lim}}^2$ are not satisfied for any value of m_χ for the lowest values of F , forbids the allowed dark green region to extend over the full extent of the m_χ axis, even when the contribution of FIMPs to DM is less than 20%. Therefore we are not able to tell the value of F_{free} from this set of data. To find

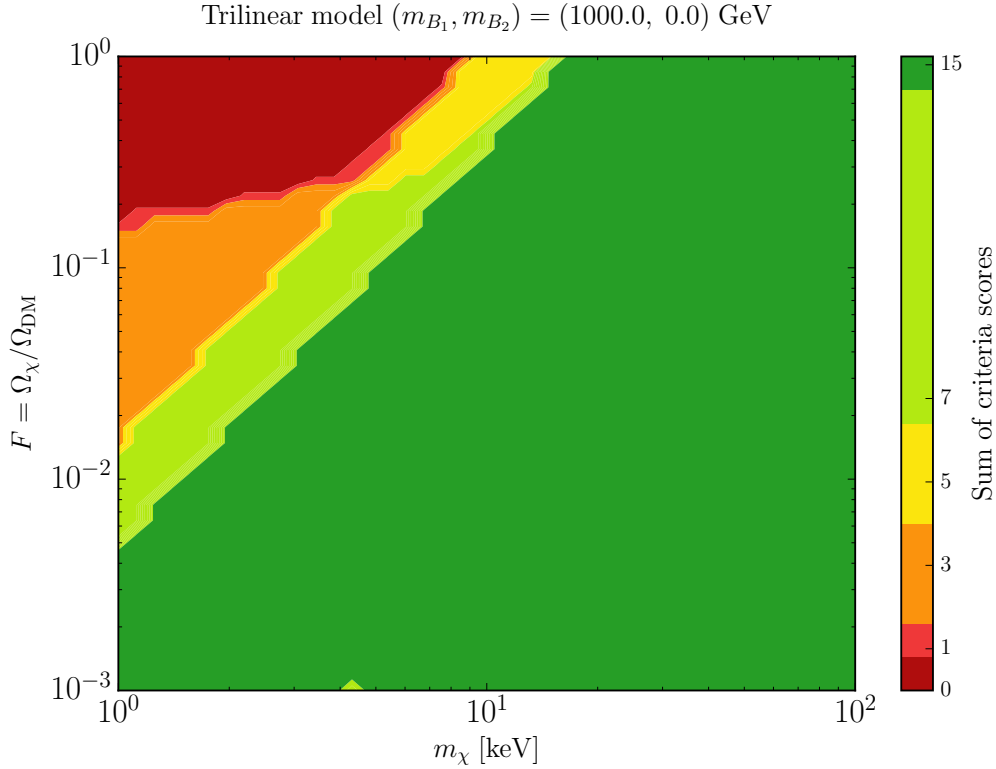


Figure 5.3: Plot of the sum of the resulting scores of the four criteria exploited to determine the allowed region in the (m_χ, F) space in the trilinear model, where FIMPs are produced via two-body decays. In this case we span the parameter space $[1, 100] \text{ keV} \times [0.001, 1]$ and exploit a log scale on the F axis. The light green point in the bottom part of the plot is just a numerical artefact.

it, we repeated the analysis for the same choices of masses but with $F_{\min} = 0.001$ and logarithmically spaced values of F . In Fig. 5.3, we show the plot representing the sum of the criteria scores in the (m_χ, F) plane in this case. We clearly evince that for this mass spectrum $F_{\text{free}} \simeq 4 \times 10^{-3}$: below this value, the structure formation do not constrain m_χ effectively.

The (m_{B_1}, r_{B_2}) plane

The analysis we performed above can be repeated for any choice of m_{B_1} and $r_{B_2} \equiv m_{B_2}/m_{B_1}$ to extract the minimum m_χ allowed by structure formation, according to one or more criteria among those considered. To span the (m_{B_1}, r_{B_2}) plane effectively we can consider only a fixed value of F , e.g. $F = 1$, since it gives the strongest constraint. Therefore we can obtain, for each point in the (m_{B_1}, r_{B_2}) plane, a value of m_χ^{\min} . For the analysis to be effective we have to discretize the parameter space $(m_{B_1}, r_{B_2}, m_\chi)$ in a proper way, in particular we need the m_χ grid to be dense enough to find the minimum precisely. A good compromise is to consider a grid of $20 \times 10 \times 40$ points in the $[10^{-3}, 10^3]$

GeV $\times [0, 0.7] \times [1, 50]$ keV region of the $(m_{B_1}, r_{B_2}, m_\chi)$ parameter space. We shrink the range of m_χ since we are looking for a minimum mass and we expect it around 10 keV and always less than 50 keV. In this way we can obtain a denser grid in the region of interest and more accurate estimates. The degeneracy parameter r_{B_2} was chosen in the range $[0, 0.7]$ to avoid computational issues if the relation $m_{B_1} > m_{B_2} + m_\chi$ is not clearly satisfied. The worst case is when m_χ is maximum (100 keV) and m_{B_1} is minimum (1 MeV): this implies $r_{B_2} \leq 0.9$. The choice of 0.9 as an upper limit protects us from issues in precision calculations and is reasonable, since a highly degenerate mass spectrum is unlikely.

To compute the minimum mass m_χ for each choice of the other masses we can exploit different combinations of criteria. In Fig. 5.4 we show the contour plots of the minimum DM mass m_χ at $F = 1$, extracted with the method presented treating the (m_χ, F) plane, for each point in the (m_{B_1}, r_{B_2}) one. In the left plot we required the $k_{1/2}$ criteria to be both satisfied (the orange, yellow and green regions in the traffic light plot), while in the right plots we required all the criteria to be satisfied (the dark green region only).

The contour levels obtained with the two criteria are very similar, a sign that both criteria can give a robust estimate of m_χ^{\min} : quantitatively the relative difference of the matrices plotted is exactly zero, except for $< 5\%$ of the points where we have a discrepancy less than 10%. However, while in the upper left plot we have a value of m_χ^{\min} for each point in the (m_{B_1}, r_{B_2}) plane¹, in the upper right one we have some holes with rhomboidal shape due to the discrete tessellation of parameter space. In these points the request that all the four tests are passed is never satisfied for any considered value of m_χ^{\min} : this is probably due to numerical artefacts in the computation of the model power spectra that make the $\mathcal{T}_{\text{lim}}^2$ criteria impossible to be satisfied, rather than to a physical reason. Since all the surrounding points do satisfy those criteria with a reasonable value of the mass, we decided to mask these points not to spoil the other nearby contours. Analysing the diagnostics of these data we see that the maximum difference for $k < k_{1/2}$, $\mathcal{T}_{\text{lim}}^2 - \mathcal{T}^2$, which, if positive, leaves the criterion unsatisfied, is quite small, usually below 10^{-3} . Therefore we have checked whether the holes could be removed simply introducing a tolerance in the $\mathcal{T}_{\text{lim}}^2$ criterion, relaxing it a bit, in a way that the value of m_χ^{\min} obtained in these points agrees with the surrounding ones and hopefully similar to the one obtained with the $k_{1/2}$ criterion. Indeed we get a reasonable result with a 1% tolerance, as it is shown in the lower plots of Fig. 5.4. When the tolerance has applied the matrices obtained with the two criteria have zero relative difference.

As a comprehensive and final result, we consider the array of m_χ^{\min} obtained requiring all criteria to be satisfied with the 1% tolerance on the $\mathcal{T}_{\text{lim}}^2$ criteria, i.e. the lower right plot in Fig. 5.4. We show this plot alone (coloured contours) in Fig. 5.5 and compare it to contours (dashed) obtained using the technique presented in [58]. The overall behaviour of m_χ^{\min} evinced from Fig. 5.5 is reasonable. We have a clear difference in m_χ^{\min} if the decaying particle has a mass smaller or greater than the GeV. In particular heavier decaying

¹At least we have an interpolated value: remember that the parameter space is discretized with a grid made of 200 points.

particles imply lower minimum FIMP DM masses, thus less stringent bounds. This is because m_{B_1} is also roughly the value of the temperature at which the freeze-in occurs and FIMP DM is produced. Therefore the dependence of m_χ^{\min} on m_{B_1} is roughly given by the relation in Eq. (2.20) and is due to the changing in the effective number of relativistic degrees of freedom. Instead, the dependence of m_χ^{\min} on r_{B_2} can be taken into account through the value of the warmness quantity $\tilde{\sigma}$, which depends on the degeneracy of the mass spectrum. To compare the obtained results with the expectations from the warmness constraint, we show the contours of Eq. (4.32) in Fig. 5.5. The values of m_χ^{\min} are found according to the formula

$$m_\chi^{\min}(m_{B_1}, r_{B_2}) = 19.1 \text{ keV} \left(\frac{106.75}{g_{\star s}(m_{B_1})} \right)^{1/3} \frac{\langle \tilde{\sigma}(m_{B_1}, r_{B_2}, m_\chi) \rangle_{m_\chi}}{3.6}. \quad (5.1)$$

We remember that $\tilde{\sigma}$ is found from

$$\tilde{\sigma}(m_{B_1}, r_{B_2}, m_\chi) = \sqrt{\frac{\int dq q^4 f_\chi(q)}{\int dq q^2 f_\chi(q)}}. \quad (5.2)$$

This value is a function of all the quantities characterizing the model, so in principle the whole mass spectrum. To get rid of the (small) dependence on the m_χ we average over all the values considered of the DM mass. The contours computed with this formula agree in shape with the ones obtained from our criteria but slightly differ in value, with the latter giving systematically higher values of m_χ^{\min} , thus more stringent constraints. Nevertheless, if one considers $F = 1$, Eq. (5.1) is a good way to easily obtain the constraints in the (m_{B_1}, r_{B_2}) plane, since it only requires the computation of the phase-space distribution which is fast. However, our procedure is more general and reliable, since we take into account the power spectra computed from the FIMP model, which depends on the full form of the non-thermal phase-space distribution, rather than on its second momentum $\tilde{\sigma}$ only. Although our method reproduces the expected bounds on m_χ is a good consistency check. The outcome is in agreement with [58], where the authors exploit the warmness quantity criterion and check the results a posteriori with the $k_{1/2}$ criterion from transfer function (i.e. our required score of 3), obtaining an agreement at 10% level. To obtain the reference value of 3.6 for $\tilde{\sigma}$ we are using $m_{\text{WDM}} = 5.3 \text{ keV}$ since we are requesting the stringent bounds to be satisfied. Finally, we have verified that the obtained values of m_χ^{\min} are robust and do not depend on the choice of the discretization of the parameter space by comparing the results obtained exploiting different grids to compute them.

5.2.2 Quadrilinear model for single production

In the quadrilinear model for single production, FIMP DM is produced via scatterings and three-body decays involving three bath particles, which are in principle all different. Therefore this model is characterized by an additional parameter, the mass m_{B_3} , concerning the basic trilinear model we considered above. To perform an analysis similar to the one we did in the previous case, we kept B_3 to be massless throughout the analysis.

The (m_χ, F) plane

In order to study the (m_χ, F) section of parameter space, we fix $m_{B_1} = 1$ TeV and consider B_2 and B_3 to be massless. We computed a 42×42 grid in the $[1, 100]$ keV $\times [F_{\min}, 1]$ region in the (m_χ, F) plane, choosing $F_{\min} = 0.1$. In Fig. 5.6 we show the obtained bounds in the (m_χ, F) plane, considering separately the $k_{1/2}$ criteria (left) and $\mathcal{T}_{\text{lim}}^2$ criteria (right), using the score convention explained above to distinguish the stringent and conservative bounds. The plots are very similar in shape to the ones obtained in the trilinear model: this is reasonable because DM production happens at the same energy scale. We find that for $F = 1$ both criteria agree that $m_\chi > 8.45$ keV if Lyman- α bounds are satisfied by WDM with $m_{\text{WDM}} > 3.5$ keV (stringent bound) and $m_\chi > 14.82$ keV for the conservative case $m_{\text{WDM}} > 5.3$ keV. These values are slightly lower than the ones obtained in the trilinear model. We can visualize these two plots together in the traffic light-like plot in Fig. 5.7. While the $k_{1/2}$ criterion is always satisfied for $F \lesssim 0.2$, the $\mathcal{T}_{\text{lim}}^2$ is not, like in the trilinear model case. To get a value of F , called F_{free} , for which all the criteria are satisfied, we need to go to lower values of F . We find out, as shown in Fig. 5.8, that $F_{\min} \simeq 5 \times 10^{-3}$.

The (m_{B_1}, r_{B_2}) plane

We explore the (m_{B_1}, r_{B_2}) section of the parameter space as we did in the case of the trilinear model. We focus on the same region of parameter space as before and use the same grid to discretize it. The only difference is that now the degeneracy parameter r_{B_2} is allowed to go all the way up to 1, since $2 \rightarrow 2$ scatterings are always kinematically allowed. We repeated the procedure outlined above and we obtained the plots shown in Fig. 5.9. In the upper panels, we show the results obtained with no tolerance in the $\mathcal{T}_{\text{lim}}^2$ criterion. We notice that also in this case there are some holes, points where the criteria are never satisfied for any value of m_χ considered. However, imposing again a tolerance of 1% we can obtain a perfect agreement between the left and right plots, as shown in the lower panel. We show the lower right plot of Fig. 5.9 more in detail in Fig. 5.10 and present it as our lower mass bound for FIMP DM produced in the quadrilinear model for the single production. Let us compare this plot with the one obtained in the trilinear model. The m_{B_1} dependence in m_χ^{\min} is mostly due to the behaviour of $g_{\star s}$ as a function of the temperature at which FIMPs are mainly produced and because of that it is common in the two models. The difference in the two models is in the process through which DM is produced and this impacts the shape of the phase-space distribution function. So, while in the trilinear case we had a significant dependence on the degeneracy parameter r_{B_2} , which is very important in the kinematics of the two-body decay, in the single production model this dependence is weaker and high degeneracies only allow lower m_χ^{\min} at slightly lighter values of m_{B_1} . The degeneracy is relevant in the kinematics of decays, but they are a subdominant production mechanism in the quadrilinear model for the single production.

In Fig. 5.10 we also compare our results with the contours obtained Eq. (5.1) using the

warmness constraints developed in [58]. We see that contours agree in shape and the values of m_χ^{\min} at a 10 % accuracy with the result of our procedure, similarly to the trilinear model case. Again this confirms the robustness of our results and the correctness of the overall methodology.

5.2.3 Quadrilinear model for pair production

In the quadrilinear model for pair production, FIMP DM is produced via scatterings and three-body decays involving two bath particles. This model is characterized by three mass scales, m_{B_1} , m_{B_2} and m_χ , similarly to the trilinear model.

The (m_χ, F) plane

We study (m_χ, F) section of parameter space fixing $m_{B_1} = 1$ TeV and considering B_2 to be massless. As in the previous cases, we computed a 42×42 grid in the $[1, 100]$ keV $\times [F_{\min}, 1]$ region of the (m_χ, F) plane, choosing $F_{\min} = 0.1$. In Fig. 5.11 we show the obtained bounds considering separately the $k_{1/2}$ criteria (left) and the more stringent $\mathcal{T}_{\text{lim}}^2$ criteria (right), using the usual score convention to distinguish the different bounds. The plots are qualitatively and quantitatively similar to the ones obtained in the trilinear and quadrilinear model for single production. In particular we find the same bounds for $F = 1$ we obtained for the trilinear case.

To have a comprehensive picture of the allowed regions in the (m_χ, F) plane we exploit the score convention and build a traffic light-like plot shown in Fig. 5.12. Again the obtained picture is very similar to the ones we found in the other two considered models. In particular, in this case, the value F_{free} for which all the criteria are satisfied in the whole m_χ range is well below our initial choice of F_{\min} . Therefore we compute another 42×42 grid, like the previous one but with $F_{\min} = 10^{-3}$. We show the result in Fig. 5.13 and find, as in the other models, $F_{\text{free}} \simeq 5 \times 10^{-3}$.

The (m_{B_1}, r_{B_2}) plane

As in the previous cases, we explore the mass spectrum parameter space considering the (m_{B_1}, r_{B_2}) plane. We focus on the usual region of this plane and exploit the same discretization, again with r_{B_2} free to go all the way up to 1. Repeating the procedure outlined in the case of the trilinear model, we obtain the plots in Fig. 5.14, with lower plots obtained applying a 1% tolerance on the $\mathcal{T}_{\text{lim}}^2$ criterion. As usual, the tolerance is enough to get rid of numerical issues leading to the holes, points where the criteria are never satisfied for the considered masses. Moreover, with the tolerance $k_{1/2}$ criteria and $\mathcal{T}_{\text{lim}}^2$ produce the same results for m_χ^{\min} , assuring the robustness of the lower bound. We show the lower right plot of Fig. 5.14 more in detail in Fig. 5.15 and present it as our final estimate of the mass bounds on FIMP DM produced via the quadrilinear pair production operator. If we

compare this plot with the one obtained in the other quadrilinear model (single production), we notice a stronger dependence on the spectrum degeneration parameter r_{B_2} . Indeed this stronger dependence is expected, since r_{B_2} strongly affects the kinematics of three-body decays and in pair production, these processes are much more important in making the final distribution function than in the single production case. In particular, a significant change in shape is expected when three-body decays are not kinematically allowed because r_{B_2} is too large. Instead, the dependence on m_{B_1} is the usual one, expected from the temperature dependence in $g_{\star s}$. Like in the previous cases, we compared our results with the estimate obtained from the warmness constraints developed from the work of [58]. We obtain the usual agreement in the shape of contours and the value of m_χ^{\min} at 10%, with our constraints being more stringent.

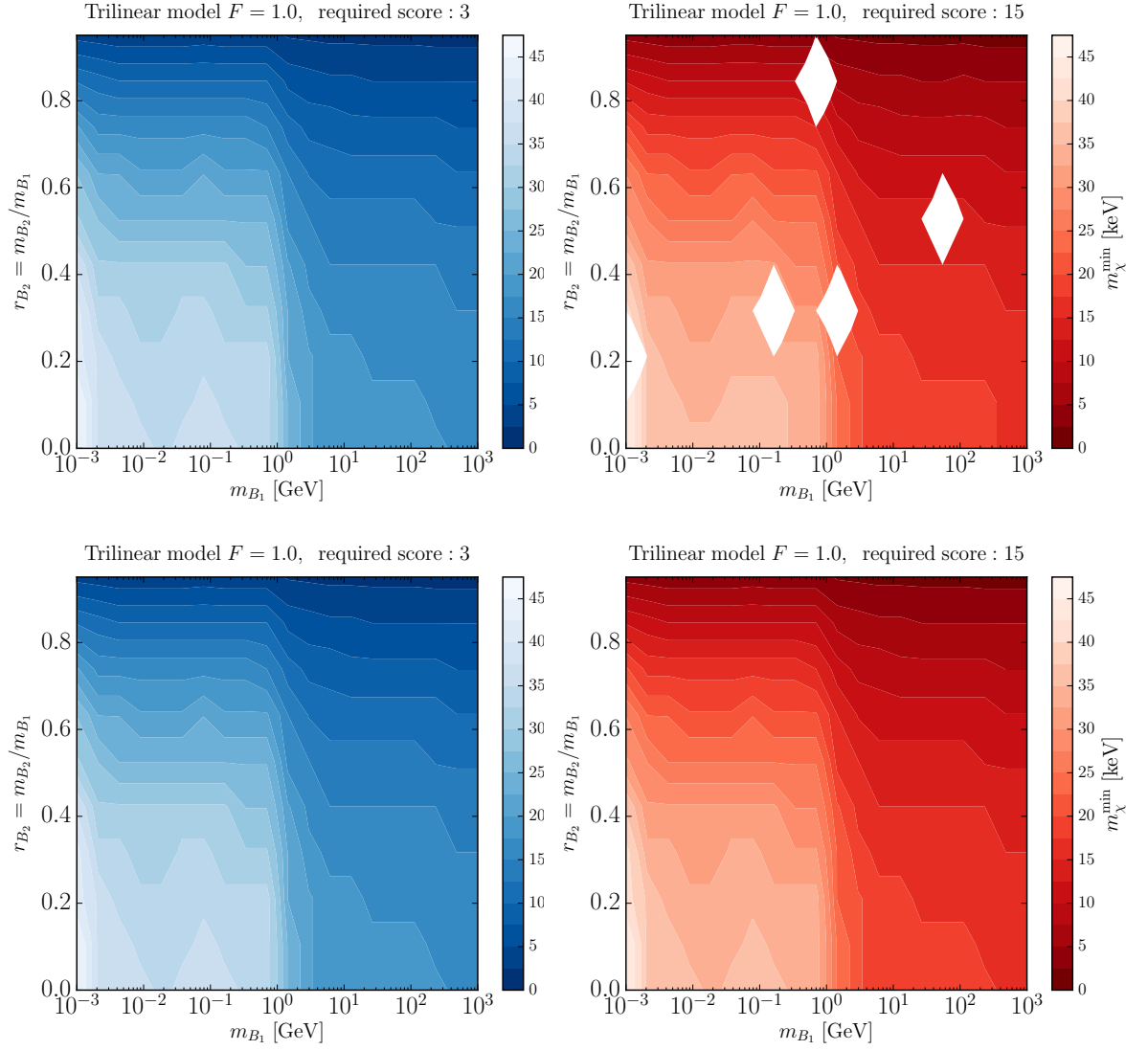


Figure 5.4: Contour plots of the values of m_χ^{\min} for $F = 1$ as functions of the chosen mass spectrum (m_{B_1}, r_{B_2}) in the trilinear model, where FIMPs are produced via two-body decays. To determine the minimum FIMP DM mass allowed by structure formation, we requested the two $k_{1/2}$ to be satisfied (right plots) or all the four tests to be passed by the model (left plots). Upper plots are obtained with no tolerance in the $\mathcal{T}_{\text{lim}}^2$ criterion, while lower ones are obtained using a 1% tolerance. The meaning of the holes in the upper right plot is explained in the text.

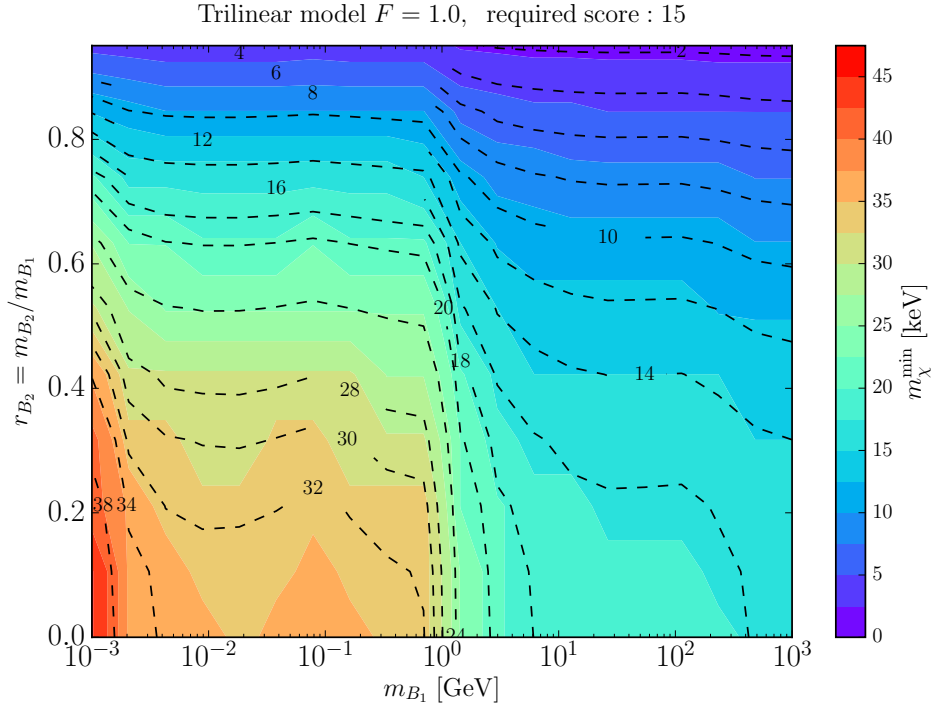


Figure 5.5: Contour plot of our estimate of m_χ^{\min} for $F = 1$ as functions of the chosen mass spectrum (m_{B_1}, r_{B_2}) in the trilinear model, where FIMPs are produced via two-body decays. The contour plot is the lower right of Fig. 5.4. For comparison, we also show the prediction obtained exploiting the warmness constraint from Eq. (4.32) as dashed level curves with numbers showing the m_χ^{\min} in keV as computed with (5.1).

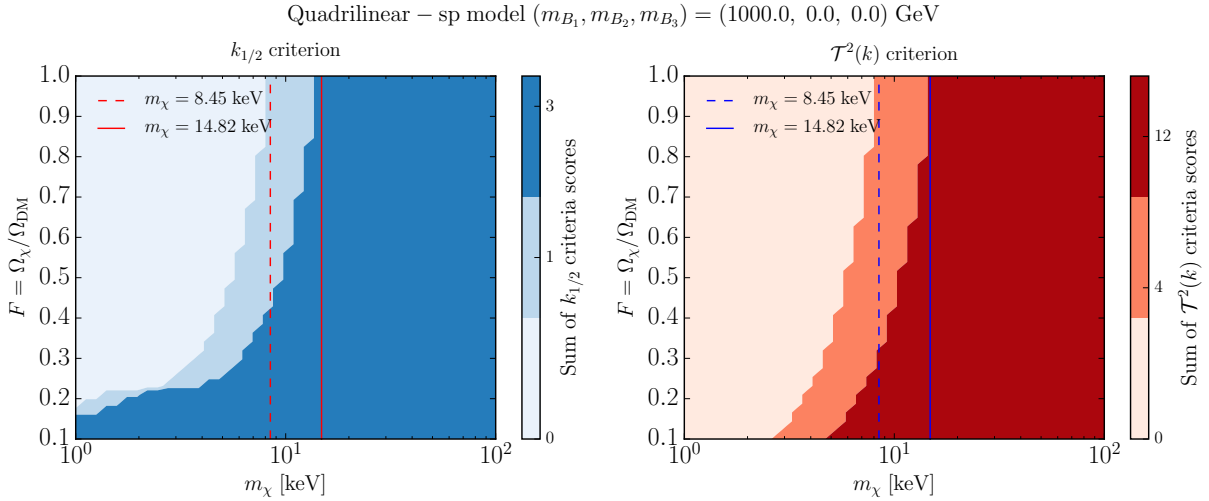


Figure 5.6: Plot of the results of the $k_{1/2}$ criteria (left) and $\mathcal{T}_{\text{lim}}^2$ criteria (right) scores in the (m_χ, F) plane with $F_{\min} = 0.1$ in the quadrilinear single production model, where FIMPs are produced via $2 \rightarrow 2$ scatterings and three-body decays (when kinematically allowed). The vertical lines show the value of the minimum m_χ allowed by the stringent (solid) and conservative (dashed) bounds at $F = 1$.

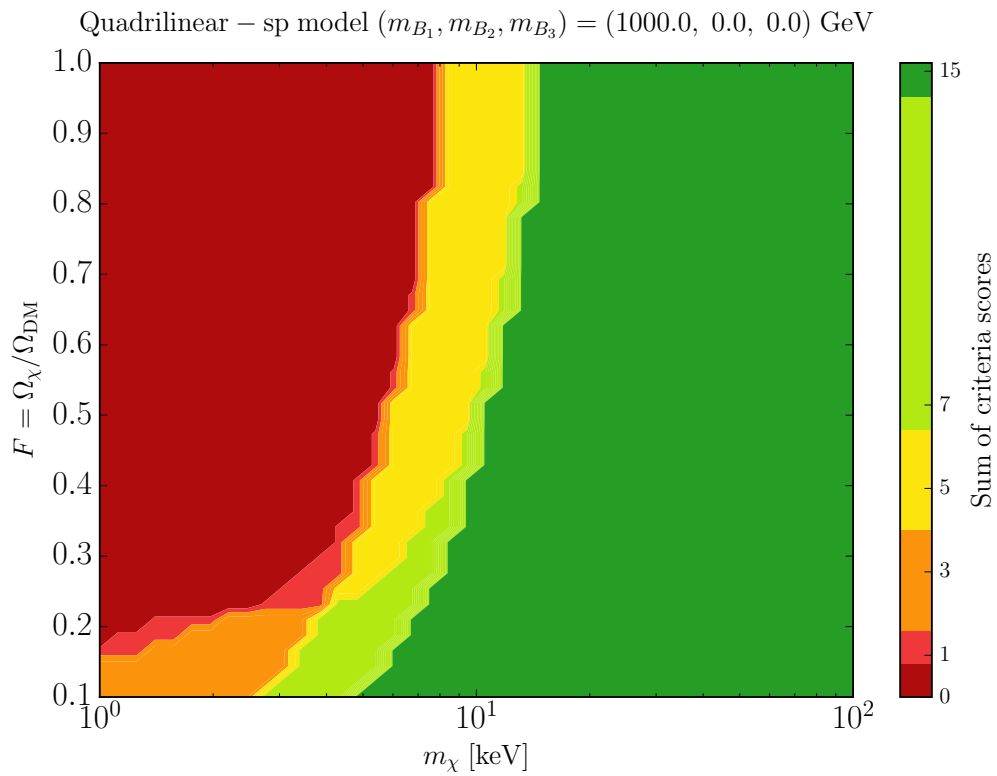


Figure 5.7: Plot of the sum of the resulting scores of the four criteria exploited in the quadrilinear single production model, where FIMPs are produced via $2 \rightarrow 2$ scatterings and three-body decays (when kinematically allowed). The use of colours is described in the text and is the same in Fig. 5.2.

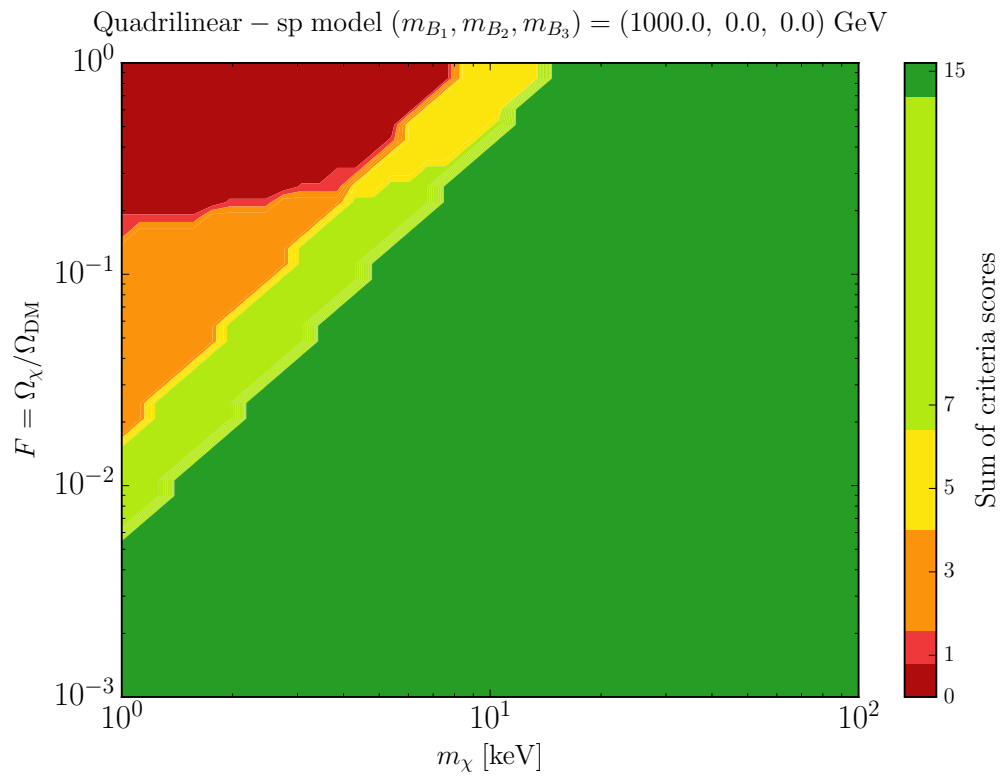


Figure 5.8: Plot of the sum of the resulting scores of the four criteria exploited in the quadrilinear single production model, where FIMPs are produced via $2 \rightarrow 2$ scatterings and three-body decays (when kinematically allowed). The use of colours is described in the text and is the same in Fig. 5.3.

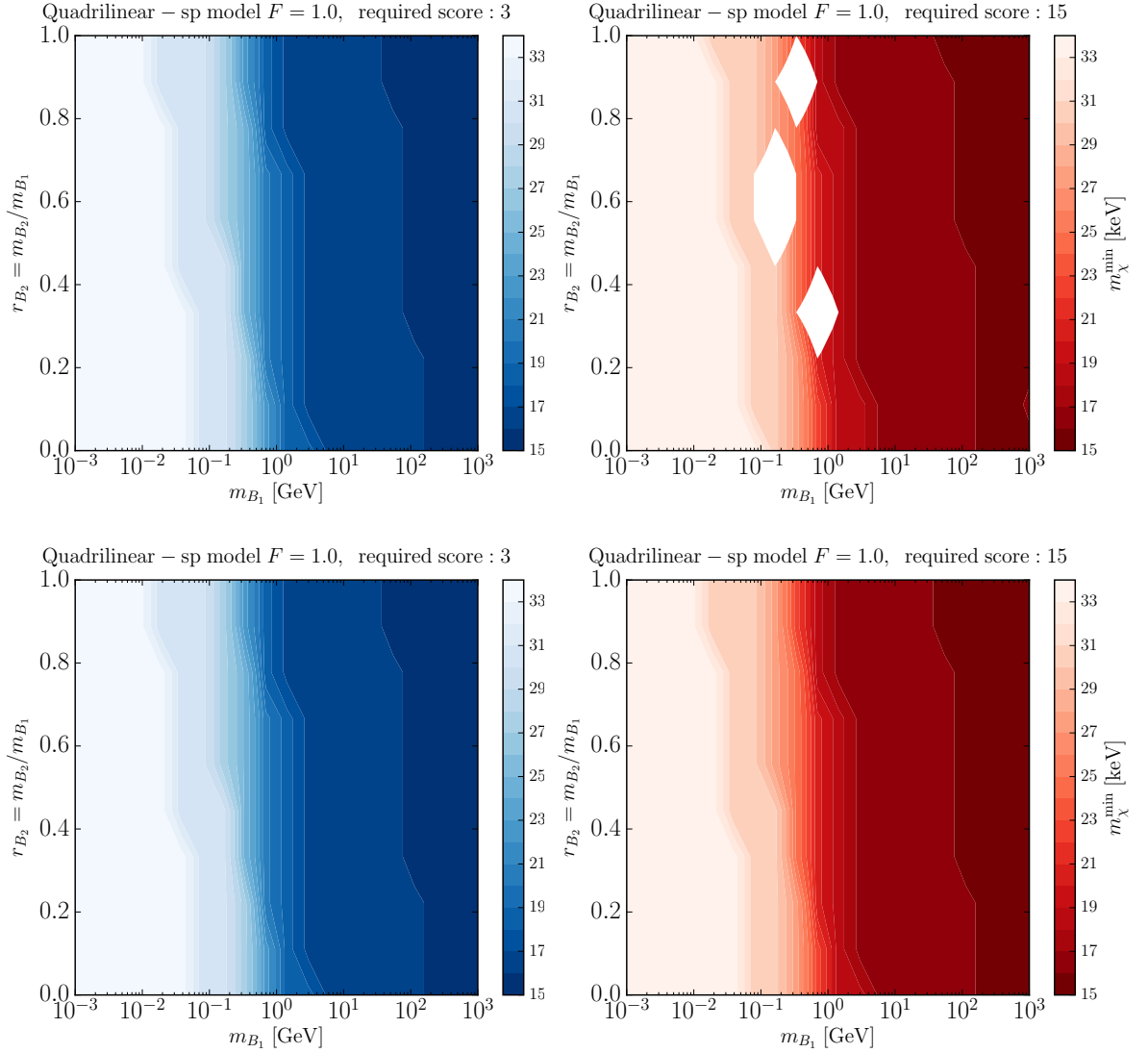


Figure 5.9: Contour plot of the values of m_χ^{\min} for $F = 1$ as functions of the chosen mass spectrum (m_{B_1}, r_{B_2}) in the quadrilinear single production model, where FIMPs are produced via $2 \rightarrow 2$ scatterings and three-body decays (when kinematically allowed). The plots are organized and obtained in the same way as in Fig. 5.4.

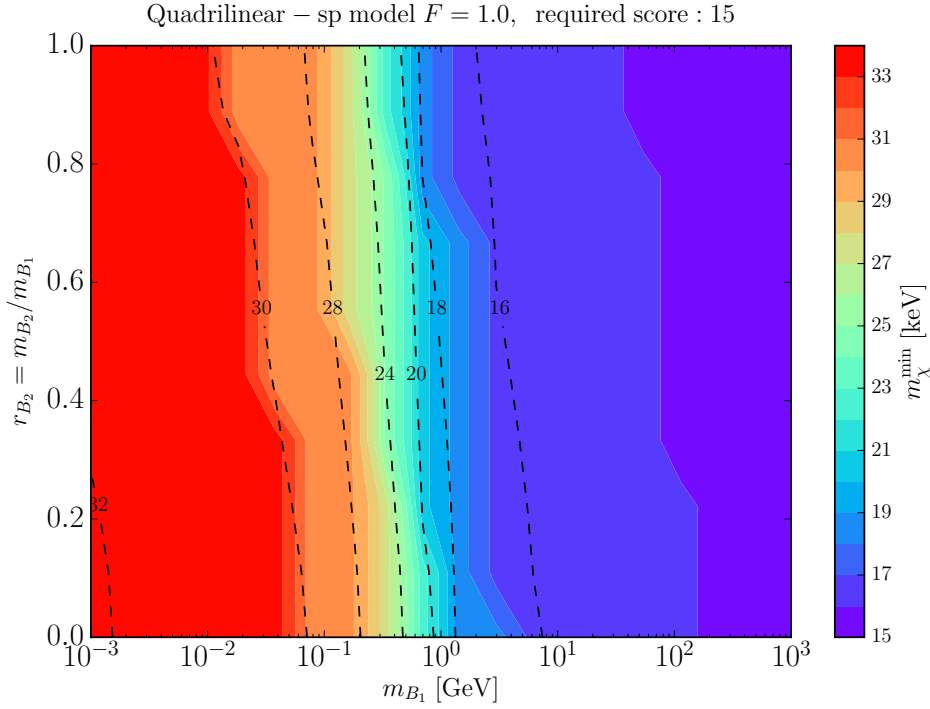


Figure 5.10: Contour plot of the values of m_χ^{\min} for $F = 1$ as functions of the chosen mass spectrum (m_{B_1}, r_{B_2}) in the quadrilinear single production model. The plot is the one in the lower right panel of Fig. 5.9 but, for comparison, we also show the prediction obtained exploiting the warmness constraint from Eq. (4.32) as dashed level curves with numbers showing the m_χ^{\min} in keV as computed with Eq. (5.1).

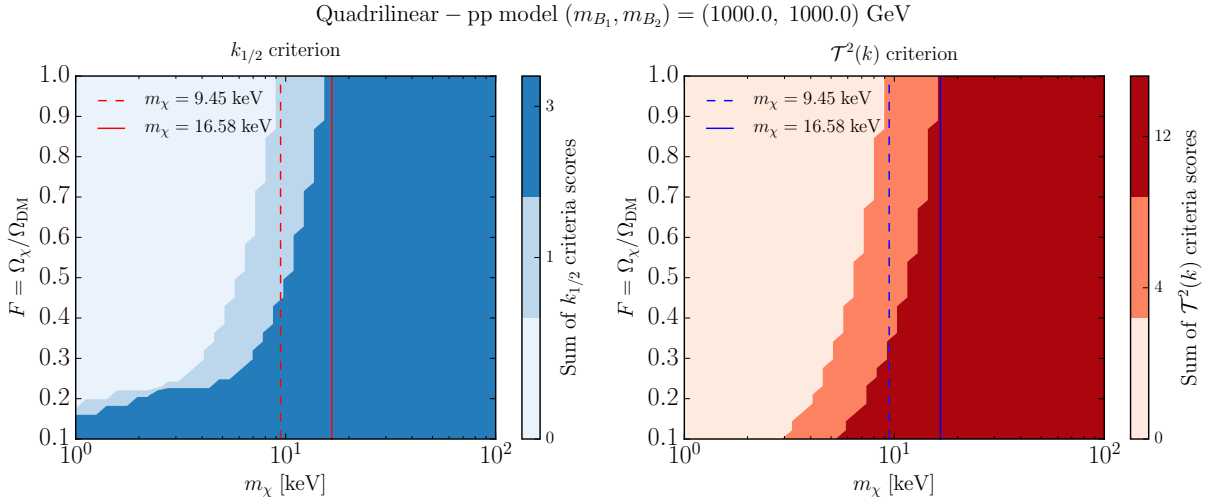


Figure 5.11: Plot of the results of the $k_{1/2}$ criteria (left) and $\mathcal{T}_{\text{lim}}^2$ criteria (right) scores in the (m_χ, F) plane with $F_{\min} = 0.1$ in the quadrilinear pair production model, where FIMPs are produced via $2 \rightarrow 2$ scatterings and three-body decays (when kinematically allowed). The vertical lines show the value of the minimum m_χ allowed by the stringent (solid) and conservative (dashed) bounds at $F = 1$.

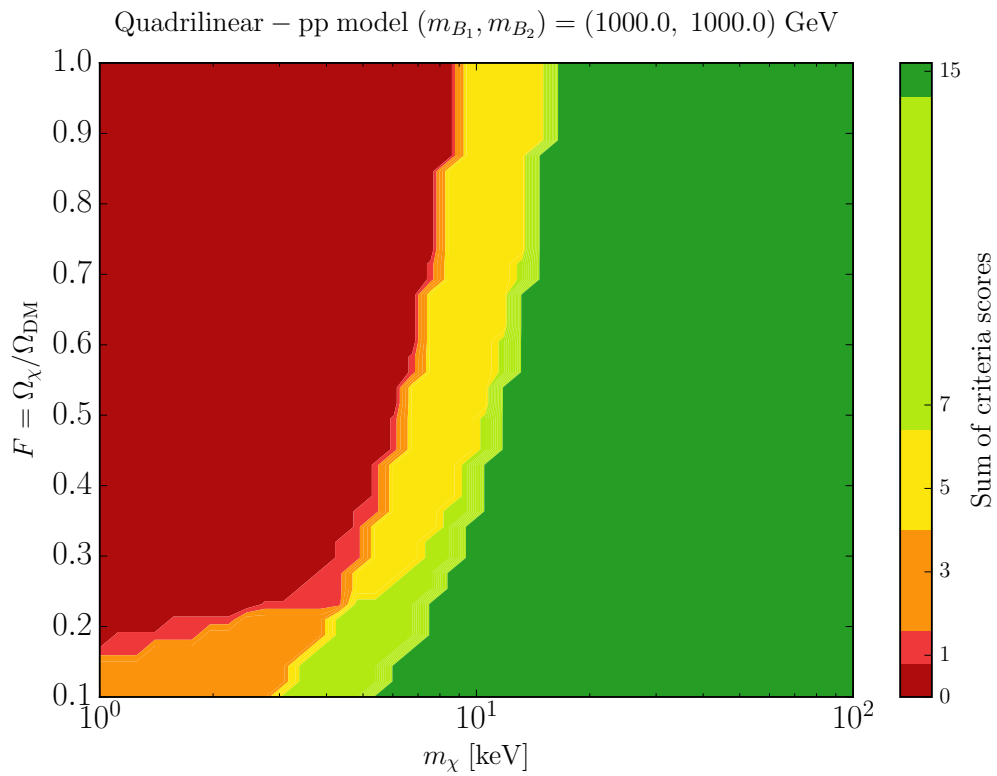


Figure 5.12: Plot of the sum of the resulting scores of the four criteria exploited in the quadrilinear pair production model, where FIMPs are produced via $2 \rightarrow 2$ scatterings and three-body decays (when kinematically allowed). The use of colours is described in the text.

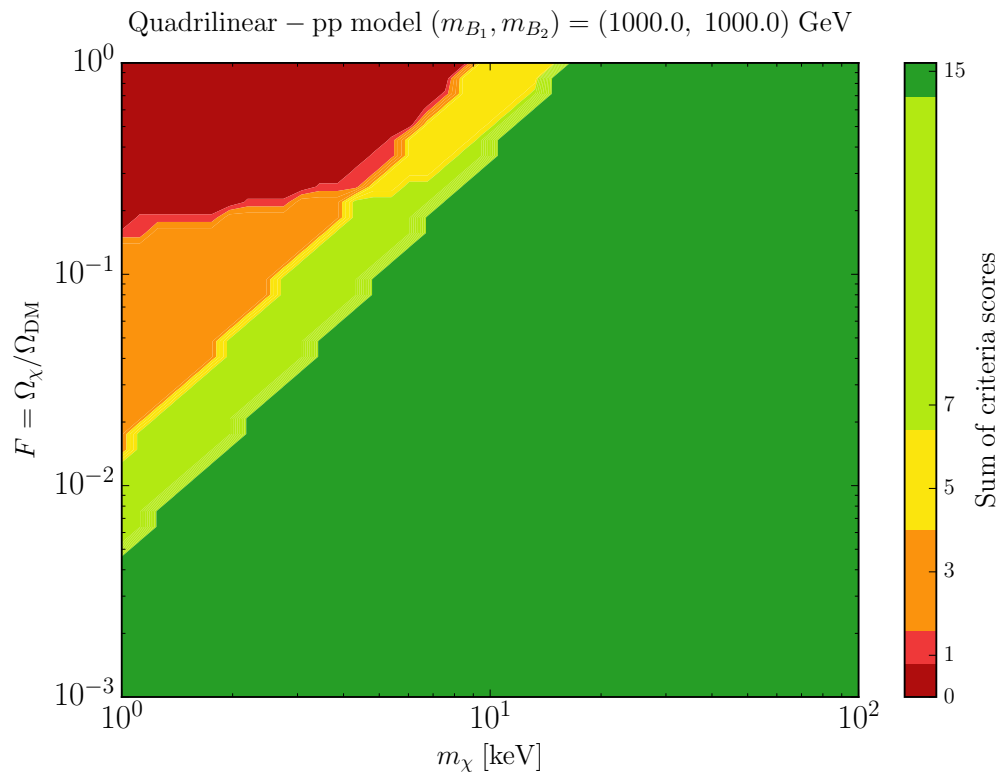


Figure 5.13: Plot of the sum of the resulting scores of the four criteria exploited in the quadrilinear pair production model, where FIMPs are produced via $2 \rightarrow 2$ scatterings and three-body decays (when kinematically allowed). In this case we span the parameter space $[1, 100] \text{ keV} \times [0.001, 1]$ and exploit a log scale on the F axis.

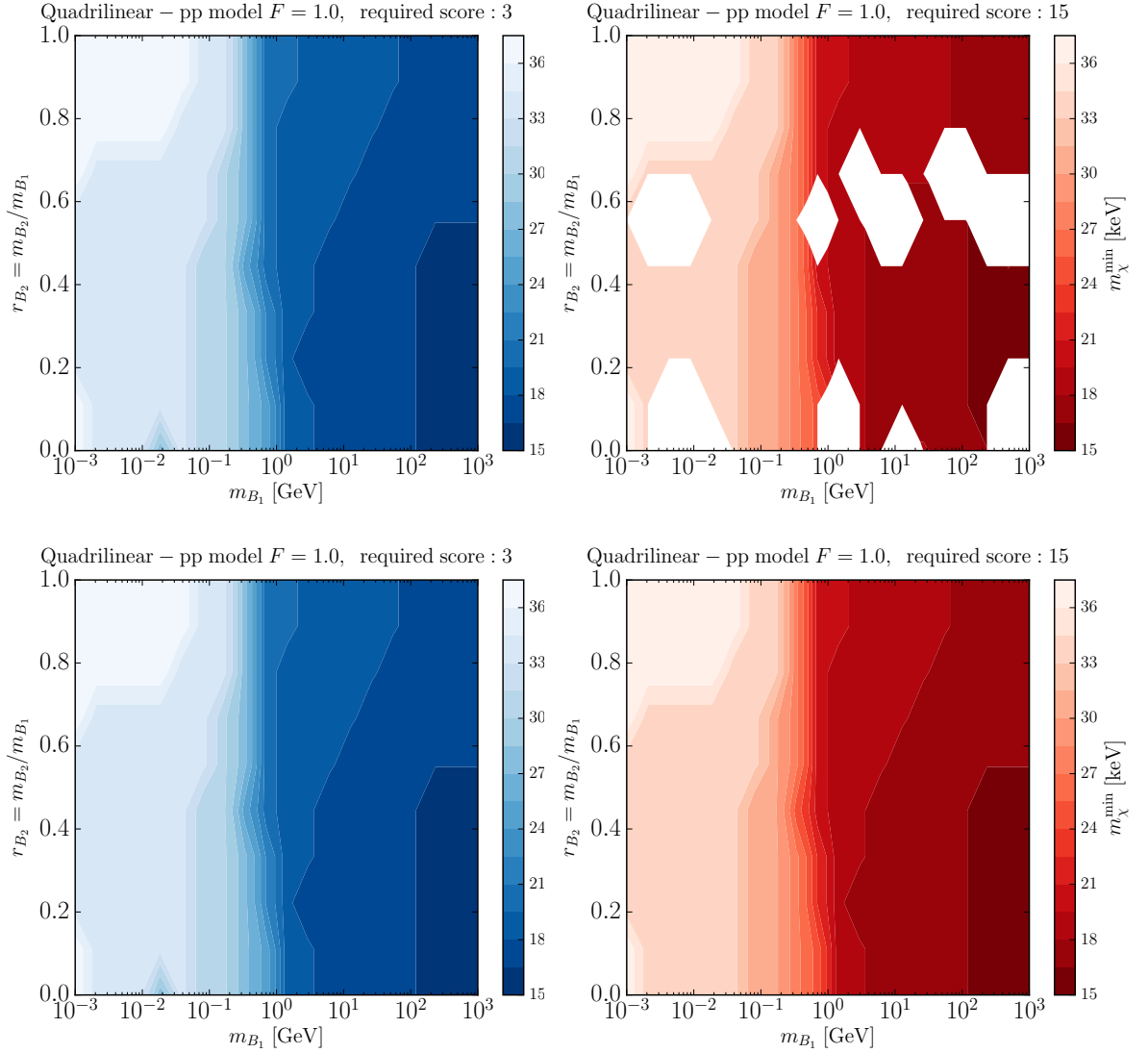


Figure 5.14: Contour plot of the values of m_χ^{\min} for $F = 1$ as functions of the chosen mass spectrum (m_{B_1}, r_{B_2}) in the quadrilinear pair production model, where FIMPs are produced via $2 \rightarrow 2$ scatterings and three-body decays (when kinematically allowed). The plots are organized and obtained in the same way as in Fig. 5.4.

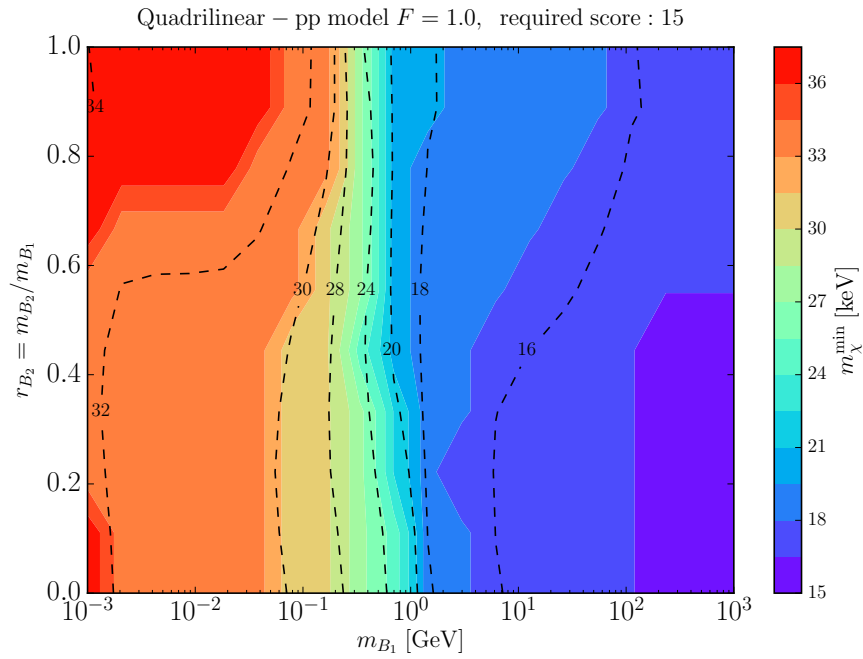


Figure 5.15: Contour plot of the values of m_{χ}^{\min} for $F = 1$ as functions of the chosen mass spectrum (m_{B_1}, r_{B_2}) in the quadrilinear pair production model, where FIMPs are produced via $2 \rightarrow 2$ scatterings and three-body decays (when kinematically allowed). The plot is the lower right one in Fig. 5.14 but, for comparison, we also show the prediction obtained exploiting the warmness constraint from Eq. (4.32) as dashed level curves with numbers showing the m_{χ}^{\min} in keV as computed with Eq. (5.1).

Conclusions

As we reviewed in detail in Chapter 1, observations point out the existence of dark matter (DM), which is invisible and non-baryonic and, as far as we know, interacts only gravitationally with the known matter. The evidence at our disposal includes observations on galactic scales (galactic rotation curves, gravitational lensing), on galaxy cluster scales and on cosmological scales (CMB, BBN, supernovae type Ia and, remarkably, structure formation). In particular, observations claim that the DM must be described by beyond-Standard-Model physics. This fact opens up maybe the most prominent challenge that the fundamental physics community has to face in this century: the understanding of the nature of DM.

Under the assumption that the DM is made of some unknown particle, in Section 1.5 we summarized the main model-independent features of such particle candidate. In general, to track the evolution of the properties of the DM particle species during its cosmological history, we exploit the well-established Boltzmann equation formalism, described in Chapter 2. In this framework, the particle species is described by a phase-space distribution which satisfies the Boltzmann equation, taking into account the expansion of the Universe and all the processes the DM particles are involved in. Over the last decades, a large theoretical effort has been put in the DM model building around a few leading paradigms. The best-known one is undoubtedly the freeze-out paradigm, both for its simplicity and a large number of motivated candidates (WIMPs) falling naturally in this framework: we analysed, in a model-independent way, the freeze-out paradigm in Section 2.4. However, recent experiments, among which XENON1T [34] stands out for its high sensitivity, are constraining the parameter space of WIMP DM mass and WIMP DM-nuclei cross-section in this framework, leading to the necessity to explore other mechanisms for DM production.

One of such interesting possibilities is given by the freeze-in scenario. This idea, first introduced by L.J. Hall et al. [1], in its standard form, shares many appealing features of the freeze-out framework, such as its simplicity and the independence on high-energy physics and initial conditions. However, freeze-in DM candidates, called FIMPs, are characterized by a much smaller interaction rate with visible matter, such that they never attain thermal equilibrium with the primordial plasma of radiation and baryonic matter. In Chapter 3 we proved that the freeze-in paradigm is able to reproduce the observed DM relic density. Moreover, we explicitly showed the abundance evolution for three scalar toy models, in

which FIMPs are produced via two-body decays, three-body decays and scatterings and pair production processes, respectively.

The fact that FIMPs are only very weakly coupled with visible matter is appealing since more parameter space is unconstrained in model building. However, DM produced in the freeze-in scenario can nevertheless leave observational signatures in direct, indirect and collider searches of DM. We explored these possibilities in Section 3.3, briefly reviewing the concrete example of the dark photon model with milli-charged freeze-in DM, which is going to be probed by XENON1T. Moreover, a crucial way to observationally constrain freeze-in models is to exploit the theory of structure formation, i.e. measurements of the linear matter power spectrum (extrapolated from the non-linear one) at the smallest scales we can probe. One of such observables is the Lyman- α forest, which is able to constrain light DM models, such as thermal WDM. Similarly to WDM, FIMP DM with low mass heavily impacts on structure formation, providing a small-scale cutoff in the matter power spectrum. However, since FIMPs are produced non-thermally, non-trivial differences can arise in the power spectra computed from WDM models and in the freeze-in scenario, and they can produce different constraints on the DM model.

In this work, we addressed the problem of constraining FIMP parameters in the standard freeze-in scenario using bounds from structure formation. Since a proper analysis of Lyman- α data with FIMP DM is model-dependent and time-consuming, we developed a general methodology that can be applied to any model. From the work of M. Viel et al. [56], we know that depending on the assumptions in the data analysis, WDM models with $m_{\text{WDM}} > 3.5$ keV (conservative bound) and $m_{\text{WDM}} > 5.3$ keV (stringent bound) are in agreement with Lyman- α data. Therefore, we can take the transfer functions (the ratio of the computed power spectra with the usual Λ CDM one) as limits, and impose that our FIMP models never produce suppression of power at scales larger than the cutoff of the WDM transfer functions. This procedure quickly produces more stringent constraints than performing the full analysis directly from Lyman- α data. In the first part of Chapter 4 we presented the procedure to constrain the free parameters of a given model, made of operators, couplings and a mass spectrum. For each point in parameter space, the phase-space distribution of the FIMP DM candidate is computed numerically by solving the Boltzmann equation. The distribution is passed to the CLASS code [68, 69] which computes the linear matter power spectrum in this model and, subsequently, the transfer function to be compared with the WDM ones. To test the robustness of the bound, we exploited two different criteria to tell if our model is allowed by the WDM constraint. On the basis of this methodology, it is possible to analyse the parameter space of the given model. In the simplest case, it is made of the masses of the particles involved in the FIMP DM production, the FIMP mass and the final relic abundance that the model is required to reproduce.

To test our procedure, we applied it to three simple scalar FIMP DM toy models, each one allowing different DM production processes: the trilinear model, involving two-body decays, and two quadrilinear models, describing single and pair production through

scatterings and three-body decays. In the second part of Chapter 4 we showed how to compute the phase-space distribution for these toy models. Finally, in Chapter 5, we presented the code exploited to perform calculations and we showed the obtained constraints on the parameter space of the considered models. In particular, we focused on lower bounds on the FIMP DM mass m_χ studying two slices of the parameter space: (i) the mass of FIMP DM and its fractional abundance F , which is used to fix the coupling in the considered operator (the (m_χ, F) plane) and (ii) the mass spectrum of the involved bath particles (the $(m_{B_1}, m_{B_2}/m_{B_1})$ plane). In the first analysis we showed which region of the (m_χ, F) plane is allowed by the structure formation constraints and which region is in tension instead, exploiting the above-mentioned criteria based on the power spectrum. In the second analysis, instead, we computed the value of the minimum m_χ allowed in the case $F = 1$ for each point in the $(m_{B_1}, m_{B_2}/m_{B_1})$ plane. In this case, we showed that both criteria give the same lower bound on m_χ at 1% accuracy. This shows that our results are robust and do not depend strongly on the criteria nor on the discretization of the parameter space. Moreover, we compared the outcome of the analysis in the $(m_{B_1}, m_{B_2}/m_{B_1})$ plane with the lower bounds obtained exploiting the warmness quantity, introduced by A. Kamada and K. Yanagi in [58]. For all models, our bounds, obtained from the full transfer function, agree with the ones obtained from the warmness constraint at a 10% accuracy and show similar dependences on the free parameters. Interestingly, our procedure, which takes into account the full shape of the distribution function rather than its second moment only, provides always more stringent lower bounds on the FIMP DM mass.

The developed procedure is general: we can exploit it considering different FIMP DM candidates and freeze-in models, changing the type of operator responsible for DM production. Moreover, we can change the cosmological history during the FIMP DM production epoch, which in the standard picture, is simply the FRW one during the radiation-dominated era. All the changes can be fairly easily introduced in the code which provides the same analysis we performed for the scalar toy models. Moreover, it is possible to straightforwardly introduce other observational constraints as limit transfer functions to include other bounds from structure formation or to update the Lyman- α ones. An interesting and natural follow-up for this work could be to consider classes of models and try to constrain the parameter space in freeze-in scenarios on the basis of the mechanisms of FIMP DM production. In this way it would be possible to generally tell which couplings and mass spectra are available to produce FIMP DM at a given energy scale with a specific mechanism, easing model building within the freeze-in paradigm.

Acknowledgements

Я ждал это время, и вот это время пришло,
Те, кто молчал, перестали молчать.
Те, кому нечего ждать, садятся в седло,
Их не догнать, уже не догнать.

—Виктор Цой

There are many people I would like to thank for their direct or indirect support for this thesis work, which was conceived and written mainly during the months of lockdown in the 2020 pandemic. First of all, I thank my supervisor Francesco D'Eramo for his availability and his precious suggestions: we came up with bright ideas for many projects, and I hope we shall collaborate again in the future. Secondly, I thank Annachiara Picco for her love and pieces of advice throughout those months, which have been full of relevant life-changing choices. I want to thank Giovanni Cataldi and Umberto Tomasini for the suggestion to request access to our regional centre of calculus: most of this work would not have been possible without those resources. Also, I thank my friends Davide Maniscalco, Andrea Boido, and Omar Pagliarini with whom I shared moments of leisure, during which often new ideas came to my mind.

This work comes both as the conclusion of my academic path as a student in Padova and, possibly, as the start of my research activity. Therefore, I want to thank the people who have helped me during these whole five years, friends, colleagues and flatmates. In particular, I thank my roommate Alessandra Carissoni, my friends Paola Bogarelli, Barbara Gallazzi and my distant sister Diana Istratii for their constant encouragement and emotional support. Last but not least, I thank my parents Maria Luisa Damiano and Sabino Lenoci, which have always encouraged and supported all the choices I have made so far.

Appendix A

Friedmann-Robertson-Walker cosmology

With the word *cosmology*, we refer to the study of the Universe as a whole, i.e. seen on scales comparable with its size. In this appendix, we review the set of tools we need to study the Universe as a system and to understand the present and past role of DM in our Universe.

A.1 The expanding Universe

Today, the standard cosmological model has its funding core in the so-called Big Bang scenario, in which the Universe is a system evolving from an extremely dense state around 10 Gyr ago. From Hubble's discovery that the Universe was expanding, this scenario has survived all cosmological observations. The expansion of the Universe is described by the Hubble constant H_0 : it sets the timescale of the evolution of the Universe, hence its age, indeed $H_0^{-1} \sim 10$ Gyr.

$$H_0 = 100h \text{ km s}^{-1}\text{Mpc}^{-1} = 2.14h \times 10^{-33} \text{ eV} = 3.33h \times 10^{-4} \text{ Mpc}^{-1}. \quad (\text{A.1})$$

The parametrization of the Hubble constant historically accounts for the uncertainty on its precise value. In this work, if necessary, we rely on the value obtained by the Plack experiment [17].

$$h = 0.674 \pm 0.005. \quad (\text{A.2})$$

The Hubble constant sets also the size of the observable Universe, the distance travelled by light in a Hubble time, that is the Hubble radius $R_H(t_0) = cH_0^{-1}$.

Around the Big Bang scenario, cosmologists have built a sophisticated model which allows us to explain at a high level of accuracy the thermal history of the Universe and

other observables as the abundance of elements, cosmic relic background radiation and large scales structures. The model is based on Einstein's theory of gravity, General Relativity (GR), and consists of three main building blocks:

1. the *metric*, showing the symmetries of the Universe and its geometry;
2. the *Einstein field equations* relating the geometry of the Universe with its matter-energy content;
3. the *equations of state* specifying the nature of the matter content of the Universe and its physical properties. Our best knowledge of the fundamental constituent of the Universe is encoded in the *Standard Model of particle physics*.

We study the three ingredients separately in the next subsections.

A.1.1 The Friedmann-Robertson-Walker metric

Usually, cosmologists assume the *cosmological principle*, i.e. that on cosmological scales our Universe is characterized by statistical homogeneity and isotropy. These properties imply a high level of symmetry and greatly simplify the study of the Universe. They are confirmed by observations to a high level of accuracy. In particular, observations of the Cosmic Microwave Background (CMB) have shown the Universe is isotropic up to deviations of the order of 10^{-5} . If the Universe is isotropic about any point in space, it is also homogeneous: this is the case if we assume to live in a completely general region of the Universe. Nevertheless, we probe homogeneity directly through galaxy surveys: data suggest a homogeneous distribution on scales greater than 100 Mpc, about 1% of the size of the observable Universe. The study of inhomogeneities and anisotropies, which make the structures we observe, e.g. galaxies and clusters, can be done perturbatively on the base of this background spacetime.

Spatial homogeneity and isotropy imply a specific form of the metric. We consider a foliation of the spacetime in spacelike slices which are maximally symmetric

$$ds^2 = -dt^2 + a^2(t)d\gamma^2, \quad (\text{A.3})$$

where $a(t)$ is called *scale factor*. $d\gamma$ is the line element on the spacelike surface

$$d\gamma^2 = \gamma_{ij}dx^i dx^j, \quad (\text{A.4})$$

with $i, j = 1, 2, 3$. For a maximally symmetric space, the spatial Ricci tensor reads $R_{ij} = 2k\gamma_{ij}$. The constant k describes the spatial (geometric) curvature and in general it can take the values $k = -1, 0, +1$. If the spacelike surface is maximally symmetric it is surely spherically symmetric. It can be shown that the metric takes the form, in spherical coordinates

$$d\gamma^2 = f^2(r)dr^2 + r^2 d\Omega_2^2, \quad (\text{A.5})$$

with $d\Omega_2^2$ the infinitesimal solid angle. Computing the spatial Ricci tensor for this metric and comparing it to $R_{ij} = 2k\gamma_{ij}$, one finds that $f^2(r) = (1 - kr^2)^{-1}$. Hence we obtain the Friedmann-Robertson-Walker (FRW) metric

$$ds^2 = -dt^2 + a^2(t) \left[\frac{1}{1 - kr^2} dr^2 + r^2 d\Omega_2^2 \right]. \quad (\text{A.6})$$

We assume a spatially flat FRW Universe, i.e. we put $k = 0$. This hypothesis is observationally verified to per mille accuracy by Planck satellite [17]; this fact implies that the curvature plays no relevant role in the early FRW Universe. Therefore the spatial line element is simply Euclidean:

$$ds^2 = -dt^2 + a^2(t) \delta_{ij} dx^i dx^j. \quad (\text{A.7})$$

This will be our reference metric throughout our work. The coordinate t is the cosmic time while x^i are comoving coordinates, which are not affected by the expansion of the Universe. Physical coordinates are obtained simply as $r^i(t) = a(t)x^i$.

A.1.2 Friedmann equations

The Friedmann equations are Einstein field equations for the FRW metric. Einstein equations come from the minimization of the Einstein-Hilbert action plus the matter action

$$S = \frac{M_{\text{Pl}}^2}{2} \int d^4x \sqrt{-g} (R - 2\Lambda) + S_M, \quad (\text{A.8})$$

$$\frac{\delta S}{\delta g^{\mu\nu}} = 0 \iff R_{\mu\nu} - \frac{1}{2} g_{\mu\nu} R = \frac{1}{M_{\text{Pl}}^2} T_{\mu\nu} - \Lambda g_{\mu\nu}. \quad (\text{A.9})$$

Here $g_{\mu\nu}$ is the metric tensor ($g \equiv \det g$), $R_{\mu\nu}$ and $R = g^{\mu\nu} R_{\mu\nu}$ are, respectively, the Ricci tensor and scalar for the full spacetime, $M_{\text{Pl}} = (8\pi G)^{-1/2}$ is the reduced Planck mass, parametrizing the strength of gravity;

$$T_{\mu\nu} = -\frac{2}{\sqrt{-g}} \frac{\delta S_M}{\delta g^{\mu\nu}} \quad (\text{A.10})$$

is the energy-momentum tensor and Λ is the so-called cosmological constant. The Einstein equations simply tell us that the geometry of the Universe (left-hand side) is determined by the matter content (right-hand side) plus the cosmological constant term. The latter represents vacuum energy associated with the space-time itself and acts as a source of gravity even in absence of matter. Today we know from the analysis of the CMB [17] together with type Ia supernovae [19] (see section 1.3.3 for more details), that the cosmological constant can play a very important role in determining the expansion of the Universe. In particular, we assume the existence of an exotic fluid, called dark energy, which behaves like a cosmological constant in the Einstein equation, i.e. has an energy-momentum tensor

of the form

$$T_{\mu\nu}^{\Lambda} = -M_{\text{Pl}}^2 \Lambda g_{\mu\nu}. \quad (\text{A.11})$$

Now we want to write the Einstein equations for the FRW metric. To do that, we have to explicit the Ricci tensor for the FRW metric and also specify the matter source. First, we introduce the Christoffel symbols or affine connection coefficients

$$\Gamma^{\mu}_{\alpha\beta} = \frac{1}{2} g^{\mu\nu} \left[\partial_{\alpha} g_{\beta\nu} + \partial_{\beta} g_{\alpha\nu} - \partial_{\nu} g_{\alpha\beta} \right] \quad (\text{A.12})$$

and compute them. Using the fact that FRW metric is diagonal and $g_{00} = -1$,

$$\Gamma^0_{\alpha\beta} = -\frac{1}{2} \left[\partial_{\alpha} g_{\beta 0} + \partial_{\beta} g_{\alpha 0} - \partial_0 g_{\alpha\beta} \right] = \frac{1}{2} \partial_0 g_{\alpha\beta}, \quad (\text{A.13})$$

hence

$$\Gamma^0_{00} = 0, \quad \Gamma^0_{0i} = \Gamma^0_{i0} = 0, \quad \Gamma^0_{ij} = a^2 H \delta_{ij}, \quad (\text{A.14})$$

with dots denoting cosmic time derivatives ∂_0 and H the Hubble parameter

$$H \equiv \frac{\dot{a}}{a}. \quad (\text{A.15})$$

We go on with the computation:

$$\Gamma^i_{\alpha\beta} = \frac{1}{2} g^{ij} \left[\partial_{\alpha} g_{\beta j} + \partial_{\beta} g_{\alpha j} - \partial_j g_{\alpha\beta} \right] = \frac{1}{a^2} \delta^{ij} (\delta_{\alpha 0} \delta_{\beta k} + \delta_{\beta 0} \delta_{\alpha k}) \partial_0 g_{jk}, \quad (\text{A.16})$$

hence

$$\Gamma^i_{0k} = \Gamma^i_{k0} = \delta_{ik} H. \quad (\text{A.17})$$

The other Christoffel symbols vanish. The Ricci tensor is expressed in terms of the Christoffel symbols

$$R_{\mu\nu} = \partial_{\alpha} \Gamma^{\alpha}_{\mu\nu} - \partial_{\nu} \Gamma^{\alpha}_{\mu\alpha} + \Gamma^{\alpha}_{\beta\alpha} \Gamma^{\beta}_{\mu\nu} - \Gamma^{\alpha}_{\beta\nu} \Gamma^{\beta}_{\mu\alpha} \quad (\text{A.18})$$

Let us compute R_{00} using the above found Christoffel symbols. It is evident that we are left with only two terms of the four inside R_{00} :

$$R_{00} = -\partial_0 \Gamma^i_{0i} - \Gamma^i_{j0} \Gamma^j_{0i} = -\delta_{ii} \partial_0 H - H^2 \delta_{ij} \delta^{ij} = -3 \frac{\ddot{a}}{a} + 3H^2 - 3H^2. \quad (\text{A.19})$$

Therefore

$$R_{00} = -3 \frac{\ddot{a}}{a}. \quad (\text{A.20})$$

Then

$$R_{0i} = R_{i0} = -\Gamma^{\alpha}_{\beta i} \Gamma^{\beta}_{0\alpha} = -\Gamma^k_{\ell i} \Gamma^{\ell}_{0k} = 0 \quad (\text{A.21})$$

and

$$\begin{aligned} R_{ij} &= \partial_0 \Gamma^0_{ij} + \Gamma^\alpha_{0\alpha} \Gamma^0_{ij} - \Gamma^\alpha_{\beta j} \Gamma^\beta_{i\alpha} \\ &= \partial_0 (a^2 H) \delta_{ij} + 3H a^2 H \delta_{ij} - H a^2 H \delta_{ij} - H a^2 H \delta_{ij} = [2a^2 H^2 + a\ddot{a}] \delta_{ij}. \end{aligned} \quad (\text{A.22})$$

The last ingredient of the left-hand side of Eq. (A.9) is the Ricci scalar, which reads

$$R = g^{00} R_{00} + g^{ij} R_{ij} = 6 \left[\frac{\ddot{a}}{a} + H^2 \right]. \quad (\text{A.23})$$

Now we focus on the right-hand side of Eq. (A.9). Being the source of the FRW metric, the energy-momentum tensor has to respect the symmetries of our spacetime. Then the only possible form of the energy-momentum tensor is

$$T^\mu{}_\nu = \text{diag}(-\rho, \mathcal{P}, \mathcal{P}, \mathcal{P}), \quad (\text{A.24})$$

i.e. the one of a perfect isotropic fluid. Here ρ is the energy density of the fluid and \mathcal{P} is the isotropic pressure. We model the matter content of the Universe on cosmological scales as a *perfect isotropic fluid*. This can also include the cosmological constant term since it is sufficient to require that $\rho = -\mathcal{P} = M_{\text{Pl}}^2 \Lambda$. So we absorb the cosmological constant in the energy-momentum tensor. In the next subsection, we will specialize it to the known families of particle species: radiation and matter.

Let us finally write the Friedmann equations.

- 00 - Einstein equation

$$R_{00} + \frac{1}{2} R = \frac{1}{M_{\text{Pl}}^2} (-1) T^0_0 \quad (\text{A.25})$$

gives

$$H^2 = \frac{1}{3M_{\text{Pl}}^2} \rho. \quad (\text{A.26})$$

This equation is often called the energy constraint, since it is not a dynamical equation for $a(t)$, involving only first-order time derivatives for the scale factor. From this equation, we can define the *critical density* as the energy density of a flat FRW universe today

$$\rho_c \equiv 3H_0^2 M_{\text{Pl}}^2 \simeq 1.1 h^2 \times 10^{-5} \text{ GeV cm}^{-3} = 8.4 h^2 \times 10^{-47} \text{ GeV}^4, \quad (\text{A.27})$$

which we use to normalize the energy density, introducing the *density parameter*

$$\Omega(t) \equiv \frac{\rho(t)}{\rho_c}. \quad (\text{A.28})$$

With this definition, Eq. (A.26) reads simply

$$\Omega(t) = 1, \quad (\text{A.29})$$

meaning the sum of the density parameters of all the constituents of the Universe gives one throughout the history of the flat FRW Universe. We can now better understand the name energy constraint for Eq. (A.26).

- ij - Einstein equations

$$R_{ij} - \frac{1}{2}a^2\delta_{ij}R = \frac{1}{M_{\text{Pl}}^2}a^2\delta_{ik}T^k_j \quad (\text{A.30})$$

give

$$\frac{\ddot{a}}{a} + \frac{1}{2}H^2 = -\frac{1}{2M_{\text{Pl}}^2}\mathcal{P}. \quad (\text{A.31})$$

This equation is indeed dynamical. Combining it with the energy constraint we obtain the so-called acceleration equation

$$\frac{\ddot{a}}{a} = -\frac{1}{6M_{\text{Pl}}^2}(\rho + 3\mathcal{P}). \quad (\text{A.32})$$

We can write another equation, dependent on the previous two, which is the conservation of the energy-momentum tensor:

$$D_\mu T^\mu_\nu = 0. \quad (\text{A.33})$$

This equation comes straightly from Bianchi identities, which state that the left-hand side of Eq. (A.9) is conserved. Let us consider the $\nu = 0$ component of Eq. (A.33)

$$\begin{aligned} 0 &= \partial_\mu T^\mu_0 + \Gamma^\mu_{\alpha\mu}T^\alpha_0 - \Gamma^\alpha_{0\mu}T^\mu_\alpha \\ &= -\partial_0\rho - \Gamma^\mu_{0\mu}\rho - \Gamma^\alpha_{0\mu}T^\mu_\alpha. \end{aligned} \quad (\text{A.34})$$

Since $\Gamma^\alpha_{0\mu} = 0$ unless α and μ are equal spatial indices, we finally obtain the so-called fluid (continuity) equation

$$\dot{\rho} + 3H(\rho + \mathcal{P}) = 0. \quad (\text{A.35})$$

This conservation law is very useful because it can be directly applied, given an equation of state, to model the evolution of the energy content of the Universe during its expansion history.

A.1.3 The equation of state

The Friedmann equations Eq. (A.26) and Eq. (A.32) we have derived above contain three unknown functions $a(t)$, $\rho(t)$, $\mathcal{P}(t)$. To solve the system and know the time evolution of these quantities, we need another equation. Indeed we need an equation of state, specifying the nature of the perfect isotropic fluid we are considering. In general, the equation of state is written as $\mathcal{P} = \mathcal{P}(\rho)$ and can be a very complicated function. In FRW cosmology equations of state are usually parametrized considering *barotropic fluids*, i.e. an equation of state

$$\mathcal{P} = w\rho. \quad (\text{A.36})$$

Here we distinguish three ingredients of the Universe energy budget by the value of the constant w :

$$w = \begin{cases} 0 & \text{non-relativistic pressureless matter} \\ 1/3 & \text{radiation} \\ -1 & \text{vacuum energy} \end{cases} \quad (\text{A.37})$$

We can use this equation of state to get the dependence of the energy density ρ on the scale factor and then use the energy constraint to find the dependence on cosmic time. From the continuity equation Eq. (A.35)

$$\frac{d\rho}{\rho + \mathcal{P}} = -3 \frac{da}{a} \iff \log \rho = -3(1+w) \log a, \quad (\text{A.38})$$

that is

$$\rho \propto a^{-3(1+w)} \propto \begin{cases} a^{-3} & \text{non-relativistic pressureless matter} \\ a^{-4} & \text{radiation} \\ \text{const} & \text{vacuum energy} \end{cases} \quad (\text{A.39})$$

These three scalings give us a picture of the history of the FRW Universe. If the initial state was extremely dense $a \ll 1$, the initially dominant component in the energy budget (hence with the greatest density parameter) was radiation. Since we know today matter is relevant, after the so-called radiation domination epoch, radiation was diluted by the expansion and matter came to dominate the Universe. According to recent observations, only recently, about 4 Gyr ago, the cosmological constant became the dominant constituent of the Universe. The exact history depends on the precise energy budget today. Now we substitute this behaviour in the energy constraint obtaining

$$H = \frac{\dot{a}}{a} = \frac{1}{\sqrt{3}M_{\text{Pl}}} \rho^{1/2}, \quad (\text{A.40})$$

which, for $w \neq -1$ gives

$$da \propto a^{-\frac{3(1+w)}{2}+1} dt \implies a(t) \propto t^{\frac{2}{3(1+w)}}, \quad (\text{A.41})$$

while for $w = -1$, $\rho = -M_{\text{Pl}}^2 \Lambda$ and

$$\frac{da}{a} \propto \sqrt{\frac{\Lambda}{3}} dt \implies a(t) \propto e^{\sqrt{\frac{\Lambda}{3}} t}. \quad (\text{A.42})$$

So we summarize the dependence of the scale factor on cosmic time as

$$a(t) \propto \begin{cases} t^{\frac{2}{3(1+w)}} & \begin{cases} t^{2/3} & \text{non-relativistic pressureless matter} \\ t^{1/2} & \text{radiation} \end{cases} \\ e^{\sqrt{\frac{\Lambda}{3}} t} & \text{vacuum energy} \end{cases} \quad (\text{A.43})$$

From the scale factor, one finds the Hubble parameter

$$H(t) \propto \begin{cases} \frac{2}{3(1+w)} \frac{1}{t} & \begin{cases} \frac{2}{3t} & \text{non-relativistic pressureless matter} \\ \frac{1}{2t} & \text{radiation} \end{cases} \\ \sqrt{\frac{\Lambda}{3}} & \text{vacuum energy} \end{cases} \quad (\text{A.44})$$

A.2 Thermodynamics in the expanding Universe

As we have said, the early FRW Universe was dominated by radiation, i.e. a primordial plasma of relativistic particles. These particles are of different species, we shall label with index i , all characterized by different masses m_i and internal degrees of freedom g_i . As we discuss in Chapter 2, each species is effectively described by its *phase-space distribution* f_i , which, in a homogeneous and isotropic FRW Universe, is a function of energy (or momentum) of the particle species

$$E_i(p) = \sqrt{p^2 + m_i^2}, \quad (\text{A.45})$$

and of cosmic time. Here the momentum p is the physical one, which redshifts with the expansion as a^{-1} . In fact, in a relativistic framework, the comoving momentum is the derivate of the comoving coordinates with respect to the affine parameter, describing the motion of the particle along a worldline:

$$P^\mu = \frac{dx^\mu}{d\lambda} = (E, P^i). \quad (\text{A.46})$$

Instead, the physical momentum is given by

$$p^2 \equiv g_{ij} P^i P^j = a^2 \delta_{ij} P^i P^j. \quad (\text{A.47})$$

If P^i does not feel the expansion of the Universe, being defined from comoving coordinates, then $p \propto a^{-1}$. The on-shellness condition reads indeed

$$-m^2 = P^\mu P_\mu = g_{\mu\nu} P^\mu P^\nu = -E^2 + a^2 \delta_{ij} P^i P^j = -E^2 + p^2 \quad (\text{A.48})$$

Usually, the time dependence in the distribution function f_i is traded for temperature dependence, as a more effective variable to track the evolution of the Universe. Nevertheless, the two variables are related, as we shall see at the end of this appendix. In this section, we focus on the definition of thermodynamical quantities and their computation in the thermal equilibrium situation. In particular, we want to see how a thermal bath of relativistic particles can be modelled. This thermal bath will be the environment with whom the DM will interact, either strongly or feebly.

So, the crucial function to extract thermodynamical quantities for each particle species is the phase-space distribution

$$f_i = f_i(p, T), \quad (\text{A.49})$$

which is the occupation number density in phase-space, counting the number of particles in a unit phase-space. From that, we can define, for each particle species, the number density

$$n_i = g_i \int \frac{d^3 p}{(2\pi)^3} f_i(p, T) \quad \text{number density} \quad (\text{A.50})$$

The expression comes straightly from the definition of the phase-space distribution. Then, the full GR expression for the energy-momentum tensor in terms of the distribution function is [16]

$$T^\mu{}_\nu(x) \Big|_i = g_i \int \frac{d^3 P}{(2\pi)^3} \sqrt{-g} \frac{P^\mu P_\nu}{P^0} f_i(x, P) \quad (\text{A.51})$$

In the case of FRW metric, it is easy to see that $d^3 P = a^{-3} d^3 p$ and to obtain from the above expression the ones for energy density and isotropic pressure, taking $\rho = T^0_0$ and $\mathcal{P} = T^j_j / 3$:

$$\begin{aligned} \rho_i &= g_i \int \frac{d^3 p}{(2\pi)^3} f_i(p, T) E_i(p) && \text{energy density} \\ \mathcal{P}_i &= g_i \int \frac{d^3 p}{(2\pi)^3} f_i(p, T) \frac{p^2}{3E_i(p)} && \text{isotropic pressure} \end{aligned} \quad (\text{A.52})$$

These two expressions satisfy the fluid equation Eq. (A.35), since $T^\mu{}_\nu$ is conserved. Another crucial thermodynamical variable in the study of the expanding FRW Universe is the *entropy density*, defined as

$$s_i = \frac{\rho_i + \mathcal{P}_i}{T} \quad \text{entropy density} \quad (\text{A.53})$$

A.2.1 Equilibrium results

As we discuss in section 2.2, if scatterings and number-changing processes between the particles of the plasma are efficient, we say that these particle species are in *thermal equilibrium*. This implies a specific form for the phase-space distribution function, that is Fermi-Dirac and Bose-Einstein distributions, depending on the particle species' statistics. The chemical potential is usually negligible in this situation for almost all particle species $\mu \ll T$, so the equilibrium distribution is

$$f_i^{\text{eq}}(E, T) = \left[e^{E/T} \pm 1 \right]^{-1}, \quad (\text{A.54})$$

with a minus sign for bosons and a plus for fermions. We can compute the thermodynamical quantities we introduced above using this distribution. Firstly we take advantage of isotropy

and rewrite the measure appearing in all integrals over momenta as

$$\frac{d^3p}{(2\pi)^3} = \frac{4\pi p^2 dp}{(2\pi)^3} = \frac{1}{2\pi^2} \sqrt{E^2 - m_i^2} E dE. \quad (\text{A.55})$$

The lower extremum of integration is the mass of the particle species, m_i .

Equilibrium number density

For the equilibrium number density, we have

$$n_i^{\text{eq}} = \frac{g_i}{2\pi^2} \int_{m_i}^{\infty} dE \frac{E \sqrt{E^2 - m_i^2}}{e^{E/t} \pm 1}. \quad (\text{A.56})$$

We can compute this expression in the relativistic regime, i.e. for $T \gg m_i$. In this case, we can put to zero the mass m_i in the above integral and find

$$n_i^{\text{eq}} = \frac{g_i}{2\pi^2} \int_0^{\infty} dE \frac{E^2}{e^{E/t} \pm 1} = \frac{g_i}{\pi^2} T^3 \times \begin{cases} \zeta(3) & \text{bosons} \\ \frac{3}{4}\zeta(3) & \text{fermions} \end{cases} \quad T \gg m_i \quad (\text{A.57})$$

with $\zeta(3) \simeq 1.20206$ the Riemann zeta. We also want a general expression valid for any temperature. We can obtain it neglecting the quantum statistics and treating bosons and fermions in the same way. This can be done as long as we do not have degeneracies in the plasma, which is almost always the case. Nevertheless, in our cosmological framework, we know degeneracies can appear only in the relativistic limit, where quantum statistics provide a small correction, a factor of $\zeta(3)$ or $3\zeta(3)/4$ for bosons and fermions respectively. So, if we use Maxwell-Boltzmann classical distribution, we get

$$n_i^{\text{eq}} = \frac{g_i}{2\pi^2} \int_{m_i}^{\infty} dE E \sqrt{E^2 - m_i^2} e^{-E/t} = \frac{g_i T^3}{2\pi^2} \left(\frac{m_i}{T}\right)^2 K_2\left(\frac{m_i}{T}\right). \quad (\text{A.58})$$

K_2 is the modified Bessel function of the second kind. In our work, we will make frequent use of this expression and its limits. Using the asymptotic behaviour of the expression

$$x^2 K_2(x) = \begin{cases} 2 - \frac{x^2}{2} + \mathcal{O}(x^3) & x \ll 1 \\ e^{-x} \sqrt{\frac{\pi}{2}} \left[x^{3/2} + \frac{15}{8} x^{1/2} + \mathcal{O}(x^{-1/2}) \right] & x \gg 1 \end{cases} \quad (\text{A.59})$$

we can write

$$n_i^{\text{eq}} \simeq \begin{cases} \frac{g_i}{\pi^2} T^3 & m_i \ll T \\ g_i \left(\frac{m_i T}{2\pi}\right)^{3/2} e^{-m_i/T} & m_i \gg T \end{cases} \quad (\text{A.60})$$

Notice we have lost the order one quantum correction factors in the relativistic regime.

Equilibrium energy density

We can write the energy density as

$$\rho_i^{\text{eq}} = \frac{g_i}{2\pi^2} \int_{m_i}^{\infty} dE \frac{E^2 \sqrt{E^2 - m_i^2}}{e^{E/t} \pm 1}. \quad (\text{A.61})$$

We can give the limiting expression for the integral. In the relativistic case, we can set $m_i = 0$ and

$$\rho_i^{\text{eq}} = \frac{g_i}{2\pi^2} \int_0^{\infty} dE \frac{E^3}{e^{-E/t} \pm 1} = g_i \frac{\pi^2}{30} T^4 \times \begin{cases} 1 & \text{bosons} \\ 7/8 & \text{fermions} \end{cases} \quad T \gg m_i \quad (\text{A.62})$$

A general expression for ρ_i^{eq} can be found again neglecting the quantum statistics. We obtain

$$\rho_i^{\text{eq}} = \frac{g_i}{2\pi^2} \int_{m_i}^{\infty} dE E^2 \sqrt{E^2 - m_i^2} e^{-E/t} = \frac{g_i T^4}{2\pi^2} \left(\frac{m_i}{T}\right)^2 \left[\frac{m_i}{T} K_1\left(\frac{m_i}{T}\right) + 3K_2\left(\frac{m_i}{T}\right) \right]. \quad (\text{A.63})$$

Using the asymptotic behaviour of the expression

$$x^2 \left[xK_1(x) + 3K_2(x) \right] = \begin{cases} 6 - \frac{x^2}{2} + \mathcal{O}(x^3) & x \ll 1 \\ e^{-x} \sqrt{\frac{\pi}{2}} \left[x^{5/2} + \frac{27}{8} x^{3/2} + \mathcal{O}(x^{1/2}) \right] & x \gg 1 \end{cases} \quad (\text{A.64})$$

we can write

$$\rho_i^{\text{eq}} \simeq \begin{cases} g_i \frac{3}{\pi^2} T^4 & m_i \ll T \\ g_i \left(\frac{m_i^{5/3} T}{2\pi} \right)^{3/2} e^{-m_i/T} = mn_i^{\text{eq}} & m_i \gg T \end{cases} \quad (\text{A.65})$$

Indeed we find the canonical expression $\rho = mn$ for the energy density of non-relativistic particles, where the energy of a particle is dominated by its mass. In the relativistic case the factor in front of $g_i T^4$ is very similar to the one found using the quantum statistics: $\pi^2/30 \simeq 0.33$, while $3/\pi^2 \simeq 0.30$. To find the expressions for the pressure we can simply exploit the equation of state of a barotropic fluid $\mathcal{P}_i = w_i \rho_i$.

Entropy density

We can consider the equilibrium FRW Universe as a system undergoing an adiabatic expansion, i.e. in which entropy is conserved in time. The entropy is conserved for each particle species in thermal equilibrium. Indeed it can be shown that $S = a^3 s$ is constant by thermodynamics, using the fact that at equilibrium dS is an exact differential form and the continuity equation Eq. (A.35). Following [16], we will show the same result holds assuming the distribution function f_i depends only on the ratio E/T , as it is the case for

thermal equilibrium, where the chemical potential is negligible. It holds that

$$\frac{df_i^{\text{eq}}}{dT} = -\frac{E}{T} \frac{df_i^{\text{eq}}}{dE}, \quad (\text{A.66})$$

so, if we take the temperature derivative of the isotropic pressure, we get

$$\begin{aligned} \frac{d\mathcal{P}_i}{dT} &= -\frac{1}{T} \frac{g_i}{2\pi^2} \int_{m_i}^{\infty} dE (E^2 - m_i^2)^{3/2} \frac{E}{3} \frac{df_i^{\text{eq}}}{dE} \\ &= -\frac{1}{T} \frac{g_i}{2\pi^2} \left[(E^2 - m_i^2)^{3/2} \frac{E}{3} f_i^{\text{eq}} \Big|_{m_i}^{\infty} - \int_{m_i}^{\infty} dE \left(E^2 (E^2 - m_i^2)^{1/2} + \frac{1}{3} (E^2 - m_i^2)^{3/2} \right) f_i^{\text{eq}} \right] \\ &= \frac{\rho_i + \mathcal{P}_i}{T} = s_i. \end{aligned} \quad (\text{A.67})$$

To show that $s_i \propto a^{-3}$, we rewrite Eq. (A.35) in the form

$$a^{-3} \frac{\partial}{\partial t} \left[(\rho_i + P_i) a^3 \right] - \frac{\partial \mathcal{P}_i}{\partial t} = 0. \quad (\text{A.68})$$

Then we rewrite the time derivative of pressure as $\partial \mathcal{P}_i / \partial t = dT/dt \partial \mathcal{P}_i / \partial T$ and introduce s_i

$$0 = a^{-3} \frac{\partial}{\partial t} \left[(\rho_i + P_i) a^3 \right] - \frac{dT}{dt} s_i = a^{-3} T \frac{\partial}{\partial t} \left[s_i a^3 \right]. \quad (\text{A.69})$$

Hence $S_i = \text{const}$ and $s_i \propto a^{-3}$. Although we have done our calculation for a single species, the scaling clearly holds for the total entropy density, obtained as the sum of all the species in equilibrium. In particular, if two species are in equilibrium “with themselves”, as it is for decoupled species, the sum of their entropy densities still scales as a^{-3} . Let us write limit expressions for s_i in the relativistic and non-relativistic regime

$$s_i = \begin{cases} \frac{4}{3} \frac{\rho_i}{T} = \frac{2\pi^2}{45} g_i T^3 \times \begin{cases} 1 & \text{bosons} \\ 7/8 & \text{fermion} \end{cases} & T \gg m_i \\ \frac{\rho_i}{T} = g_i \left(\frac{m_i T}{2\pi} \right)^{3/2} \frac{m_i}{T} e^{-m_i/T} & T \ll m_i \end{cases} \quad (\text{A.70})$$

Notice that, once the particle species become non-relativistic, its entropy density drops exponentially.

A.2.2 Effective number of degrees of freedom

In the very early FRW Universe, Standard Model particle species constitute the primordial plasma, a bath of particles interacting so effectively that they are in thermal equilibrium. This thermal bath dominates the energy density and is characterized by the radiation temperature T (by reference, the black body temperature of photons) and a given number of effective degrees of freedom. As the Universe expands and consequently cools down, various particle states become non-relativistic and their number density is

exponentially suppressed. In other words, they disappear from the thermal bath and the plasma loses degrees of freedom. The mass spectrum of the Standard Model and the features of the interactions between its particles add peculiarities to the process of depletion of degrees of freedom. Two particularly delicate moments are the electroweak phase transition (EWPT) and the QCD phase transition (QCDPT), where the particle content of the Universe changes drastically. Other peculiar cases are the decoupling of relativistic degrees of freedom, such as neutrinos. Their number density is not exponentially suppressed: neutrinos simply cease to interact with the thermal bath and free-stream, making a thermal bath with conserved entropy on their own, with a possibly independent temperature.

We describe the radiation thermal plasma in terms of its energy density

$$\rho = \sum_i \rho_i \equiv \frac{\pi^2}{30} g_{\star\rho}(T) T^4, \quad (\text{A.71})$$

and entropy density

$$s = \sum_i s_i \equiv \frac{2\pi^2}{45} g_{\star s}(T) T^3. \quad (\text{A.72})$$

The sum is over all relativistic states. The functions $g_{\star\rho}(T)$ and $g_{\star s}(T)$ describe the effective number of active relativistic degrees of freedom in energy density and entropy, respectively. If we neglect the details of the complex physics involved in phase transitions and we consider sharp mass thresholds, we can write approximate expressions for the two functions. From their above definition, we can write, in the relativistic limit $T_i \gg m_i$

$$\begin{aligned} g_{\star\rho}(T) &= \sum_{i, \text{ bosons}} g_i \left(\frac{T_i}{T} \right)^4 + \frac{7}{8} \sum_{i, \text{ fermions}} g_i \left(\frac{T_i}{T} \right)^4 & T_i \gg m_i \\ g_{\star s}(T) &= \sum_{i, \text{ bosons}} g_i \left(\frac{T_i}{T} \right)^3 + \frac{7}{8} \sum_{i, \text{ fermions}} g_i \left(\frac{T_i}{T} \right)^3 & T_i \gg m_i \end{aligned} \quad (\text{A.73})$$

We have allowed species to have their temperatures, to take into account decoupled species. In this limit, the two functions are approximated as step functions, but the actual behaviour is smooth.

Throughout our work, we use the fitting expressions found by [32] for the effective degrees of freedom in density and entropy as functions of the photon temperature T . These results are obtained from the Standard Model and other approximations used to model all the details of phase transitions in the early Universe, at the best of our knowledge. We define $\tau = \log(T/\text{GeV})$.

For $120 \text{ GeV} < T < 10^{16} \text{ GeV}$ we have

$$g_{\star\rho}(T) \simeq \frac{\sum_{i=0}^{11} a_i \tau^i}{\sum_{i=0}^{11} b_i \tau^i}, \quad g_{\star s}(T) \simeq g_{\star\rho}(T) \left(1 + \frac{\sum_{i=0}^{11} c_i \tau^i}{\sum_{i=0}^{11} d_i \tau^i} \right)^{-1}. \quad (\text{A.74})$$

The coefficients a_i, b_i, c_i, d_i given in the following table.

i	a_i	b_i	c_i	d_i
0	1	1.43382e-02	1	7.07388e+01
1	1.11724e+00	1.37559e-02	6.07869e-01	9.18011e+01
2	3.12672e-01	2.92108e-03	-1.54485e-01	3.31892e+01
3	-4.69049e-02	-5.38533e-04	-2.24034e-01	-1.39779e+00
4	-2.65004e-02	-1.62496e-04	-2.82147e-02	-1.52558e+00
5	-1.19760e-03	-2.87906e-05	2.90620e-02	-1.97857e-02
6	1.82812e-04	-3.84278e-06	6.86778e-03	-1.60146e-01
7	1.36436e-04	2.78776e-06	-1.00005e-03	8.22615e-05
8	8.55051e-05	7.40342e-07	-1.69104e-04	2.02651e-02
9	1.22840e-05	1.17210e-07	1.06301e-05	-1.82134e-05
10	3.82259e-07	3.72499e-09	1.69528e-06	7.83943e-05
11	-6.087035e-09	-6.74107e-11	-9.33311e-08	7.13518e-05

Instead, for $T < 120$ MeV the fitting formulae are the following ones:

$$g_{\star\rho}(T) \simeq 2.030 + 1.353S^{4/3}(x_e) + 3.495f_\rho(x_e) + 3.466f_\rho(x_\mu) + 1.05b_\rho(x_{\pi^0}) + 2.08b_\rho(x_{\pi^\pm}) \\ + 4.165b_\rho(x_1) + 30.55b_\rho(x_2) + 89.4b_\rho(x_3) + 8209b_\rho(x_4), \quad (\text{A.75})$$

$$g_{\star s}(T) \simeq 2.008 + 1.923S(x_e) + 3.442f_s(x_e) + 3.468f_s(x_\mu) + 1.034b_s(x_{\pi^0}) + 2.068b_s(x_{\pi^\pm}) \\ + 4.16b_s(x_1) + 30.55b_s(x_2) + 90b_s(x_3) + 6209b_s(x_4), \quad (\text{A.76})$$

having defined $x_i = m_i/T$ where $m_e = 511 \times 10^{-6}$ GeV, $m_\mu = 0.1056$ GeV, $m_{\pi^0} = 0.135$ GeV, $m_{\pi^\pm} = 0.140$ GeV, $m_1 = 0.5$ GeV, $m_2 = 0.77$ GeV, $m_3 = 1.2$ GeV, and $m_4 = 2$ GeV. The functions used in the right-hand sides of Eq. (A.75), Eq. (A.76) are

$$h(x) = e^{-Ax}(1 + Bx + Cx^2 + Dx^3), \\ S(x) = 1 + \frac{7}{4}e^{-Ax}(1 + Bx + Cx^2 + Dx^3), \quad (\text{A.77})$$

with $h(x) = f_\rho(x), b_\rho(x), f_s(x), b_s(x)$ and coefficients A, B, C, D given in the following table. We show in Fig. A.1 the behaviour of the relativistic degrees of freedom as functions of

	A	B	C	D
$f_\rho(x)$	-1.04855	1.03757	0.508630	0.0893988
$b_\rho(x)$	-1.03149	1.03317	0.398264	0.0648056
$f_s(x)$	-1.04190	1.03400	0.456426	0.059524
$b_s(x)$	-1.03365	1.03397	0.34258	0.0506182
$S(x)$	-1.0419	1.034	0.456426	0.0595249

the temperature.

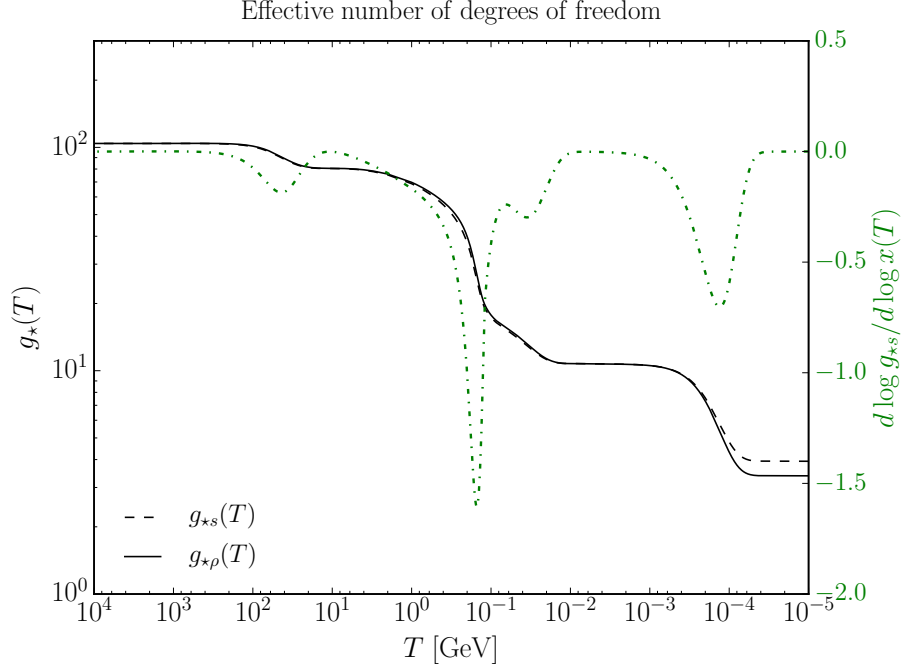


Figure A.1: The evolution of the number of relativistic degrees of freedom throughout the thermal history of the early Universe, according to Eqs. (A.74), (A.75), (A.76), from [32]. In green (right y-axis) we show the log-derivative $d \log g_{*s}(T)/d \log x$ with $d \log x = -d \log T$.

A.2.3 Temperature as time variable

Usually, the temperature is used as a more appropriate time variable to describe the evolution of quantities in the expanding Universe with respect to cosmic time. The most suitable choice is to use the temperature of the photon bath T . Exploiting conservation of entropy, we can write the derivative of time with respect to the radiation temperature

$$\frac{dS^{1/3}}{dT} = 0 \implies \frac{d}{dT}(g_{*s}^{1/3}(T)Ta) = 0, \quad (\text{A.78})$$

$$\begin{aligned} 0 &= \frac{d}{dT}(g_{*s}^{1/3}(T)Ta) = \frac{1}{3}g_{*s}^{-2/3} \frac{dg_{*s}}{dT} Ta + g_{*s}^{1/3} a + g_{*s}^{1/3} Ta H \frac{dt}{dT} \\ &= \frac{1}{3} \frac{d \log g_{*s}}{d \log T} + 1 + H \frac{dt}{d \log T}. \end{aligned} \quad (\text{A.79})$$

We can relate time derivatives of a generic function ξ to temperature derivatives through the following relation:

$$\frac{d\xi}{dt} = - \left(1 + \frac{1}{3} \frac{d \log g_{*s}}{d \log T} \right)^{-1} H \frac{d\xi}{d \log T}. \quad (\text{A.80})$$

This expression is completely general and it is valid throughout the FRW thermal history.

Appendix B

Λ CDM on small scales

The CDM hypothesis emerged in the early 1980s and quickly became a central element of the theory of cosmic structure formation. By the end of the 1990s, the pure CDM model with scale-invariant primordial fluctuations and a critical matter density had run against many observational pieces of evidence: the shape of the galaxy power spectrum, estimates of the mean matter density from galaxy clusters and galaxy motions, the age of the Universe inferred from estimates of the Hubble constant, and the amplitude of matter density contrast predicted from the fluctuations measured in the CMB. To address these challenges, many variants of the pure CDM were proposed and, by the new century, the combination of supernova evidence for cosmic acceleration and CMB witness for a flat Universe led to the need to incorporate a cosmological constant Λ and inflationary initial conditions to give the Λ CDM model.

B.1 Controversies

On scales larger than those of the stellar distribution in normal galaxies (> 10 kpc), the predictions of Λ CDM have been amply tested, and, although neither semianalytic theory nor numerical simulations can yet match all experimental data, the correspondence between calculation and observation is now good enough to guarantee that at large scales the Λ CDM model is correct. This model is the best way we have to account for the most important observed features of our Universe, such as its accelerated expansion, the abundances of light elements and Big Bang Nucleosynthesis, the CMB and the formation of large scale structures. Moreover, the initial spectral index of the perturbations normalized to the observed fluctuations in the CMB is slightly less than unity, consistently with an early inflationary stage. The power spectrum of these matter density fluctuations, determined at redshift $z \sim 10^3$ by observations of the CMB, correctly produces the present time power spectrum, at redshift $z = 0$, with per cent precision, even though the amplitude changes over 5 orders of magnitude.

However, on small, galactic scales $\lesssim 10$ kpc, the Λ CDM predictions of the distribution of DM are, in most cases, inconsistent with observations. Following the short review in [48] and the analysis in [49] we summarize the three main problems.

The cusp-core problem N -body simulations with initial linear fluctuations in a Λ CDM framework evince that the formed non-linear DM structures (called *halos* if isolated, *subhalos* if embedded in a larger halo) show singular density cusps at their centres. In fact, the density profile of a halo of mass $M = (4\pi r_v^3/3)200\rho_b$, with r_v the virial radius (defined as the radius at which the density is 200 times the background one) and ρ_b the background density of the Universe, follows the fitting form found by Navarro, Frank and White (NFW) [50, 51]

$$\rho(r, M) \simeq \frac{200}{3} f(C) \rho_b \left(\frac{r}{R_c} \right)^{-\alpha} \left(1 + \frac{r}{R_c} \right)^{-2}. \quad (\text{B.1})$$

The factor $f(C)$ is defined as $f(C) = C^3 [\log(1+C) - C(1+C)^{-1}]^{-1}$ with C a concentration parameter varying from halo to halo and weakly depending on its mass, and R_c is the characteristic radius of the halo, defined as the radius at which $d \log \rho / d \log r = -2$; it can also be expressed as $R_c = r_v / C$. The profile implies a cuspy behaviour $\rho \sim r^{-\alpha}$ inside the characteristic radius, with $\alpha \in [1, 1.5]$. Instead, observations of DM-dominated dwarf spherical galaxies (dSphs) and low surface brightness galaxies are in general better described by a cored density profile. As shown in Fig. B.1, the inner mass profile of a DM halo can be probed by rotation curve measurements: for circular motions in a spherical matter distribution, the rotation speed is simply

$$v(r) = \sqrt{\frac{GM(r)}{r}}, \quad (\text{B.2})$$

and it can be estimated from neutral-hydrogen redshift lines. It is evident that once normalized to match the observed rotation at large radii, the NFW halo overpredicts the rotation speed in the inner few kpc, by a factor of two or more. Indeed, many authors have reported evidence that the Milky Way satellites Fornax and Sculptor have cored density profiles.

The missing satellite problem Fig. B.2 left panel illustrates the “missing satellite” problem. N -body simulations show that DM halos retain a large number of substructures formed by earlier collapses on smaller scales hierarchically, predicting hundreds or thousands of subhalos, on which luminous galaxies could have formed [48]. Since there are about ten dwarf satellite galaxies known within the ~ 250 kpc virial radius of the Milky Way halo, a comparison suggests that the predicted satellite population far exceeds the observed one¹. Another way of stating the problem is that the number density of galaxies varies with their

¹Actually establishing the “correspondence” between satellite stellar dynamics and subhalo properties is a key technical point we won’t address here.

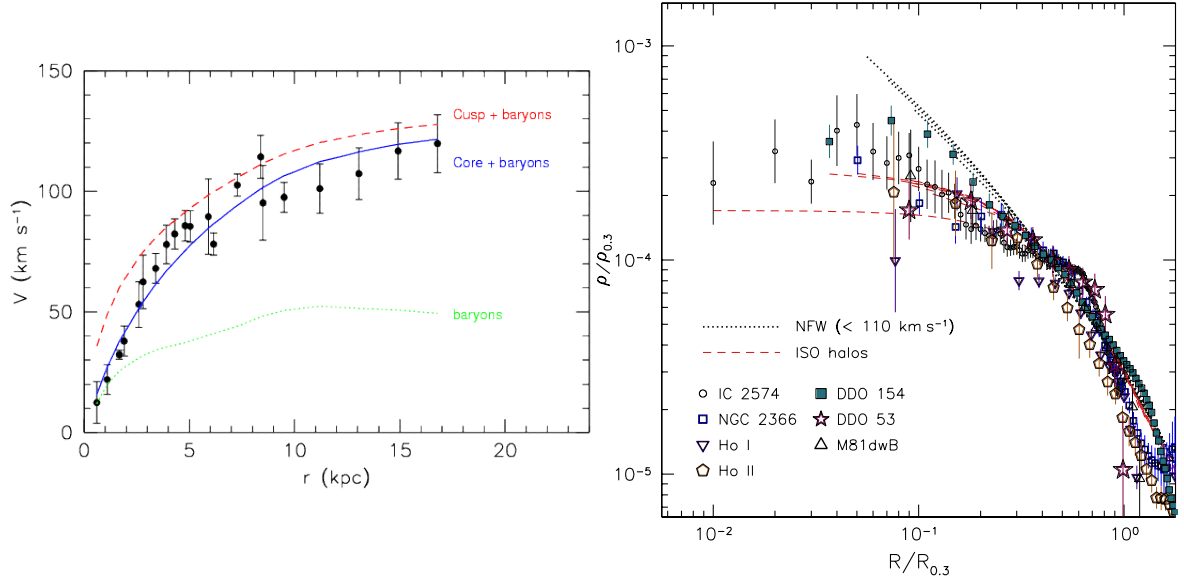


Figure B.1: The cusp core problem. Left: the measured rotation curve of F568-3 (points) compared to model fits assuming a cored DM halo (blue solid curve) or a cuspy DM halo with an NFW profile (red dashed curve), concentration $C = 9.2$, $v = 110 \text{ km s}^{-1}$, published by [52]. The dotted green curve shows the contribution of baryons (stars+gas) to the rotation curve, which is included in both model fits. Right: DM halo density profiles inferred from rotation curves of seven low surface brightness galaxies, from [53]. The dotted black curve indicates the cuspy density profile that diverges toward small radii and characterises CDM halos formed in N -body simulations. Profiles inferred from observations of real galaxies (dashed red curves) tend to be cored, converging to approximately constant central density.

total stellar mass roughly as $dn(M_\star) \propto M_\star^{-1.2} dM_\star$ while the predicted number density of halos increases with decreasing halo mass much more steeply, $dn(M_h) \propto M_h^{-2} dM_h$ [55].

The too-big-to-fail problem As we can see from Fig. B.2, right, the mass in the central regions of the subhalos in simulations exceeds the mass inferred from stellar dynamics of observed dwarfs, by a factor ~ 5 . In principle it might be that these massive subhalos are dark, i.e. they do not host any galaxy, and that the observed dwarfs reside in less massive hosts but this explanation is quite unphysical. Therefore, in its present form, this problem is related to the cusp-core problem: numerical simulations of CDM structure formation predict too much mass in the central regions of halos and subhalos.

To summarize, we can say that none of the key features associated to the CDM model on galactic scales has ever been detected.

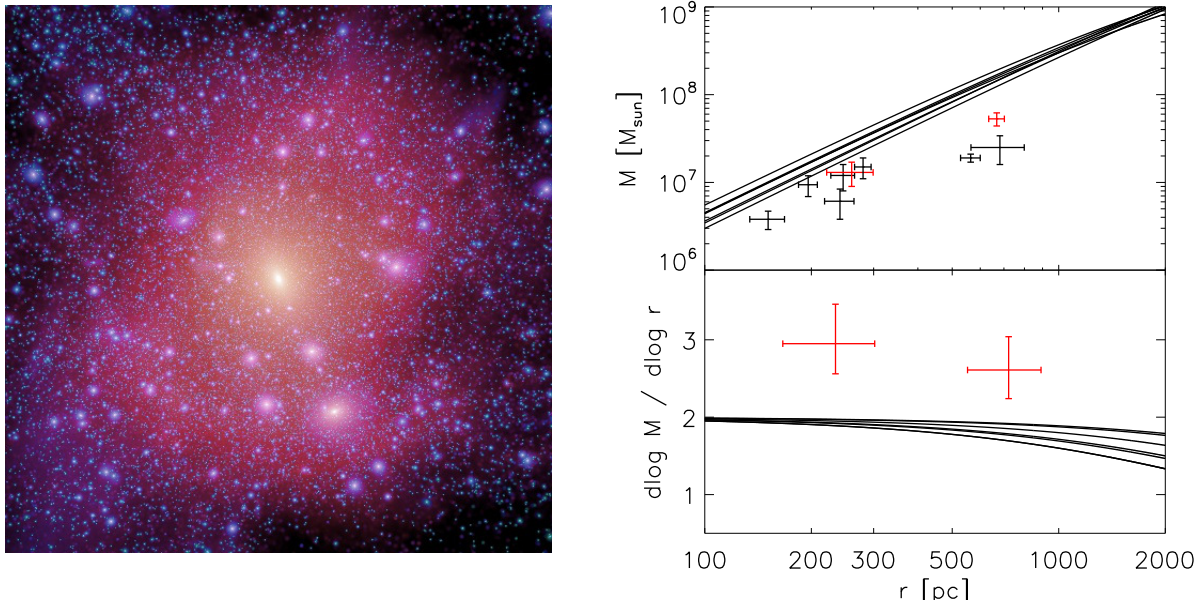


Figure B.2: Left: the missing satellites problem. Spatial distribution of DM (pixel brightness scales with density) obtained in the $\sim 1 \text{ Mpc}^2$ simulation box from a high-resolution Λ CDM N -body simulation by [54]. The simulated DM distribution shows much richer substructure than does the observed luminous distribution, e.g. considering Andromeda’s or Milky Way’s satellites. Right: the too-big-to-fail problem. Black curves display profiles of enclosed mass, $M(r)$ (top), and its logarithmic slope (bottom), for the most massive CDM subhalos formed in simulations of the Milky Way neighbourhood. Data points indicate estimates of (i) dynamical masses enclosed within the projected half-light radii of the Milky Way’s most luminous dwarf spheroidal satellites and, for two dwarfs (shown in red) with estimated core sizes, (ii) the slopes defined by masses enclosed within the different half-light radii of distinct stellar subpopulations. With respect to observations of real dwarf satellites, the simulated subhalos have more mass enclosed at the measured half-light radii and their enclosed-mass profiles have shallower slopes. Figure from [49].

B.2 Possible solutions

There are mainly two ways by which the small scale conflicts between N -body predictions and observed galaxy properties can be solved: one is through complex “baryonic physics” (gas cooling, star formation, and associated feedback), the other is to require different properties of the DM itself.

B.2.1 Baryonic physics

As stated in [55], the missing satellite and too-big-to-fail problems might be solved by baryonic physics that causes the efficiency of transforming baryons into stars to be lower in systems of lower mass. The idea is that molecular cooling physics may make star formation

efficiency highly stochastic at a halo mass as high as $10^{10} M_{\odot}$, such that even the Milky Way's most massive subhalos are not too-big-to-fail; then, ram pressure in the galactic halo could remove the gas from the dark subhalos. Consequently, thousands of optically invisible low-mass halos, $M_h \lesssim 10^{8.5} M_{\odot}$ are predicted to exist in our Galaxy and others.

The cusp-core problem is addressed by considering supernovae explosions that blow out baryonic material, leaving the halo less concentrated. Another point of view is to consider the feedback of these explosions on the gravitational potential: the rapid fluctuations pump energy into the DM orbits so they no longer penetrate the centre of the halo, leading to a nearly constant density core. However, there is no agreement on the fact that the model can work for dwarf galaxies with masses $M_{\star} < 10^7 M_{\odot}$ which, having few stars, i.e. a small baryonic fraction, have not the necessary supernovae reservoir to create DM cores of ~ 1 kpc. Therefore it is argued that isolated dwarf galaxies, being DM-dominated, cannot receive a significant contribution from baryonic physics. The fact that the central density problem persists even for these systems [48] somehow calls for a solution to the small-scale shortcomings to be found in the DM sector, rather than in complex baryonic physics.

B.2.2 Warm dark matter

Instead of the relevance of complex baryonic effects, the small-scale problems could indicate a failure of the CDM hypothesis itself. One potential solution is to consider Warm Dark Matter (WDM), e.g. thermal relics with a mass around 1 keV so that its higher free-streaming velocities in the early Universe are large enough to suppress primordial fluctuations on sub-galactic scales. In this case, the linear power spectrum with WDM would be suppressed below the free-streaming scale, and there will be no room for low-mass halos or subhalos. Although the collisionless collapse of WDM would lead nevertheless to a cuspy halo [48], the central concentration is lower when the mass scale is close to the spectral cutoff: the mass function drops at low masses because there are no small scale perturbations to produce collapsed objects. This can drive predictions into an agreement with dwarf satellite observations. However, WDM is an *ad hoc* solution to the CDM problems on small scales and remarkably it encounters further shortcomings. In particular, WDM would be even too efficient in erasing small scale structures such that we would face the opposite problem of not being able to take into account the few subhalos needed to host the Milky Way's known satellites. Moreover, constraints at high redshift, e.g. from the Lyman- α forest [56], put lower bounds on the WDM particle mass forcing it to be colder. Nevertheless, WDM can alleviate the CDM shortcomings on small scales.

B.2.3 Self Interacting dark matter

An interesting idea is to consider strong self-interactions among DM particles, i.e. Self Interacting Dark Matter (SIDM). The idea is that the halo is thermalized by elastic scatterings so that a core of constant density is created. In the work of [57] it is shown that there is a region of parameter space for the cross-section and mass where SIDM can

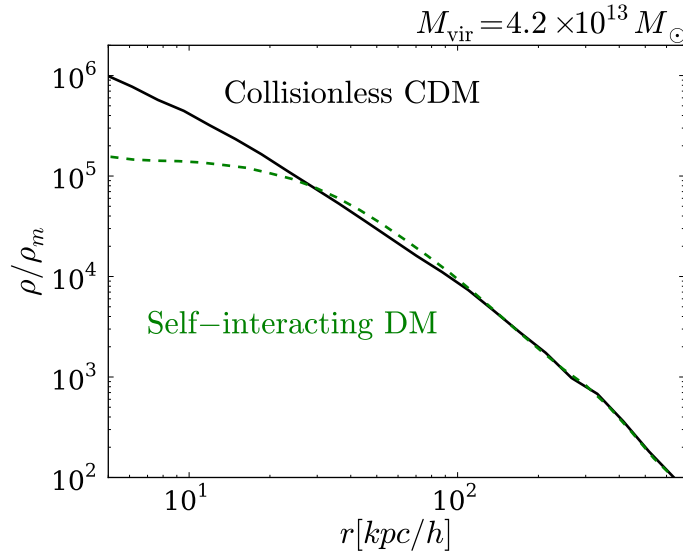


Figure B.3: Effect of self-interacting dark matter (SIDM) on halo structure, from simulations by [57], with cross-section of $\sigma \simeq 1$ barn. The plot shows clearly the flattening in the core due to elastic scattering comparing, CDM and SIDM halo density profiles.

be consistent with observations while giving cored halo profiles. In Fig. B.3, we see a comparison between the density profiles of CDM and SIDM in case of a self-interaction cross-section of $\sigma \simeq 1$ barn (i.e. a nuclear cross-section approximately): the collisions flatten the cusp and favour spherical symmetry over triaxiality. Moreover, despite being more easily subject to tidal disruption caused by the fact that SIDM is less bound, SIDM subhalos are produced in a fair number to match the number of satellites of the Milky Way. Also, triaxiality is preserved to a certain degree such that it fits data. So, unlike standard WDM, SIDM is still a viable DM model and it is being tested and deepened both from the particle physics sector and from the astrophysical and cosmological observation point of view.

Appendix C

The collision operator from first principles

In this appendix, we want to understand from first principles the form of the collision operator, the right-hand side of the Boltzmann equation. This term only accounts for processes (scatterings and decays) in which the particle, whose phase-space distribution we are studying, is involved. Therefore the form of the collision operator is completely independent of the geometry of the spacetime we are considering, i.e. of the metric. Hence, we can find the general expression for the collision operator in the simplest case of a Minkowski spacetime with metric

$$ds^2 = -dt^2 + \delta_{ij} dx^i dx^j. \quad (\text{C.1})$$

Moreover, we will consider a finite region of space, a box of volume V in which the particle of interest χ is involved in the generic process

$$\chi + a + \dots + b \longrightarrow i + j + \dots + k, \quad (\text{C.2})$$

with n particles in the initial state and m particles in the final state. We define the collision operator simply as the right-hand side of the Boltzmann equation; we put ourselves in a relativistic framework and write the Boltzmann equation in the Lorentz-invariant (or in general covariant) form

$$L[f_\chi] = C[f_\chi], \quad (\text{C.3})$$

for the phase-space distribution $f_\chi(x^\mu, p^\mu)$. For our simple choice of the metric, Eq. 2.8 gives

$$L[f_\chi] = E_\chi \frac{df_\chi}{dt} \quad (\text{C.4})$$

since the affine connection coefficients are identically zero and homogeneity assures $f_\chi = f_\chi(t, |\vec{p}|)$ is independent on positions and directions of momenta. Notice that, if there were no collisions, $C[f_\chi] = 0$, the result of the Boltzmann equation would be that the phase-

space distribution is constant in time. Instead, if collisions are present, the phase-space distribution is altered and evolves in time.

From its definition, if we integrate f_χ over the whole phase-space, we get the number of χ particles in the box N_χ

$$g_\chi \int \frac{V d^3 p}{(2\pi)^3} f_\chi = N_\chi \quad (\text{C.5})$$

with g_χ the number of internal degrees of freedom of the χ particle. Taking the time derivative of both sides of Eq. (C.5), we can use the Boltzmann equation,

$$C[f_\chi] = E_\chi \frac{df_\chi}{dt} \quad (\text{C.6})$$

to get a physical understanding of the collision operator

$$g_\chi \int \frac{V d^3 p}{(2\pi)^3} \frac{C[f_\chi]}{E_\chi} = \frac{dN_\chi}{dt}. \quad (\text{C.7})$$

Defining the Lorentz-invariant measure

$$d\Pi = \frac{g d^3 p}{(2\pi)^3 2E}, \quad (\text{C.8})$$

we have

$$\int V d\Pi_\chi C[f_\chi] = \frac{1}{2} \frac{dN_\chi}{dt}. \quad (\text{C.9})$$

The collision operator accounts for the time variation of the phase-space distribution and it is responsible for the possible change in the number of χ particles in the box due to the processes considered. To find the explicit expression for the collision operator, we have to derive from first principles the right-hand side of the above equation. Throughout the discussion and also in our work, we neglect possible quantum degeneracies effects due to the quantum nature of the particles involved. The change in the number of χ particles in the box in the time interval dt is given, naively by

$$\begin{aligned} \frac{dN_\chi}{dt} &= \text{rate of collisions} \times \text{number of initial state particles} \\ &= \frac{dw}{dt} \times N_{\text{initial}} \end{aligned} \quad (\text{C.10})$$

where

$$N_{\text{initial}} = g_\chi \cdots g_b \int \frac{V d^3 p_\chi \cdots V d^3 p_b}{(2\pi)^3 \cdots (2\pi)^3} f_\chi \cdots f_b, \quad (\text{C.11})$$

is, by definition, the total number of initial state particles. Instead, dw/dt is the probability for the process to happen per time interval dt . We want to find the correct Lorentz-invariant form for this factor. Following [40] we consider the S-matrix element between the initial $|i\rangle$

and final state $\langle f|$, which is of the form

$$S_{fi} = \langle f|i\rangle = \delta_{fi} + i(2\pi)^4 \delta^{(4)}(P_i - P_f) \frac{1}{(2E_\chi V)^{1/2} \cdots (2E_b V)^{1/2} (2E_i V)^{1/2} \cdots (2E_k V)^{1/2}} \overline{\mathcal{M}}, \quad (\text{C.12})$$

with $P_i = p_\chi + p_a + \cdots + p_b$ and $P_f = p_i + p_j + \cdots + p_k$ for the ease of notation. Here $\overline{\mathcal{M}}$ is the matrix element of the process, such that its squared modulus $|\overline{\mathcal{M}}|^2$ is *summed* over final spin states and *averaged* over initial spin states. We have normalized the matrix element with the Lorentz-invariant normalization of both initial and final states in the Fock space. The probability for the process to happen is proportional to the squared S -matrix element. Since initial and final states are different, we get [40]

$$|S_{fi}|^2 = (2\pi)^4 \delta^{(4)}(P_i - P_f) \frac{V dt}{(2E_\chi V) \cdots (2E_b V)(2E_i V) \cdots (2E_k V)} |\overline{\mathcal{M}}|^2, \quad (\text{C.13})$$

having regularized time and space

$$(2\pi)^4 \delta^{(4)}(0) = V dt. \quad (\text{C.14})$$

The desired probability is obtained summing sum this expression over all final states $\langle f|$. Since we are working in a finite volume V , this is the sum over the possible discrete values of the momenta of the final particles. In the large-volume limit for each particle, we can write the sum over momenta in the continuum limit as

$$\sum_{\vec{p}_i \cdots \vec{p}_k} \simeq \int \frac{V d^3 p_i \cdots V d^3 p_k}{(2\pi)^3 \cdots (2\pi)^3}, \quad (\text{C.15})$$

as we have done to integrate over the whole phase-space. Therefore our desired probability rate reads

$$\frac{dw}{dt} = \int \frac{V d^3 p_i \cdots V d^3 p_k}{(2\pi)^3 \cdots (2\pi)^3} (2\pi)^4 \delta^{(4)}(P_i - P_f) \frac{V}{(2E_\chi V) \cdots (2E_b V)(2E_i V) \cdots (2E_k V)} |\overline{\mathcal{M}}|^2. \quad (\text{C.16})$$

We have V^{m+1} at the numerator and a V^{n+m} at the denominator. Moreover, we can introduce Lorentz-invariant measures $d\Pi$ for the final states particles, giving

$$\frac{dw}{dt} = \int d\Pi_i \cdots d\Pi_k (2\pi)^4 \delta^{(4)}(P_i - P_f) \frac{V^{1-n}}{(2E_\chi) \cdots (2E_b)} \frac{|\overline{\mathcal{M}}|^2}{g_i \cdots g_k} \cdots \quad (\text{C.17})$$

We now introduce the squared matrix element *averaged* over both initial and final states

$$|\mathcal{M}|^2 = \frac{|\overline{\mathcal{M}}|^2}{g_i \cdots g_k}, \quad (\text{C.18})$$

we use throughout this work. We can now compute the change in the number of χ particles

in the time interval dt taking the product of Eq. (C.11) and Eq. (C.17):

$$\frac{dN_\chi}{dt} = \int d\Pi_i \cdots d\Pi_k (2\pi)^4 \delta^{(4)}(P_i - P_f) \frac{V^{1-n}}{(2E_\chi) \cdots (2E_b)} |\mathcal{M}|^2 g_\chi \cdots g_b \frac{V d^3 p_\chi \cdots V d^3 p_b}{(2\pi)^3 \cdots (2\pi)^3} f_\chi \cdots f_b. \quad (\text{C.19})$$

Now we have $V^{1-n} \times V^n = V$ at the numerator. Moreover, we can collect Lorentz-invariant measures for the initial state particles, obtaining finally

$$\frac{dN_\chi}{dt} = \int d\Pi_\chi \cdots d\Pi_b d\Pi_i \cdots d\Pi_k (2\pi)^4 \delta^{(4)}(P_i - P_f) V |\mathcal{M}|^2 f_\chi \cdots f_b. \quad (\text{C.20})$$

Now we can compare Eqs. (C.9) and (C.20) to obtain the expression for the collision operator for the above process:

$$C[f_\chi] = \frac{1}{2} \int d\Pi_a \cdots d\Pi_b d\Pi_i \cdots d\Pi_k (2\pi)^4 \delta^{(4)}(p_\chi + \cdots + p_b - p_i - \cdots - p_k) |\mathcal{M}|^2 f_\chi \cdots f_b. \quad (\text{C.21})$$

We remark that this form for the collision operator is valid in general, independently of the chosen metric, since it is based only on a relativistic treatment of scatterings.

Appendix D

Collision terms for various processes

In this appendix, we find the explicit form of the collision term C for various processes, which is needed to write and solve the Boltzmann equation for the phase-space distribution f_χ . We will neglect the quantum statistics for particles χ so that the collision term is independent on f_χ . We consider the three most recurrent cases: two-body decays, $2 \rightarrow 2$ scatterings and also three-body decays.

D.1 Two-body decays

Neglecting the Pauli-blocking and Bose-enhancement effects for the particle χ , $1 \mp f_\chi \simeq 1$, the collision term for decays

$$1 \rightarrow 2 + \chi \tag{D.1}$$

is

$$\frac{g_\chi C(T, p)}{E} = \frac{g_\chi}{2E} \int d\Pi_1 d\Pi_2 (2\pi)^4 \delta^{(4)}(p_1 - p_2 - p) |\mathcal{M}_{1 \rightarrow 2\chi}|^2 f_1(T, E_1) (1 \mp f_2(T, E_2)). \tag{D.2}$$

We denote quantities relative to χ without any subscript and $p_i = (E_i, \vec{p}_i)$ are four-momenta of $i = 1, 2$ particles. Here $|\mathcal{M}_{1 \rightarrow 2\chi}|^2$ is the process amplitude squared averaged over both initial and final degrees of freedom. This is independent of any momentum, since we can find the momenta of the decay products in the particle 1 centre-of-mass frame p_\star as functions of masses only solving the equation

$$m_1 = \sqrt{m_2^2 + p_\star^2} + \sqrt{m_\chi^2 + p_\star^2}. \tag{D.3}$$

Being the amplitude a Lorentz scalar, it is independent on the frame we are computing it. We can use the three-dimensional Dirac delta $\delta^{(3)}(\vec{p}_1 - \vec{p}_2 - \vec{p})$ to get rid of the integration

in d^3p_1 . We obtain

$$\frac{g_\chi C(T, p)}{E} = \frac{g_\chi g_1}{2E} |\mathcal{M}_{1 \rightarrow 2\chi}|^2 \int d\Pi_2(2\pi) \delta(E_1 - E_2 - E) f_1(T, E_1) [1 \mp f_2(T, E_2)], \quad (\text{D.4})$$

with now E_1 a fixed function

$$E_1 = E_1(p, p_2, \cos \theta) = \sqrt{m_1^2 + (\vec{p}_2 + \vec{p})^2} = \sqrt{m_1^2 + p^2 + p_2^2 + 2pp_2 \cos \theta}, \quad (\text{D.5})$$

getting back to the notation $p_i \equiv |\vec{p}_i|$ and calling θ the angle between vectors \vec{p} and \vec{p}_2 . Let us write the integral in a more explicit form, performing the trivial integration over all the angles but θ

$$\begin{aligned} \frac{g_\chi C(T, p)}{E} = & \frac{g_\chi g_1 g_2}{2E} |\mathcal{M}_{1 \rightarrow 2\chi}|^2 \int \frac{(2\pi) p_2 E_2 dE_2 d\cos \theta}{(2\pi)^2 4E_1(p, p_2, \cos \theta) E_2} \delta(E_1(p, p_2, \cos \theta) - E_2 - E) \\ & \times f_1(T, E_1(p, p_2, \cos \theta)) [1 \mp f_2(T, E_2)] \end{aligned} \quad (\text{D.6})$$

We can exploit the remaining Dirac delta to perform the integration over $\cos \theta$. From the conservation of energy we find

$$E_1(p, p_2, \cos \theta) = E_2 + E \implies \cos \theta^* = \frac{(E_2 + E)^2 - m_1^2 - p^2 - p_2^2}{2pp_2}. \quad (\text{D.7})$$

Using the properties of the delta function,

$$\delta(E_1(p, p_2, \cos \theta) - E_2 - E) = \frac{E_1(p, p_2, \cos \theta)}{pp_2} \delta(\cos \theta - \cos \theta^*), \quad (\text{D.8})$$

we can perform the integration over $\cos \theta$.

$$\begin{aligned} \frac{g_\chi C(T, p)}{E} = & \frac{g_\chi g_1 g_2}{16\pi E p} |\mathcal{M}_{1 \rightarrow 2\chi}|^2 \int_0^\infty dE_2 f_1(T, E_1(p, p_2, \cos \theta^*)) [1 \mp f_2(T, E_2)] \\ & \times \int_{-1}^{+1} d\cos \theta \delta(\cos \theta - \cos \theta^*) \end{aligned} \quad (\text{D.9})$$

The integral over $\cos \theta$ gives 1 if $\cos \theta^* \in [-1, 1]$ and 0 otherwise. This puts a constraint on the possible values of E_2 we can integrate over, i.e. assuming the integral over $\cos \theta$ is 1 leads to integration over energies which has to satisfy

$$\frac{(E_2 + E)^2 - m_1^2 - p^2 - p_2^2}{2pp_2} = \cos \theta^* \in [-1, 1]. \quad (\text{D.10})$$

This means we can find the limiting solutions from the equation

$$\sqrt{m_1^2 + (p \pm p_2)^2} = \sqrt{m_2^2 + p_2^2} + \sqrt{m_\chi^2 + p^2}, \quad (\text{D.11})$$

for $\cos \theta^* = \pm 1$. We solve these equations for momentum p_2 and find

$$\begin{aligned} p_2^+ &= \frac{p(m_1^2 - m_2^2 - m_\chi^2) \pm \sqrt{(p^2 + m_\chi^2)k(m_1, m_2, m_\chi)}}{2m_\chi^2} & \text{if } \cos \theta^* = +1 \\ p_2^- &= \frac{-p(m_1^2 - m_2^2 - m_\chi^2) \pm \sqrt{(p^2 + m_\chi^2)k(m_1, m_2, m_\chi)}}{2m_\chi^2} & \text{if } \cos \theta^* = -1 \end{aligned} \quad (\text{D.12})$$

remembering $k(b, c, d) \equiv [b^2 - (c + d)^2][b^2 - (c - d)^2]$. However, since $p_i > 0$ and $m_1^2 \geq (m_2 + m_\chi)^2 \geq m_2^2 + m_\chi^2$ to allow the decay, the physical solutions are only two of them

$$\begin{aligned} p_2^+ &= \frac{p(m_1^2 - m_2^2 - m_\chi^2) + \sqrt{(p^2 + m_\chi^2)k(m_1, m_2, m_\chi)}}{2m_\chi^2} & \text{if } \cos \theta^* = +1 \\ p_2^- &= \left| \frac{p(m_1^2 - m_2^2 - m_\chi^2) - \sqrt{(p^2 + m_\chi^2)k(m_1, m_2, m_\chi)}}{2m_\chi^2} \right| & \text{if } \cos \theta^* = -1 \end{aligned} \quad (\text{D.13})$$

Clearly Eq. (D.10) is satisfied for $p_2 \in [p_2^-, p_2^+]$. These two expressions are not valid explicitly if $m_\chi = 0$, so we provide limiting expressions for $m_\chi \ll m_2, m_1$, which will be exploited in our work:

$$\begin{aligned} p_2^+ &= p \left(\frac{m_1^2 - m_2^2}{m_\chi^2} - \frac{m_1^2}{m_1^2 - m_2^2} \right) + \frac{m_1^2 - m_2^2}{4p} + \mathcal{O}(m_\chi^2), \\ p_2^- &= p \left(\frac{m_2^2}{m_1^2 - m_2^2} \right) - \frac{m_1^2 - m_2^2}{4p} + \mathcal{O}(m_\chi^2). \end{aligned} \quad (\text{D.14})$$

We see that, for $m_\chi \rightarrow 0$ we have $p_2^+ \rightarrow \infty$, while p_2^- is finite. At the end, we are left with only the integral over $E_2 \in [E_2^-, E_2^+]$ with

$$E_2^\pm = \sqrt{m_2^2 + (p_2^\pm)^2}, \quad (\text{D.15})$$

reading

$$\frac{g_\chi C(T, p)}{E} = \frac{g_\chi g_1 g_2}{16\pi} \frac{|\mathcal{M}_{1 \rightarrow 2\chi}|^2}{Ep} \int_{E_2^-}^{E_2^+} dE_2 f_1(T, E_2 + E) [1 \mp f_2(T, E_2)]. \quad (\text{D.16})$$

This is the general result for any distribution functions $f_{1,2}$. The integral can be computed numerically if one knows their expressions. However, if we assume thermal distributions¹

$$f_i^{\text{eq}}(T, E_i) = \left\{ 1 \pm e^{E_i/T} \right\}^{-1}, \quad (\text{D.17})$$

¹The \pm signs refer to fermions and bosons respectively, they are not associated with the solutions p_2^\pm .

we can perform the integral analytically, obtaining

$$\frac{g_\chi C(T, p)}{E} = \frac{g_\chi g_1 g_2}{16\pi} |\mathcal{M}_{1 \rightarrow 2\chi}|^2 \frac{T}{Ep} h_{\text{eq}}(T, p), \quad (\text{D.18})$$

with $h_{\text{eq}}(T, p)$ depending on the quantum statistics of 1 and 2:

$$h_{\text{eq}} = \begin{cases} 2 \log \left[\frac{1 + e^{-(E_2^- + E)/T}}{1 + e^{-(E^+ + E)/T}} \right] + \frac{1}{e^{E/T} - 1} \log \left[\left(\frac{1 + e^{E_2^+/T}}{1 + e^{E_2^-/T}} \right) \left(\frac{1 + e^{(E_2^- + E)/T}}{1 + e^{(E^+ + E)/T}} \right) \right] & 1 \text{ FD, } 2 \text{ FD} \\ -2e^{E/T} \log \left[\frac{1 + e^{-(E_2^- + E)/T}}{1 + e^{-(E^+ + E)/T}} \right] + \frac{1}{e^{E/T} + 1} \log \left[\left(\frac{1 + e^{E_2^-/T}}{1 + e^{E_2^+/T}} \right) \left(\frac{1 - e^{(E_2^- + E)/T}}{1 - e^{(E^+ + E)/T}} \right) \right] & 1 \text{ BE, } 2 \text{ FD} \\ \frac{1}{1 - e^{E/T}} \log \left[\frac{\sinh \left(\frac{E_2^+}{2T} \right) \sinh \left(\frac{E + E_2^-}{2T} \right)}{\sinh \left(\frac{E_2^-}{2T} \right) \sinh \left(\frac{E + E_2^+}{2T} \right)} \right] & 1 \text{ BE, } 2 \text{ BE} \\ \frac{1}{1 + e^{E/T}} \log \left[\frac{\sinh \left(\frac{E_2^+}{2T} \right) \cosh \left(\frac{E + E_2^-}{2T} \right)}{\sinh \left(\frac{E_2^-}{2T} \right) \cosh \left(\frac{E + E_2^+}{2T} \right)} \right] & 1 \text{ FD, } 2 \text{ BE} \end{cases} \quad (\text{D.19})$$

A simpler form is obtained if we neglect the quantum behaviour of particle 2, assuming $(1 \mp f_2) \simeq 1$

$$h_{\text{eq}}(T, p) = \pm \log \left[\frac{1 \pm e^{-(E_2^- + E)/T}}{1 \pm e^{-(E^+ + E)/T}} \right], \quad (\text{D.20})$$

with + sign if 1 is a fermion, – if it is a boson. This formula agrees with the one found in [64, 67]. Furthermore, if we neglect the quantum nature of all particles and assume a Maxwell-Boltzmann statistics for particle 1, i.e. $f_1 \simeq e^{-(E+E_2)/T}$, we end up simply with

$$h_{\text{eq}}^{\text{MB}}(T, p) = e^{-(E_2^- + E)/T} - e^{-(E_2^+ + E)/T}. \quad (\text{D.21})$$

D.2 Scatterings

D.2.1 Single production

Now we focus on scatterings of the type

$$1 + 2 \longrightarrow 3 + \chi. \quad (\text{D.22})$$

The general collision term is

$$\frac{g_\chi C(T, p)}{E} = \frac{g_\chi}{2E} \int d\Pi_1 d\Pi_2 d\Pi_3 (2\pi)^4 \delta^{(4)}(p_1 + p_2 - p_3 - p) |\mathcal{M}_{12 \rightarrow 3\chi}|^2 F_{123}(T, E_1, E_2, E_3), \quad (\text{D.23})$$

where we have defined $F_{123} = f_1(T, E_1) f_2(T, E_2) (1 \mp f_3(T, E_3))$. The integration is better performed in terms of Lorentz-invariant quantities such as the Mandelstam variables s and

t :

$$\begin{aligned} s &= -(p_1 + p_2)^2 = -(p_3 + p)^2, \\ t &= -(p_1 - p)^2 = -(p_3 - p_2)^2. \end{aligned} \quad (\text{D.24})$$

Indeed, unlike the case of decays, the averaged squared amplitude is not constant in general but it is a function of s and t . Therefore we will not be able to take it out of the integrals. Let us recast the integrals over p_1 and p_2 in a more convenient form. First, we remove the integration over p_2 exploiting the three-dimensional part of the Dirac delta

$$\frac{d^3 p_1}{(2\pi)^3 2E_1} \frac{d^3 p_2}{(2\pi)^3 2E_2} (2\pi)^4 \delta^{(4)}(p_1 + p_2 - p_3 - p) = \frac{2\pi d \cos \theta_{1\chi} p_1^2 dp_1}{(2\pi)^2 4E_1 E_2^*} \delta(E_1 + E_2^* - E_3 - E), \quad (\text{D.25})$$

where $E_2^* = \sqrt{m_2^2 + (\vec{p}_3 + \vec{p} - \vec{p}_1)^2}$ and $\theta_{1\chi}$ is the angle between \vec{p}_1 and \vec{p} . Now we exploit the Lorentz invariance of measures $d\Pi_1$ and $d\Pi_2$ to evaluate them in the centre-of-mass frame. In this frame, momenta of 1 and 2 are equal and opposite in direction $\vec{p}_{12} = -\vec{p}_{21}$ and moreover, their modulus is fully determined as a function of s when we exploit the delta function

$$s = \left(\sqrt{m_1^2 + p_{12}^2} + \sqrt{m_2^2 + p_{12}^2} \right)^2 \implies p_{12}(\sqrt{s}) = \frac{k^{1/2}(\sqrt{s}, m_1, m_2)}{2\sqrt{s}}. \quad (\text{D.26})$$

The same happens for particles 3 and χ :

$$s = \left(\sqrt{m_3^2 + p_{3\chi}^2} + \sqrt{m_\chi^2 + p_{3\chi}^2} \right)^2 \implies p_{3\chi}(\sqrt{s}) = \frac{k^{1/2}(\sqrt{s}, m_3, m_\chi)}{2\sqrt{s}}. \quad (\text{D.27})$$

In the centre-of-mass the constrained energy of particle 2 is $E_2^* = \sqrt{m_1^2 + p_{12}^2}$. So evaluating everything in the centre-of-mass frame the right hand side of Eq. (D.25) reads

$$\frac{d \cos \theta_{1\chi} p_{12}^2 dp_{12}}{8\pi E_1^{\text{cm}} E_2^{*,\text{cm}}} \delta \left(\sqrt{m_1^2 + p_{12}^2} + \sqrt{m_2^2 + p_{12}^2} - \sqrt{s} \right). \quad (\text{D.28})$$

We trade the integration over $\cos \theta_{1\chi}$ for an integration over t ,

$$t = m_1^2 + m_\chi^2 - 2(E_1^{\text{cm}} E_\chi^{\text{cm}} - p_{12} p_{3\chi} \cos \theta_{1\chi}) \implies d \cos \theta_{1\chi} = \frac{dt}{2p_{12} p_{3\chi}}. \quad (\text{D.29})$$

Using the properties of the Dirac delta, we make it a function of p_{12} to eliminate the integration over this variable.

$$\delta \left(\sqrt{m_1^2 + p_{12}^2} + \sqrt{m_2^2 + p_{12}^2} - \sqrt{s} \right) = \frac{E_1^{\text{cm}} E_2^{*,\text{cm}}}{p_{12} \sqrt{s}} \delta[p_{12} - p_{12}(\sqrt{s})]. \quad (\text{D.30})$$

Exploiting these relations, we are now able to conclude that

$$\frac{d^3 p_1}{(2\pi)^3 2E_1} \frac{d^3 p_2}{(2\pi)^3 2E_2} (2\pi)^4 \delta^{(4)}(p_1 + p_2 - p_3 - p) = \frac{dt}{16\pi p_{3\chi}(\sqrt{s}) \sqrt{s}}. \quad (\text{D.31})$$

Hence the collision term reads

$$\frac{g_\chi C(T, p)}{E} = \frac{g_\chi g_1 g_2 g_3}{32\pi E} \int \frac{d^3 p_3}{(2\pi)^3 2E_3 p_{3\chi}(\sqrt{s})\sqrt{s}} |\mathcal{M}_{12 \rightarrow 3\chi}|^2(s, t) F_{123}(T, s, t, E_3). \quad (\text{D.32})$$

The integration over \vec{p}_3 can be rewritten as the integration over E_3 and s using ²

$$s = m_3^2 + m_\chi^2 + 2(E_3 E + p_3 p \cos \theta_{3\chi}), \quad (\text{D.34})$$

to replace the dependence on the angle between \vec{p}_3 and \vec{p}

$$\frac{d^3 p_3}{E_3} = \frac{2\pi d \cos \theta_{3\chi} p_3 E_3 dE_3}{E_3} = \frac{\pi dE_3 ds}{p}. \quad (\text{D.35})$$

However, the integration over E_3 is constrained by Eq. (D.34). From the form of this equation, it is clear that, for fixed masses, and any suitable value of p (hence of s , which will be constrained by masses and p), the maximum value available for p_3 is obtained when $\cos \theta_{3\chi} = -1$ since to satisfy the equality the negative piece allows p_3 to be larger. Likewise, the minimum value of p_3 is obtained when $\cos \theta_{3\chi} = +1$, since now another positive p_3 -dependent term is added, further constraining the size of p_3 . Solving the equation in the two cases we obtain

$$\begin{aligned} p_3^+(s) &= \frac{p(s - m_3^2 - m_\chi^2) + \sqrt{(p^2 + m_\chi^2)k(\sqrt{s}, m_3, m_\chi)}}{2m_\chi^2} && \text{if } \cos \theta_{3\chi} = -1 \\ p_3^-(s) &= \left| \frac{p(s - m_3^2 - m_\chi^2) - \sqrt{(p^2 + m_\chi^2)k(\sqrt{s}, m_3, m_\chi)}}{2m_\chi^2} \right| && \text{if } \cos \theta_{3\chi} = +1 \end{aligned} \quad (\text{D.36})$$

These two expressions are not valid explicitly if $m_\chi = 0$, so as for decays, we provide limiting expressions for $m_\chi \ll m_1, m_2, m_3$, which will be exploited in our work:

$$\begin{aligned} p_3^+(s) &= p \left(\frac{s - m_3^2}{m_\chi^2} - \frac{s}{s - m_3^2} \right) + \frac{s - m_3^2}{4p} + \mathcal{O}(m_\chi^2), \\ p_3^-(s) &= p \left(\frac{m_3^2}{s - m_3^2} \right) - \frac{s - m_3^2}{4p} + \mathcal{O}(m_\chi^2). \end{aligned} \quad (\text{D.37})$$

We see that, for $m_\chi \rightarrow 0$ we have $p_3^+ \rightarrow \infty$, while p_3^- is finite. We can write the integral over $E_3 \in [E_3^-(s), E_3^+(s)]$ with

$$E_3^\pm(s) = \sqrt{m_3^2 + (p_3^\pm(s))^2}, \quad (\text{D.38})$$

²We defined the angle $\theta_{3\chi}$ to let the $\cos \theta_{3\chi}$ appear with plus sign in the expression of s : this helps to change the integration variable from $\cos \theta_{3\chi}$ to s without making mistakes; with our choice, the usual order of extrema of integration is preserved:

$$\int_{-1}^1 d \cos \theta_{3\chi} = \int_{s_{\min}=s(\cos \theta_{3\chi}=-1)}^{s_{\max}=s(\cos \theta_{3\chi}=1)} ds. \quad (\text{D.33})$$

reading

$$\frac{g_\chi C(T, p)}{E} = \frac{g_\chi g_1 g_2 g_3}{512\pi^3 p E} \int_{s_{\min}}^{s_{\max}} \frac{ds}{p_{3\chi}(\sqrt{s})\sqrt{s}} \int_{E_3^-(s)}^{E_3^+(s)} dE_3 \int_{t_{\min}(s)}^{t_{\max}(s)} dt |\mathcal{M}_{12 \rightarrow 3\chi}|^2(s, t) F_{123}(T, s, t, E_3). \quad (\text{D.39})$$

This is the general expression for any choice of the distribution functions f_1, f_2, f_3 . Let us write the boundaries for Mandelstam variables s and t needed to perform the integrals. Clearly, the minimum value of s is obtained if particles have zero momentum in the centre-of-mass in the initial or final state, depending on which is the heavier one. Hence

$$s \in [s_{\min}, +\infty[\equiv \left[\max \left\{ (m_1 + m_2)^2, (m_3 + m_\chi)^2 \right\}, +\infty \right]. \quad (\text{D.40})$$

The variable t in the centre-of-mass frame is given by

$$t = m_1^2 + m_\chi^2 - E_1^{\text{cm}}(s)E^{\text{cm}}(s) + 2 \cos \theta_{B_i\chi} p_{12}(s)p_{3\chi}(s); \quad (\text{D.41})$$

here all variables involved but $\cos \theta_{1\chi}$ are known functions of s . Then the maximum and minimum values of t are found setting $\cos \theta_{1\chi} = +1$ and $\cos \theta_{1\chi} = -1$, respectively:

$$\begin{aligned} t_{\max}(s) &\equiv m_1^2 + m_\chi^2 - E_1^{\text{cm}}(s)E^{\text{cm}}(s) + 2p_{12}(s)p_{3\chi}(s), \\ t_{\min}(s) &\equiv m_1^2 + m_\chi^2 - E_1^{\text{cm}}(s)E^{\text{cm}}(s) - 2p_{12}(s)p_{3\chi}(s). \end{aligned} \quad (\text{D.42})$$

If we assume equilibrium distributions for all particles but χ , we can perform at least the integral over E_3 analytically. We can exploit the detailed balance equation to write, as done in [64]

$$f_1^{\text{eq}} f_2^{\text{eq}} (1 \mp f_3^{\text{eq}}) = (1 \mp f_1^{\text{eq}}) (1 \mp f_2^{\text{eq}}) f_3^{\text{eq}} e^{-E/T} \quad (\text{D.43})$$

The detailed balance forces us to take the Maxwell-Boltzmann distribution for χ since we have neglected the enhancement and blocking factors from scratch. Instead, we can still consider the statistics for the other particles. In the approximation in which we neglect Pauli-blocking and Bose-enhancement factors for particles 1 and 2, this relation allows getting rid of the problem of determining E_1 and E_2 as functions of the integration variables and E . Then we can simply perform the integration over E_3 as we did in the case of decays

$$\frac{g_\chi C(T, p)}{E} = \frac{g_\chi g_1 g_2 g_3}{512\pi^3} \frac{T e^{-E/T}}{p E} \int_{s_{\min}}^{s_{\max}} \frac{ds}{p_{3\chi}(\sqrt{s})\sqrt{s}} h_{\text{eq}}(s, p, T) \int_{t_{\min}(s)}^{t_{\max}(s)} dt |\mathcal{M}_{12 \rightarrow 3\chi}|^2(s, t), \quad (\text{D.44})$$

where

$$h_{\text{eq}}(s, p, T) = \pm \log \left(\frac{1 \pm e^{-E_3^-(s)/T}}{1 \pm e^{-E_3^+(s)/T}} \right), \quad (\text{D.45})$$

with upper signs for fermions and lower for bosons. If we neglect all quantum statistics, we obtain

$$h_{\text{eq}}(s, p, T) = \left(e^{-E_3^-(s)/T} - e^{-E_3^+(s)/T} \right). \quad (\text{D.46})$$

D.2.2 Pair production

Here we treat scatterings of the type

$$1 + 2 \longrightarrow \chi + \chi, \quad (\text{D.47})$$

modelling pair production of χ particles. The analysis is very similar to the previous case with particle 3 now replaced by a χ particle. The collision term is the following The general collision term is

$$\frac{g_\chi C(T, p)}{E} = \frac{g_\chi}{E} \int d\Pi_1 d\Pi_2 d\Pi_\chi (2\pi)^4 \delta^{(4)}(p_1 + p_2 - p_\chi - p) |\mathcal{M}_{12 \rightarrow 3\chi}|^2 F_{123}(T, E_1, E_2), \quad (\text{D.48})$$

where we have defined $F_{12} = f_1(T, E_1) f_2(T, E_2)$ since in our hypothesis we can neglect the blocking and enhancement factors for χ . We have included a factor of 2 at numerator to take into account that each process produces two particles instead of one. We distinguish the momentum p_χ , which is integrated and p , which is instead free. We can write the final result exploiting the outcome of the calculations in the single production case.

$$\frac{g_\chi C(T, p)}{E} = \frac{g_\chi^2 g_1 g_2}{256\pi^3 p E} \int_{s_{\min}}^{s_{\max}} \frac{ds}{p_{3\chi}(\sqrt{s})\sqrt{s}} \int_{E_\chi^-(s)}^{E_\chi^+(s)} dE_\chi \int_{t_{\min}(s)}^{t_{\max}(s)} dt |\mathcal{M}_{12 \rightarrow \chi\chi}|^2(s, t) F_{12}(T, s, t, E_\chi). \quad (\text{D.49})$$

This is the general expression for any choice of the distribution functions f_1, f_2 . Integration limits and $p_{3\chi}$ are found simply by replacing particle 3 with χ is the single production results. If we assume thermal equilibrium distributions, we can write, for the detailed balance

$$f_1^{\text{eq}} f_2^{\text{eq}} = (1 \mp f_1^{\text{eq}})(1 \mp f_2^{\text{eq}}) e^{-(E_\chi + E)/T} \quad (\text{D.50})$$

since we neglected blocking and enhancement factors for χ from scratch. Neglecting quantum statistics for 1 and 2, we perform the integration over E_χ analytically:

$$\frac{g_\chi C(T, p)}{E} = \frac{g_\chi^2 g_1 g_2}{256\pi^3} \frac{T}{p E} \frac{1}{e^{E/T} \pm 1} \int_{s_{\min}}^{s_{\max}} \frac{ds}{p_{3\chi}(\sqrt{s})\sqrt{s}} h_{\text{eq}}(s, p, T) \int_{t_{\min}(s)}^{t_{\max}(s)} dt |\mathcal{M}_{12 \rightarrow \chi\chi}|^2(s, t), \quad (\text{D.51})$$

where

$$h_{\text{eq}}(s, p, T) = \left(e^{-E_\chi^-(s)/T} - e^{-E_\chi^+(s)/T} \right). \quad (\text{D.52})$$

All functions of s are obtained from the expression found in the case of single production but replacing particle with χ . We study the two spectra

D.3 Three-body decays

D.3.1 Single production

In the case of three-body decays

$$1 \rightarrow 2 + 3 + \chi, \quad (\text{D.53})$$

the collision term reads

$$\frac{g_\chi C(T, p)}{E} = \frac{g_\chi}{2E} \int d\Pi_1 d\Pi_2 d\Pi_3 (2\pi)^4 \delta^{(4)}(p_1 - p_2 - p_3 - p) |\mathcal{M}_{1 \rightarrow 23\chi}|^2 G_{123}(T, E_1, E_2, E_3), \quad (\text{D.54})$$

with

$$G_{123} = f_1(T, E_1)[1 \mp f_2(T, E_2)][1 \mp f_3(T, E_3)]. \quad (\text{D.55})$$

As in the case of scatterings, we want to rewrite the integration in terms of Lorentz-invariant quantities, which will be analogous to the Mandelstam variables s and t . In this case, it is convenient to perform the integration over E_1 as the last one, as we did in the previous case with E_3 : if we neglect the Pauli-blocking and Bose-enhancement factors we have only $f_1(T, E_1)$ to integrate and this is easy in the case of equilibrium distributions. In the case of scattering the particles 1 and 2 were treated in the same way, while now we will treat 2 and 3 in the same way. So we can define the following Lorentz-invariant quantities [40]

$$\begin{aligned} s &= -(p_2 + p_3)^2 = -(p_1 - p)^2, \\ t &= -(p_3 + p)^2 = -(p_1 - p_2)^2. \end{aligned} \quad (\text{D.56})$$

The first step is to exploit Lorentz invariance to rewrite the integrations over \vec{p}_2 and \vec{p}_3 in a simpler way. First, we integrate over \vec{p}_2 using the three-dimensional delta

$$\frac{d^3 p_2}{(2\pi)^3 2E_2} \frac{d^3 p_3}{(2\pi)^3 2E_3} (2\pi)^4 \delta^{(4)}(p_1 - p_2 - p_3 - p) = \frac{2\pi d \cos \theta_{3\chi} p_3^2 dp_3}{(2\pi)^2 4E_3 E_2^*} \delta(E_1 - E_2^* - E_3 - E), \quad (\text{D.57})$$

where $E_2^* = \sqrt{m_2^2 + (\vec{p}_1 - \vec{p}_3 - \vec{p})^2}$ and $\theta_{3\chi}$ is the angle between \vec{p}_3 and \vec{p} . Since this expression is Lorentz-invariant, we can compute all the quantities in the centre-of-mass frame of 3 and 2, in which these particles has opposite momenta $\vec{p}_{32} = -\vec{p}_{23}$ with modulus

$$p_{23}(\sqrt{s}) = \frac{k^{1/2}(\sqrt{s}, m_2, m_3)}{2\sqrt{s}} \quad (\text{D.58})$$

and particles 1 and χ have equal momenta $\vec{p}_{1\chi} = \vec{p}_{\chi 1}$ with modulus

$$p_{1\chi}(\sqrt{s}) = \frac{k^{1/2}(\sqrt{s}, m_1, m_\chi)}{2\sqrt{s}}. \quad (\text{D.59})$$

In this reference frame $E_2^* = \sqrt{m_2^2 + (\vec{p}_{23})^2}$ and the right hand side of Eq. (D.57) reads

$$\frac{d \cos \theta_{3\chi} p_{23}^2 dp_{23}}{8\pi E_3^{\text{cm}} E_2^{*,\text{cm}}} \delta \left(\sqrt{s} - \sqrt{m_3^2 + p_{23}^2} - \sqrt{m_2^2 + p_{23}^2} \right). \quad (\text{D.60})$$

We can trade the integration over the angle with the one over t , which in the chosen frame reads

$$t = m_3^2 + m_\chi^2 + 2(E_3^{\text{cm}} E_3^{\text{cm}} - p_{1\chi} p_{23} \cos \theta_{3\chi}). \quad (\text{D.61})$$

We obtain

$$\frac{d^3 p_2}{(2\pi)^3 2E_2} \frac{d^3 p_3}{(2\pi)^3 2E_3} (2\pi)^4 \delta^{(4)}(p_1 - p_2 - p_3 - p) = -\frac{dt}{16\pi p_{1\chi}(\sqrt{s})\sqrt{s}}. \quad (\text{D.62})$$

We rewrite the integration over \vec{p}_1 replacing the angle dependence with s :

$$\frac{d^3 p_1}{E_1} = \frac{2\pi d \cos \theta_{1\chi} p_1 E_1 dE_1}{E_1} = -\frac{\pi ds dE_3}{p}. \quad (\text{D.63})$$

Therefore the collision term reads

$$\frac{g_\chi C(T, p)}{E} = \frac{g_\chi g_1 g_2 g_3}{512\pi^3 p E} \int \frac{ds dE_1}{p_{1\chi}(\sqrt{s})\sqrt{s}} \int dt |\mathcal{M}_{1 \rightarrow 23\chi}|^2(s, t) G_{123}(T, s, t, E_1). \quad (\text{D.64})$$

The integration over E_1 is constrained by s , like in the case of scatterings considered above. The boundaries are found exactly in the same way as before, with a difference in sign in the expression of s . Notice that $s \leq m_1^2 + m_\chi^2$. We quote the resulting expressions

$$p_1^+(s) = \frac{p(m_\chi^2 + m_1^2 - s) + \sqrt{(p^2 + m_\chi^2)k(\sqrt{s}, m_1, m_\chi)}}{2m_\chi^2} \quad \text{if } \cos \theta_{1\chi} = +1$$

$$p_1^-(s) = \left| \frac{p(m_\chi^2 + m_1^2 - s) - \sqrt{(p^2 + m_\chi^2)k(\sqrt{s}, m_1, m_\chi)}}{2m_\chi^2} \right| \quad \text{if } \cos \theta_{1\chi} = -1 \quad (\text{D.65})$$

These two expressions are not valid explicitly if $m_\chi = 0$, so as usual, we provide limiting expressions for $m_\chi \ll m_1, m_2, m_3$, which will be exploited in our work:

$$p_1^+(s) = p \left(\frac{m_1^2 - s}{m_\chi^2} - \frac{s}{m_1^2 - s} \right) + \frac{m_1^2 - s}{4p} + \mathcal{O}(m_\chi^2),$$

$$p_1^-(s) = p \left(\frac{m_1^2}{m_1^2 - s} \right) - \frac{m_1^2 - s}{4p} + \mathcal{O}(m_\chi^2). \quad (\text{D.66})$$

We see that, for $m_\chi \rightarrow 0$ we have $p_1^+ \rightarrow \infty$, while p_1^- is finite. We can write the integral over $E_1 \in [E_1^-(s), E_1^+(s)]$ with

$$E_1^\pm(s) = \sqrt{m_1^2 + (p_1^\pm(s))^2}, \quad (\text{D.67})$$

reading

$$\frac{g_\chi C(T, p)}{E} = \frac{g_\chi g_1 g_2 g_3}{512\pi^3 p E} \int_{s_{\min}}^{s_{\max}} \frac{ds}{p_{1\chi}(\sqrt{s})\sqrt{s}} \int_{E_1^-(s)}^{E_1^+(s)} dE_1 \int_{t_{\min}(s)}^{t_{\max}(s)} dt |\mathcal{M}_{1 \rightarrow 23\chi}|^2(s, t) G_{123}(T, s, t, E_1). \quad (\text{D.68})$$

This is the general expression for any choice of the distribution functions f_1, f_2, f_3 . We have to explicit the limits of integration over s and t . The minimum value of s is $(m_2 + m_3)^2$, obtained when 2 and 3 are produced still in their centre-of-mass frame. The maximum value is obtained when $E = m_\chi$, hence when the χ particle is produced still. Hence

$$s \in \left[(m_2 + m_3)^2, (m_1 - m_\chi)^2 \right]. \quad (\text{D.69})$$

The variable t in the centre-of-mass frame is given by

$$t = m_3^2 + m_\chi^2 + 2E_3^{\text{cm}}(s)E^{\text{cm}}(s) - 2\cos\theta_{3\chi}p_{1\chi}(s)p_{23}(s) \quad (\text{D.70})$$

and it is fully determined as a function of s apart from $\cos\theta_{3\chi}$. Therefore the maximum and minimum are obtained respectively for $\cos\theta_{3\chi} = -1$ and $\cos\theta_{3\chi} = +1$:

$$\begin{aligned} t_{\max}(s) &= m_3^2 + m_\chi^2 + 2E_3^{\text{cm}}(s)E^{\text{cm}}(s) + 2p_{1\chi}(s)p_{23}(s), \\ t_{\min}(s) &= m_3^2 + m_\chi^2 + 2E_3^{\text{cm}}(s)E^{\text{cm}}(s) - 2p_{1\chi}(s)p_{23}(s). \end{aligned} \quad (\text{D.71})$$

If we assume equilibrium distributions for all particles but χ we can perform at least the integral over E_1 analytically. As before, if we neglect Pauli-blocking and Bose-enhancement factors for particles 2 and 3, we get the usual result

$$\frac{g_\chi C(T, p)}{E} = \frac{g_\chi g_1 g_2 g_3}{512\pi^3} \frac{T}{pE} \int_{s_{\min}}^{s_{\max}} \frac{ds}{p_{1\chi}(\sqrt{s})\sqrt{s}} h_{\text{eq}}(s, p, T) \int_{t_{\min}(s)}^{t_{\max}(s)} dt |\mathcal{M}_{1 \rightarrow 23\chi}|^2(s, t), \quad (\text{D.72})$$

with

$$h_{\text{eq}}(s, p, T) = \pm \log \left(\frac{1 \pm e^{-E_1^-(s)/T}}{1 \pm e^{-E_1^+(s)/T}} \right) \quad (\text{D.73})$$

and upper signs for fermions and lower for bosons. Finally, neglecting all corrections from quantum statistics, we obtain

$$h_{\text{eq}}(s, p, T) = e^{-E_1^-(s)/T} - e^{-E_1^+(s)/T}. \quad (\text{D.74})$$

D.3.2 Pair production

The analysis of three-body decays of the type

$$1 \rightarrow 2 + \chi + \chi, \quad (\text{D.75})$$

is practically identical to the single production case. The collision term reads

$$\frac{g_\chi C(T, p)}{E} = \frac{g_\chi}{E} \int d\Pi_1 d\Pi_2 d\Pi_\chi (2\pi)^4 \delta^{(4)}(p_1 - p_2 - p_\chi - p) |\mathcal{M}_{1 \rightarrow 2\chi\chi}|^2 G_{12}(T, E_1, E_2), \quad (\text{D.76})$$

with

$$G_{12} = f_1(T, E_1)[1 \mp f_2(T, E_2)]. \quad (\text{D.77})$$

We have multiplied the collision term by a factor of 2 to take into account that each process produces two particles χ , which both contribute to the final phase-space distribution. The final general result is

$$\frac{g_\chi C(T, p)}{E} = \frac{g_\chi^2 g_1 g_2}{256\pi^3 p E} \int_{s_{\min}}^{s_{\max}} \frac{ds}{p_{1\chi}(\sqrt{s})\sqrt{s}} \int_{E_1^-(s)}^{E_1^+(s)} dE_1 \int_{t_{\min}(s)}^{t_{\max}(s)} dt |\mathcal{M}_{1 \rightarrow 2\chi\chi}|^2(s, t) G_{12}(T, s, t, E_1). \quad (\text{D.78})$$

If we assume thermal distributions for particles 1 and 2 and neglect Bose-enhancement and Pauli-blocking factors, we get

$$\frac{g_\chi C(T, p)}{E} = \frac{g_\chi^2 g_1 g_2}{256\pi^3 p E} \frac{T}{p E} \int_{s_{\min}}^{s_{\max}} \frac{ds}{p_{1\chi}(\sqrt{s})\sqrt{s}} h_{\text{eq}}(s, p, T) \int_{t_{\min}(s)}^{t_{\max}(s)} dt |\mathcal{M}_{1 \rightarrow 2\chi\chi}|^2(s, t), \quad (\text{D.79})$$

with

$$h_{\text{eq}}(s, p, T) = \pm \log \left(\frac{1 \pm e^{-E_1^-(s)/T}}{1 \pm e^{-E_1^+(s)/T}} \right) \quad (\text{D.80})$$

and upper signs for fermions and lower for bosons. Finally, neglecting all corrections from quantum statistics, we obtain

$$h_{\text{eq}}(s, p, T) = e^{-E_1^-(s)/T} - e^{-E_1^+(s)/T}. \quad (\text{D.81})$$

All functions of s are obtained simply replacing particle 3 with χ in the expressions derived for the single production in three-body decays.

Bibliography

- [1] L.J. Hall, K. Jedamzik, J. March-Russell, et al., Freeze-in production of FIMP Dark Matter, *JHEP* **80**, (2010), [https://doi.org/10.1007/JHEP03\(2010\)080](https://doi.org/10.1007/JHEP03(2010)080).
- [2] G. Bertone, D. Hooper & J. Silk, Particle Dark Matter: Evidence, Candidates and Constraints, *Phys. Rept.* **405** 279-390 (2005) , <https://arxiv.org/abs/hep-ph/0404175>.
- [3] K. Freese, Status of Dark Matter in the Universe, (2017), <https://arxiv.org/abs/1701.01840>
- [4] M. Bauer, T. Plehn, Yet Another Introduction to Dark Matter, (2017), <https://arxiv.org/abs/1705.01987>.
- [5] F. Zwicky, Die Rotverschiebung von extragalaktischen Nebeln, *Helvetica Physica Acta* **6**, 110-127 (1933), <https://arxiv.org/abs/1711.01693>.
- [6] G. Bertone & D. Hooper, A History of Dark Matter, *Rev. Mod. Phys.* **90**, 045002 (2018), <https://arxiv.org/abs/1605.04909>.
- [7] J. de Swart, G. Bertone & J. van Dongen, How Dark Matter Came to Matter, *Nature Astron.* **1**, 0059 (2017), <https://arxiv.org/abs/1703.00013>.
- [8] K. C. Freeman, On the Disks of Spiral and S0 Galaxies. *Astrophysical Journal* **160**, 811 (1970).
- [9] V. C. Rubin, J. Ford W. Kent, Rotation of the Andromeda Nebula from a Spectroscopic Survey of Emission Regions, *Astrophysical Journal* **159**, 379 (1970).
- [10] K. G. Begeman, A. H. Broeils & R. H. Sanders, *MNRAS* **249**, 523 (1991).
- [11] F. Iocco, M. Pato & G. Bertone, Evidence for dark matter in the inner Milky Way, *Nature Physics* **11**, 245-248 (2015), <https://arxiv.org/abs/1502.03821>.
- [12] R. Massey, T. Kitching & J. Richard, The dark matter of gravitational lensing, *Rep. on Prog. in Physics* **73**, 8 (2010), <https://arxiv.org/abs/1001.1739v2>.
- [13] R.P. Olling & M.R. Merrifield, *MNRAS* **311**, 361 (2000).

- [14] J. Sakstein & B. Jain, Implications of the Neutron Star Merger GW170817 for Cosmological Scalar-Tensor Theories. *Phys. Rev. Lett.* **119**, 251303 (2017), <https://arxiv.org/abs/1710.05893>.
- [15] D. Clowe, M. Bradač, A. H. Gonzalez, M. Markevitch, S. W. Randall, C. Jones & D. Zaritsky, A direct empirical proof of the existence of dark matter, *Astrophysics J.*, **648**, L109-L113 (2006), <https://arxiv.org/abs/astro-ph/0608407>.
- [16] S. Dodelson, *Modern Cosmology*, Academic Press Elsevier (2003).
- [17] Planck Collaboration: N. Aghanim et al., Planck 2018 results. VI. Cosmological parameters, (2018), <https://arxiv.org/abs/1807.06209>.
- [18] B.D. Fields & S. Sarkar Big-bang nucleosynthesis, *Phys. Rev. D* **66**, 010001 162 (2002), <https://arxiv.org/abs/1412.1408>.
- [19] The Supernova Cosmology Project: S. Perlmutter et al., Measurements of Omega and Lambda from 42 High-Redshift Supernovae, *Astrophys.J.* **517**, 565-586 (1999), <https://arxiv.org/abs/astro-ph/9812133>.
- [20] E. W. Kolb & M. S. Turner, *The Early Universe*, Frontiers in Physics, Westview Press (1994).
- [21] V.A. Rubakov, *Cosmology*, CERN Yellow Report CERN-2014-003, 151-196 (2004), <https://arxiv.org/abs/1504.03587>.
- [22] SDSS Collaboration: M. Tegmark et al., *Astrophys. J.* **606**, 702 (2004), <https://arxiv.org/abs/astro-ph/0310725>.
- [23] S. Colombi, S. Dodelson & L. M. Widrow Large, Scale Structure Tests of Warm Dark Matter, *Astrophys. J.* **458**, 1 (1996), <https://arxiv.org/abs/astro-ph/9505029>.
- [24] L. Perotto et al., Reconstruction of the CMB lensing for Planck, (2009), <https://arxiv.org/abs/0903.1308>.
- [25] S. Profumo, L. Giani, O.F. Piattella, An Introduction to Particle Dark Matter, *Universe* 2019, 5(10) 213 (2019), <https://doi.org/10.3390/universe5100213>.
- [26] J. B. Muñoz, A. Loeb, A small amount of mini-charged dark matter could cool the baryons in the early Universe. *Nature* **557**, 684-686 (2018), <https://www.nature.com/articles/s41586-018-0151-x>.
- [27] T. Brinckmann, J. Zavala, D. Rapetti et al., The structure and assembly history of cluster-sized haloes in self-interacting dark matter, *MNRAS* **474**, 746-759 (2018), <https://arxiv.org/abs/1705.00623>.
- [28] M. Rocha, A. H. G. Peter, J. S. Bullock et al., *Cosmological Simulations with Self-*

- Interacting dark matter I: Constant Density Cores and Substructure, *MNRAS* **430**, 81-104 (2013).
- [29] S. Tremaine & J.E. Gunn, Dynamical Role of Light Neutral Leptons in Cosmology, *Phys. Rev. Lett.* **42**, 407–410 (1979), doi:10.1103/PhysRevLett.42.407.
- [30] T. R. Slatyer & C-L Wu, General Constraints on Dark Matter Decay from the Cosmic Microwave Background, *Phys. Rev. D* **95**, 023010 (2017), <https://arxiv.org/abs/1610.06933>.
- [31] B. Audren et al., Strongest model-independent bound on the lifetime of Dark Matter, *JCAP* **12**, 028 (2014), <https://arxiv.org/abs/1407.2418>.
- [32] K. Saikawa & S. Shirai, Primordial gravitational waves, precisely: The role of thermodynamics in the Standard Model, *JCAP* **05**, 035 (2018), <https://arxiv.org/abs/1803.01038>.
- [33] G. Bertone, T. M.P. Tait, A New Era in the Quest for Dark Matter, *Nature* **562**, 51-56 (2018) <https://arxiv.org/abs/1810.01668>.
- [34] E. Aprile et al. (XENON Collaboration) *Phys. Rev. Lett.* **121**, 111302 (2018), <https://arxiv.org/abs/1805.12562>.
- [35] D. S. Akerib et al. (LUX Collaboration), *Phys. Rev. Lett.* **118** 021303 (2017).
- [36] X. Cui et al. (PandaX-II Collaboration), *Phys. Rev. Lett.* **119**, 181302 (2017).
- [37] J. Billard, E. Figueroa-Feliciano, & L. Strigari *Phys. Rev. D* **89**, 023524 (2014), <https://arxiv.org/abs/1805.12562>.
- [38] N. Bernal et al., The Dawn of FIMP Dark Matter: A Review of Models and Constraints, *Int. J. of Mod. Phys. A*, **32**, 27 1730023 (2017), <https://arxiv.org/abs/1706.07442>.
- [39] F. D’Eramo, N. Fernandez, S. Profumo, Dark Matter Freeze-in Production in Fast-Expanding Universes, *JCAP* **1802**, 046 (2018), <https://arxiv.org/abs/1712.07453>
- [40] M. Maggiore, *A Modern Introduction to Quantum Field Theory*, Oxford University Press (2005).
- [41] T. Hambye, M. H. G. Tytgat, J. Vandecasteele and L. Vanderheyden, *Phys. Rev. D* **98**, 075017 (2018), <https://arxiv.org/abs/1807.05022>
- [42] B. Holdom, Two U(1)’s and Epsilon Charge Shifts, *Phys. Lett.* **166B**, 196-198 (1986).
- [43] M. Chianese and A. Merle, A Consistent Theory of Decaying Dark Matter Connecting IceCube to the Sesame Street, *JCAP* **1704**, 017 (2017), <https://arxiv.org/abs/1607.05283>.

- [44] R. Essig, E. Kuflik, S. D. McDermott, T. Volansky, and K. M. Zurek, Constraining Light Dark Matter with Diffuse X-Ray and Gamma-Ray Observations, *JHEP* **11** (2013), <https://arxiv.org/abs/1309.4091>.
- [45] A. Boyarsky, O. Ruchayskiy, D. Iakubovskiy, and J. Franse, Unidentified Line in X-Ray Spectra of the Andromeda Galaxy and Perseus Galaxy Cluster, *Phys. Rev. Lett.* **113**, 251301 (2014), <https://arxiv.org/abs/1402.4119>.
- [46] M. Heikinheimo and C. Spethmann, Galactic Centre GeV Photons from Dark Technicolor, *JHEP* **12**, 084 (2014), <https://arxiv.org/abs/1410.4842>.
- [47] R. T. Co, F. D’Eramo, L. J. Hall, and D. Pappadopulo, Freeze-In Dark Matter with Displaced Signatures at Colliders, *JCAP* **1512**, 024 (2015), <https://arxiv.org/abs/1506.07532>.
- [48] D. H. Weinberg, J. S. Bullock, F. Governato, R. K. de Naray, and A. H. G. Peter. Cold dark matter: controversies on small scales. *Proc. Nat. Acad. Sci.*, **112**, 12249-12255 (2015).
- [49] M. G. Walker et al. *Contemp.Phys.* **55** no.3, 198-211 (2014) <https://arxiv.org/abs/1401.1146>.
- [50] J. F. Navarro, C. S. Frenk, and S. D. M. White, The Structure of cold dark matter halos, *Astrophys. J.*, **462**, 563-575 (1996).
- [51] W. Hu, R. Barkana, and A. Gruzinov. Cold and fuzzy dark matter. *Phys. Rev. Lett.*, **85**, 1158-1161 (2000).
- [52] R. K. de Naray, S. S. McGaugh, W. J. and de Blok, Mass Models for Low Surface Brightness Galaxies with High-Resolution Optical Velocity Fields, *Astrophys. J.*, **676**, 920 (2008).
- [53] S.-H. Oh et al., Dark and Luminous Matter in THINGS Dwarf Galaxies. *Astronomical Journal* **141**, 193, June (2011).
- [54] V. Springel et al., The Aquarius Project: the subhaloes of galactic haloes. *Monthly Notices of the Royal Astronomical Society* **393**, 1685–1711, December (2008).
- [55] L. Hui, J. P. Ostriker, S. Tremaine, and E. Witten. Ultralight scalars as cosmological dark matter. *Phys. Rev. D* **95(4)** 043541, (2017).
- [56] V. Iršič et al., New Constraints on the free-streaming of warm dark matter from intermediate and small scale Lyman- α forest data, *Phys. Rev. D* **96**, 023522 (2017), <https://arxiv.org/abs/1702.01764>.
- [57] M. Rocha, A. H. G. Peter, J. S. Bullock, M. Kaplinghat, S. Garrison-Kimmel, J. Onorbe, and L. A. Moustakas. Cosmological Simulations with Self-Interacting dark

- matter I: Constant Density Cores and Substructure. *Mon. Not. Roy. Astron. Soc.*, **430** 81–104, (2013).
- [58] A. Kamada, K. Yanagi, Constraining FIMP from the structure formation of the Universe: analytic mapping from m_{WDM} *JCAP* **1911**, 029 (2019), <https://arxiv.org/abs/1907.04558>.
- [59] H. An, M. Pospelov, J. Pradler, A. Ritz, Direct Detection Constraints on Dark Photon Dark Matter, *Phys.Lett. B* **747**, 331-338 (2015), <https://arxiv.org/abs/1412.8378>.
- [60] J. H. Chang, R. Essig, S. D. McDermott, Revisiting Supernova 1987A Constraints on Dark Photons, *JHEP* **1701**, 107 (2017), <https://arxiv.org/abs/1611.03864>.
- [61] A. Fradette, M. Pospelov, J. Pradler, and A. Ritz, Cosmological Constraints on Very Dark Photons, *Phys. Rev. D* **90**, 3 035022 (2014), <https://arxiv.org/abs/1407.0993>.
- [62] A. Biswas and A. Gupta, Freeze-in Production of Sterile Neutrino Dark Matter in $U(1)_{B-L}$ Model, *JCAP* **1609**, 044 (2016), <https://arxiv.org/abs/1607.01469>.
- [63] J. König, A. Merle, and M. Totzauer, keV Sterile Neutrino Dark Matter from Singlet Scalar Decays: The Most General Case, *JCAP* **1611**, 038 (2016), <https://arxiv.org/abs/1609.01289>.
- [64] K. J. Bae, A. Kamada, S. P. Liew, and K. Yanagi, Light axinos from freeze-in: production processes, phase-space distributions, and Ly- α forest constraints, *JCAP* **1801**, 054 (2018), <https://arxiv.org/abs/1707.06418>.
- [65] A. Biswas and A. Gupta, Calculation of Momentum Distribution Function of a Non-thermal Fermionic Dark Matter, *JCAP* **1703**, 033 (2017), <https://arxiv.org/abs/1612.02793>.
- [66] M. Viel, J. Lesgourgues, M. G. Haehnelt, S. Matarrese and A. Riotto, Constraining warm dark matter candidates including sterile neutrinos and light gravitinos with WMAP and the Lyman-alpha forest, *Phys. Rev. D* **71**, 063534 (2005), <https://arxiv.org/abs/astro-ph/0501562>.
- [67] J. Heck, D. Teresi, Cold keV dark matter from decays and scatterings, *Phys. Rev. D* **96**, 035018 (2017), <https://arxiv.org/abs/1706.09909>.
- [68] D. Blas, J. Lesgourgues, and T. Tram, “The Cosmic Linear Anisotropy Solving System (CLASS) II: Approximation schemes,” *JCAP* **1107**, 034 (2011), <https://arxiv.org/abs/1104.2933>.
- [69] J. Lesgourgues and T. Tram, The Cosmic Linear Anisotropy Solving System (CLASS) IV: efficient implementation of non-cold relics, *JCAP* **1109**, 032 (2011), <https://arxiv.org/abs/1104.2933>.

arxiv.org/abs/1104.2935.

- [70] G. Mangano et al., Relic neutrino decoupling including flavour oscillations, Nucl.Phys. B729, 221-234 (2005), <https://arxiv.org/abs/hep-ph/0506164>.